Modeling electrochemical CO_2 and N_2 reduction reactions on transition metals and metal oxides

Ebrahim Tayyebi

Faculty of Industrial Engineering, Mechanical Engineering and Computer Science
University of Iceland

Modeling electrochemical CO_2 and N_2 reduction reactions on transition metals and metal oxides

Ebrahim Tayyebi

Dissertation submitted in partial fulfillment of a
Philosophiae Doctor degree in Chemical Engineering

Advisor
Prof. Egill Skúlason

PhD Committee
Prof. Egill Skúlason
Prof. Hannes Jónsson
Dr. Elvar Örn Jónsson

Opponents
Prof. Anders Hellman
Prof. Lars C. Grabow

Faculty of Industrial Engineering, Mechanical Engineering
and Computer Sciences
University of Iceland
Reykjavik, October 2020

Modeling electrochemical CO_2 and N_2 reduction reactions on transition metals and metal oxides.
Dissertation submitted in partial fulfillment of a *Philosophiae Doctor* degree in Chemical Engineering

Faculty of Industrial Engineering, Mechanical Engineering
and Computer Sciences
University of Iceland
Tæknigarði, Dunhaga 5
107, Reykjavik
Iceland

Telephone: 525 4000

Bibliographic information:
Ebrahim Tayyebi, 2020, Modeling electrochemical CO_2 and N_2 reduction reactions on transition metals and metal oxides, PhD dissertation, Faculty of Industrial Engineering, Mechanical Engineering and Computer Sciences,
University of Iceland, 115 pp.

Author ORCID: 0000-0002-9461-0410

Printing: Háskólaprent, Fálkagata 2, 107 Reykjavík
Reykjavik, Iceland, October 2020

Abstract

The main target of this thesis is to use density functional theory-based simulations to study electrochemical CO_2 and N_2 reductions by employing a recent theoretical model of an electrochemical solid-liquid interface. This model is used to investigate the kinetics of such reactions. However, initially, a simple thermochemical model is used to study electrochemical CO_2 reduction reaction (CO_2RR) on 12 transition metal oxides (TMOs). We utilize models of rutile oxide (110) surfaces to investigate trends and limitations of CO_2RR on those TMOs. We construct scaling law based thermodynamic volcano relation for CO_2RR. Accordingly, we propose guidelines for hydrogen and OH binding free energy range where low overpotentials and high selectivity are predicted for CO_2RR using certain oxides. Therefore, this provides guidance to future development of oxide catalysts for CO_2RR.

To get more insight into CO_2RR on TMOs more detailed calculations are required which take into account the kinetics involved of various possible branching paths and towards different products. Since such calculations are computationally demanding we focus on the $RuO_2(110)$ surface where most experiments have been reported. Ab initio molecular dynamic simulations at room temperature and total energy calculations are used to improve the model system and methodology for CO_2RR on $RuO_2(110)$ by including both explicit solvation effects and calculate proton-electron transfer energy barriers to elucidate the reaction mechanism towards various products; methanol, methane, CO(g), formic acid, methanediol and hydrogen. A significant difference in energy barriers towards methane and methanol is observed. The formation and role of CO as a spectator species is justified. We conclude that hydrogen is the main product at the potential range of -0.2 V to -0.9 V which is in agreement with recent experimental results. The calculated overpotential for methanol formation is found to be around -1 V. Furthermore, the calculations show why RuO_2 also catalyzes CO_2RR towards formic acid and CO(g) in a trace amount, in agreement with experimental observations.

Finally, the possibility of synthesizing ammonia electrochemically is explored. Density functional theory calculations are used to elucidate the mechanism of the nitrogen reduction reaction (NRR) in an electrochemical double layer on the Ru(0001) electrode. The first protonation step of N_2 to NNH is found to be the potential limiting step in agreement with thermodynamic calculations and the additional proton-electron transfer barrier is neglectable. The optimal mechanism of NRR towards ammonia on Ru(0001) follows an associative mechanism where after the third proton−electron transfer, the N−N bond is broken in $N{-}NH_3$, releasing the first NH_3 molecule and leaving N adsorbed on the surface. We find that this detailed kinetic study using a realistic model of the electrochemical solid-liquid interface predicts quiet similar reaction pathway as previously reported using the simple thermochemical model.

Útdráttur

Meginmarkmið þessarar ritgerðar er notkun tölvureikninga sem byggja á þéttifellafræði við rannsóknir á rafefnafræðilegri afoxun á CO_2 og N_2. Stuðst er við nýlegt líkan af rafefnafræðilegum samskeytum rafskauts og rafvaka sem gerir okkur kleyft að rannsaka hreyfifræði fyrrnefndra afoxunarhvarfa. Fyrst er einfalt varmafræðilegt líkan notað við athuganir á rafefnaræðilegri CO_2 afoxun á 12 hliðarmálma-oxíðum. Notast er við yfirborð rútíl kristalbyggingarinnar til að kanna fýsileika CO_2 afoxunar á málmoxíða-hvötum. Skölun bindiorku mismunandi milliefna er reiknuð og notuð til þess að leggja fram viðmið fyrir bindifríorku vetnis og hýdroxíðs á hvötum sem sýna bæði góða virkni og sértækni við afoxun CO_2. Þær niðurstöður má í framhaldinu nota við frekari þróun hvata fyrir rafefnafræðilega CO_2 afoxun.

Til að öðlast frekari innsýn á afoxunarhvarfi CO_2 á hliðarmálmsoxíðum þarf að framkvæma nákvæmari reikninga. Slíkir reikningar krefjast mikils tölvutíma svo framkvæmd þeirra fyrir öll 12 hliðarmálmsoxíðin er ekki fýsileg fyrir eitt og sama doktorsverkefnið. Þar af leiðandi einbeittum við okkur að RuO_2(110) yfirborði. Við framkvæmum hermanir sem byggja á grunnlögmálum náttúrunar til þess að spá fyrir um hreyfifræði sameinda við stofuhita, auk reikninga á heildarorku kerfisins, til þess að bæta bæði líkanið og aðferðafræðina sem notast hefur verið við hingað til. Þessir reikningar varpar ljósi á hvarfgang rafefnafræðilegrar CO_2 afoxunar á RuO_2 með því að kanna áhrif vatns á hvarfið auk þess sem rafefnafræðilegir virkjunarhólar eru reiknaðir. Hægt er að áætla hlutfallslegt magn mismunandi myndefna, svo sem metans, metnóls, CO(g), maurasýru, metandíóls og vetnis. Við finnum talsverðan mun á virkjunarhólum fyrir myndun metans og metanóls í samræmi við tilraunir sem hafa sýnt metanól myndun en ekki metan. Myndun og óbein áhrif CO sameindarinnar í CO_2 afoxun er útskýrt. Einnig finnum við að vetni er meginmyndefnið fyrir álagða spennu á bilinu -0.2 V til -0.9 V, sem er í góðu samræmi við nýlegar tilraunir. Áætluð yfirspenna fyrir myndun metanóls er um -1 V. Reikningarnir sýna auk þess hvers vegna RuO_2 virkar sem hvati fyrir afoxun CO_2 í maurasýru og CO(g) í snefilmagni, í samræmi við tilraunir.

Loks athugum við rafefnafræðilega myndun ammoníaks á Ru yfirborði. Notast er við þéttnifellafræðireikninga til að varpa ljósi á hvarfgang niturafoxunar á mótum rafvaka og Ru(0001) rafskauts. Enginn virkjunarhóll annar en varmafræðilegur fannst fyrir fyrsta prótonu-rafeinda flutnings skrefið þar sem NNH millisameind myndast frá nitursameind, en við teljum þetta skref vera spennu takmarkandi fyrir afoxun niturs á Ru(0001) yfirborði. Hvarfgangurinn sem við spáum fyrir afoxun niturs á Ru(0001) er þar sem nitursamdeindin sundrast ekki strax heldur afoxast sameindin á yfirborðinu þangað til þrjú prótónu-rafeinda pör hafa bundist á ytra nituratómið. Þá sundrast N-NH_3 tengið og myndar fyrstu NH_3 sameindina og nitur atóm verður eftir á yfirborðinu og afoxað að lokum í ammóníak. Hér finnum við að nákvæm rannókn á hraðafræði hvarfsins, þar sem notast er við rafefnafræðilegt rafskauts-vökva samskeyta líkan, spáir fyrir um svipaðan hvarfgang og áður hefur verið gert með einföldu varmafræðilegu líkani.

Nobel-winning physicist Richard P. Feynman (May 11, 1918–February 15, 1988) was a champion of scientific culture, graphic novel hero, crusader for integrity, holder of the key to science, adviser of future generations, bongo player, no ordinary genius.

Richard P. Feynman's Famous Monologue on Knowledge and Mystery

I have a friend who's an artist and has sometimes taken a view which I don't agree with very well. He'll hold up a flower and say, "look how beautiful it is," and I'll agree. Then he says, "I as an artist can see how beautiful this is but you as a scientist take this all apart and it becomes a dull thing," and I think that he's kind of nutty. First of all, the beauty that he sees is available to other people and to me too, I believe…

I can appreciate the beauty of a flower. At the same time, I see much more about the flower than he sees. I could imagine the cells in there, the complicated actions inside, which also have a beauty. I mean it's not just beauty at this dimension, at one centimeter; there's also beauty at smaller dimensions, the inner structure, also the processes. The fact that the colors in the flower evolved in order to attract insects to pollinate it is interesting; it means that insects can see the color. It adds a question: does this aesthetic sense also exist in the lower forms? Why is it aesthetic? All kinds of interesting questions which the science knowledge only adds to the excitement, the mystery and the awe of a flower. It only adds. I don't understand how it subtracts.

Video link:

https://www.youtube.com/watch?v=cRmbwczTC6E

or you can also search "THE FEYNMAN SERIES – Beauty" on YouTube.

Preface

This thesis is submitted in candidacy for a Ph.D. degree from the University of Iceland. The work has been conducted between August 2016 and July 2020 at Faculty of Industrial Engineering, Mechanical Engineering and Computer Sciences supervised by Prof. Egill Skúlason.

Icelandic Research Fund (grant no. 196437-051, 152619-051), the Research Fund of the University of Iceland and the 'Nordic Consortium for CO_2 Conversion' (NordForsk project no. 85378, http://site.uit.no/nordco2) financially supported the work.

Ebrahim Tayyebi

October 2020

Table of Contents

List of Figures

List of Papers

I. Tayyebi, E.; Hussain, J.; Abghoui, Y.; Skúlason, E. Trends of Electrochemical CO_2 Reduction Reaction on Transition Metal Oxide Catalysts. **J. Phys. Chem. C.,** 2018, 122, 10078−10087.

II. Tayyebi, E.; Hussain, J.; Skúlason, E. Why do RuO_2 electrodes catalyze electrochemical CO_2 reduction to methanol rather than methane or perhaps neither of those? **Chemical Science.,** 2020, 11, 9542-9553.

III. Tayyebi, E.; Abghoui, Y.; Skúlason, E. Elucidating the Mechanism of Electrochemical N_2 Reduction at the Ru (0001) Electrode. **ACS Catalysis.,** 2019, 9, 11137-11145.

My contribution to the publications

Paper I

I performed most of the calculations. I did all the analysis of data. I wrote the first draft of the manuscript.

Paper II

I performed all the calculations and all the analysis of data. I wrote the first draft of the manuscript.

Paper III

I performed all the calculations and all the analysis of data. I wrote the first draft of the manuscript.

Abbreviations and symbols

TM	Transition Metals
TMO	Transition Metal Oxides
DFT	Density Functional Theory
CHE	Computational Hydrogen Electrode
HER	Hydrogen Evolution Reaction
CO_2RR	Carbon Dioxide Reduction Reaction
NRR	Nitrogen Reduction Reaction
SHE	Standard Hydrogen Electrode
U	Applied Potential
ML	Mono Layer
MEP	Minimum Energy Path
PDS	Potential Determining Step
RDS	Rate Determining Step
IS	Initial State
TS	Transition State
FS	Final State
PES	Potential Energy Surface
NEB	Nudge Elastic Band
CI-NEB	Climbing Image Nudge Elastic Band
HF	Hartree-Fock
HK	Hohenberg-Kohn
KS	Kohn-Sham
LDA	Local Density Approximation

GGA	Generalized Gradient Approximation
PAW	Projector Augmented Wave
PBE	Perdew-Burke-Eernzerhof
BEEF	Bayesian-Error-Estimation-Functional
RPBE	Revised Perdew-Burke-Eernzerhof
Ψ	Wave Function
$\hat{\mathrm{H}}$	Hamiltonian Operator
$\mathrm{E_{xc}}$	Exchange Correlation Energy
μ	Chemical Potential
$\Delta \mathrm{G}$	Free Energy Changes
$\mathrm{E_a}$	Activation Energy
i	Current Density
$\mathrm{q^M}$	Charge on the Metal Electrodes
$\mathrm{q^S}$	Charge in the Solution
σ	Charge Density
$\mathrm{C_d}$	Capacitance
G_{int}	Integral Free Energy
U_{pzc}	Potential of Zero Charge
N	Number of Surface Metal Atoms
n	Number of Protons in Double Layer

Acknowledgements

I am very grateful to my thesis supervisor, Prof. Egill Skúlason, for his guidance, support and encouragement throughout my stay, which allowed me to explore and learn at my own pace. I would like to thank to Prof. Hannes Jónsson for his fruitful discussions and helpful comments and suggestions and for serving as a member of my Ph.D. committee. Special thanks to Dr. Elvar Örn Jónsson for serving as a committee member of my Ph.D. dissertation and Dr. Javed Hussain who has been always a mentor for me.

A special acknowledging goes to Prof. Anders Hellman (Chalmers University of Technology) and Prof. Lars C. Grabow (University of Houston) for agreeing to serve as opponents of my Ph.D. thesis and defence.

My special thanks to Prof. Jan Rossmeisl, Dr. Alexander Bagger and Dr. Logi Arnarson (Copenhagen University, Denmark) for wonderful discussion on modeling pH and potential in dynamic structure of water-solid interface during my research visit at Copenhagen University. I would also like to thank Dr. Henrik H. Kristoffersen (Technical University of Denmark) for having an invaluable discussion about advanced ab initio molecular dynamics techniques during my visit at DTU. It's my pleasure to thank Prof. Samira Siahrostami (University of Calgary) for her invaluable comments on my first paper during SUNCAT summer school at Stanford University. I also thank Dr. Arghya Bhowmik (Technical University of Denmark) for having a helpful discussion on CO_2 reduction reaction on transition metal oxides.

I would also like to thank Prof. Peter Blaha (Technical University of Vienna) for giving me a deep insight on exchange correlation functionals in density functional theory during ICAMM at University of Rennes. My special thanks to Prof. Martjin Marsman (University of Vienna) for a wonderful discussion and great help on ab initio simulations in VASP during VASP training school at University of Rennes. It's my pleasure to thank Prof. Andrew J. Medford (Georgia Institute of Technology) for an insightful discussion on nitrogen oxidation reactions during our meetings and his stay at University of Iceland.

I am also thankful to all the members of Nordic Consortium for CO_2 Conversion, specially the project co-leader of NordCO_2, Prof. Kathrin H. Hopmann (University of Tromso) for giving me the opportunity to be a member of the Consortium.

I would like to thank all my colleagues in VRIII for their good company during these years, both present and former members, especially: Narges Atrak (Nini), Árni Björn Höskuldsson, André P. Wark, Siri Harsha Pulumati, Dr. Kuber Singh Rawat, and Dr. Hemanadhan Myneni (Future) for helping me during my carrier and proof-reading my thesis. I also thank Fatemeh Hanifpour, Dr. Asmus Ougaard Dohn, Vilhjálmur Ásgeirsson, Dr. Ragnar Björnsson, Barði Benediktsson, Benedikt Orri Birgisson, Dr. Donato Fantauzzi, Dr. Maxime Van den Bossche, Dr. Ming Geng (Robot), Abid Ali, Dr. Aleksie V. Ivanov, Dr. Gianluca Levi, Björn Kirchhoff, Dr. Younes Abghoui for having wonderful times in VRIII.

Finally, I would also like to especially thank to the wonderful people from Otago University, Prof. Anna L. Garden, Charlie Ruffman, Geoffrey Weal (Jaffar), Caitlin A. Casey-Stevens for having great time and invaluable discussion during their stay at University of Iceland.

Thanks

Ebrahim Tayyebi

1 Introduction

In the present thesis, two of the most important reduction reactions are investigated, namely carbon dioxide reduction reactions (CO_2RR) and nitrogen reduction reactions (NRR). The introduction is divided into two sections. The first section is focused on the history and reaction mechanism of the CO_2RR. The second section introduces the NRR and its crucial role in ammonia synthesis.

1.1 Carbon Dioxide Reduction Reactions

The release of carbon dioxide and other greenhouse gases due to human activity is increasing global average surface air temperatures, disrupting weather patterns, and acidifying the ocean. Left unchecked, the continued growth of greenhouse gases could cause global average temperatures to increase by another 4℃ or more by 2100[1]. The ultimate dream for a sustainable future is to be able to capture CO_2 gas from both industrial sources and the atmosphere and convert it to particular hydrocarbons (HCAs) of choice, which can then be used as synthetic fuels or other carbon-based products[2]. A particularly appealing approach is to use CO_2 as a reactant and a renewable energy source (such as geothermal, wind or solar energy) to make synthetic fuels or plastics. A plant operating in Iceland, Carbon Recycling International, is already commercially producing methanol using electricity and CO_2 from a geothermal power plant[3]. There, H_2 is first produced by electrolysis of water and then reacted with CO_2 to form methanol. The possibility of direct electroreduction of CO_2 has been demonstrated in laboratory experiments. Such a one-step process could be more energy efficient and would facilitate small-scale, decentralized production of synthetic fuels[4].

The problem with electrochemical CO_2 reduction reaction (CO_2RR) to make synthetic fuels is that an energy-efficient and selective catalyst has not yet to be identified and made for this process. Cu is the only pure metal electrode tested so far for CO_2RR to HCAs and alcohols with any significant yield, whereas other pure metal electrodes make only H_2, CO or formate. However, Cu is neither selective (15 different HCAs products[5]) nor efficient (due to the large overpotential to reduce CO_2 to HCAs) as a CO_2RR catalyst which has thus far prevented a commercial application of direct CO_2 electroreduction. Furthermore, methanol is only a minor product (less than 0.1%) for CO_2RR on Cu, but methanol would be one of the most useful products to use as synthetic fuel.

Transition metal oxide surfaces have been tested experimentally to catalyze CO_2RR to formic acid and methanol with high yields (2-76%), depending on the applied potential and other reaction conditions, where the bulk of studies have focused on RuO_2-based electrodes[6–10]. None of the experimental works report, methane, CO or methanediol detection, with one exception, where trace amounts of methane and CO were reported[9].

Recently, Mezzavilla *et al*[11] revisited RuO_2 experimentally and found the formation of H_2 via the hydrogen evolution reaction (HER) to dominate other products, contradicting

previous experimental works[6–10] where formic acid or methanol is observed to be the major product. Additionally, trace amount of formate and CO(g) were detected at high overpotentials. They also show that despite RuO_2 not being an active catalyst for electrocatalytic conversion of CO_2 to methanol it can bind both CO and CO_2 to the surface. In this newly published experimental paper[11], they almost tried to repeat all the old experimental ones[6–10] and they could not detect any methanol as a product in the experiment under any condition. Here, we will try to demystify the current contradictions between TCM-CHE models and the published results from newly experimental paper[11]. We will also propose a possible explanation for why methanol has not been detected there.

Water is directly involved in many chemical reactions to build and break down important components. Due to its rich chemical properties, water a key participates in numerous important reactions. The electrocatalytic CO_2RR is one of the reactions where water as a solvent, plays an important role. In electrocatalytic reactions carried out in aqueous solutions, the binding strength, configurations and stability of adsorbates on the surface are affected by the presence of water. Therefore, taking its solvation impact on reactants, intermediates, and products into account is of high importance[12–15]. However, modeling solid-liquid interfaces using density functional theory (DFT) calculations is revealed to be complex and efficient functionals are required to describe the hydrogen bonding interactions[16–19]. Nevertheless, in order to explain the catalytic trends, rates, reaction pathways and mechanisms in reactions, some efficient and reasonable solid-liquid interface models have been developed [20–32].

Electrochemical reduction of CO_2 towards particular products such as hydrocarbons and alcohols crucially require coherent design of selective catalysts and the presence of water affects the reaction mechanism for the process. Accordingly, a complete description of the electrochemical solid-liquid interface is essential. Recently, such a model has been observed to be successful in predicting the experimental product distribution of CO_2RR on metals as a function of applied potential[20]. However, while the thermochemical model (TCM) and computational hydrogen electrode (CHE) are unable to capture these trends, they do capture the overpotentials for CO_2RR and other electrochemical reactions quite well[33–35],[24,36]. This can be attributed to the better-known molecular structure of water on metals rather than their oxide counterparts (transition metal oxides, TMOs) and therefore realistic model systems have not completely been developed for TMOs. TMO surfaces have been shown to chemisorb water molecules strongly through their oxygen atoms on coordinately unsaturated site (CUS)[13,14,37] whereas on metals the water molecules are physiosorbed onto the surface[18–20,28,31]. An experimental study on RuO_2(110) surface using high resolution electron energy loss spectroscopy (HREELS) and thermal desorption spectroscopy (TDS)[13] confirm the binding of oxygen atom of water on CUS sites and no water dissociation was observed on the perfect RuO_2(110) surface where as its dissociation occurs in small amount on some vacant Ru bridge sites.

1.2 Nitrogen Reduction Reactions

Recently ammonia has received numerous attentions as a fertilizer for food supply for an ever-growing global population which has been always one of the most serious challenges for mankind. Today, Fertilizers are playing an imperative role in the process of food production. The synthesis of ammonia (NH_3) is also the key factor in the processes that

convert fertilizer to food. At present, industrial NH_3 synthesis is dominated by the Haber-Bosch process, in which NH_3 is formed based on the chemical reaction between N_2 and H_2. In this process, nitrogen and hydrogen gas molecules are heated to 430 °C, pressurized to 150 bar and passed over either Fe or Ru surface to catalyze the overall reaction[38].

$$N_2(g) + 3H_2(g) \rightarrow 2NH_3(g)$$

The H_2 (g) is also at the cost of excessive fossil fuels consumption, accompanied with large CO_2 emission. Today, most industrial process for ammonia production lead to 1% of global annual CO_2 emissions which is more than any other industrial chemical-making reactions. Therefore, Chemists and chemical engineers across the globe are trying to make ammonia synthesis sustainable. Recent theoretical works have opened up new windows for production of ammonia at ambient conditions. In this process which is mimicking a biological version of ammonia production in nature[39], NH_3 is produced from solvated protons, electrons and atmospheric nitrogen but at ambient conditions. In this process, transition metals (TMs)[31,40,41], transition metal nitrides (TMNs)[42,43], and transition metal oxides (TMOs)[44] as an electrode catalyst have crucial roles. In other word, the protons come from a proton-donor containing solution (mainly water) and the electrons are driven to the electrode surface (catalyst) by an applied electric potential.

Recently, Ru has been tested experimentally by Andersen *et al.*[45] and Yao *et al.*[46]. They reported low reaction rates and current efficiency for NRR in aqueous solutions, in agreement with previous DFT calculations[40]. In the work conducted by Andersen *et al.* the ammonia concentration was reported to be around 10 ppb with a substantially low current efficiency slightly above 0.001% at -1.5 V vs. RHE, with almost all the current used for H_2 formation[45]. Yao et al. also performed NRR in 0.1 M $HClO_4$ solution. The aim of that study was to gain more insight into the NRR mechanism on a Ru catalyst by using powerful surface-enhanced infrared absorption spectroscopy (SEIRAS).[46] From the SEIRAS measurements, N_2, NNH, NHNH and NH_2 were identified as intermediates on the surface.

Ru has been chosen among available metal catalysts since it is one of the metals having the lowest thermochemical barrier for NRR, despite the fact that HER will dominate on that surface[40]. Moreover, the water structure on Ru (0001) flat surface is relatively well-understood[47,48] and many available experiments have been carried out on.

1.3 Thesis Outline

In this thesis we use TCM-CHE approach to obtain trends for CO_2RR on 12 different TMO surfaces in their rutile structure. We use scaling relations to construct "activity" volcano-plots to estimate the overpotential for each of the rutile oxides. Then we utilize a more detail model to elucidate the reaction mechanism for CO_2RR on RuO_2(110) towards several products such as formic acid, CO, methanediol, methanol, methane and as well as H_2 evolution.

Finally, we use a novel theoretical model (the electrochemical solid-liquid interface, ESLI, model) to gain further insight into the mechanism of the electrochemical NRR on Ru (0001). The NRR is a complex reaction and there are experimental limitations to identify

reaction intermediates, limiting steps and optimal reaction pathway on the Ru (0001) electrode. Therefore, DFT calculations are used to determine the reaction mechanism. Here, we try to explicitly calculate the elementary reaction barriers of NRR on Ru (0001) at -0.6 V applied potential. Finally, we investigate whether any substantial additional barriers exist for NRR on Ru or if the thermodynamics of intermediates is sufficient in describing the reaction mechanism.

2 Introduction to electrochemical operations

By carefully controlled chemical reactions, electrical work can be obtained, but not for the reactions proceeding spontaneously. For example, the reaction to form hydrogen chloride in aqueous solution in the standard state of pure gases of hydrogen and chlorine at 1 bar and 298 K

$$\frac{1}{2}H_2(g) + \frac{1}{2}Cl_2(g) = HCl(aq) \quad (1)$$

has a Gibbs energy change of -13.12 $kJ/mol\ HCl$. Therefore, the reaction can occur spontaneously; however, this will produce no useful work. An alternative way is to run the reaction in an electrolytic cell. Then hydrogen and chlorine gases are fed into separate electrodes, and by applying an external voltage, the electromotive force (EMF) or voltage produced is almost balanced. Therefore, the reaction will occur at a very slow rate, and electrical work can be obtained from the cell. This is a process in which chemical energy is directly converted to electrical energy. Electrochemical processes occur in batteries, fuel cells, electrolysis, electrolytic plating, and corrosion (generally an undesirable process). Electrochemical processes can be utilized to generate electricity, to recover metals from solution, and to measure the thermodynamic properties of electrolyte solutions. An electrochemical cell is a tool used to study electrochemical reactions. The cell consists of two electrodes (metallic conductors) in electrolytes that are usually liquids containing salts but may be solids, as in solid-state batteries. As shown in Figure l (a), the two electrodes may be in the same electrolyte, or each electrode may be in a separate compartment with its own electrolyte, as in Figure l (b). In this case, the two compartments are connected by a salt bridge, an electrolyte that completes the electrical circuit. A third alternative type that is not shown here is for the two compartments to be in direct contact through a porous membrane.

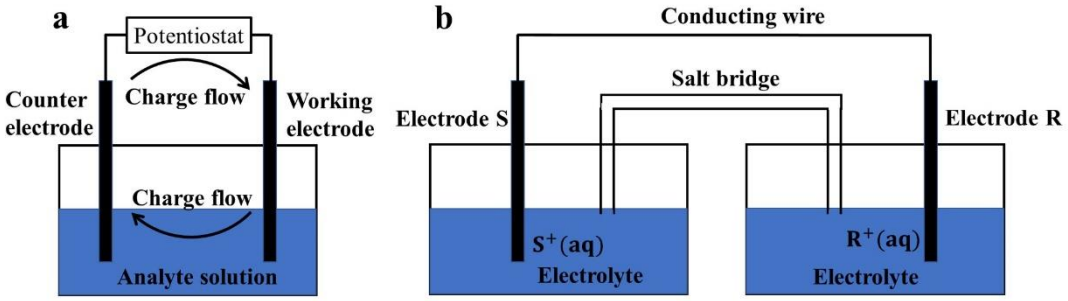

Figure 1. Two types of electrochemical cells: (a) a cell with two electrodes and shared electrolyte. (b) a cell with two separate compartments connected by a salt bridge.

The term galvanic cell is used to illustrate when electricity is produced by the chemical reaction that occurs spontaneously and the two electrodes are connected through a potentiometer or electrical resistance; it is considered to be a fuel cell if the reagents are

continually supplied to the cell. Batteries are galvanic cells. When an electrochemical cell operated in the reverse is referred to as an electrolytic cell. More precisely, an external voltage is used to cause a nonspontaneous reaction to occur, as in the electrolysis of water. An automobile battery and other storage batteries are considered to be galvanic cells since they are supplying electricity and electrolytic cells when they are being recharged. Electrochemica1 cells can be analyzed thermodynamically in several ways. One is for when to compute the work, or equivalently the voltage, that can be produced by a galvanic cell. Alternatively, in order to determine the equilibrium constant of the reaction taking place within the cell, one can use the measured cell voltages. Finally, the third application of electrochemical cells is to measure the thermodynamic activity or activity coefficients of the ions in electrolyte solutions.

In electrochemical cells, oxidation and reduction reactions: or redox reactions are occurring simultaneously. More precisely, at one electrode, the anode, a reduced species is oxidized and releasing electrons, while at the other electrode, the cathode, an oxidized species is reduced and absorbs electrons. Therefore, it is common to consider an electrochemical cell consisting of two half-cells (one containing the anode and the other one containing the cathode) and to describe the processes in terms of half-cell reactions[49].

2.1 Electrocatalysis

In chemistry, a substance that can change the rate of chemical reactions without any chemical change is defined as a catalyst. This definition can be directly applied to electrocatalysis. An electrode material that interacts with some certain species during a Faradaic reaction but remains unaltered is called an electrocatalyst. Since in electrocatalysis, the reactions take place on the surfaces of catalysts and catalyst is not a part of the reaction medium, electrode reactions are heterogeneous, so electrocatalysts are usually heterogeneous catalysts. There also exist adsorption/desorption steps on the surfaces of electrocatalysts.

To compare the catalytic activity of different electrode materials, one way is to compare the current density at a constant overpotential or measure the overpotential at a constant current density. Therefore, a good electrocatalyst should show high current density at low overpotential.

2.2 Faradaic and nonfaradaic process

In electrocatalysis, two types of processes occur at electrodes, namely faradaic and nonfaradaic reactions. The faradaic reaction is for when the charges (e.g., electrons) are transferred across the metal solution interface, and electron transfer causes oxidation or reduction to occur. Such reactions are governed by Faraday's law of electrolysis (i.e., the amount of chemical reaction caused by the flow of current is proportional to the amount of electricity passed). Hence, charge transfer electrodes are electrodes at which faradaic processes occur. At some certain potential a given electrode solution interface will show no charge transfer reactions and due to this, such reactions are thermodynamically or kinetically unfavorable. However, adsorption and desorption processes can change the

structure of the electrode solution interface with changing potential or solution composition. Such processes are called nonfaradaic processes. Although charge does not cross the interface, external currents can flow (at least transiently) when the potential, electrode area, or solution composition changes[50].

2.3 Nernst equation and equilibrium constant

It has been known that for any process occurring at constant temperature and pressure the maximum work that can be gained is equal to the change in Gibbs energy of the process, that is,

$$\mathrm{W}^{\max} = \Delta\mathrm{G} \tag{2}$$

This maximum work is obtained if the process is reversible, e.g., no resistive heating as a result of the current flow. This indicates that the rate of reaction is very slow, and accordingly, the produced electrical potential is balanced by an external potential so that the current flow is infinitesimal. This electrical potential produced by the cell is called the zero-current cell potential and specified by E. The work done by the electrical cell W_{elec} in moving n moles of electrons across a potential difference of E is

$$\mathrm{W_{elec}} = -\mathrm{nFE} \tag{3}$$

where $F = 96485\ C/mol$ is the Faraday constant, and n is the number of electrons transferd in the cell reaction. If the cell potential is positive, the negative sign shows that work is done by the cell on the surroundings. [Also, for later reference, at 25℃, the quantity RT/F is equal to 25.7 mV.] Consequently, we have

$$\Delta\mathrm{G} = \mathrm{W}^{\max} = \mathrm{W_{elec}} = -\mathrm{nFE} \tag{4}$$

or simply

$$\Delta\mathrm{G} = -\mathrm{nFE} \tag{5}$$

A generic electrochemical reaction can be written as

$$\nu_{1+}\mathrm{M}_{1+}^{z_1^+}(\mathrm{aq}) + \nu_2\mathrm{M}_2(\mathrm{s}) + \nu_1\mathrm{M}_1(\mathrm{s}) + \nu_{2+}\mathrm{M}_{2+}^{z_1^+}(\mathrm{aq}) = 0 \tag{6}$$

or, more generally (using our standard notation for chemical reactions),

$$\sum_{\mathrm{i}} \nu_{\mathrm{i}}\mathrm{M}_{\mathrm{i}} = 0 \tag{7}$$

For example, the reaction

$$\mathrm{Cu}^{2+}(\mathrm{aq}) + \mathrm{Zn}(\mathrm{s}) \rightarrow \mathrm{Cu}(\mathrm{s}) + \mathrm{Zn}^{2+}(\mathrm{aq}) \tag{8}$$

will be written as $Zn^{2+}(aq) + Cu(s) - Cu^{2+}(aq) - Zn(s) = 0$, so that $\upsilon_{Zn^{2+}} = 1$, $\nu_{Cu} = 1$, $\nu_{Cu} = -1$, and $\upsilon_{Cu^{2+}} = -1$. Also, we can write the Gibbs energy of any species as

$$\overline{\mathrm{G}}_\mathrm{i}(\mathrm{T},\mathrm{P},\underline{\mathrm{x}}) = \overline{\mathrm{G}}_\mathrm{i}^{0}(\mathrm{T}^0,\mathrm{P}^0,\mathrm{x}_\mathrm{i}^0) + \mathrm{RTln}\frac{\bar{\mathrm{f}}_\mathrm{i}(\mathrm{T},\mathrm{P},\underline{\mathrm{x}})}{\bar{\mathrm{f}}_\mathrm{i}^{0}(\mathrm{T}^0,\mathrm{P}^0,\mathrm{x}_\mathrm{i}^0)} = \overline{\mathrm{G}}_\mathrm{i}^{0}(\mathrm{T}^0,\mathrm{P}^0,\mathrm{x}_\mathrm{i}^0) + \mathrm{RTln}\mathrm{a}_\mathrm{i}(\mathrm{T},\mathrm{P},\underline{\mathrm{x}}) \quad (9)$$

where P^0 and x_i^0 are the standard-state pressure and composition, $\overline{f}_i^{0}(T^0,P^0,x_i^0)$, $\overline{G}_i^{0}(T^0,P^0,x_i^0)$ and a_i are the standard-state fugacity, Gibbs energy, and activity of species i, respectively. Combining equations (5), (7), and (9), we obtain

$$\Delta_\mathrm{rxn}\mathrm{G} = \Delta_\mathrm{rxn}\mathrm{G}^0 + \mathrm{RTln}\prod_\mathrm{i}\mathrm{a}_\mathrm{i}^{\nu_\mathrm{i}} = -\mathrm{nFE} = -\mathrm{nFE}^0 + \mathrm{RTln}\prod_\mathrm{i}\mathrm{a}_\mathrm{i}^{\nu_\mathrm{i}} \quad (10)$$

where E^0 is the-zero-current cell potential if the ions are in their standard states. E is also the actual (measurable) zero-current cell potential with the ions at the concentration of the cell. The equation (9) is known as the **Nernst equation**. We also know that

$$-\frac{\Delta_\mathrm{rxn}\mathrm{G}^0}{\mathrm{RT}} = \mathrm{lnK}_\mathrm{a} \quad (11)$$

where K_a is the chemical equilibrium constant, we have

$$\mathrm{lnK}_\mathrm{a} = \frac{\mathrm{nFE}^0}{\mathrm{RT}} \quad (12)$$

This equation shows how to compute the chemical equilibrium constant from measured standard-state electrochemical cell potentials (usually referred to as standard cell potentials). The standard potential of an electrochemical cell is obtained by combining the two relevant half-cell potentials[49].

2.4 Capacitance and the charge of an electrode

The interface between a conductive electrode and an adjacent solution has been shown experimentally to behave like a capacitor, and a model of the interfacial region somewhat resembling a capacitor can be given. At a given potential, the double layer is created, and this cause a charge imbalance across the interface which must be neutralized by rearrangement of charge species. Accordingly, q^M indicates charge on the electrode and charge in the solution is shown by q^s. The charge on the metal, q^M, is made up of an excess or deficiency of electrons and resides in a very thin layer (< 0.1 Å) on the metal surface while the charge in solution, q^s, represents an excess of either cations or anions in the vicinity of the electrode surface. The charge on the metal is negative or positive with respect to the solution depends on the potential across the interface and the composition of the solution. The term charge density is defined often to illustrate the amount of charge divided by the electrode area, such as, ($\sigma_M = q^M/A$, usually given in $\mu C/cm^2$). The whole array of charged species and oriented dipoles existing at the metal solution interface is referred to the electrical double layer. At a certain potential, the electrode solution interface is characterized by a double layer capacitance, C_d, typically in the range of 10 to 40

$\mu F/cm^2$. However, unlike real capacitors, whose capacitances are independent of the voltage across them, C_d is often a function of potential[50].

2.5 Electrical double layer

The solution side of the double layer is usually made up of several "layers." The one which is close to the electrode (the inner layer) contains solvent molecules and sometimes other species (ions or molecules) that are said to be specifically adsorbed (Figure 2). This inner layer is sometimes referred to the compact, Helmholtz, or Stern layer. The position of the electrical centers of the specifically adsorbed ions is referred to the inner Helmholtz plane (IHP), which is located at the distance of x_1 from the surface. The total charge density from specifically attracted ions into the electrode surface is $\sigma^i(\mu C/cm^2)$. Solvated ions can approach the metal only to a distance of x_2 which is called the outer Helmholtz plane (OHP). The charged metal interacts with the solvated ions only through long-range electrostatic forces; therefore, their interaction is fundamentally independent of the chemical properties of the ions. These ions are considered to be nonspecifically adsorbed. These ions are also assumed to move in solution and so the electrostatic interactions are in competition with Brownian motion. The result is still a region close to the electrode surface containing an excess of one type of ion but now the potential drop occurs over the region called the diffuse layer. The excess charge density in the diffuse layer is σ^d, hence the total excess charge density on the electrolyte side of the double layer, σ^s, is then given by

$$\sigma^s = \sigma^i + \sigma^d = -\sigma^M \tag{13}$$

The thickness of the diffuse layer can vary depends on the total ionic concentration in the solution; for example if the concentrations of ions is greater than $10^{-2}M$ a thickness of less than ~100Å is expected. The potential profile across the double layer region is shown in Figure 2. The structure of the double layer can essentially affect the rates of electrochemical reactions[50].

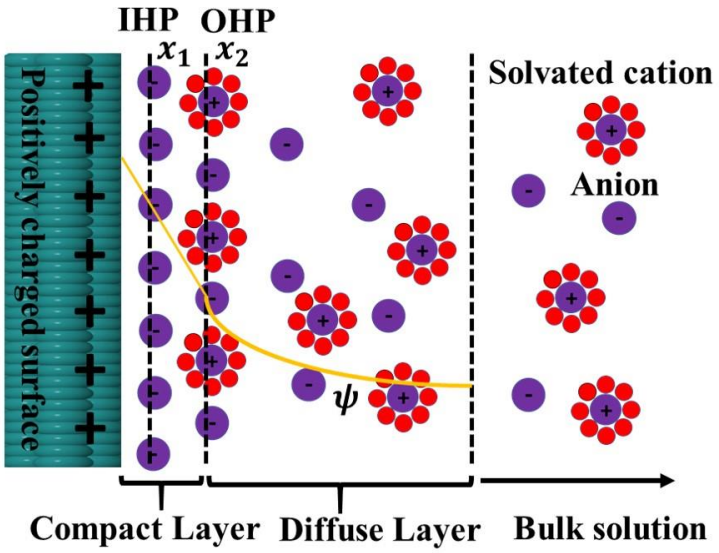

Figure 2. Electrical double layer. $\boldsymbol{\psi}$ indicates the potential profile across the double layer.

3 Theory and Methodology

"It doesn't matter how beautiful your theory is, it doesn't matter how smart you are. If it doesn't agree with experiment, it's wrong."

— Richard P. Feynman

In the current thesis Kohn-Sham DFT[51] has been utilized to determine the static geometry optimization and ab initio molecular dynamic simulations, using the Vienna Ab initio Simulation Package (VASP)[52,53] and the freely available program package CP2K/Quickstep[54,55]. The density functional implementation in Quickstep is based on a hybrid gaussian plain wave (GPW) scheme while VASP uses a plain-wave expansion of the wave function and project-augmented wave representation of the ionic cores.

Recent developments in computational catalysis have been linked the catalyst performance to the energetics of reaction intermediate, binding to the catalyst surface and as well as the kinetics of elementary reaction steps. The physics-based models used for this PhD project to understand those reaction intermediates and reactions rates at atomic scale, rely on tremendous development of DFT computational methods. Here we mention some basic concepts in density functional theory and computational electrocatalysis briefly. Activity of chemical reactions on catalyst surfaces are linked to the adsorption strength of reaction intermediates, which in turn depends on the electronic structure of the catalyst surface. The catalyst electronic structure can be described by using computational methods, utilizing the theory of quantum mechanics. The reaction thermodynamics and kinetics can be predicted from ab-initio simulations if one can calculate the total energy of catalyst with reaction intermediates. DFT has helped us during the last two decades to gain more insight into chemical reactions on surfaces[56]. It is possible to evaluate the complete thermodynamic and kinetics for chemical reactions based solely on DFT calculations.

3.1 Born-Oppenheimer approximation

The Born-Oppenheimer approximation is one of the basic concepts in quantum chemistry. This approximation allows the motion of the nuclei and the motion of the electrons to be distinguished. In describing the electrons in a molecule the Born-Oppenheimer approximation neglects the motion of the atomic nuclei. This approximation uses the fact that the mass of an atomic nucleus in a molecule is much larger than the mass of an electron (more than 1000 times). This large difference in mass causes the motion of nuclei to be much slower than of the electrons. We use this approximation throughout the thesis.

3.2 Density functional theory

The prediction of ground state properties for a system of N interacting electrons exposed to an external local potential $V(r)$ is one of the central problems in theoretical chemistry. In order to achieve this one requires to solve the Schrodinger equation for the ground state wave function $|\Psi(r_1, \dots, r_n)\rangle$ of the electronic system.

$$\mathrm{H}|\Psi\rangle = [T + V_{ee} + V]\,|\Psi\rangle = \left[\sum_{i=1}^{N} -\frac{1}{2}\nabla_i^2 + \sum_{i<j}^{N}\frac{1}{r_i - r_j} + \sum_{i=1}^{N} V(r_i)\right]|\Psi\rangle = E|\Psi\rangle \qquad (1)$$

Here, H is the Hamiltonian operator, T is operator for the kinetic energy, V_{ee} is the Coulomb interaction and V is an external potential. The energy of the system is indicated by E and the index i labels the individual electrons. Equation (1) shows a differential equation of second order and the number of independent variables is $3N$ and this illustrate that the solution of this problem is an extremely difficult task. In fact, when $N = 1$ one can find the exact analytical solution for this equation.

The Ritz variational principle is an alternative method to specify the ground state wave function $|\Psi\rangle$ and in order to obtain the ground state wave function the expectation value of the Hamiltonian operator should be minimized, i.e. the energy of the ground state

$$E_0 = \min_{\Psi \to N}\langle\Psi|\mathrm{H}|\Psi\rangle = \langle\Psi|T + V_{ee} + V|\Psi\rangle \qquad (2)$$

Here, the notation " $\Psi \to N$" illustrates a search over all allowed, normalizable and antisymmetric N-electron wave functions. In practice, the application of this variational principle leads to no simplification of the problem itself. A possibility to avoid these problems is the strategy to focus on the electronic ground state density

$$\rho(r) = N\int d\sigma dX_2 \dots dX_N |\Psi(r, \sigma, X_2, \dots, X_N)|^2 \qquad (3)$$

as the crucial parameter of the many-particle problem. The quantity $X_i = (r_i, \sigma_i)$ now introduces an additional spin variable σ. Using this approach, one can skip redundant information stored in the N-particle wave function and utilize the fact that $\rho(r)$ entirely depends on the three spatial variables $r = (X, Y, Z)$, which is obviously a remarkable simplification of this problem[57].

3.3 Hohenberg-Kohn theorems

The main idea of the first Hohenberg and Kohn[58] was the fact that the electronic density of a physical system suffices to determine all of its properties. Therefore, this legitimizes the use of the electron density as the basic variable.

Hohenberg-Kohn Theorem 1: The first Hohenberg-Kohn theorem states that apart from an additive constant the external potential $V(r)$ can be determined by the electronic ground state density $\rho(r)$. As a consequence, the density $\rho(r)$ uniquely specifies the

corresponding Hamiltonian operator as well as the ground state wave function $|\Psi[\rho]\rangle$ and all electronic properties of the underlying system. Consequently, the kinetic energy and the electron-electron interaction energy can be determined using the density. For a system of electrons subjected to an external potential $V(r)$ the functional for the total energy results in the expression

$$E[\rho] = T[\rho] + V_{ee}[\rho] + \int drV(r)\rho(r) \equiv F[\rho] + \int drV(r)\rho(r) \tag{4}$$

with the HK-functional $\boldsymbol{F}[\boldsymbol{\rho}]$ defined to

$$F[\rho] = T[\rho] + V_{ee}[\rho] = \langle\Psi[\rho]|T + V_{ee}|\Psi[\rho]\rangle \tag{5}$$

By definition the electron-electron term can be separated in two terms

$$V_{ee}[\rho] \equiv U[\rho] + E_{xc}[\rho] \tag{6}$$

containing the classical Coulomb energy

$$U[\rho] = \frac{1}{2}\iint drdr' \frac{\rho(r)\rho(r')}{|r - r'|} \tag{7}$$

and the functional $E_{xc}[\boldsymbol{\rho}]$ indicating the nonclassical term to the electron-electron interaction. $E_{xc}[\boldsymbol{\rho}]$ includes quantum mechanical exchange and as well as a correction for the self-interaction, and all correlation effects. It should be noted that all intrinsic properties of the electronic system are completely absorbed in the Hohenberg-Kohn functional $F[\boldsymbol{\rho}]$.

Hohenberg-Kohn Theorem 2: The second Hohenberg-Kohn theorem states that the functional $\boldsymbol{E}[\boldsymbol{\rho}]$ of the total energy satisfies a variational principle with respect to the density, more precisely the total energy $\boldsymbol{E}[\boldsymbol{\rho}]$ reaches its minimal value E_0 for the correct ground state density ρ_0:

$$E_0 = \min_{\rho \to N} E[\rho] = E[\rho_0] \tag{8}$$

The notation "$\rho \to N$" hereby indicates a variation over all ground state densities of arbitrary N-electron systems.

The first Hohenberg-Kohn Theorem shows that for any arbitrary density $\rho(r)$ there should exist an external potential of $V(r)$, which is then called V-representable. Since it is possible to construct densities that cannot be related to a corresponding external potential $V(r)$, this implication clearly brings us to formal problems, which can however be fixed by using a more general formulation of the Hohenberg-Kohn Theorem called "constrained"-search formulation[57].

3.4 Kohn-Sham scheme

The essential intuition of Kohn-Sham (KS) picture is to map the real interacting system of electrons to a fictious system of noninteracting electrons which yields exactly the same ground state density and ground state energy as the realistic system would do. By doing so, the electrons then behave like uncharged particles and do not interact with each other through the Coulomb repulsion. More precisely, each of the electrons is subjected to a field averaged over all other electrons which introduces the KS method as a mean-field theory.

The KS wave function $\Phi[\rho]$ of the KS system is defined as the wave function that minimizes the constrained search minimization

$$T_S[\rho] = \min_{\Psi\to\rho}\langle\Psi|T|\Psi\rangle \tag{9}$$

This yields the functional $\boldsymbol{T_S[\rho]}$ of the kinetic energy of the KS system. By defining the exchange energy

$$E_x[\rho] = \langle\Phi[\rho]|V_{ee}|\Phi[\rho]\rangle - U[\rho_0] \tag{9}$$

and the correlation energy

$$E_c[\rho] = \langle\Psi[\rho]|T + V_{ee}|\Psi[\rho]\rangle - \langle\Phi[\rho]|T + V_{ee}|\Phi[\rho]\rangle \tag{10}$$

the total energy can then be expressed as

$$E[\rho] = T[\rho] + V_{ee}[\rho] + \int drV(r)\rho(r) \equiv T_S[\rho] + U[\rho] + E_x[\rho] + E_c[\rho] + \int drV(r)\rho(r) \tag{11}$$

The exchange-correlation functional

$$E_{xc}[\rho] = E_x[\rho] + E_c[\rho] \tag{12}$$

contains the difference of the kinetic energies and the difference of the expectation values of the electron-electron interaction of the two systems and reads

$$E_{xc}[\rho] = T[\rho] - T_S[\rho] + V_{ee}[\rho] - U[\rho] \tag{13}$$

Here the problem reformulates in a way that the main part of the energy is treated in an exact manner and all other unknown contributions are included in the exchange-correlation functional E_{xc}. This conceptual feature is one of the main advantages of KS-DFT. Moreover, one has to perceive the fact that up to now, the original problem of solving the many-body Schrodinger equation (1) has only been transformed onto the problem of finding the exact expression for the exchange-correlation functional $E_{xc}[\rho]$, which is unknown.

The variation of the total energy reads

$$\delta\left[E[\rho]-\mu\left(\int dr\rho(r)-N\right)\right]=0 \tag{14}$$

Where the Lagrange parameter μ comes from the constraint of constant particle number N. Varying the expression of the total energy (14) with respect to the density gives the Euler-Lagrange equation of KS theory

$$\mu=\frac{\delta E[\rho]}{\delta\rho(r)}=\frac{\delta T_S[\rho]}{\delta\rho(r)}+\frac{\delta U[\rho]}{\delta\rho(r)}+\frac{\delta E_{xc}[\rho]}{\delta\rho(r)}+V(r) \tag{15}$$

Defining the KS potential as

$$V_s(r)=V(r)+\frac{\delta U[\rho]}{\delta\rho(r)}+\frac{\delta E_{xc}[\rho]}{\delta\rho(r)}=V(r)+V_H(r)+V_{xc}(r) \tag{16}$$

the Lagrange multiplier becomes

$$\mu=\frac{\delta T_S[\rho]}{\delta\rho(r)}+V_s(r) \tag{17}$$

with the conventional Hartree potential

$$V_H(r)=\int dr'\frac{\rho(r')}{|r-r'|} \tag{18}$$

and the exchange-correlation potential

$$V_{xc}(r)=\frac{\delta E_{xc}[\rho]}{\delta\rho(r)} \tag{19}$$

Since the functional $\boldsymbol{T_S[\rho]}$ is not known explicitly, solving the Euler-Lagrange equation is not possible in practice. In order to solve the problem Kohn and Sham originally introduced orbitals as follow

$$\frac{\delta}{\delta\Phi_i^\dagger}\left[E[\rho]-\sum_{j,k}^{N}\epsilon_{jk}\int dr'\Phi_j^\dagger(r')\Phi_k(r')\right]=0 \tag{20}$$

with the Lagrange multipliers $\boldsymbol{\epsilon_{jk}}$ showing a constraint of orthonormality of the orbitals. The variation finally results in the equations

$$\mathrm{H}_s(r)\phi_i(r)=\left[-\frac{1}{2}\nabla^2+V_s(r)\right]\phi_i(r)=\sum_{j=1}^{N}\epsilon_{jk}\phi_j(r) \tag{21}$$

Where V_s representing the potential in equation (21). Needless to say, the Hamiltonian $\mathrm{H}_s(r)$ is Hermitian, which then furthermore holds for the matrix ϵ_{ij}. This can be diagonalized using a unitary transformation, which keeps the associated physical observables invariant. Therefore, one can get the KS equations in their canonical form

$$\mathrm{H}_s(r)\phi_i(r) = \left[-\frac{1}{2}\nabla^2 + V(r) + V_s(r) + V_{xc}(r)\right]\phi_i(r) = \epsilon_i\phi_i(r) \tag{22}$$

In this equation, KS orbitals $\phi_i$indicates a set of decoupled equations for the typical form of a Hamiltonian characterizing a system of noninteracting electrons. For such a noninteracting system Slater determinant represent the (nondegenerate) ground state wave function

$$|\Phi\rangle = \frac{1}{\sqrt{N!}}det[\phi_1, \phi_2, \dots, \phi_n], \tag{23}$$

In this equation the KS orbitals $\phi_i$are determined by the one-particle equations (22). Using equation (23) the density $\rho(r)$ is simply built out of the KS orbitals via

$$\rho(r) = \sum_{i=1}^{N} |\phi_i(r)|^2 \tag{24}$$

and this equivalent to the density of the interacting system ρ_0. In the framework of variational principle, the KS wave function of equation (23) can equivalently be defined as the minimizing wave function in the constrained search minimization

$$T_S[\rho_0] = \underset{\Psi\to\rho_0(r)}{\mathrm{Min}}\langle\Psi|T|\Psi\rangle \tag{25}$$

This leads to the kinetic energy functional of the noninteracting system having the real ground state density ρ_0.

All potentials in (22), and especially the exchange-correlation potential, depend only on the spatial variable r, therefore they are multiplicative. This fact opposed to the equations underlying e.g. the Hartree-Fock (HF) approximation with their nonlocal exchange term.

The total energy can explicitly be written as

$$E[\rho] = -\int dr \sum_{i=1}^{N} \phi_i^{\dagger}(r)\frac{1}{2}\nabla^2\phi_i(r) + \frac{1}{2}\iint drdr'\frac{\rho(r)\rho(r')}{|r-r'|} + E_{xc}[\rho] + \int drV(r)\rho(r) \tag{26}$$

here the orbitals are implicitly density dependent. Hence, the energy within the KS formalism rely on both, density and orbitals. The KS Hamiltonian operator within the KS equation depends on the density, which in turn results from the orbitals. Thus, the system of KS equations (22) need to be solved in a self-consistent way.

One should realize that in order to solve exactly the many-particle Schrodinger equation knowing the exchange-correlation functional $\boldsymbol{E_{xc}[\rho]}$ (12) is imperative. Therefore, the complexity of the underlying problem has been transferred in a very complex, nonlocal dependence of the KS potential on the density. In practical calculations people always use some approximation for the exchange-correlation functional. Finding simple systematic methods for constructing such energy functionals is almost impossible but one can separate the exchange from the correlation part as follow

$$E_{xc}[\rho] = E_x[\rho] + E_c[\rho] \tag{27}$$

The same then is valid for the exchange and correlation potentials

$$V_x = \frac{\delta E_x[\rho]}{\delta\, \rho(r)};\; V_c = \frac{\delta E_c[\rho]}{\delta\, \rho(r)} \tag{28}$$

In DFT the exchange energy functional is defined by the relation

$$\begin{aligned} E_x^{DFT}[\rho] &\equiv \langle \Phi[\rho]|V_{ee}|\Phi[\rho]\rangle - U[\rho] \\ &= -\frac{1}{2}\sum_{i,j=1}^{N} \iint dr dr' \frac{\phi_i^\dagger(r)\phi_j^\dagger(r')\phi_j(r)\phi_i(r')}{|r-r'|} \end{aligned} \tag{29}$$

Where the Slater determinant $|\Phi\rangle$ represents the ground state of the KS system. In equation (29) the expectation value of the electron-electron interaction of the KS state represented by the term $\langle \Phi[\rho]|V_{ee}|\Phi[\rho]\rangle$. Comparison of equation (29) with equation (13) shows that the difference between the true electron-electron interaction energy and the expectation value $\langle \Phi[\rho]|V_{ee}|\Phi[\rho]\rangle$ is absorbed in the correlation energy, which also contains the kinetic energy differences of the real and the KS-noninteracting electronic systems. The correlation energy can then be written as[57]

$$E_c[\rho] = T - T_s(r) + V_{ee}(r) - \langle \Phi[\rho]|V_{ee}|\Phi[\rho]\rangle \tag{30}$$

3.5 Approximate exchange-correlation functionals

It is clear that the quality and reliability of the KS formalism itself is mainly influenced by the exchange-correlation functional and therefore gives no practical method at hand. In order to be able to solve the corresponding KS equations, the exchange-correlation functional needs to be approximated. For historical reasons, the simplest approximation is to assume that the density behaves locally, and this refers to the local density approximation (LDA), which lies at the roots of DFT and the KS-formalism and has been proposed by Kohn and Sham themselves.

The most successful approach for the LDA is the homogeneous electron gas, i.e. a system of N interacting electrons moving into a volume V. To ensure electrical neutrality, the background is considered to be positively charged. Then, N and V approach infinity in the manner that the electron density $\rho = N/V$ reaches a constant value, which is the same for

each spatial point r. Within the LDA, inhomogeneous systems such as an atom, molecule or solid is then treated as a homogeneous system at each spatial point r with the associated exchange and correlation energy per electron $\epsilon_{xc}^{LDA}(\rho(r))$ at each point r. Therefore, the LDA approximation is well applicable to systems which the density varying slowly, but formally it is not suitable for highly inhomogeneous systems. In fact, the LDA is mostly employed in solid state physics and it has no comparable impact in computational chemistry that atoms and molecules treat by a more rapidly varying density. Since the homogeneous electron gas is completely determined by the value of its density, the exchange correlation energy within the LDA approximation is gained by integrating the parameter $\epsilon_{xc}^{LDA}(\rho(r))$ weighted with the local density $\rho(r)$ at each point in space.

$$E_{xc}^{LDA}[\rho] = \int dr \rho(r) \epsilon_{xc}^{LDA}(\rho(r)) \tag{31}$$

In order to obtain more accuracy, the next step in treating inhomogeneous systems is to include the gradient of the density in the exchange-correlation functional. By applying this, one hopes to constitute the nonhomogeneity of the true electron density. General gradient approximation (GGA) is the general approach for these and then given by a functional of the form

$$E_{xc}^{GGA}[\rho] = \int dr f_{xc}^{GGA}\left((\rho(r)), (\nabla\rho(r))\right) \tag{32}$$

which explicitly contains the density gradient $\nabla\rho(r)$. Again, the exchange and correlation term can be treated separately

$$E_{xc}^{GGA}[\rho] = E_{x}^{GGA}[\rho] + E_{c}^{GGA}[\rho] \tag{33}$$

In most cases the GGA functionals for the exchange part can be written in the form

$$E_{x}^{GGA}[\rho] = \int dr \rho(r) \epsilon_{x}^{LDA}(\rho(r)) F(S) \tag{34}$$

with the dimensionless parameter

$$s = \frac{|\nabla\rho(r)|}{2k_f(r)\rho(r)} \tag{35}$$

and a scaling function F that can have a pretty complicated form in practice. The quantity $k_f(r)$ denotes the Fermi wave vector given by $k_f(r) = \left(\mathbf{3\pi^2}\rho(r)\right)^{\mathbf{1/3}}$.[57]

Optimized flavors for GGA functionals have been developed like PBE[59,60] and BEEF[61] for good accuracy in atomistic catalysis process simulation. BEEF functional along with vdW-DF2 nonlocal correlation energy and potential function have been used throughout this work. Often non-local interactions like hydrogen bonding are key to the behavior of molecular systems like large adsorbate on catalysts surface. Such interactions can be captured by special exchange correlation functional like vdW-DF2.

3.6 Long range dispersion correction

In both HF and DFT methods, the proper description of noncovalent interactions which requires the inclusion of long-range electron correlation effects are missing. In particular, the presence of the weak London forces is imperative due to their attractive and ubiquitous nature. They play an important role in many phenomena such as the crystal packing of molecular solids and the physisorption of molecules on surfaces or in microporous materials. In order to include the missing dispersion energy in DFT one way is to augment the total energy as computed for a given density functional approximated method with a dispersion term:

$$E^{DFT-D} = E^{DFT} + E^{Disp} \tag{36}$$

Using a simple pairwise (i.e. 2-body) correction seems to be an efficient and cost-effective approach to include the long-range dispersion energy through the asymptotic series:

$$E^{Disp} = -\sum_{AB}\sum_{n=6,8,10}\left(\frac{C_n^{AB}}{R_{AB}^n}\right) \tag{37}$$

Among different proposals, the semiclassical D2[62] and the more recent D3[63] Grimme's dispersion corrections are the most widely used.

3.7 Density functional theory for periodic systems

The pseudopotential approach in combination with a plane wave basis set has turned out to be a widespread technique for performing DFT calculations for periodic systems. The pseudopotential method uses the fact that the core electrons are more or less chemically inert and valence electrons are responsible for the chemical properties of atoms and the solid states. Within the pseudopotential in practice the one particle equations (22) must be explicitly solved only for the valence states.

The decision to choose a plane wave basis set for the treatment of periodic systems is quite natural, because the corresponding representation of orbitals is then done by usual Fourier series that are the common mathematical objects for describing periodic functions[57].

3.8 Born-Oppenheimer molecular dynamics

Born-Oppenheimer approximation is an approach in which nuclear positions are considered to be fixed at an instant of time while the electronic structure in molecular dynamics simulations consists in straightforwardly solving the static electronic structure problem in each molecular dynamic step. Therefore, the electronic structure part is solved using a time-independent quantum problem, e.g. by solving the time-independent, stationary Schrodinger equation, simultaneously to propagating the nuclei according to classical mechanics. This means that the time dependence of the electronic structure is dictated by its parametric dependence on the classical dynamics of the nuclei which it just

follows. Consequently, Born–Oppenheimer molecular dynamics method can be written as follow

$$M_I \ddot{R}_I(t) = -\nabla_I \min_{\Psi_0}\{\langle \Psi_0 | H_e | \Psi_0 \rangle\} \tag{38}$$

$$E_0 \Psi_0 = H_e \Psi_0 \tag{39}$$

Born–Oppenheimer framework allows us to easily apply the scheme to some specific excited electronic state Ψ_k, $k > 0$, but without considering any interferences with other states $\Psi_{l \neq k}$ nor with itself. Hence, Born–Oppenheimer molecular dynamics should not be called "adiabatic molecular dynamics" as is sometimes done, since both the nondiagonal and diagonal corrections are neglected[64].

3.9 Computational tools

3.9.1 Free energy of molecules and reaction intermediates

The binding free energy of a reaction intermediate on a catalyst surface can be estimated from free energy estimates of the surface with the protonated adsorbate, that of the surface without the protonated adsorbate and free energy of reference molecules. For example, the binding free energy of AH* (ΔG_{AH*}) without applied potential U will be

$$\Delta G_{AH*}(U = 0) = G_{AH*} - G_{A*} - \frac{1}{2} G_{H_2} \tag{40}$$

where, G_{AH*} is the free energy of the surface with the protonated adsorbate AH*, G_A* is that of the surface with the unprotonated adsorbate A*, G_{H_2} are the free energy of H_2 molecules. A* denotes an adsorbate A bound to that active site *. The reason for approximating the included protonation free energy by G_{H_2} is since the Computational Hydrogen Electrode (CHE) model is utilized here. This model is being explained more detailed in the next section.

3.9.2 Quantum and thermal corrections to the ground-state potential energy

We use the following relation to estimate the free energy of an adsorbate configuration.

$$G(U = 0) = E_{DFT} + E_{ZPE} + H_{0K \to T} - T\mathrm{S} \tag{41}$$

Here E_{DFT} is ground-state energy calculated with DFT and E_{ZPE} and S are zero-point energy corrections and entropy which are calculated within harmonic approximation. $H_{0K \to T}$ is changes in integral energy because of temperature. According to quantum formulation, moving from T = 0 K to an arbitrary temperature will change the internal energy of system, since in higher temperatures excited quantum states will be available for system. At T = 0 K, only the ground state will be occupied. With the increasing of

temperature, some of the other low-lying quantum states will be accessible for system. Boltzmann distribution function is a fundamental formula in the analysis of thermal properties based on probability theories. In fact, Boltzmann´s relation for the system (in thermal contact with a heat reservoir) which is in different quantum states, describes the energy difference between the states and the system temperature through the equation:

$$\frac{P(E_i)}{P(E_j)} = e^{\frac{(E_j - E_i)}{K_b T}} \tag{42}$$

E_i and E_j are internal energy for two different quantum states.

From statistical mechanics, internal energy for a system in T:

$$E(T) = \frac{\sum_{i=0}^{\infty} E_i e^{\frac{-E_i}{K_B T}}}{Z} \tag{43}$$

where Z is partition function. In order to calculate $E(T)$ one needs to know all accessible energies for a specific system. Another way to calculate this temperature correction is that we imagine this system as a classical one. Classically, in order to heat up a system, one needs to transfer energy to the system by moving atoms around and vibrating faster. If the energy of the system increase subsequently the temperature of system will increase. The amount of energy that needs to be transferred per temperature is the heat capacity (at constant pressure), $\mathrm{C_p(T)}$. The sum of the ground-state energy, E_0, and the thermal energy of the system will be considered as the system's internal energy, $E(T)$. By knowing the heat capacity $\mathrm{C_p(T)}$ changes with temperature one can calculate the internal energy in the relevant temperature:

$$E(T) = E_{DFT}(T = 0) + \int_0^T C_p(T')dT' \tag{44}$$

The integral term on the right side of equation (5) has a very small contribution to internal energy at room temperature.

In order to find Gibbs binding free energy of adsorbed intermediate from equation 41 the normal modes of vibration for different intermedates have been utilized to calculate E_{ZPE} , S, and $H_{0K\to T}$. Therefore, following relations have been used for this purpose:

$$E_{ZPE} = \frac{1}{2}\sum_i h\nu_i \tag{45}$$

$$TS_{vib} = \sum_i \left(\frac{h\nu_i}{e^{h\nu_i/k_B T} - 1} - k_B T ln\left(1 - e^{-h\nu_i/k_B T}\right) \right) \tag{46}$$

$$H_{0K\to T} = \sum_i \left(\frac{h\nu_i}{e^{h\nu_i/k_B T} - 1} \right) \tag{47}$$

where $h, k_B, and\ \nu_i$ are Plank constant, Boltzman constant and vibrational frequency, respectively. $E_{ZPE}, TS_{vib}\ and\ H_{0K\rightarrow T}$ for molcules have been extracted from thermodynamic tables[65].

3.9.3 Computational hydrogen electrode model

The estimation of the free energy of adsorption for electrochemical reaction intermediates is a very difficult in a realistic electrochemical system because of the presence of electrolyte molecules and electric field. It is computationally very demanding to simulate such a large number of adsorbate/catalyst surface configurations with the full details of electrolyte-catalyst interface. The CHE model is a tool which helps to approximate the reaction free energy of an electrochemical reaction[66] at certain potential. The reaction free energy of the electrochemical system is calculated at a given U from the reaction free energy calculated without explicitly considering the potential or the electrolyte. The model links the reaction free energy of each step involving a coupled electron-proton transfer to the applied U by a simple linear relation by

$$\Delta G_{AH}(U) = \Delta G_{AH}(U = 0) + eU \tag{48}$$

where ***e*** is the elementary charge. Therefore, for any elementary step, one can calculate the free energy change associated with the transformation at U= 0 V and predict the electrochemical potential required to drive the reaction step forward. $\Delta G_{step,i}$ for any reaction step is estimated as the difference between the binding free energy of any initial and any subsequent adsorbate $\Delta G_{j,i}$ and $\Delta G_{f,i}$. So, every $\Delta G_{step,i}$ is defined as

$$\Delta G_{step,i} = \Delta G_{f,i} - \Delta G_{j,i} \tag{49}$$

$\Delta G_{j,i}$ and $\Delta G_{f,i}$ are calculated as demonstrated in (48). If the potential is chosen to be on a reversible hydrogen electrode (RHE) scale, where the following reaction is reversible at 0 V vs RHE (V-RHE).

$$\frac{1}{2}H_2 = H^+ + e^- \tag{50}$$

In CHE model, the free energy of an adsorbate (e.g. ΔG_{AH}) is estimated with respect to hydrogen gas. Utilizing the adsorbate binding free energies for calculation of ΔG_{step}, at U = 0 V, the energies for the proton and electron gets included implicitly. For the overall reaction to happen at an appreciable rate, all such steps must have $\Delta G_{step} < 0$. The reaction step requiring the largest negative potential for making the forward reaction feasible is called the potential limiting step and the required potential is the limiting potential for the overall reaction.

3.9.4 Nudged elastic band method

The slowest reaction step is a rare event in comparison to other fast reaction steps or molecular vibrations. The most important problem in catalysis is to find the activation energy barrier and the transition state for a given reaction. The energetically highest point in the minimum energy path is transition state which connects the initial state and final

state. As it is a saddle point in the minimum energy path, the reaction rate is maximum through this path. In order to find the minimum energy path, the nudged elastic band (NEB) method, the initial and final positions of the system are connected with a linear chain of images or replicas of the system. To search for a minimum energy path between the initial and final state and to keep the images evenly distributed along the path a spring potential is applied between adjacent images. The system is then relaxed and minimized with respect to total energy, the tangential component of the spring force and the perpendicular component of the real force is used. To force one of the images at the saddle point, the image with the highest energy is released from the spring system and relaxed with a reversal of the force component along the direction of the path. This trick is known as climbing image NEB[67,68].

3.9.5 The electrochemical solid-liquid interface (ESLI) model

The electrode/electrolyte interface is modeled using metal slabs with water bilayer(s) on top. To create the bias, excess H atoms are included in the water layer as shown in Figure 3. Adding this extra H atom to the water and calculating the electronic structure of the system results in the formation of solvated protons in the water layer and transfer of the electrons to the metal. This is because the electron from this additional H atoms transfer to the metal surface rather than in the water. By varying the number of hydrogen atoms added and/or the unit cell size used in the calculations, the electrostatic potential of the double layer can be varied. The potential is deduced from the work function.

To calculate the electrostatic potential of the double layer, here we consider a number of different area super cells with N surface metal atoms along with n protons in the double layer. The integral free energy (G_{int}) per surface metal atom (or surface area) relative to H_2 is then calculated as

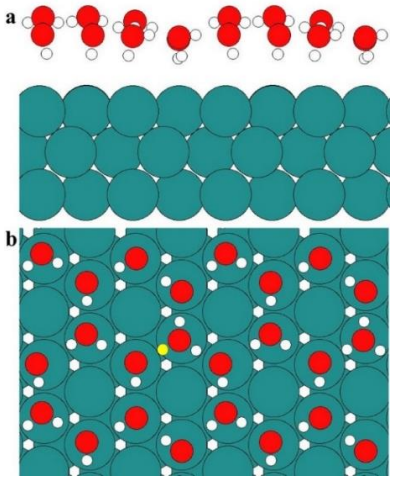

Figure 3. a) Side view and b) top view of water bilayer on Ru (0001) in the presence of one extra proton (-0.6 V applied potential). The extra proton is colored yellow[31].

$$G_{int} = \frac{\left(G(N,n) - G(N,0) - \frac{n\mu H_2}{2}\right)}{N} \tag{51}$$

G_{int} is a function of charge per surface area $\theta = n/N$. Here μH_2 indicates the chemical potential of molecular hydrogen. First, we choose μH_2 such that G_{int} has its minimum for the configuration with no proton in the water layer, more precisely G_{int} is zero by definition which corresponds to a potential scale of $U - U_{pzc}$. Here U is the electrode potential calculated from the work function and U_{pzc} is the potential of zero charge.

G_{int} corresponds to the free energy stored in the capacitator set up by the protons in the water layer and their counter charge in the metal. It should therefore be quadratic in potential

$$G_{int} = \frac{1}{2} C (U - U_{pzc})^2 \tag{52}$$

where the C is capacitance. Figure 4 illustrates the calculated G_{int} at varying unit cell sizes and varying charge, and the quadratic behavior can be seen clearly in this figure.

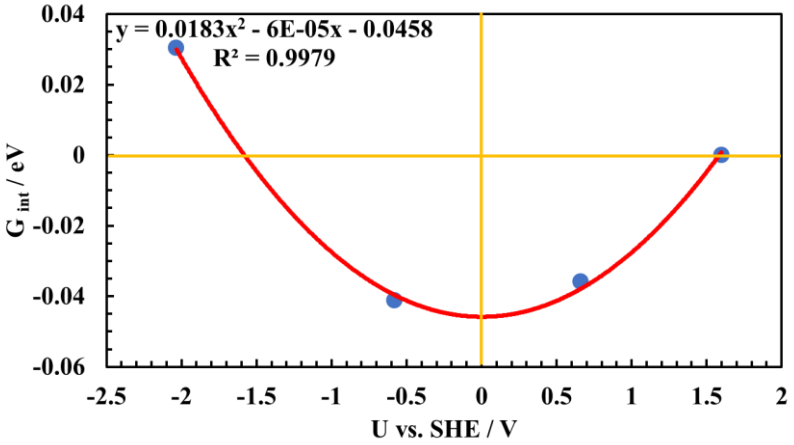

Figure 4. Integral free energy of the protons in the double layer as a function of the applied potential obtained from the work function[31].

3.9.6 A brief comparison of different solid-liquid interfacial models

Determining electrochemical barriers under a constant driving force or applied potential has remained as one of the most important open challenges in ab initio simulations of the electrochemical interface. Two types of techniques are currently used for such purposes; one is extrapolation techniques[28,69], which are based on a fully explicit definition of the electrolyte and the other one is implicit solvent models[70–74], which represent the solvent as a continuous medium allowing a continuous variation in electrolyte charge. Recently, hybrid explicit-implicit solvent models have emerged in the field[23,75]; there, the implicit part accounts for the electrolyte with little computational cost while retaining part treats explicitly.

Over the past several decades, computational chemistry has been developed enormously, which helps us to understand a wide variety of interface phenomena at an unprecedented level[76–82]. Particularly, electrocatalysis has been grown rapidly with the advent of DFT. Over the past 15 years, the computational hydrogen electrode model[66] has been served as a useful tool to determine the thermochemistry of coupled proton−electron transfers using simple surface science calculations. For several applications such as electrochemical reaction barriers, electric field, and pH effects, one must carefully consider the electrolyte effect. Several methods have been developed to model the electrochemical interface in ab initio simulations. Recently, in addition to a fully development in explicit simulations of the electrolyte[69,83], different implicit solvation methods[70–74] have also been developed and implemented in the most commonly used DFT codes. Each of these techniques comes with their own pros and cons. As we mentioned earlier, fully explicit models represent an atomistic insight into the effects of solvation and the effect of electric field on reaction energetics[20,31,69]. However, they suffer from issues related to expensive electrolyte sampling methods. On the contrary, continuum solvation methods do not rely on expensive sampling techniques, but they still suffer from a variety of challenges[84], such as connecting the classical treatment of solvation with the atomistic treatment of the surface. Above all, in continuum methods, the chemical interaction of ions with the surface cannot be reproduced because of the smearing of surface charge over the entire electrode. Solvation energies in these methods have essentially been fit to molecular solutes in order to be able to compare them with experimental reference data[71,85]. Moreover, hydrogen bonding has been necessary for these energies while investigating proton-electron reactions on extended surfaces[86,87]. To fix this issue, hybrid approaches have been introduced, including explicit electrolyte molecules and continuum solvation[23,75]. These approaches are receiving a growing amount of attention recently.

Among explicit methods, we can refer to the one we discussed before in section 3.8.5. We should mention the charge extrapolation method as another explicit method which has been developed in Norskov's group[88]. In this method in order to predict the slope of energy as a function of potential, one needs to rely on the mean-field approximation of the interface mainly. The primary difficulty with this method is identifying the charge in each state, and due to this fact, most of the results from the cell extrapolation method[28,69], which consider being a benchmark, are not correctly reproducible through the charge extrapolation method. Another solid-liquid interfacial model is the one that has been developed in Janik's group[89–91]. The model of the "electrochemical interface" is very simplified, and only one H_2O molecule is included. This model is the so-called H-shuttle model. In this model, the proton starts as an H adatom on the surface before it is transferred to the water molecule and then reacts with the adsorbate. The mechanism for a reduction reaction in this model always starts with a Volmer oxidation step of a hydrogen adatom. A hydronium ion is then formed above the surface along this pathway, but it is unsolvated because no other water molecules are used in the model. The problem with this model is that all proton-electron transfer barriers are treated as nonelectrochemical barriers, and a symmetry factor of 0.5 is then used to get the effect of applied potential. Therefore this will raise concern regarding the application of such a solid-liquid interfacial model for electrochemical applications operating at a constant applied electrode potential.

Finally, continuum methods, which mainly rely on continuous variation in charge, are mostly designed to keep the work function constant between states at a little additional

computational cost. Those methods have their own challenges and problems, and they are beyond the scope of the current thesis.

3.10 Concepts in catalysis

3.10.1 Scaling relations

Generally, it has been found that the binding energy of different intermediates that bind to the surface through the same atom(s) scale with each other. In other words, density functional theory-based simulations have shown that[92] the binding energy of any of a given adsorbate scales approximately with the binding energy of the central atom. This behavior attributes to the fact that the central atom mainly participates in direct chemical bonding with the catalyst surface. These observed linear relations which show energy of adsorbates as a function of binding energy of central atom is popularly known as scaling relations within the field of theoretical catalysis[92–94]. For example, Figure 5 shows the scaling relation between OH* and CH_3O* intermediates bind to the surface through oxygen atoms.

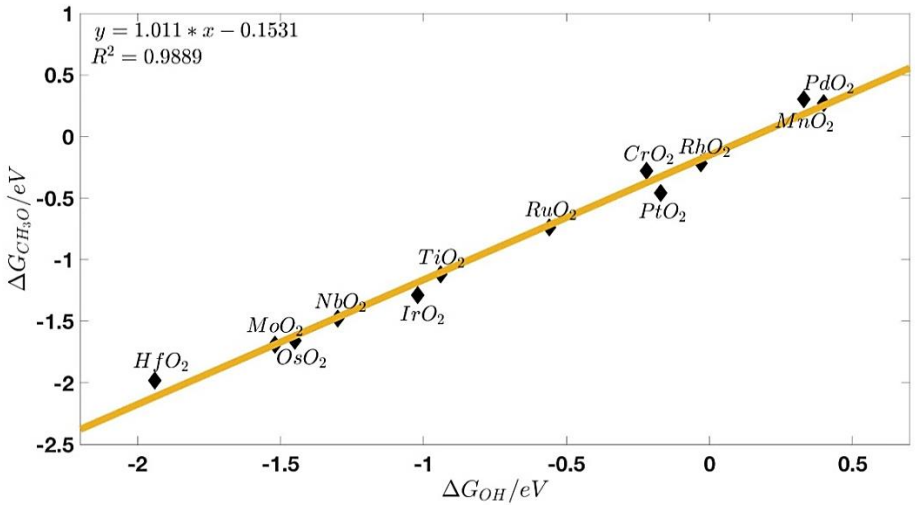

Figure 5. Scaling relation for CH_3O vs OH[95].

3.10.2 Volcano relation in multistep reaction

Sabatier's empirical law states that for a reaction, by using the linear relations there is an optimum binding energy for an intermediate where both stronger and weaker binding leads to lower activity. This volcano shaped relationship between activity and binding energy is straightforward to understand for a simple reaction like HER[96]. If the hydrogen atom binds too weakly to the surface then it is inefficient to form H*, and if it binds too strongly then removal of H* to synthesize hydrogen gas takes too much energy. However, the relationship between adsorbate binding energies and overall activity is non-intuitive for a complex reaction like CO_2RR due to the large number of adsorbates and possible pathways. Simple linear relations based on scaling laws help reducing this complexity. Utilizing correlation between the binding energy of different adsorbates, the activity can be modeled as a function of only one or two binding energy parameters. Finally, this simplification lead to a volcano like binding energy–activity relation similar to Sabatier's

volcano concept. The binding energy to which one can correlate all other binding energy parameters and activity, is often termed as the descriptor for the catalytic process. Figure 6 shows a volcano plot for formic formation.

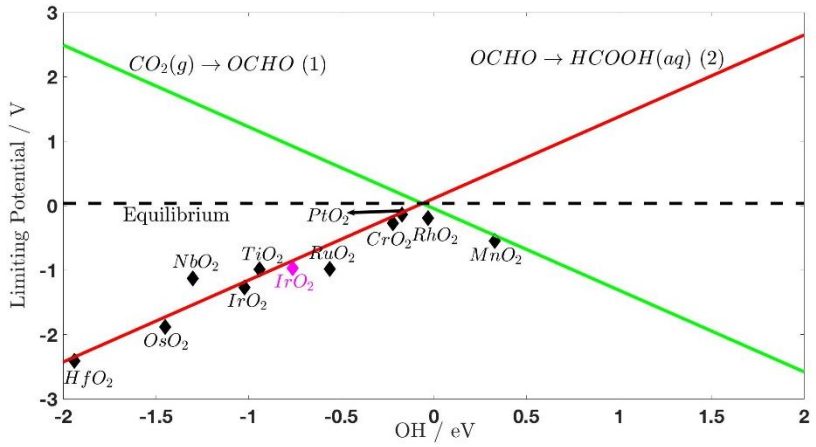

Figure 6. Theoretical volcano for formation of formic acid from scaling relations[95].

4 Summary of Papers

4.1 Paper I

In the first paper, we used density functional theory to investigate reactivity trends of the electrochemical CO_2 reduction reaction (CO_2RR) towards formic acid, methanediol, methanol, and methane on 12 transition metal oxides catalysts in their rutile structure. Using scaling relation of adsorbed intermediates activity and selectivity volcanos for various products are constructed. We found that RuO_2, IrO_2, TiO_2, NbO_2, MoO_2, OsO_2 and HfO_2 are selective towards methanol while RhO_2, PtO_2, MnO_2 and PdO_2 are selective towards formic acid. We also obtained scaling figure for OH binding free energy *vs* hydrogen binding free energy. The hydrogen binding free energy is used to estimate activity of hydrogen evolution reaction.

4.2 Paper II

In the second paper *ab initio* molecular dynamic simulations at room temperature have been used to improve the model system and methodology by including solvation effects. Using this improved model system then nudge elastic band method has been utilized to calculate proton-electron transfer barriers to elucidate the reaction mechanism for CO_2RR on $RuO_2(110)$ towards several products such as formic acid, CO, methanediol, methanol, methane and as well as H_2 evolution. A significant difference for energy barrier towards methanol and methane has been observed and the calculated barrier for methane has been found to be substantially higher than methanol. Our results show why RuO_2 catalysis CO_2RR towards formic acid and not to CO(g) and methanol. Our calculations also indicate that RuO_2 is much more selective towards H_2 formation than for CO_2RR at any applied potential.

4.3 Paper III

In the third paper, density functional theory has been used to elucidate the mechanism of the nitrogen reduction reactions (NRR) on the Ru (0001) electrode. In this regard, electrochemical solid liquid interface model has been used to gain further insight into reaction mechanism and subsequently different pathways towards ammonia are investigated. We found that the initial activation of $N_2(g)$ is the rate limiting step. The optimal mechanism of NRR towards ammonia on Ru (0001) follows an associative mechanism up to the second proton-electron transfer step. We propose that dissociation of the N-N bond will take place after the addition of a proton to the NH_2N species in a vertical position, releasing the first NH_3 molecule and leaving N adsorbed on the surface. we also found two other possible pathways towards different products, one toward diazine and the other one towards hydrazine.

5 Conclusion and outlook

5.1 Conclusion

This thesis is a detail investigation of electrochemical CO_2 and N_2 reduction reactions on transition metal oxides and transition metals to gain better insight into reaction mechanisms. Regarding CO_2RR using simple thermochemical model selectivity and activity volcano plots for formic acid, methanediol, methanol and methane have been constructed. There, RuO_2, IrO_2, TiO_2, NbO_2, MoO_2, OsO_2 and HfO_2 are predicted to be selective towards methanol while RhO_2, PtO_2, MnO_2 and PdO_2 are predicted to be selective towards formic acid. In a more detail study on RuO_2 by improving the model system and methodology we found that despite the fact that TCM-CHE shows RuO_2 is more selective towards CO_2RR than HER, more detail analysis using calculated activation energies reveal that RuO_2 is more selective towards HER and CO_2RR is a very unlikely to happen which is in agreement with the recent experimental results. Our calculations here also show a very high barrier towards methane compare to methanol in close agreement with experiment where methane has not been detected at any condition. Regarding NRR, our detail analysis also illustrates that protonation of N_2(g) to NNH is rate limiting step. We found that the optimal reaction mechanism towards ammonia leading to N_2, NNH, NH_2N/NHNH and NH_2 in perfect agreement with the intermediates measured in surface enhanced infrared absorption spectroscopy (SEIRAS) experiment (N_2, NNH, NHNH and NH_2).

5.2 Outlook

Optimal performance for reduction reactions highly depends on the proper choice of catalyst and operating condition. The overall kinetics of the reduction reactions are related to many factors, for instance including catalyst composition/structure, and reaction conditions such as electrolyte type, pH, applied potential, the membrane separating the anolyte and catholyte, temperature, reactants partial pressure and cell dimensions. Therefore, it is highly demanding to develop a mathematical model that is capable of simulating the performance of the electrochemical cell such that the influence of each variable on cell performance can be easily discerned. Such a model can also be utilized to check the consistency between the calculated mechanism for CO_2RR or NRR with experimental results.

The overall performance of the system is related to the immediate environment of the CO_2RR or NRR catalyst. The concentrations of reactive and non-reactive species in the close proximity of the catalyst surface, as well as their mutual interactions, can directly affect the catalytic behavior, and therefore change the achievable activity and selectivity. Mass transport becomes a crucial factor for these reactions because of the very limited solubility of N_2 or CO_2 in aqueous solutions and can also change the concentration of N_2/CO_2 and protons in the local environment during reaction due to the continuous

consumption of nitrogen/carbon dioxide and production of hydroxide (OH^-) ions. Designing more desirable reaction interfaces will help to achieve performance gains and this emphasizes the importance of mass transport as a controlling optimization parameter for the CO_2RR or NRR systems. What constitutes the local reaction environment in these electrocatalytic systems, however, is still an open question. Further investigations need to be carried out to search for the physical phenomena that contribute to the local environment of the catalyst and that appropriately represent the parameters most crucial for the performance. Most of the quantum mechanical simulations done so far only include the adsorbed intermediates on the cathode (not even region 1 in Figure 7(b)). The poor agreement between experimental data and simulations reported so far is mainly because of this very approximated model system. Recently, we went beyond this approximated model system by including region 1 in our simulations, and a better agreement was observed with experimental results[31,97]. Still, this perspective is not enough to properly explain most of the experimental observations in this field. Unfortunately, quantum mechanical simulations alone are not able to go beyond region 1 due to their very limited simulation capabilities. Therefore, in some studies, the model has been improved by combining quantum mechanical simulations with a microkinetic model, as has been done recently for the CO_2 reduction reaction (CO_2RR) (region 1+2 in Figure 7(b))[98]. However, those simulations are still limited to a region very close to the cathode surface and the effect of mass transport of species from the bulk solution to region 2 is ignored. Recently, Singh *et al.*[99] and Bohra *et al.*[100] have included the whole boundary layer region (region 1+2+3 in Figure 7(b)) for CO_2RR. There, a continuum model for species transport was combined with a microkinetic model for the cathode reactions and the results were in notably good agreement with experimental observations. Therefore, building up such a robust simulation to improve NRR and CO_2RR technology for it to be scalable and economically viable is imperative.

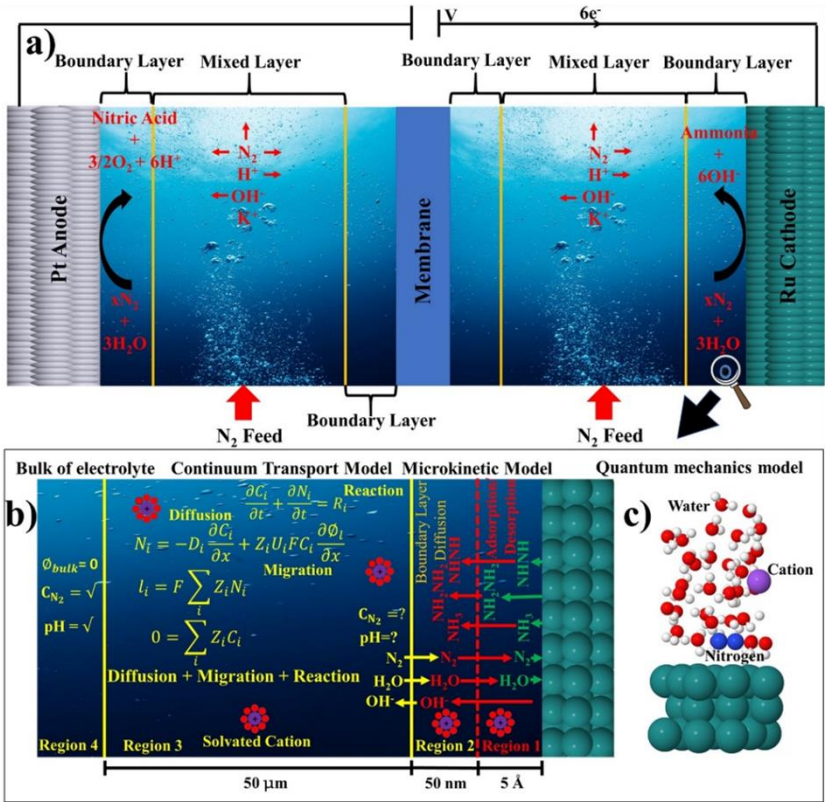

Figure 7. A realistic model system proposed to simulate NRR on Ru electrode.

Figure 8 shows the flowchart for the multiscale simulation which couples continuum transport model, microkinetic model, and quantum mechanical simulations. The input for the simulation is the applied potential to the cathode. The concentration of CO_2/N_2 (C_{N_2}/C_{CO_2}) and pH (C_{N_2}/C_{CO_2}= ? and pH =? at the left boundary of region 2 in Figure 7(b)) are determined using their initial bulk values (region 4). Then, the quantum mechanical simulations are performed in the VASP software to obtain the energetics and geometry of the electrochemical solid-liquid interface (region 1 in Figure 7(b), where the model system is shown in Figure 7(c)). Using ab initio molecular dynamics, 5 ps of explicit water dynamics will be performed. After performing molecular dynamics, geometry optimizations and transition state searches will be carried out using quantum mechanical techniques to calculate the free energies of activation, reaction, adsorption and desorption. Then, those values will be used to calculate rate constants and equilibrium constants for each elementary reaction and adsorbates. Partial current densities of products will be calculated using the supplied rate parameters to the microkinetic model (region 1+2). The continuum model utilizes (region 3) the partial current densities from the microkinetic model to calculate the concentration of CO_2/N_2 and pH at the left boundary of region 2. The simulation will be iterated sequentially until the convergence in the concentration of CO_2/N_2 and pH is reached.

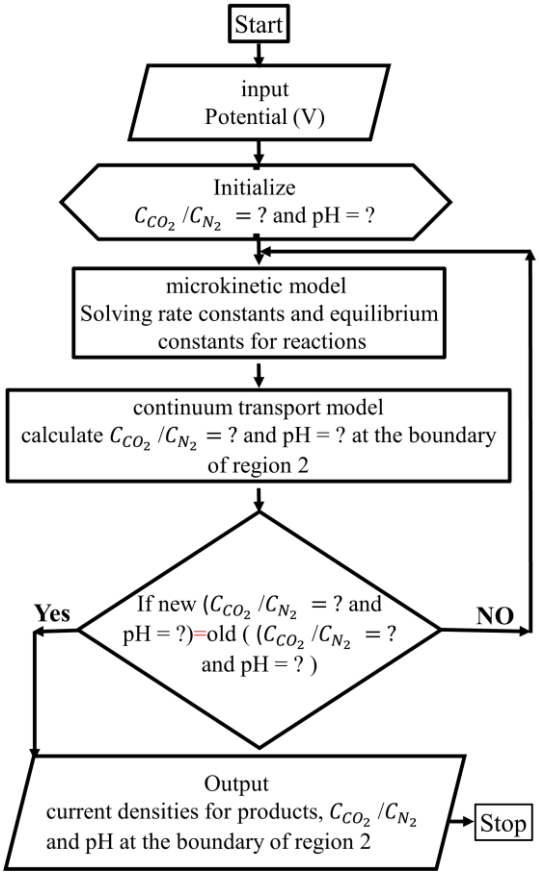

Figure 8. Proposed flowchart of the multiscale simulation.

References

1 B. Obama, *Science.*, 2017, **355**, 126–129.

2 X. Lim, *Nature*, 2015, **526**, 628–630.

3 G. Harp, K. C. Tran, C. Bergins, T. Buddenberg, I. Drach, O. Sigurbjornsson, C. Bergins, M. Hitachi, P. Systems and E. Gmbh, *METEC 2nd ESTAD, Düsseldorf, Ger.*, 2016, 15–19.

4 D. T. Whipple and P. J. A. Kenis, *J. Phys. Chem. Lett.*, 2010, **1**, 3451–3458.

5 K. P. Kuhl, E. R. Cave, D. N. Abram and T. F. Jaramillo, *Energy Environ. Sci.*, 2012, **5**, 7050–7059.

6 A. Bandi, *J. Electrochem. Soc.*, 1990, **137**, 2157.

7 A. Bandi, *J. Electrochem. Soc.*, 1992, **139**, 1605.

8 J. P. Popić, M. L. Avramov-Ivić and N. B. Vuković, *J. Electroanal. Chem.*, 1997, **421**, 105–110.

9 N. Spataru, K. Tokuhiro, C. Terashima, T. N. Rao and A. Fujishima, *J. Appl. Electrochem.*, 2003, **33**, 1205–1210.

10 J. Qu, X. Zhang, Y. Wang and C. Xie, *Electrochim. Acta*, 2005, **50**, 3576–3580.

11 S. Mezzavilla, Y. Katayama, R. Rao, J. Hwang, A. Regoutz, Y. Shao-Horn, I. Chorkendorff and I. E. L. Stephens, *J. Phys. Chem. C*, 2019, **123**, 17765–17773.

12 M. A. Henderson, *Surf. Sci. Rep.*, 2002, **46**, 1–308.

13 A. Lobo and H. Conrad, *Surf. Sci.*, 2003, **523**, 279–286.

14 R. Mu, Z. J. Zhao, Z. Dohnálek and J. Gong, *Chem. Soc. Rev.*, 2017, 46, 1785–1806.

15 A. Rendón-Calle, S. Builes and F. Calle-Vallejo, *Appl. Catal. B Environ.*, 2020, **276**, 119147.

16 P. J. Feibelman, *Science.*, 2002, **295**, 99–102.

17 H. Ogasawara, B. Brena, D. Nordlund, M. Nyberg, A. Pelmenschikov, L. G. M. Pettersson and A. Nilsson, *Phys. Rev. Lett.*, 2002, **89**, 276102.

18 S. Schnur and A. Groß, *New J. Phys.*, 2009, **11**, 125003.

19 X. Lin and A. Groß, *Surf. Sci.*, 2012, **606**, 886–891.

20 J. Hussain, H. Jónsson and E. Skúlason, *ACS Catal.*, 2018, **8**, 5240–5249.

21 A. Bagger, L. Arnarson, M. H. Hansen, E. Spohr and J. Rossmeisl, *J. Am. Chem. Soc.*, 2019, **141**, 1506–1514.

22 X. Liu, J. Xiao, H. Peng, X. Hong, K. Chan and J. K. Nørskov, *Nat. Commun.*, 2017, **8**, 15438.

23 J. D. Goodpaster, A. T. Bell and M. Head-Gordon, *J. Phys. Chem. Lett.*, 2016, **7**, 1471–1477.

24 S. Siahrostami and A. Vojvodic, *J. Phys. Chem. C*, 2015, **119**, 1032–1037.

25 A. Bagger, R. M. Arán-Ais, J. Halldin Stenlid, E. Campos dos Santos, L. Arnarson, K. Degn Jensen, M. Escudero-Escribano, B. Roldan Cuenya and J. Rossmeisl, *ChemPhysChem*, 2019, **20**, 3096–3105.

26 M. Van Den Bossche, E. Skúlason, C. Rose-Petruck and H. Jónsson, *J. Phys. Chem. C*, 2019, **123**, 4116–4124.

27 P. Lindgren, G. Kastlunger and A. A. Peterson, *ACS Catal.*, 2020, **10**, 121–128.

28 E. Skúlason, V. Tripkovic, M. E. Björketun, S. Gudmundsdóttir, G. Karlberg, J. Rossmeisl, T. Bligaard, H. Jónsson and J. K. Nørskov, *J. Phys. Chem. C*, 2010, **114**, 18182–18197.

29 M. H. Hansen and J. Rossmeisl, *J. Phys. Chem. C*, 2016, **120**, 29135–29143.

30 T. Cheng, H. Xiao and W. A. Goddard, *J. Phys. Chem. Lett.*, 2015, **6**, 4767–4773.

31 E. Tayyebi, Y. Abghoui and E. Skúlason, *ACS Catal.*, 2019, **9**, 11137–11145.

32 C. Zhang, J. Hutter and M. Sprik, *J. Phys. Chem. Lett.*, 2019, **10**, 3871–3876.

33 K. P. Kuhl, T. Hatsukade, E. R. Cave, D. N. Abram, J. Kibsgaard and T. F. Jaramillo, *J. Am. Chem. Soc.*, 2014, **136**, 14107–14113.

34 A. A. Peterson, F. Abild-Pedersen, F. Studt, J. Rossmeisl and J. K. Nørskov, *Energy Environ. Sci.*, 2010, **3**, 1311–1315.

35 A. A. Peterson and J. K. Nørskov, *J. Phys. Chem. Lett.*, 2012, **3**, 251–258.

36 J. Rossmeisl, Z. W. Qu, H. Zhu, G. J. Kroes and J. K. Nørskov, *J. Electroanal. Chem.*, 2007, **607**, 83–89.

37 J. Lee, D. C. Sorescu, X. Deng and K. D. Jordan, *J. Phys. Chem. Lett.*, 2013, **4**, 53–57.

38 J. R. Jennings, *„Catalytic ammonia synthesis: Fundamentals and Practice“ Plenum Press, New York*, Plenum Press, 1991.

39 L. Stryer, *Stryer Biochemistry*, 1995.

40 E. Skúlason, T. Bligaard, S. Gudmundsdóttir, F. Studt, J. Rossmeisl, F. Abild-Pedersen, T. Vegge, H. Jónsson and J. K. Nørskov, *Phys. Chem. Chem. Phys.*, 2012, **14**, 1235–1245.

41 S. Back and Y. Jung, *Phys. Chem. Chem. Phys.*, 2016, **18**, 9161–9166.

42 Y. Abghoui, A. L. Garden, V. F. Hlynsson, S. Björgvinsdóttir, H. Ólafsdóttir and E. Skúlason, *Phys. Chem. Chem. Phys.*, 2015, **17**, 4909–4918.

43 Y. Abghoui, A. L. Garden, J. G. Howalt, T. Vegge and E. Skúlason, *ACS Catal.*, 2016, **6**, 635–646.

44 Á. B. Höskuldsson, Y. Abghoui, A. B. Gunnarsdóttir and E. Skúlason, *ACS Sustain. Chem. Eng.*, 2017, **5**, 10327–10333.

45 S. Z. Andersen, V. Čolić, S. Yang, J. A. Schwalbe, A. C. Nielander, J. M. McEnaney, K. Enemark-Rasmussen, J. G. Baker, A. R. Singh, B. A. Rohr, M. J. Statt, S. J. Blair, S. Mezzavilla, J. Kibsgaard, P. C. K. Vesborg, M. Cargnello, S. F. Bent, T. F. Jaramillo, I. E. L. Stephens, J. K. Nørskov and I. Chorkendorff, *Nature*, 2019, 570, 504–508.

46 Y. Yao, H. Wang, X. Z. Yuan, H. Li and M. Shao, *ACS Energy Lett.*, 2019, **4**, 1336–1341.

47 C. Clay, S. Haq and A. Hodgson, *Chem. Phys. Lett.*, 2004, **388**, 89–93.

48 S. Maier and M. Salmeron, *Acc. Chem. Res.*, 2015, **48**, 2783–2790.

49 S. I. Sandler, *Chemical, Biochemical and Engineering Thermodynamics*, Wiley, Fourth Edi., 2006.

50 A Bard and L. Faulkner, *Russ. J. Electrochem.*, 2002, **38**, 1505–1506.

51 W. Kohn and L. J. Sham, *Phys. Rev.*, 1965, **140**, A1133.

52 G. Kresse and J. Furthmüller, *Phys. Rev. B - Condens. Matter Mater. Phys.*, 1996, **54**, 11169–11186.

53 G. Kresse and D. Joubert, *Phys. Rev. B - Condens. Matter Mater. Phys.*, 1999, **59**, 1758–1775.

54 J. Vandevondele, M. Krack, F. Mohamed, M. Parrinello, T. Chassaing and J. Hutter, *Comput. Phys. Commun.*, 2005, **167**, 103–128.

55 J. Hutter, M. Iannuzzi, F. Schiffmann and J. Vandevondele, *Wiley Interdiscip. Rev. Comput. Mol. Sci.*, 2014, **4**, 15–25.

56 J. K. Nørskov, T. Bligaard, J. Rossmeisl and C. H. Christensen, *Nat. Chem.*, 2009, 1, 37–46.

57 S. B. Rohra, Exact-Exchange Kohn-Sham Spin-Current Density-Functional Theory. Ph.D. thesis, 2006.

58 P. Hohenberg and W. Kohn, *Phys. Rev.*, 1964, **136**, B864.

59 J. P. Perdew, J. A. Chevary, S. H. Vosko, K. A. Jackson, M. R. Pederson, D. J. Singh and C. Fiolhais, *Phys. Rev. B*, 1992, **46**, 6671–6687.

60 J. P. Perdew, J. A. Chevary, S. H. Vosko, K. A. Jackson, M. R. Pederson, D. J. Singh and C. Fiolhais, *Phys. Rev. B*, 1993, **48**, 4978.

61 J. Wellendorff, K. T. Lundgaard, A. Møgelhøj, V. Petzold, D. D. Landis, J. K. Nørskov, T. Bligaard and K. W. Jacobsen, *Phys. Rev. B - Condens. Matter Mater. Phys.*, , DOI:10.1103/PhysRevB.85.235149.

62 S. Grimme, *J. Comput. Chem.*, 2006, **27**, 1787–1799.

63 S. Grimme, J. Antony, S. Ehrlich and H. Krieg, *J. Chem. Phys.*, 2010, **132**, 148–150.

64 M. Born and R. Oppenheimer, *Ann. Phys.*, 1927, **389**, 457–484.

65 J. K. Nørskov, F. Studt, F. Abild-Pedersen and T. Bligaard, *Fundamental Concepts in Heterogeneous Catalysis*, John Wiley & Sons, Inc, Hoboken, NJ, USA, 2014, vol. 9781118888957.

66 J. K. Nørskov, J. Rossmeisl, A. Logadottir, L. Lindqvist, J. R. Kitchin, T. Bligaard and H. Jónsson, *J. Phys. Chem. B*, 2004, **108**, 17886–17892.

67 G. Henkelman, B. P. Uberuaga and H. Jónsson, *J. Chem. Phys.*, 2000, **113**, 9901–9904.

68 G. Henkelman and H. Jónsson, *J. Chem. Phys.*, 2000, **113**, 9978–9985.

69 J. Rossmeisl, E. Skúlason, M. E. Björketun, V. Tripkovic and J. K. Nørskov, *Chem. Phys. Lett.*, 2008, **466**, 68–71.

70 O. Andreussi, I. Dabo and N. Marzari, in *Journal of Chemical Physics*, American Institute of PhysicsAIP, 2012, vol. 136, p. 064102.

71 S. Ringe, H. Oberhofer, C. Hille, S. Matera and K. Reuter, *J. Chem. Theory Comput.*, 2016, **12**, 4052–4066.

72 C. D. Taylor, S. A. Wasileski, J. S. Filhol and M. Neurock, *Phys. Rev. B - Condens. Matter Mater. Phys.*, 2006, **73**, 165402.

73 R. Jinnouchi and A. B. Anderson, *J. Phys. Chem. C*, 2008, **112**, 8747–8750.

74 K. Mathew, R. Sundararaman, K. Letchworth-Weaver, T. A. Arias and R. G. Hennig, *J. Chem. Phys.*, 2014, **140**, 084106.

75 M. Saleheen and A. Heyden, *ACS Catal.*, 2018, 8, 2188–2194.

76 C. Arrouvel, B. Diawara, D. Costa and P. Marcus, *J. Phys. Chem. C*, 2007, **111**, 18164–18173.

77 S. Irrera, D. Costa and P. Marcus, *J. Mol. Struct. THEOCHEM*, 2009, **903**, 49–58.

78 D. J. Appelhans, Z. Lin and M. T. Lusk, *Phys. Rev. B - Condens. Matter Mater. Phys.*, 2010, **82**, 073410.

79 T. Ludwig, J. A. Gauthier, K. S. Brown, S. Ringe, J. K. Nørskov and K. Chan, *J. Phys. Chem. C*, 2019, **123**, 5999–6009.

80 C. F. Dickens and J. K. Nørskov, *J. Phys. Chem. C*, 2017, **121**, 18516–18524.

81 E. Wimmer, C. L. Fu and A. J. Freeman, *Phys. Rev. Lett.*, 1985, **55**, 2618–2621.

82 R. Kortlever, J. Shen, K. J. P. Schouten, F. Calle-Vallejo and M. T. M. Koper, *J. Phys. Chem. Lett.*, 2015, **6**, 4073–4082.

83 K. Chan and J. K. Nørskov, *J. Phys. Chem. Lett.*, 2016, **7**, 1686–1690.

84 J. A. Gauthier, S. Ringe, C. F. Dickens, A. J. Garza, A. T. Bell, M. Head-Gordon, J. K. Nørskov and K. Chan, *ACS Catal.*, 2019, **9**, 920–931.

85 K. Mathew, R. Sundararaman, K. Letchworth-Weaver, T. A. Arias and R. G. Hennig, *J. Chem. Phys.*, 2014, **140**, 084106.

86 G. S. Karlberg, *Phys. Rev. B - Condens. Matter Mater. Phys.*, 2006, **74**, 153414.

87 L. G. V. Briquet, M. Sarwar, J. Mugo, G. Jones and F. Calle-Vallejo, *ChemCatChem*, 2017, **9**, 1261–1268.

88 K. Chan and J. K. Nørskov, *J. Phys. Chem. Lett.*, 2015, **6**, 2663–2668.

89 X. Nie, M. R. Esopi, M. J. Janik and A. Asthagiri, *Angew. Chemie - Int. Ed.*, 2013, **52**, 2459–2462.

90 S. Maheshwari, G. Rostamikia and M. J. Janik, *J. Chem. Phys.*, 2019, **150**, 041708.

91 G. Rostamikia, S. Maheshwari and M. J. Janik, *Catal. Sci. Technol.*, 2019, **9**, 174–181.

92 F. Abild-Pedersen, J. Greeley, F. Studt, J. Rossmeisl, T. R. Munter, P. G. Moses, E. Skúlason, T. Bligaard and J. K. Nørskov, *Phys. Rev. Lett.*, 2007, **99**, 016105.

93 I. C. Man, H. Y. Su, F. Calle-Vallejo, H. A. Hansen, J. I. Martínez, N. G. Inoglu, J. Kitchin, T. F. Jaramillo, J. K. Nørskov and J. Rossmeisl, *ChemCatChem*, 2011, **3**, 1159–1165.

94 G. Jones, T. Bligaard, F. Abild-Pedersen and J. K. Nørskov, Using scaling relations to understand trends in the catalytic activity of transition metals, https://iopscience.iop.org/article/10.1088/0953-8984/20/6/064239,2008.

95 E. Tayyebi, J. Hussain, Y. Abghoui and E. Skúlason, *J. Phys. Chem. C*, 2018, **122**, 10078–10087.

96 A. B. Laursen, A. S. Varela, F. Dionigi, H. Fanchiu, C. Miller, O. L. Trinhammer, J. Rossmeisl and S. Dahl, *J. Chem. Educ.*, 2012, **89**, 1595–1599.

97 E. Tayyebi, J. Hussain and E. Skúlason, *Chem. Sci.*, 2020, **11**, 9542–9553.

98 X. Liu, P. Schlexer, J. Xiao, Y. Ji, L. Wang, R. B. Sandberg, M. Tang, K. S. Brown, H. Peng, S. Ringe, C. Hahn, T. F. Jaramillo, J. K. Nørskov and K. Chan, *Nat. Commun.*, , DOI:10.1038/s41467-018-07970-9.

99 M. R. Singh, J. D. Goodpaster, A. Z. Weber, M. Head-Gordon and A. T. Bell, *Proc. Natl. Acad. Sci. U. S. A.*, 2017, **114**, E8812–E8821.

100 D. Bohra, J. H. Chaudhry, T. Burdyny, E. A. Pidko and W. A. Smith, *Energy Environ. Sci.*, 2019, **12**, 3380–3389.

Paper I

Trends of Electrochemical CO_2 Reduction Reaction on Transition Metal Oxide Catalysts.

Tayyebi, E.; Hussain, J.; Abghoui, Y.; Skúlason, E.

J. Phys. Chem. C 2018, 122, 10078−10087.

JPCCK

JULY 23, 2020
VOLUME 124
NUMBER 29
pubs.acs.org/JPCC

THE JOURNAL OF PHYSICAL CHEMISTRY C

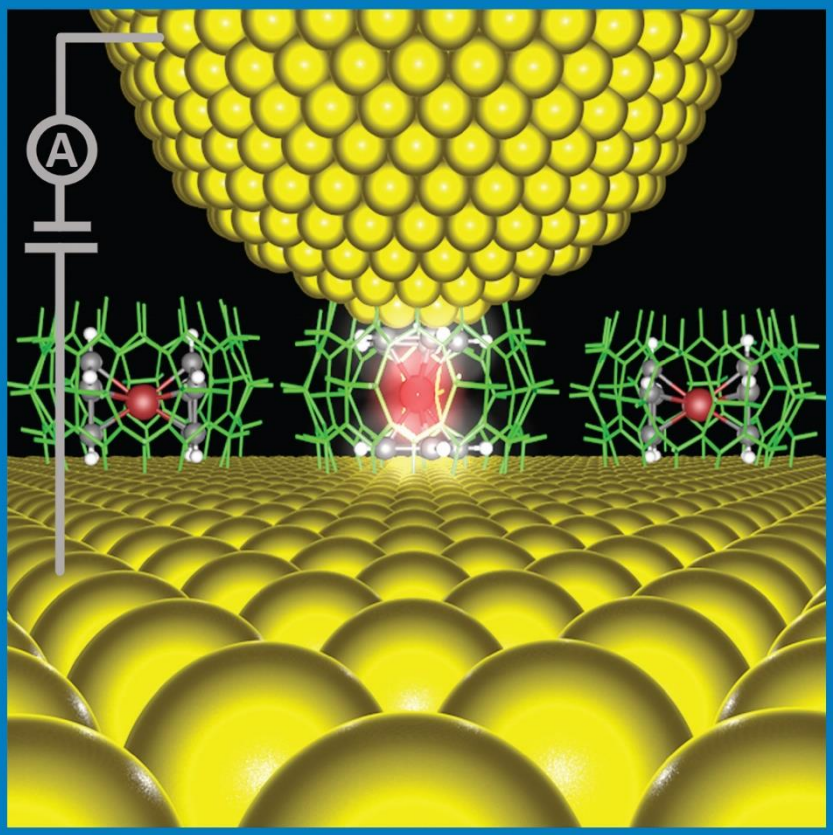

Reliably Probing the Conductance of an Encapsulated Molecule via van der Waals Contacts

ENERGY CONVERSION AND STORAGE; CATALYSIS; OPTICAL, ELECTRONIC, AND MAGNETIC PROPERTIES AND PROCESSES; INTERFACES; NANOMATERIALS AND HYBRID MATERIALS

ACS Publications
Most Trusted. Most Cited. Most Read.

www.acs.org

THE JOURNAL OF PHYSICAL CHEMISTRY C

Article

Cite This: J. Phys. Chem. C 2018, 122, 10078−10087

pubs.acs.org/JPCC

Trends of Electrochemical CO_2 Reduction Reaction on Transition Metal Oxide Catalysts

Ebrahim Tayyebi,[†] Javed Hussain,[†] Younes Abghoui,[†] and Egill Skúlason*[,†]

[†]Science Institute and Faculty of Physical Sciences, University of Iceland, VR-III, 107 Reykjavík, Iceland

Supporting Information

ABSTRACT: Density functional theory calculations were used to explore reactivity trends of the electrochemical CO_2 reduction reaction (CO_2RR) toward methanol, methane, methanediol, and formic acid on 12 transition metal dioxide (TMO) surfaces in their rutile structure. The (110) facet of the TMOs was used as a model system to investigate the thermodynamic limiting potentials of CO_2RR. Activity and selectivity volcano plots for various products were obtained through the scaling relations of adsorbed intermediates. RhO_2 is predicted to be a good catalyst for production of formic acid with low onset potential of around −0.2 V. In addition to its high activity, hydrogen evolution reaction (HER) is predicted to not limit its efficiency due to weak hydrogen binding free energy on this oxide. CrO_2 is another promising candidate for CO_2RR with onset potential of around −0.3 V toward most of the products. CrO_2 seems to be more interesting than RhO_2 for production of methanol, methane, and methanediol as it adsorbs HCOOH on its surface in a dissociated form. CrO_2 is also predicted to be more selective toward these CO_2RR products than toward forming hydrogen gas.

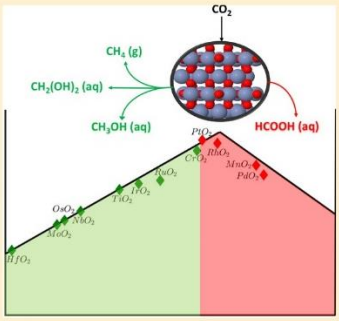

INTRODUCTION

Converting fossil resources into fuels and chemicals is an essential process in modern life. Presently more than 80%[1] of global energy needs are met from fossil fuels and their daily increasing use has dire consequences on global energy requirements. Over the past few decades, balance in nature has been lost because of the dramatic increase in CO_2 emission, mainly from the burning of carbonaceous fuels, resulting in global warming. In order to lower the CO_2 content of the atmosphere much effort on many levels have been made. One of the most important measures in this regard is to lower CO_2 emission in the first place and to convert it back to fuel or other chemicals. To pursue this goal, a novel catalyst that operates at ambient conditions and electrochemically reduces CO_2 to high-value-added products is the key technology.[2] This catalyst could be used in a decentralized device powered by renewable energy sources (such as solar, wind, or geothermal power) consuming CO_2 as a reactant and directly converting it to fuels.[3] There are, however, a number of challenges that needs to be overcome in order to develop such catalyst that is active, energy efficient and selective toward a particular product such as formic acid, methane, or methanol.[4,5]

From many experimental works on the electrochemical CO_2 reduction reaction (CO_2RR) conducted on different metal catalysts, Cu has been confirmed to be the best pure metal catalyst for producing hydrocarbons with reasonable current efficiency, whereas other metal electrodes mainly form formate, CO or H_2 gas.[6,7] Cu is, however, not efficient enough for commercial applications since it requires a large overpotential. It also produces 15 different carbon-containing products as well as H_2 gas[8,9] where separation of these wide range of products is a costly process.[10] At around −1 V, Cu electrode produces methane (40%), methanol (0.1%), ethylene (25%), ethanol (10%), and propanol (4%). However, it has been recently shown that Cu is very active to reduce CO to C2 and C3 aldehydes as well as ethylene at smaller overpotentials of around −0.4 to −0.6 V.[11] This shows that the Cu electrode is more efficient toward producing hydrocarbons rather than alcohols, and only insignificant amount of methanol is produced, which would be the most attractive product as transportation fuel.

A number of theoretical studies have been carried out over the past few years to model the CO_2RR using density functional theory (DFT) calculations. Insight into the mechanism or the reaction pathway for reducing CO_2 to CH_4 on the stepped Cu(211) surface was first proposed by Peterson et al.[12] There, the most important aspects of the overall system were calculated explicitly, or the free energy of adsorbed intermediates on the catalyst surface. This is what we refer to the thermochemical model (TCM). The TCM approach has been successfully applied on a number of electrochemical systems; including the water oxidation reaction on transition metal oxides (TMOs),[13,14] the N_2 electro-reduction reaction on the surfaces of transition metals,[15] transition metal nitrides[16−20] as well as transition metal oxides,[21] hydrogen evolution reaction (HER) on transition metal nitrides[22] and CO_2RR on transition metals[12,23] and TMOs.[24−26] The effect of the applied potential can be included implicitly using the computational hydrogen electrode

Received: March 6, 2018
Published: April 12, 2018

DOI: 10.1021/acs.jpcc.8b02224
J. Phys. Chem. C 2018, 122, 10078−10087

(CHE).[27] However, other parts of the electrochemical environment (solvent effects, pH dependency, etc.) are usually not taken explicitly into account. Energy barriers of proton−electron transfer reactions are not included in the TCM approach but other studies have modeled that with various approaches.[28−33] Those studies have improved the reaction mechanism and it has been concluded that energy barriers are needed to capture the trends in product distribution seen in the experiments on the pure metals.[30] However, it has been concluded that the TCM-CHE approach is sufficient in obtaining a good estimate of the overpotential needed, both toward various products on Cu[12] and toward methane on various metal electrodes.[7,23]

Recently, it has been observed that the product distribution is different when TMOs are used as catalysts for CO_2RR than when the pure metal electrodes are used. Experimental works have shown that some particular TMOs, especially RuO_2, and RuO_2 in combination with other transition metal oxides such as IrO_2 or TiO_2, are active for CO_2RR and more selective toward methanol formation than any of the pure metals tested so far. Current efficiency toward methanol formation has been measured to be between 2 and 76% depending on the catalyst composition/structure and reaction conditions such as electrolyte type, pH, and applied potential.[34−38] However, a mixture of other carbon-containing compounds is also formed, such as formic acid and methane, as well as hydrogen gas.

Karamad et al.[24] used DFT calculations to get insight into the mechanism and reaction pathway for CO_2RR on RuO_2 using the TCM-CHE approach.[24] Following that study, Bhowmik et al.[25] used the same methodology to study the effect of different TMO overlayers on the RuO_2 (110) surface. In both of these studies on the TMO surfaces, it is concluded that reaction intermediates of the carbon-containing species bind through the oxygen atom(s). This is in contrast to the intermediates on the metal surfaces where it is concluded that most intermediates bind through the carbon atom.[12,23,28−31] This might be a justifying reason why metal oxide catalysts are more selective toward methanol, while pure metals are more selective toward methane and ethylene since there the oxygen atoms are reduced to water molecules. Therefore, metal oxides might open up new avenues for efficient liquid fuel production from CO_2.

In this article, we use the same methodology and model (GGA-DFT and TCM-CHE approach) as implemented by Karamad et al.[24] and Bhowmik et al.,[25] while here we use it to obtain trends for CO_2RR on 12 different TMO surfaces in their rutile structure. We calculate the adsorption free energy for various possible intermediates on these surfaces to search for the lowest free energy pathway for CO_2RR toward formic acid, methane, methanol and methanediol formation. We then use scaling relations between adsorbed species to construct "activity" volcano-plots in order to estimate the onset potential for each of the rutile oxides and to estimate the selectivity toward different products on the surface of these oxides.

■ COMPUTATIONAL METHODS AND MODEL SYSTEMS

The electronic structure calculations were performed using DFT within the BEEF-vdW functional in the VASP software.[39] This functional is particularly useful as it has been designed for accurate description of surface processes and also allows for the estimation of the uncertainty in the calculated energetics arising from the choice of exchange-correlation functional. All the calculations have been carried out at the GGA level of DFT and this has been shown to reliably capture trends in energetics compared to experiments for TMOs, see for instance formation energies of TMOs[40,41] and onset potentials for water splitting at TMO surfaces.[13] There are a number of higher-level functionals or methods available, such as the meta-GGA,[42−45] hybrid functionals[46] or Perdew−Zunger self-interaction corrected DFT,[47] which are crucial to use when information on the electronic structure is needed such as band gaps or electronic defects. However, they are all computationally more expensive than the GGAs, and since here we are doing a computational screening for reaction pathways for a range of TMOs, we have chosen BEEF-vdW in this work.

All the lattice parameters were optimized based on BEEF-vdW for ruthenium oxide (RuO_2), iridium oxide (IrO_2), niobium oxide (NbO_2), platinum oxide (PtO_2), titanium oxide (TiO_2), chromium oxide (CrO_2), manganese oxide (MnO_2), rhodium oxide (RhO_2), osmium oxide (OsO_2), hafnium oxide (HfO_2), molybdenum oxide (MoO_2), and palladium oxide (PdO_2) in their rutile crystal structure. The BEEF-vdW lattice parameters for these metal oxides are calculated and presented in the Supporting Information, Table S1. A plane wave basis set with a cutoff energy of 350 eV was used to expand the valence electron orbitals and the PAW method was used to represent core electrons.[48] Monkhorst Pack grid was used in order to reduce the number of k-points, which were $4 \times 4 \times 1$ in all cases. The atomic structure of the various reactants and products was found by minimizing the energy until atomic forces had dropped below 0.03 eV/Å.

The electrode was represented by a slab of four atomic layers with four metal atoms and eight oxygen atoms in each layer, and the slabs were separated with at least 16 Å of vacuum. Atoms in the bottom two layers were fixed while the atoms in the top two layers along with the adsorbed intermediates were allowed to fully relax. The dipole correction was used in all cases to decouple the electrostatic interaction between the periodically repeated slabs.

The rutile (110) surface contains metal atoms of two different coordination environments. Rows of 6-fold coordinated metal atoms alternate with rows of 5-fold coordinated metal atoms along the [001] direction. Whereas the 6-fold coordinated metal atoms have approximately the same geometry as bulk, the 5-fold coordinated metal atoms have an unsaturated bond perpendicular to the surface. Thus, two distinct surface sites are found, coordinatively unsaturated sites (cus-sites) on top of the 5-fold coordinated metal atoms and bridging sites (br-sites) between two 6-fold coordinated metal atoms (Figure 1). We found that the br-sites generally bind adsorbates stronger than the cus-sites do. On the stoichiometric (110) surface, the br-sites are occupied by oxygen, while the cus-sites are vacant. The bridging oxygen atoms are undercoordinated and can be reduced from the surface. In order to create a realistic model system of our rutile (110) surfaces for the CO_2RR, we use the same assumptions as previously made by Karamad et al. and Bhowmik et al.[24,25] According to Bhowmik et al.,[25] the most active sites for CO_2RR on their overlayers on RuO_2 are the bridge sites in the presence of CO spectator which is located on every other bridge sites. For the TMO surfaces considered in this work, we also find the bridge sites to be most active for CO_2RR, except for PtO_2 where some intermediates prefer to bind the *cus* sites. For some adsorbed species they adsorb bidentate on all the TMOs and there they adsorb on both a bridge site and on a cus site. The model

DOI: 10.1021/acs.jpcc.8b02224
J. Phys. Chem. C 2018, 122, 10078−10087

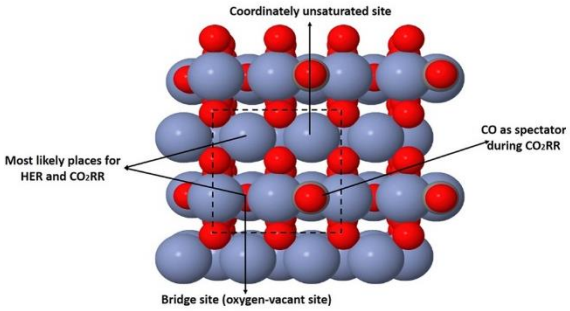

Figure 1. A model system of a (110) surface of a TMOs in its rutile structure. Purple balls indicate metal atoms, gray balls indicate carbon atoms and red balls indicate oxygen atoms. CO is spectator and, in all cases, located on bridge site (except for IrO_2 where we both report results when CO is on a bridge site or on a cus site) while CO_2RR takes place on other bridge and cus sites.

system is thus the rutile (110) surfaces in their reduced form, but with 1/4 ML of CO adsorbed on the bridge sites for all the TMOs considered here (see Figure 1). The only exception is IrO_2 (two different free energy diagrams in the Supporting Information) since the differences between free energy of adsorbed CO when it is on the br-site and cus-site is 0.11 eV, and CO_2RR will happen while CO is on cus-site as spectator. In order to maintain generality, we also include IrO_2 when CO is on the bridge site. Throughout this paper, the pink bullet is for IrO_2 when the CO spectator is on a br-site, while the black bullet is for when the CO spectator is on a cus-site.

The computational hydrogen electrode (CHE) model is a tool to approximate the reaction free energy of an electrochemical reaction[27] at a certain applied potential. The potential effects have been included by adding an implicit term, eU. The reaction free energy at an arbitrary potential U vs the standard hydrogen electrode (SHE) is given by

$$\Delta G_i(U) = \Delta G_i(U = 0) + eU \quad (1)$$

where **e** is the elementary charge. $\Delta G_i\ (U = 0)$ is calculated for each elementary step:

$$\Delta G(U = 0) = \Delta E_{DFT} + \Delta E_{ZPE} + \Delta E_{Sol} + \Delta H_{0K\to T} - TS \quad (2)$$

where ΔE_{DFT} is calculated with DFT and ΔE_{ZPE} and ΔS are zero-point energy corrections and entropy differences which are calculated within the harmonic approximation for the adsorbed species, while the values for the gas phase species are taken from thermodynamical tables.[49] ΔE_{Sol} is the adsorbate stabilization term due to the solvent, which is not included in this study. $\Delta H_{0K\to T}$ is changes in internal energy because of temperature and it can be calculated by the following relation:

$$\Delta H_{0K\to T} = \int_0^T C_p(\acute{T})\, d\acute{T} \quad (3)$$

The integral term on the right side of eq 3 has a very small contribution to internal energy at room temperature, or less than 0.1 eV.[50]

The energy of molecular CO_2, H_2 and HCOOH are corrected by +0.3, + 0.1, and +0.15 eV, respectively, to correct for systematic DFT errors.[51] Reported reaction free energies and adsorbate binding free energies are referenced to the electronic energy of clean slab and $CO_{2(g)}$, $H_2O_{(l)}$ and $H_{2(g)}$ free energies. Since CO_2RR is typically done in a 0.1 to 0.5 M solution of $KHCO_3$ or $NaHCO_3$,[6,36,52,53] such solutions allow dilute formic acid to exist in a hydrated anion form ($HCOO^-$). A free energy correction of −0.19 eV for deprotonation and solvation has therefore been included.[54] The free energy of $H_2C(OH)_2$(aq) has been obtained from ref55.

SIMULATION RESULTS

1. Methane, Methanol, Methanediol, and Formic Acid Pathways and Corresponding Onset Potentials. In the first electron−proton transfer step of CO_2RR, two possible intermediates can be formed: OCHO (formate) or COOH (carboxyl). OCHO is found to be a more stable intermediate compared to COOH on all the TMO surfaces studied in this work. Therefore, all the reactions follow the pathways containing OCHO as an intermediate. The OCHO intermediate binds to the surface through both oxygen atoms (bidentate adsorption on one cus site and one bridge site)

Table 1. Onset Potentials toward Various Products, OH Removal Potentials, and Methane and Methanol Pathways along with Potential Limiting Steps (Number in Parentheses, Extracted from Tables 2 and 3)

Oxides	Onset potential for different reactions in V vs RHE						OH strength	Methanol and methane production pathways (from Tables 2 and 3) along with potential limiting steps (numbers)	
	HER	Formic acid	Methanol	Methane	Methanediol	OH removal		Methanol	Methane
RuO2	-0.25	-0.98	-0.80	-0.80	-0.95	-0.56	Moderate	C (2)	F (2)
IrO2	-0.70	-1.27	-1.12	-1.02	-1.37	-1.02	Moderate	C (6)	G (8)
IrO2	-0.57	-0.97	-0.85	-0.76	-1.23	-0.76	Moderate	C (6)	F (8)
NbO2	-0.84	-1.13	-1.3	-1.30	-1.23	-1.3	Strong	C (6)	G (8)
PtO2	-0.16	-0.14	-0.27	-0.27	-0.27	-0.17	Moderate	A (3)	E (3)
TiO2	-0.19	-0.99	-0.95	-0.95	-1.09	-0.94	Moderate	C (2)	G (2)
OsO2	-0.97	-1.88	-1.49	-1.45	-1.98	-1.45	Strong	C (6)	G (8)
HfO2	-0.76	-2.41	-1.94	-1.94	-2.22	-1.94	Strong	D (6)	G (8)
MnO2	-0.63	-0.55	-1.2	-1.2	-1.2	0.33	Weak	A (3)	E (3)
RhO2	-0.06	-0.19	-0.23	-0.23	-0.23	-0.03	Moderate	A (3)	E (3)
CrO2	-0.29	-0.27	-0.31	-0.31	-0.31	-0.22	Moderate	B (3)	F (3)
PdO2	-0.29	-0.77	-1.1	-1.1	-1.1	0.4	Weak	A (3)	E (3)
MoO2	-0.41	-1.9	-1.51	-1.52	-1.86	-1.52	Strong	D (5)	G (8)

DOI: 10.1021/acs.jpcc.8b02224
J. Phys. Chem. C 2018, 122, 10078−10087

whereas COOH binds to the surface via its carbon atom to a bridge site.

A major competing reaction with CO_2RR is the HER. In Table 1, we estimate the onset potential for HER on the TMOs by calculating the binding free energy of a H adatom on the surfaces. In the discussion section, we will compare the onset potentials for CO_2RR toward different products with that of HER in order to estimate the selectivity between these two reactions.

In addition to HER, CO formation should also be taken into account, as it can result in CO poisoning. CO formation only happens via COOH intermediate where CO_2 is protonated to form carboxyl through the following reaction:

$$CO_{2(g)} + * + (H^+ + e^-) \rightarrow COOH \quad (4)$$

where * is an active site on the catalysts surface. In this paper we do not include the * for the adsorbed intermediates but the state of the reactant and desorbed products are indicated with (g), (aq), or (l). Further protonation leads to CO formation on the surface:

$$COOH + (H^+ + e^-) \rightarrow CO + H_2O(l) \quad (5)$$

which may poison the surface of the catalyst because we find that the CO reduction to CHO or COH has high thermochemical barriers on those TMOs. The CO admolecules that may be formed on the surfaces are therefore spectator species during CO_2RR. The ultimate goal of our current study is to determine the CO_2RR overpotentials toward different products using metal oxides as catalysts in order to find catalysts that are selective toward methanol. The presence of CO on the surface as spectator is assumed not to lead to CORR as it is thermodynamically very slow compared to CO_2RR on these materials. COOH binding free energy at $U = 0$ V was found to be negative for RuO_2, IrO_2, OsO_2, MoO_2, and HfO_2, but positive for TiO_2, NbO_2, CrO_2, RhO_2, PtO_2, and PdO_2. However, at the onset potentials for CO_2RR, the COOH adsorption is usually exergonic (but never as exergonic as the OCHO adsorption), and therefore a low CO coverage is expected to build up on the surfaces, while OCHO is the key intermediate of CO_2RR.

The first two protonation steps in CO_2RR may lead to the formation of aqueous formic acid or adsorbed HCOOH species on the surface. Käckell et al.[56,57] have shown that HCOOH(aq) on TiO_2 surface should be in a dissociated form ($HCOO^-$ + H^+) but according to the work done by Karamad et al.[24] on RuO_2, HCOOH(aq) can adsorb on the surface in undissociated form (see RuO_2 in Figure 2). We have included this possibility in this work and found that surfaces of TiO_2 and CrO_2 will rather dissociate the formic acid into the $HCOO^-$ and H^+ complex where $HCOO^-$ binds to the bridge sites on the surface through its oxygen atoms but the proton binds to a surface oxygen atom (see TiO_2 in Figure 2). However, the undissociated HCOOH species is the intermediate that forms on the RuO_2, IrO_2, HfO_2, OsO_2, and MoO_2. On the contrary, binding energy of HCOOH on PdO_2, PtO_2, MnO_2, and RhO_2 surfaces is so weak that that intermediate cannot form on those surfaces, and therefore it desorbs into the solution as HCOOH(aq). So, for those catalysts, in order to produce higher electron proton transfer products, the reaction may continue via activation of formic acid in aqueous form.

Forth protonation step results in methanediol formation and further protonation (six or eight) leads to methanol or methane

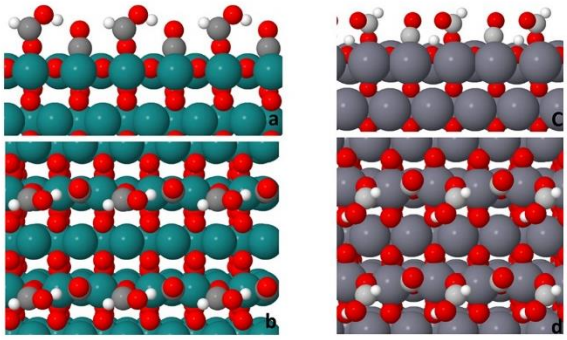

Figure 2. (a) Side view and (b) top view of HCOOH on RuO_2 surface. (c) Side view and (d) top view of $HCOO^-$ + H^+ complex on TiO_2 surface. In both cases, CO is spectator. According to our simulation only TiO_2 and CrO_2 dissociate HCOOH to the $HCOO^-$+H^+ complex but other surfaces such as IrO_2, NbO_2, MoO_2, OsO_2, HfO_2, PtO_2, RhO_2, MnO_2, and PdO_2 can form the undissociated HCOOH species on their surfaces similar to RuO_2.

products, respectively. Several possible pathways for methanol and methane formation are presented in Tables 2 and 3 (more details in the Supporting Information). For RhO_2, PtO_2, MnO_2, and PdO_2, HCOOH binds weakly to the surface and formic acid is the main product before formation of methanediol, methane, and methanol may take place. In order for the reaction to proceed to more reduced products, HCOOH in aqueous form must be activated and for this to happen the reaction needs to be run in acidic condition leading to lower methanediol, methane and methanol efficiencies.[25]

Similar to the work done by Bhowmik et al.,[25] OH adsorption free energy is also taken here as a descriptor for other adsorbate binding free energies to map the multi-dimensional problem into one variable. With this we obtain activity volcanos (and to some extent selectivity volcanos) for different products on TMO surfaces. Our pathway for methane and methanol formation on RuO_2 is quiet similar to the pathway used by Bhomwik et al.[25] A small difference exists between the pathways presented in this work and that reported by Karamad et al.,[24] which is presumably because Kramad's work is based on the RPBE functional whereas here we use the BEEF-vdW functional.

2. Formic Acid and Methanediol Formation. Formic acid and methanediol are a two and four-step electron transfer products of CO_2RR, respectively. As mentioned earlier, RhO_2, PtO_2, MnO_2, and PdO_2 cannot adsorb the HCOOH intermediate on their surfaces and therefore these catalysts have the potential of producing aqueous formic acid. Figures 3 and 4 and Table 3 show that among these candidates, PtO_2 and RhO_2 have the smallest onset potentials toward formic acid, or −0.14 and −0.19 V, respectively. In Table 1 the onset potentials for the HER are estimated from the adsorption free energy of a H adatom. For RhO_2, the hydrogen binding free energy is −0.06 eV whereas the binding free energy of OCHO is −0.19 eV, and therefore a higher efficiency toward formic acid is expected than toward H_2. On the other hand, for PtO_2 the hydrogen binding free energy is −0.16 eV but the binding free energy of OCHO is 0.14 eV, and therefore HER is expected to dominate over CO_2RR. In the other words, RhO_2 has low activity toward HER (in CO_2 saturated solution) but high activity toward formic acid, and thus these factor make RhO_2 the best candidate for production of formic acid. It

DOI: 10.1021/acs.jpcc.8b02224
J. Phys. Chem. C 2018, 122, 10078−10087

Table 2. Possible Pathways for Methanol formation

	(e^-+H^+) steps					
pathways	1	2	3	4	5	6
A	OCHO	HCOOH or HCOOH(aq)	H_2COOH	$H_2CO + H_2O(l)$	CH_3O	$CH_3OH(aq)$
B	OCHO	HCOOH or HCOOH(aq)	H_2COOH	$O + CH_3OH(aq)$	OH	$H_2O(l)$
C	OCHO	HCOOH or HCOOH(aq)	H_2COOH	$CH_3O + OH$	$CH_3O + H_2O(l)$	$CH_3OH(aq)$
D	OCHO	HCOOH or HCOOH(aq)	H_2COOH	$CH_3O + OH$	$CH_3OH(aq) + OH$	$H_2O(l)$

Table 3. Possible Pathways for Methane formation

	(e^- + H^+) steps							
pathways	1	2	3	4	5	6	7	8
E	OCHO	HCOOH or HCOOH(aq)	H_2COOH	$H_2CO + H_2O(l)$	CH_3O	$CH_4(g) + O$	OH	$H_2O(l)$
F	OCHO	HCOOH or HCOOH(aq)	H_2COOH	$CH_3O + OH$	$CH_3O + H_2O(l)$	$CH_4(g) + O$	OH	$H_2O(l)$
G	OCHO	HCOOH or HCOOH(aq)	H_2COOH	$CH_3O + OH$	$CH_4(g) + O + OH$	$O + H_2O(l)$	OH	$H_2O(l)$

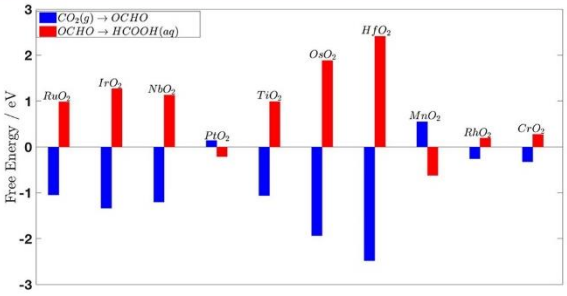

Figure 3. Free energy diagram for formic acid production at 0 vs RHE. The more endergonic step for each TMO indicates the required reducing potential.

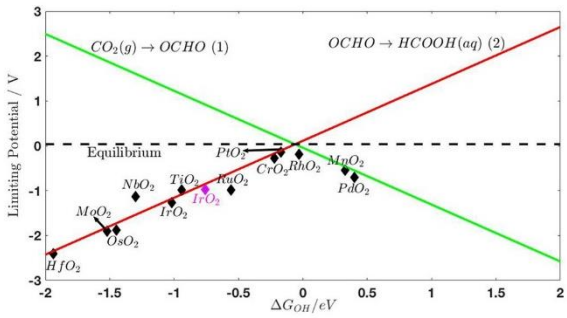

Figure 4. Theoretical volcano for formation of formic acid from scaling relations (lines). For each of the TMOs the explicit limiting potential values are included (diamond). Each line is for one electron−proton transfer step, indicated by the numbers in parentheses after each chemical equation to show the sequence of the reaction toward formic acid.

should be noted here that without CO_2 in the solution, RhO_2 is predicted here to have very small onset potential for HER.

CrO_2 is another candidate located very close to the top of the formic acid volcano (Figure 4), with predicted onset potential of −0.27 V (Table 1). The free energy of the adsorbed HCOOH species (actually as a $HCOO^-$ + H^+ complex on CrO_2 as explained above) is only 0.01 eV lower than the free energy of HCOOH(aq) and therefore CrO_2 is expected to both evolve formic acid as well as more reduced products (discussed below). The hydrogen binding free energy on CrO_2 is 0.29 eV whereas the OCHO binding free energy is −0.33 eV, meaning that this catalyst should be much more selective toward CO_2RR than HER.

CO_2RR toward methanediol requires four proton−electron transfer steps. CrO_2 is also on the top of volcano for methanediol formation (Figures 5 and 6) with predicted

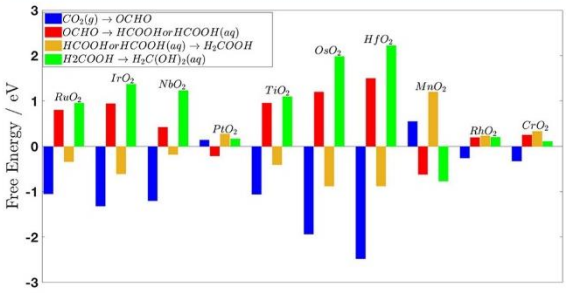

Figure 5. Free energy diagram for methanediol production at 0 vs RHE. The most endergonic step for each TMO indicates the required reducing potential.

onset potential of −0.31 V (Table 1). RhO_2 and PtO_2 are also located at the top of this volcano but those TMOs are predicted

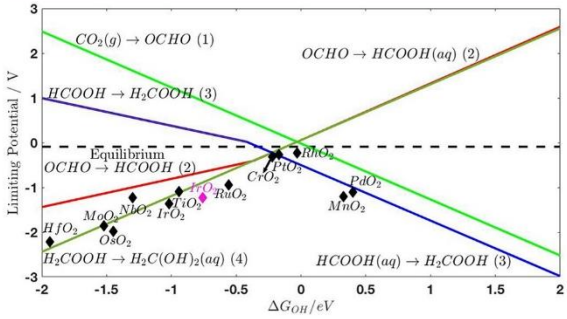

Figure 6. Theoretical volcano for formation of methanediol from scaling relations (lines). For each of the TMOs the explicit limiting potential values are included (diamond). Each line is for one electron−proton transfer step, indicated by the numbers in parentheses after each chemical equation to show the sequence of the reaction toward methanediol.

DOI: 10.1021/acs.jpcc.8b02224
J. Phys. Chem. C 2018, 122, 10078−10087

to be more selective toward formic acid formation as discussed above.

we need to clarify that the volcano plots presented here are composed of broken lines rather than straight lines (Bhomwik et al.[25]) as we are presenting the dominant elementary steps involved in the reaction pathway for each of our candidate considered here in this study.

3. Methane and Methanol Formation. CO_2RR toward methanol and methane requires 6 and 8 proton−electron transfer steps, respectively. Table 1 shows methanol and methane onset potentials and the thermodynamically potential limiting steps (PLS). The corresponding volcanos are presented in Figures 7 and 8, respectively. Since the mechanism

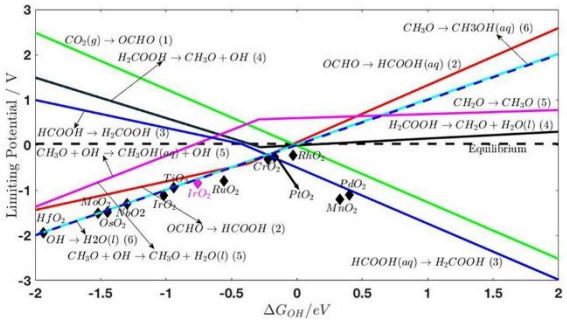

Figure 7. Theoretical volcano for formation of methanol from scaling relations (lines). For each of the TMOs the explicit limiting potential values are included (diamond). Each line is for one electron−proton transfer step, indicated by the numbers in parentheses after each chemical equation to show the sequence of the reaction toward methanol.

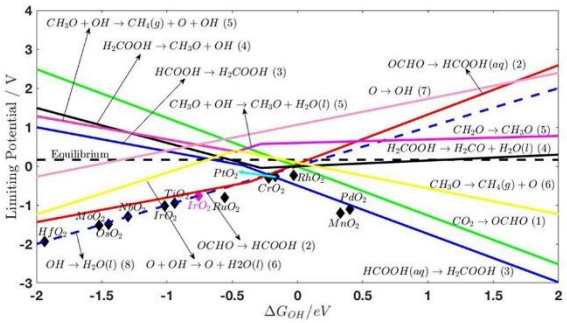

Figure 8. Theoretical volcano for formation of methane from scaling relations (lines). For each of the TMOs the explicit limiting potential values are included (diamond). Each line is for one electron−proton transfer step, indicated by the numbers in parentheses after each chemical equation to show the sequence of the reaction toward methane.

to either of those products is not the same for all TMOs, we simplify these volcano plots by only including reactions steps that exist in the minimum free energy pathway toward the products. This divides our volcano plots into different regions, depending on our descriptor; the binding energy of OH on the surfaces. As an example, in both of these volcano plots the intersection of OCHO → HCOOH and OCHO → HCOOH-(aq) lines is around −0.34 eV with respect to our descriptor. This can be seen from the change in slope of the red line at this value. Therefore, reduction of OCHO will form adsorbed HCOOH intermediate for the more reactive TMOs (binding OH stronger than −0.34 eV) while it will form desorbed HCOOH(aq) product on the less reactive TMOs (binding OH weaker than −0.34 eV). This may affect the subsequent steps, and therefore we only include the intermediates that are a part of the reaction network, for a given TMOs (or a region on the volcano plot). In several other cases, the lines are broken in a similar way.

For the left leg of the methanol volcano (Figure 7) there are three PLS; OH removal to water, $CH_3O \rightarrow CH_3OH(aq)$, and OCHO → HCOOH. The OH removal and the $CH_3O \rightarrow CH_3OH(aq)$ step overlap completely, meaning that those two reaction steps are the same in magnitude (or at least very similar) for a given TMOs. The OCHO → HCOOH step, however, only becomes the PLS close to the top of the volcano, but there it overlaps with the aforementioned steps. For the left leg of the methane volcano (Figure 8), we have the same PLS, except for the $CH_3O \rightarrow CH_3OH(aq)$ step, which is of course not a part of the reaction network. Thus, the OH removal potential may be considered as a representative of the left leg for both the methanol and the methane volcanos. For the right leg of both of the volcanos (where PtO_2, RhO_2, MnO_2, and PdO_2 are located), the $HCOOH(aq) \rightarrow H_2COOH$ step is PLS. However, as discussed above, those TMOs will start evolving formic acid at smaller potentials. It is impossible to predict here whether the desorbed HCOOH(aq) product can be reduced further, within the simple thermodynamical model used in this work.

The top of the volcano for methane and methanol is in both cases around $\Delta G_{OH} = -0.21$ eV. CrO_2 is located at the top of both volcanos with predicted onset potential of −0.31 V (Table 1). The main conclusion here is that catalysts with $\Delta G_{OH} > -0.21$ eV are selective toward formic acid, but those with $\Delta G_{OH} < -0.21$ eV are selective toward methane, methanol, and methanediol. CrO_2 is, however, predicted to produce all these products (formic acid, methane, methanol, and methanediol) at small onset potentials of around −0.3 V in all cases (Table 1).

Experimental work for methanol formation on RuO_2, TiO_2, and IrO_2 have shown that these oxides are selective toward methanol at potentials between −0.5 and −1 V vs RHE.[34−38] Our calculations confirm this and the predicted onset potentials we found for RuO_2 (−0.80 V), IrO_2 (−0.85 V), and TiO_2 (−0.99 V) are very close to the experimental values.

■ DISCUSSION

Similar to the work done by Bhomwik et al.,[25] we observed that OH adsorption energy is a very good descriptor for CO_2RR on pure TMOs, as it was for the TMO overlayers on RuO_2. All the intermediates in the reaction network (Tables 1 and 2) bind to the surface through oxygen atom(s), except the CH_2O species, which bind through both the oxygen atom and the carbon atom. Subsequent protonation of CH_2O to the next possible intermediates (CH_2OH or CH_3O), always leads to the formation of the CH_3O intermediate for all the TMOs considered in this work. Therefore, CH_2OH is not a part of the reaction pathway to methane or methanol and not included in Table 1 or 2. The reaction network presented in both the work of Karamad et al.[24] and Bhomwik et al.[25] is very similar, but not completely the same. In our work, we include all the intermediates presented in their work, and we find that the network presented in Karamad's work (for RuO_2) captures all the different lowest free energy reaction pathways on all the

DOI: 10.1021/acs.jpcc.8b02224
J. Phys. Chem. C 2018, 122, 10078−10087

TMOs considered here. We find the scaling relations of all the intermediates included in the overall reaction network as a function of the binding energy of the OH species (see Supporting Information). Those scaling relations are then used to construct volcano diagrams throughout the article.

For the TMO surfaces to catalyze the CO_2RR continuously, the surfaces need to be cleaned of OH species, but in all of the reaction pathways presented in Tables 1 and 2 the OH removal is the last or the second last step. As OH removal potentials ranges from −2 to +0.5 V for all the TMO catalysts, they can be categorized based on the strength of OH binding energy (Table 1). Because of high OH removal potential for some of these catalysts, the HER may become a dominant reaction compared to the CO_2RR, and this may affect the activity and selectivity of the catalysts. Even if the earlier intermediate steps in CO_2RR for producing methane or methanol are feasible at low overpotential, in order to remove OH, the reaction must be carried out at higher overpotentials where HER would be relatively fast.

Figure 9 presents a "selectivity volcano" for formic acid, methanediol, methanol, and methane products. Here we have

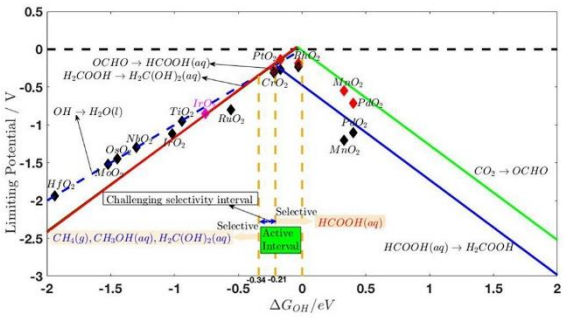

Figure 9. Theoretical activity and selectivity volcano for methane, methanol, methanediol and formic acid production. Green and red lines denote left and right sides of the volcano for formation of formic acid. Dashed blue and blue lines denote right and left sides of the volcano for formation of methane and methanol, and finally, dark green and blue lines are for formation of methanediol. Two dashed lines (one in −0.34 eV and the other in −0.21) also separate the volcano into two main areas: the right area (ΔG_{OH}>-0.21 eV) that is selective toward formic acid and the left area (ΔG_{OH} ← 0.34 eV) that is selective toward methane, methanol and methanediol. Furthermore, there is an area between −0.34 and −0.21 eV which is very active but without any specific selectivity.

added all the volcanos (Figures 4, 6, 7 and 8) into one volcano-plot for comparison. We conclude that, for ΔG_{OH} > −0.21 eV, the CO_2RR is more selective toward formic acid, but for ΔG_{OH} < −0.21 eV, the selectivity is more toward methane, methanol, and methanediol. On the left leg, the PLS toward formic acid and methanediol coincide each other, which means that the formation of those products need almost the same thermodynamic onset potentials. However, the overpotential toward methane and methanol is slightly lower and we predict here that those TMOs (from HfO_2 to RuO_2) will start forming methanol and methane at smaller onset potentials than needed to form methanediol or formic acid. CrO_2 and PtO_2 are on the top of the volcano for methane and methanol (blue line and dashed-blue line). In fact, PtO_2 is slightly on the right leg of this volcano which means it should be more selective toward formic acid. We have included the explicit values for the onset potentials toward different products on the volcano-plot and the onset potential toward formic acid on PtO_2 is −0.14 V whereas the onset potentials toward methanol, methane, and methanediol is −0.27 V. CrO_2 is located exactly at the top of the methanol-methane-methanediol volcanos and the formic acid volcano intercects those other volcanos where CrO_2 is located. Therefore, the onset potentials toward all these products for CrO_2 are very similar and all close to −0.3 V (see also Table 1).

The main conclusion about these overall volcanos (Figure 9) is that for −0.34 eV < ΔG_{OH} < −0.21 eV (−0.34 eV is approximately the intersection of the dashed-blue line and the red line in Figure 9) all these three lines (or the PLSs) in this interval closely coincide on one line. Therefore, we cannot predict the selectivity here since the onset potentials are always similar toward all products (note that CrO_2 is the only candidate within this interval). ΔG_{OH} < −0.34 eV and ΔG_{OH} > −0.21 eV are the only selective parts of this overall volcano. The former is somewhat selective toward methanol and methane, and the latter is more selective toward formic acid. As discussed above, CrO_2 is located on the top of the volcano for methanediol, methanol, and methane and the onset potential toward formic acid is very similar, and therefore it is predicted to form all these four products of CO_2RR. The important thing about CrO_2 is that it can adsorb the formic acid as an intermediate on its surface and continue its reduction toward methane, methanol, and methanediol with much smaller applied potential than compared to RuO_2, TiO_2 and IrO_2. From these calculations and analysis it seems that in order to find an active and selective catalyst among TMOs toward methane, methanol, and methanediol formation, the binding energy of the OH species on the surface needs to be between −0.5 and −0.34 eV, where the OH binding energy is moderate. In addition of being in this interval, the possible candidate needs to have a low activity toward HER as well. Another criteria that needs to be considered here is the CO poisoning. The only pathway which may lead to CO poisoning is through the COOH intermediate. Minimizing the rate toward hydrogen evolution and CO poisoning along with binding OH in a moderate way are the three criteria that should be considered at the same time in order to find a promising candidate. The binding free energy of OCHO, COOH and H are compared in Figure 10 and used in further analysis below. The candidates with weak H and COOH binding free energies will have low tendency to evolve hydrogen and poison the surface with CO. The candidates also need to bind OCHO moderately, between

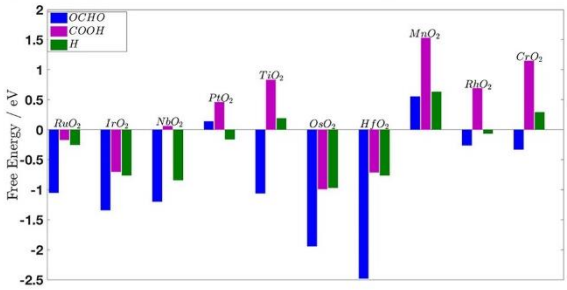

Figure 10. Free energy diagram for OCHO, H, and COOH on the TMO surfaces at 0 V. Negative values for H and COOH for each TMO are showing higher possibilities for getting poisoned by those species.

DOI: 10.1021/acs.jpcc.8b02224
J. Phys. Chem. C 2018, 122, 10078−10087

0 and −0.5 eV which is similar as the interval for the OH binding free energy since OCHO and OH scale linearly, almost one-to-one (see Supporting Information).

In Figure 11, we show that the COOH binding free energy and hydrogen binding free energy are correlated linearly. The

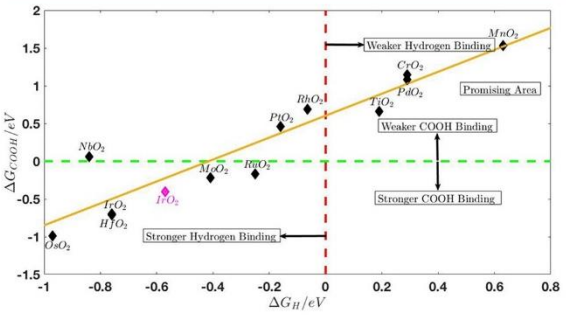

Figure 11. Scaling figure for COOH adsorption free energy vs hydrogen binding free energy. If COOH is formed as a species on the surface, it can lead to CO formation or CO poisoning. A strong H binding energy will lead to H poisoning and H_2 formation whereas a weak H adsorption would prevent proton adsorption until at more negative potentials. Here, we can see an area which indicate weaker COOH and hydrogen binding energies. On the basis of our analysis, we concluded that if a catalyst is found there, it would be the most promising candidate for CO_2RR, since there is smaller chance of surface poisoning by CO and H.

region (and candidates very close to this region) with weak (positive) hydrogen and weak COOH binding free energy is where one should be looking for the promising candidate(s) because there the rates toward HER and the CO poisoning is lower. Moderate OH binding free energy is another restriction, which needs to be added into the picture. All the design parameters (moderate OH binding, weak hydrogen binding and weak COOH binding) are included in Figure 12, where the OH binding free energy is plotted as a function of the H binding free energy (since COOH and H are correlated linearly we only include the H binding here). The most promising candidates for high CO_2RR selectivity and low HER activity

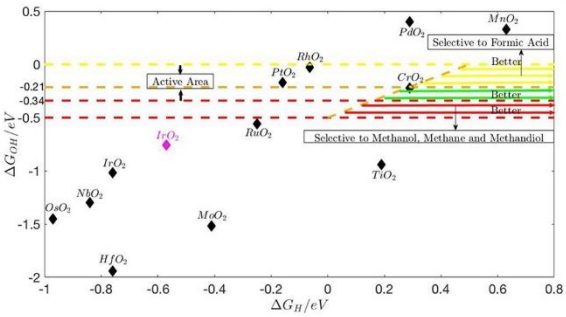

Figure 12. Scaling figure for OH binding free energy vs hydrogen binding free energy, where the OH is chosen as it is the descriptor on our volcano-graphs, and the catalysts with the lowest onset potentials for CO_2RR are located within the dashed lines. The hydrogen binding free energy can be used as an estimate of hydrogen evolution activity. Comparing hydrogen evolution activity with CO_2RR activity shows that CrO_2 is more selective toward CO_2RR than HER and the only candidate located in this active and selective area.

should be in the green, red, and yellow regions. For a candidate to be selective toward methane, methanol, and methanediol, it needs to be located in the red region (-0.5 eV < ΔG_{OH} < -0.34 eV). For a candidate to be selective toward formic acid, it should be located approximately between -0.21 eV < ΔG_{OH} < 0 eV (yellow region). Candidates located between -0.21 eV < ΔG_{OH} < -0.34 eV are predicted to evolve all four products. CrO_2 is the only candidate located in any of those regions and therefore it is promising for selective formation of CO_2RR products over HER.

In this work, all the analyses are based on the calculated thermodynamics of adsorbed intermediates on the TMO surfaces and the CHE is then used to vary the applied potential implicitly. In order to conclude whether these candidates are truly selective toward a given intermediate, one needs to consider kinetic and transport effects as well, which are beyond the scope of this study. Activation energies can be calculated for each of the proton−electron transfer steps (toward different intermediates and products) by setting up a charged double-layer model including a solid TMO electrode and an aqueous electrolyte solution as has been done for the metal-liquid interface for CO_2RR.[30,33] There, the charge difference in the double layer sets up the applied electric potential explicitly and therefore the proton−electron transfer barriers can be calculated as a function of explicitly varied potential. This approach is necessary in order to reproduce the experimentally observed product distribution as a function of both the metal type and the applied potential. Another approach has been proposed by Head-Gordon and co-workers for CO_2RR on Cu (100),[58] there they used a model that includes the effect of electrochemical potential, solvent, and electrolyte. The electrochemical potential was set by relating the applied potential to the Fermi energy and then calculating the number of electrons required by the simulation cell for that specific Fermi energy. The solvent was included as a continuum dielectric and the electrolyte described using a linearized Poisson−Boltzmann model. Goddard and co-workers used an approach similar to Head-Gordon for CORR on Cu (111).[59] They presented a methodology for density functional theory calculations to obtain accurate onset electrochemical potentials with explicit constant electrochemical potential and pH effects using implicit solvation. However, it has been shown that the TCM-CHE approach is sufficiently accurate to predict the onset potentials for various reactions on different catalyst's materials, including CO_2RR on metal catalysts, both in terms of which product is formed on Cu[12] and when the metal catalyst is varied.[7,23]

It should be noticed that some of the most promising candidates such as CrO_2 found in this work might not be very stable under reducing conditions. However, it is always possible to enhance the stability via doping or having an overlayer of these active oxides on some of the more stable oxides such as TiO_2. Pourbaix diagrams predict that not only ruthenium oxide but most of the oxides considered in this work (with the exception of TiO_2, ZrO_2, HfO_2) should be reduced under CO_2RR conditions. However, thermodynamics is not the only parameter that governs the stability of materials in electrochemical environment. The surface can be stabilized because of kinetic limitations. The CO/CO_2-rich environment might play a crucial role as well.

DOI: 10.1021/acs.jpcc.8b02224
J. Phys. Chem. C 2018, 122, 10078−10087

CONCLUSIONS

The main goal of this work was to establish trends in CO_2RR activity and selectivity for production of formic acid, methanediol, methanol, and methane on the surface of pure TMOs. We construct volcano plots through scaling relations of adsorbed intermediates that show selectivity toward methane and methanol when $\Delta G_{OH} < -0.34$ eV, but selectivity toward formic acid for $\Delta G_{OH} > -0.21$ eV. We also observe that there is an interval for OH adsorption free energy between -0.34 eV $< \Delta G_{OH} < -0.21$ eV, which is not selective toward any specific CO_2RR product, since the onset potentials toward all the products is predicted to be the same and very low. We found that CrO_2, PtO_2, and RhO_2 have smaller onset potentials compared to all other TMOs included in this work, or below -0.3 V. When the hydrogen evolution reaction is taken into account, CrO_2 and RhO_2 are predicted to be more selective toward formic acid, methane, methanol, and methanediol rather than evolving hydrogen, whereas PtO2 would be more selective toward forming hydrogen gas than the CO_2RR products. Experimental works for CO_2RR on RuO_2, IrO_2, and TiO_2 have shown that these TMOs are rather selective toward methanol at potentials between -0.5 to -1 V. Our simulation confirms this, and the calculated onset potentials for RuO_2, IrO_2, and TiO_2 are -0.80, -0.85, and -0.99 V, respectively, or within these experimental values.

ASSOCIATED CONTENT

Supporting Information

The Supporting Information is available free of charge on the ACS Publications website at DOI: 10.1021/acs.jpcc.8b02224.

Optimized lattice parameters, scaling figures for CO2RR network, and free energy diagrams (PDF)

AUTHOR INFORMATION

Corresponding Author

*(E.S.) E-mail: egillsk@hi.is.

ORCID

Javed Hussain: 0000-0003-4127-7447

Egill Skúlason: 0000-0002-0724-680X

Notes

The authors declare no competing financial interest.

ACKNOWLEDGMENTS

This work was supported by the Icelandic Research Fund and the Research Fund of the University of Iceland.

REFERENCES

(1) Olah, G. A.; Prakash, G. K. S.; Goeppert, A. Anthropogenic Chemical Carbon Cycle for a Sustainable Future. *J. Am. Chem. Soc.* **2011**, *133* (33), 12881−12898.

(2) Whipple, D. T.; Kenis, P. J. A. Prospects of CO_2 Utilization via Direct Heterogeneous Electrochemical Reduction. *J. Phys. Chem. Lett.* **2010**, *1* (24), 3451−3458.

(3) Barton Cole, E.; Lakkaraju, P. S.; Rampulla, D. M.; Morris, A. J.; Abelev, E.; Bocarsly, A. B. Using a One-Electron Shuttle for the Multielectron Reduction of CO_2 to Methanol: Kinetic, Mechanistic, and Structural Insights. *J. Am. Chem. Soc.* **2010**, *132* (33), 11539−11551.

(4) Ebbesen, S. D.; Mogensen, M. Electrolysis of Carbon Dioxide in Solid Oxide Electrolysis Cells. *J. Power Sources* **2009**, *193* (1), 349−358.

(5) Fu, Q.; Mabilat, C.; Zahid, M.; Brisse, A.; Gautier, L. Syngas Production via High-Temperature steam/CO_2 Co-Electrolysis: An Economic Assessment. *Energy Environ. Sci.* **2010**, *3* (10), 1382.

(6) Hori, Y. Electrochemical CO_2 Reduction on Metal Electrodes. *Mod. Asp. Electrochem.* **2008**, *42*, 89−189.

(7) Kuhl, K. P.; Hatsukade, T.; Cave, E. R.; Abram, D. N.; Kibsgaard, J.; Jaramillo, T. F. Electrocatalytic Conversion of Carbon Dioxide to Methane and Methanol on Transition Metal Surfaces. *J. Am. Chem. Soc.* **2014**, *136* (40), 14107−14113.

(8) Kuhl, K. P.; Cave, E. R.; Abram, D. N.; Jaramillo, T. F. New Insights into the Electrochemical Reduction of Carbon Dioxide on Metallic Copper Surfaces. *Energy Environ. Sci.* **2012**, *5* (5), 7050.

(9) Schouten, K. J. P.; Kwon, Y.; van der Ham, C. J. M.; Qin, Z.; Koper, M. T. M. A New Mechanism for the Selectivity to C1 and C2 Species in the Electrochemical Reduction of Carbon Dioxide on Copper Electrodes. *Chem. Sci.* **2011**, *2* (10), 1902.

(10) Bertheussen, E.; Abghoui, Y.; Jovanov, Z. P.; Varela, A. S.; Stephens, I. E. L.; Chorkendorff, I. Quantification of Liquid Products from the Electroreduction of CO_2 and CO Using Static Headspace-Gas Chromatography and Nuclear Magnetic Resonance Spectroscopy. *Catal. Today* **2017**, *288*, 54−62.

(11) Bertheussen, E.; Hogg, T. V.; Abghoui, Y.; Engstfeld, A. K.; Chorkendorff, I.; Stephens, I. E. L. Electroreduction of CO on Polycrystalline Copper at Low Overpotentials. *ACS Energy Lett.* **2018**, *3*, 634−640.

(12) Peterson, A. A.; Abild-Pedersen, F.; Studt, F.; Rossmeisl, J.; Nørskov, J. K. How Copper Catalyzes the Electroreduction of Carbon Dioxide into Hydrocarbon Fuels. *Energy Environ. Sci.* **2010**, *3* (9), 1311.

(13) Rossmeisl, J.; Qu, Z. W.; Zhu, H.; Kroes, G. J.; Nørskov, J. K. Electrolysis of Water on Oxide Surfaces. *J. Electroanal. Chem.* **2007**, *607* (1−2), 83−89.

(14) Siahrostami, S.; Vojvodic, A. Influence of Adsorbed Water on the Oxygen Evolution Reaction on Oxides. *J. Phys. Chem. C* **2015**, *119* (2), 1032−1037.

(15) Skúlason, E.; Bligaard, T.; Gudmundsdóttir, S.; Studt, F.; Rossmeisl, J.; Abild-Pedersen, F.; Vegge, T.; Jónsson, H.; Nørskov, J. K.; et al. A Theoretical Evaluation of Possible Transition Metal Electro-Catalysts for N_2 Reduction. *Phys. Chem. Chem. Phys.* **2012**, *14* (3), 1235−1245.

(16) Abghoui, Y.; Garden, A. L.; Hlynsson, V. F.; Björgvinsdóttir, S.; Ólafsdóttir, H.; Skúlason, E. Enabling Electrochemical Reduction of Nitrogen to Ammonia at Ambient Conditions through Rational Catalyst Design. *Phys. Chem. Chem. Phys.* **2015**, *17* (7), 4909−4918.

(17) Abghoui, Y.; Garden, A. L.; Howalt, J. G.; Vegge, T.; Skúlason, E. Electroreduction of N $_2$ to Ammonia at Ambient Conditions on Mononitrides of Zr, Nb, Cr, and V: A DFT Guide for Experiments. *ACS Catal.* **2016**, *6* (2), 635−646.

(18) Abghoui, Y.; Skúlason, E. Electrochemical Synthesis of Ammonia via Mars-van Krevelen Mechanism on the (111) Facets of Group III−VII Transition Metal Mononitrides. *Catal. Today* **2017**, *286*, 78−84.

(19) Abghoui, Y.; Skúlason, E. Onset Potentials for Different Reaction Mechanisms of Nitrogen Activation to Ammonia on Transition Metal Nitride Electro-Catalysts. *Catal. Today* **2017**, *286*, 69−77.

(20) Abghoui, Y.; Skúlason, E. Computational Predictions of Catalytic Activity of Zincblende (110) Surfaces of Metal Nitrides for Electrochemical Ammonia Synthesis. *J. Phys. Chem. C* **2017**, *121* (11), 6141−6151.

(21) Höskuldsson, Á. B.; Abghoui, Y.; Gunnarsdóttir, A. B.; Skúlason, E. Computational Screening of Rutile Oxides for Electrochemical Ammonia Formation. *ACS Sustainable Chem. Eng.* **2017**, *5* (11), 10327−10333.

(22) Abghoui, Y.; Skúlason, E. Hydrogen Evolution Reaction Catalyzed by Transition-Metal Nitrides. *J. Phys. Chem. C* **2017**, *121* (43), 24036−24045.

(23) Peterson, A. A.; Nørskov, J. K. Activity Descriptors for CO_2 Electroreduction to Methane on Transition-Metal Catalysts. *J. Phys. Chem. Lett.* **2012**, *3* (2), 251−258.
(24) Karamad, M.; Hansen, H. A.; Rossmeisl, J.; Nørskov, J. K. Mechanistic Pathway in the Electrochemical Reduction of CO_2 on RuO_2. *ACS Catal.* **2015**, *5* (7), 4075−4081.
(25) Bhowmik, A.; Vegge, T.; Hansen, H. A. Descriptors and Thermodynamic Limitations of Electrocatalytic Carbon Dioxide Reduction on Rutile Oxide Surfaces. *ChemSusChem* **2016**, *9* (22), 3230−3243.
(26) Bhowmik, A.; Hansen, H. A.; Vegge, T. Role of CO* as a Spectator in CO_2 Electroreduction on RuO_2. *J. Phys. Chem. C* **2017**, *121* (34), 18333−18343.
(27) Nørskov, J. K.; Rossmeisl, J.; Logadottir, A.; Lindqvist, L.; Kitchin, J. R.; Bligaard, T.; Jónsson, H. Origin of the Overpotential for Oxygen Reduction at a Fuel-Cell Cathode. *J. Phys. Chem. B* **2004**, *108* (46), 17886−17892.
(28) Nie, X.; Esopi, M. R.; Janik, M. J.; Asthagiri, A. Selectivity of CO_2 Reduction on Copper Electrodes: The Role of the Kinetics of Elementary Steps. *Angew. Chem., Int. Ed.* **2013**, *52* (9), 2459−2462.
(29) Cheng, T.; Xiao, H.; Goddard, W. A. Free-Energy Barriers and Reaction Mechanisms for the Electrochemical Reduction of CO on the Cu(100) Surface, Including Multiple Layers of Explicit Solvent at pH = 0. *J. Phys. Chem. Lett.* **2015**, *6* (23), 4767−4773.
(30) Hussain, J.; Jónsson, H.; Skúlason, E. Faraday Efficiency and Mechanism of Electrochemical Surface Reactions: CO_2 Reduction and H_2 Formation on Pt(111). *Faraday Discuss.* **2016**, *195* (0), 619−636.
(31) Liu, X.; Xiao, J.; Peng, H.; Hong, X.; Chan, K.; Nørskov, J. K. Understanding Trends in Electrochemical Carbon Dioxide Reduction Rates. *Nat. Commun.* **2017**, *8*, 15438.
(32) Skúlason, E.; Jónsson, H. Atomic Scale Simulations of Heterogeneous Electrocatalysis: Recent Advances. *Adv. Phys. X* **2017**, *2* (3), 481−495.
(33) Hussain, J.; Jónsson, H.; Skúlason, E. Calculations of product selectivity in electrochemical CO_2 reduction. *ACS Catal.* **2018**, DOI: 10.1021/acscatal.7b03308.
(34) Bandi, A. Electrochemical Reduction of Carbon Dioxide on Conductive Metallic Oxides. *J. Electrochem. Soc.* **1990**, *137* (7), 2157.
(35) Bandi, A.; Kühne, H.-M. Electrochemical Reduction of Carbon Dioxide in Water: Analysis of Reaction Mechanism on Ruthenium-Titanium-Oxide. *J. Electrochem. Soc.* **1992**, *139* (6), 1605.
(36) Popić, J. P.; Avramov-Ivić, M. L.; Vuković, N. B. Reduction of Carbon Dioxide on Ruthenium Oxide and Modified Ruthenium Oxide Electrodes in 0.5 M NaHCO3. *J. Electroanal. Chem.* **1997**, *421* (1−2), 105−110.
(37) Spataru, N.; Tokuhiro, K.; Terashima, C.; Rao, T. N.; Fujishima, A. Electrochemical Reduction of Carbon Dioxide at Ruthenium Dioxide Deposited on Boron-Doped Diamond. *J. Appl. Electrochem.* **2003**, *33* (12), 1205−1210.
(38) Qu, J.; Zhang, X.; Wang, Y.; Xie, C. Electrochemical Reduction of CO_2 on RuO_2/TiO_2 Nanotubes Composite Modified Pt Electrode. *Electrochim. Acta* **2005**, *50* (16), 3576−3580.
(39) Wellendorff, J.; Lundgaard, K. T.; Møgelhøj, A.; Petzold, V.; Landis, D. D.; Nørskov, J. K.; Bligaard, T.; Jacobsen, K. W. Density Functionals for Surface Science: Exchange-Correlation Model Development with Bayesian Error Estimation. *Phys. Rev. B: Condens. Matter Mater. Phys.* **2012**, *85*, 235149 DOI: 10.1103/PhysRevB.85.235149.
(40) Martínez, J. I.; Hansen, H. A.; Rossmeisl, J.; Nørskov, J. K. Formation Energies of Rutile Metal Dioxides Using Density Functional Theory. *Phys. Rev. B: Condens. Matter Mater. Phys.* **2009**, *79* (4), 045120.
(41) Castelli, I. E.; Olsen, T.; Datta, S.; Landis, D. D.; Dahl, S.; Thygesen, K. S.; Jacobsen, K. W. Computational Screening of Perovskite Metal Oxides for Optimal Solar Light Capture. *Energy Environ. Sci.* **2012**, *5* (2), 5814−5819.
(42) Perdew, J. P.; Kurth, S.; Zupan, A.; Blaha, P. Accurate Density Functional with Correct Formal Properties: A Step Beyond the Generalized Gradient Approximation. *Phys. Rev. Lett.* **1999**, *82* (12), 2544−2547.
(43) Kurth, S.; Perdew, J. P.; Blaha, P. Molecular and Solid-State Tests of Density Functional Approximations: LSD, GGAs, and Meta-GGAs. *Int. J. Quantum Chem.* **1999**, *75* (4−5), 889−909.
(44) Sun, J.; Remsing, R. C.; Zhang, Y.; Sun, Z.; Ruzsinszky, A.; Peng, H.; Yang, Z.; Paul, A.; Waghmare, U.; Wu, X.; et al. Accurate First-Principles Structures and Energies of Diversely Bonded Systems from an Efficient Density Functional. *Nat. Chem.* **2016**, *8* (9), 831−836.
(45) Mardirossian, N.; Ruiz Pestana, L.; Womack, J. C.; Skylaris, C.-K.; Head-Gordon, T.; Head-Gordon, M. Use of the rVV10 Nonlocal Correlation Functional in the B97M-V Density Functional: Defining B97M-rV and Related Functionals. *J. Phys. Chem. Lett.* **2017**, *8* (1), 35−40.
(46) Paier, J.; Marsman, M.; Hummer, K.; Kresse, G.; Gerber, I. C.; Ángyán, J. G. Screened Hybrid Density Functionals Applied to Solids. *J. Chem. Phys.* **2006**, *124* (15), 154709.
(47) Gudmundsdóttir, H.; Jónsson, E. Ö.; Jónsson, H. Calculations of Al Dopant in α -Quartz Using a Variational Implementation of the Perdew−Zunger Self-Interaction Correction. *New J. Phys.* **2015**, *17* (8), 083006.
(48) Blöchl, P. E. Projector Augmented-Wave Method. *Phys. Rev. B: Condens. Matter Mater. Phys.* **1994**, *50* (24), 17953−17979.
(49) Atkins, P.; Paula, J. De. *Atkins' Physical Chemistry*; Oxford University Press: 2009.
(50) Nørskov, J. K.; Studt, F.; Abild-Pedersen, F.; Bligaard, T. *Fundamental Concepts in Heterogeneous Catalysis* **2014**, DOI: 10.1002/9781118892114.
(51) Christensen, R.; Hansen, H. A.; Vegge, T.; et al. Identifying Systematic DFT Errors in Catalytic Reactions. *Catal. Sci. Technol.* **2015**, *5* (11), 4946−4949.
(52) Li, C. W.; Ciston, J.; Kanan, M. W. Electroreduction of Carbon Monoxide to Liquid Fuel on Oxide-Derived Nanocrystalline Copper. *Nature* **2014**, *508* (7497), 504−507.
(53) Ren, D.; Deng, Y.; Handoko, A. D.; Chen, C. S.; Malkhandi, S.; Yeo, B. S. Selective Electrochemical Reduction of Carbon Dioxide to Ethylene and Ethanol on Copper(I) Oxide Catalysts. *ACS Catal.* **2015**, *5* (5), 2814−2821.
(54) Hansen, H. A.; Shi, C.; Lausche, A. C.; Peterson, A. A.; Nørskov, J. K. Bifunctional Alloys for the Electroreduction of CO_2 and CO. *Phys. Chem. Chem. Phys.* **2016**, *18* (13), 9194−9201.
(55) Hansen, H. A.; Montoya, J. H.; Zhang, Y.-J.; Shi, C.; Peterson, A. A.; Nørskov, J. K. Electroreduction of Methanediol on Copper. *Catal. Lett.* **2013**, *143* (7), 631−635.
(56) Käckell, P.; Terakura, K. First-Principle Analysis of the Dissociative Adsorption of Formic Acid on Rutile TiO_2(110). *Appl. Surf. Sci.* **2000**, *166* (1−4), 370−375.
(57) Käckell, P.; Terakura, K. Dissociative Adsorption of Formic Acid and Diffusion of Formate on the TiO_2(110) Surface: The Role of Hydrogen. *Surf. Sci.* **2000**, *461* (1−3), 191−198.
(58) Goodpaster, J. D.; Bell, A. T.; Head-Gordon, M. Identification of Possible Pathways for C-C Bond Formation during Electrochemical Reduction of CO_2: New Theoretical Insights from an Improved Electrochemical Model. *J. Phys. Chem. Lett.* **2016**, *7* (8), 1471−1477.
(59) Xiao, H.; Cheng, T.; Goddard, W. A.; Sundararaman, R. Mechanistic Explanation of the pH Dependence and Onset Potentials for Hydrocarbon Products from Electrochemical Reduction of CO on Cu (111). *J. Am. Chem. Soc.* **2016**, *138* (2), 483−486.

DOI: 10.1021/acs.jpcc.8b02224
J. Phys. Chem. C 2018, 122, 10078−10087

Supporting Information

Trends of electrochemical CO_2 reduction reaction on transition metal oxide catalysts

Ebrahim Tayyebi[1], Javed Hussain[1], Younes Abghoui[1] and Egill Skúlason[1,*]

Affiliations:

[1]Science Institute and Faculty of Physical Sciences, University of Iceland VR-III, 107 Reykjavík, Iceland

* Corresponding author: egillsk@hi.is

1-Optimized lattice parameters:

Table S1: Optimized lattice parameters for different metal oxides studied in this work.

Oxide	a (Å)	b (Å)	c (Å)
RuO_2	4.532	4.532	3.129
IrO_2	4.54	4.54	3.18
TiO_2	4.58	4.58	2.99
NbO_2	4.95	4.95	2.97
MoO_2	4.62	4.62	3.21
OsO_2	4.52	4.52	3.21
HfO_2	4.80	4.80	3.23
CrO_2	4.42	4.42	2.99
RhO_2	4.54	4.54	3.129
MnO_2	4.42	4.42	2.95
PdO_2	4.65	4.65	3.08
PtO_2	4.55	4.55	3.197

2-Scaling Figures for CO2RR Network:

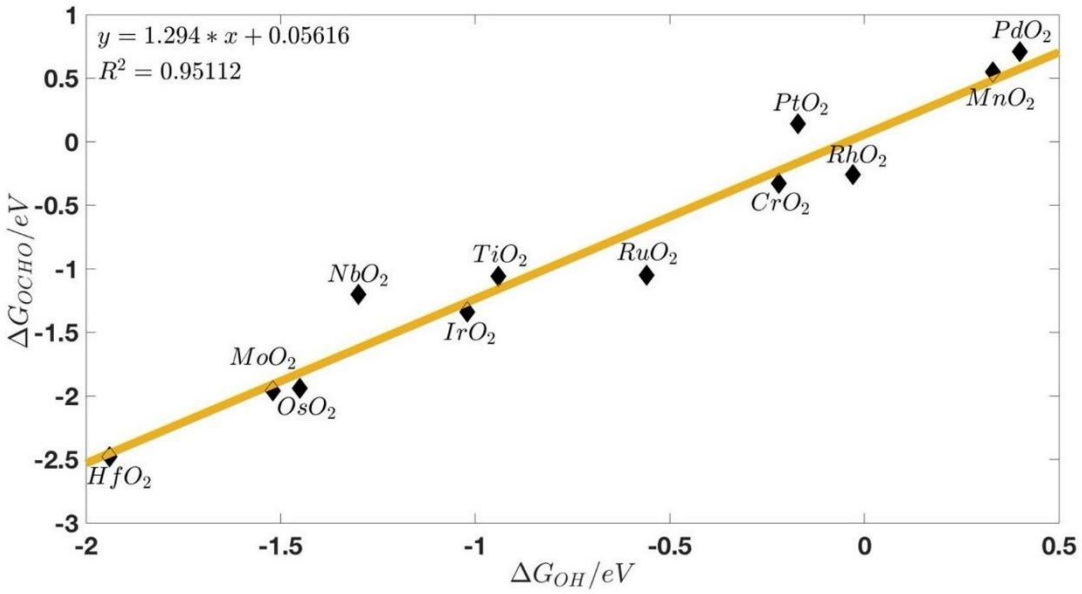

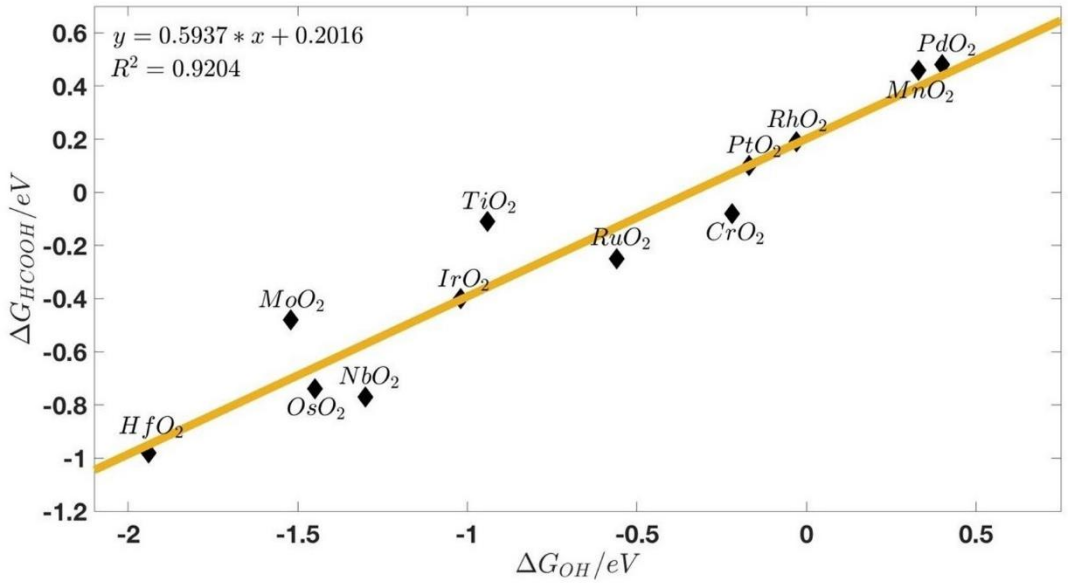

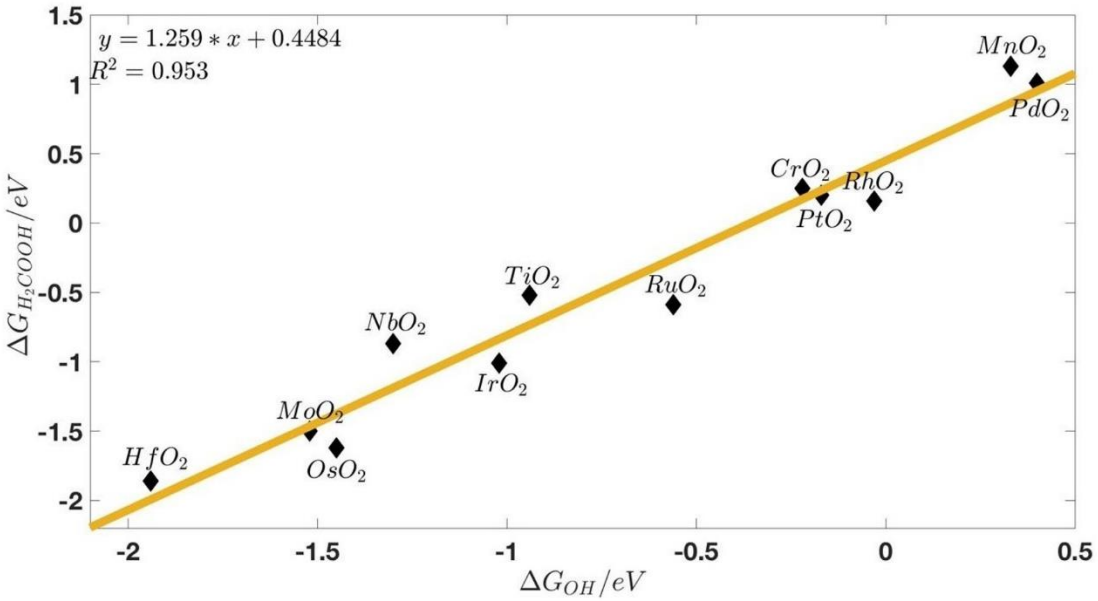
$y = 1.259 * x + 0.4484$
$R^2 = 0.953$
MnO_2
PdO_2
CrO_2
RhO_2
PtO_2
TiO_2
RuO_2
NbO_2
IrO_2
MoO_2
HfO_2
OsO_2
$\Delta G_{H_2COOH}/eV$
$\Delta G_{OH}/eV$
1.5
1
0.5
0
-0.5
-1
-1.5
-2
-2
-1.5
-1
-0.5
0
0.5

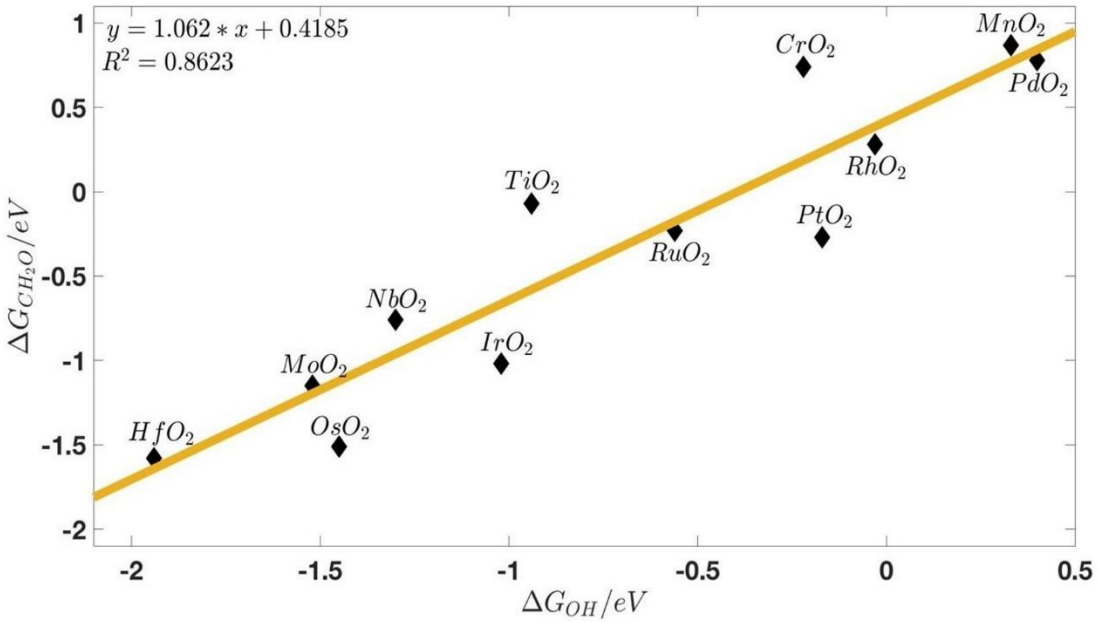
$y = 1.062 * x + 0.4185$
$R^2 = 0.8623$
MnO_2
CrO_2
PdO_2
RhO_2
TiO_2
PtO_2
RuO_2
NbO_2
IrO_2
MoO_2
HfO_2
OsO_2
$\Delta G_{CH_2O}/eV$
$\Delta G_{OH}/eV$
1
0.5
0
-0.5
-1
-1.5
-2
-2
-1.5
-1
-0.5
0
0.5

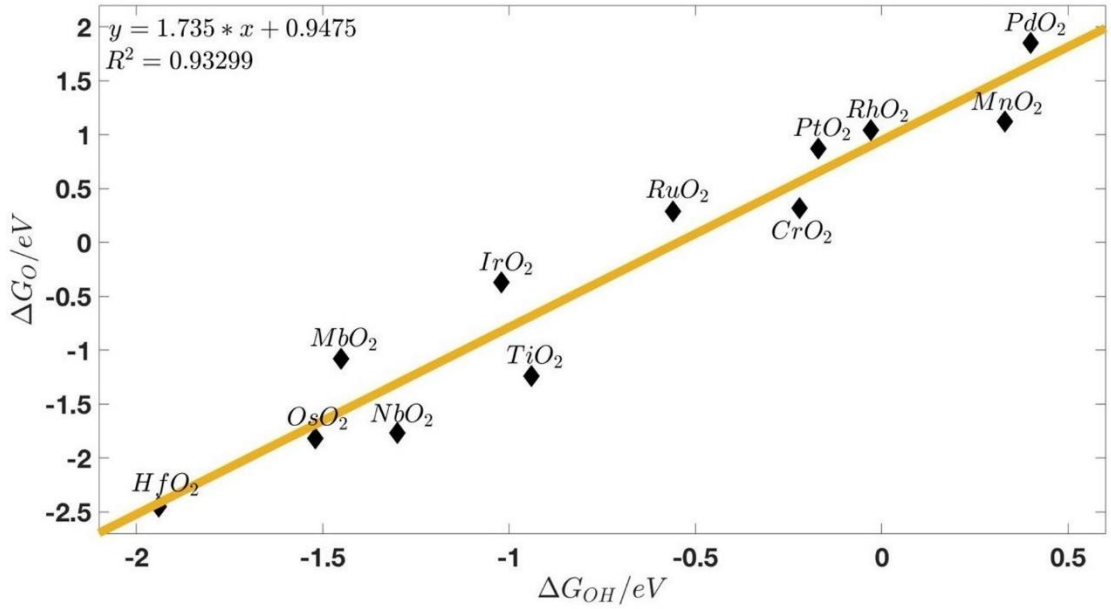
$y = 1.735 * x + 0.9475$
$R^2 = 0.93299$
PdO_2
MnO_2
RhO_2
PtO_2
RuO_2
CrO_2
IrO_2
MbO_2
TiO_2
OsO_2
NbO_2
HfO_2
$\Delta G_O/eV$
$\Delta G_{OH}/eV$

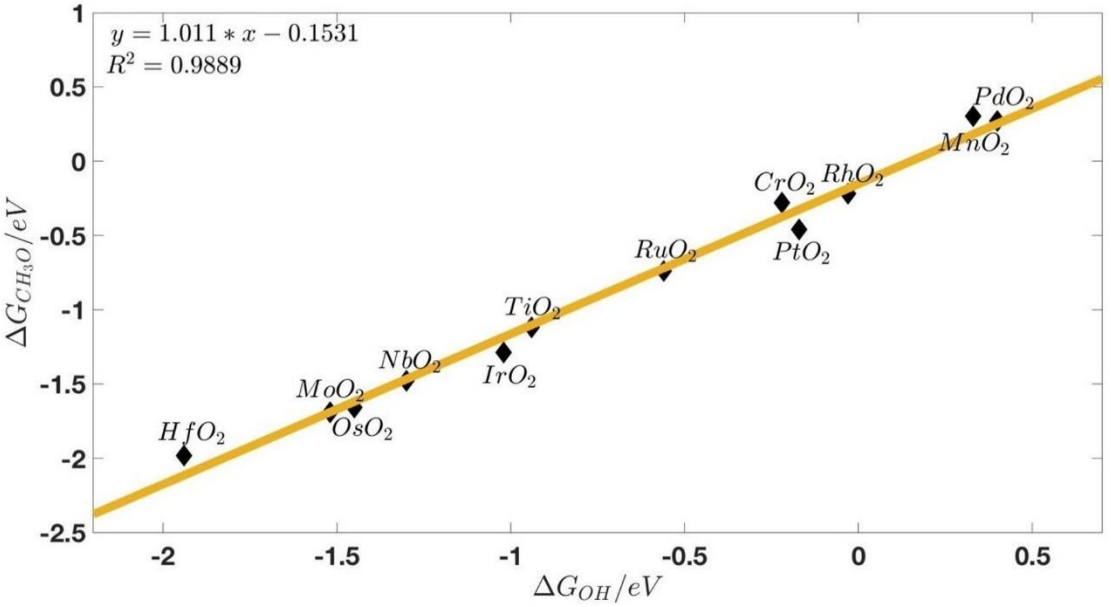
$y = 1.011 * x - 0.1531$
$R^2 = 0.9889$
PdO_2
MnO_2
CrO_2
RhO_2
PtO_2
RuO_2
TiO_2
NbO_2
IrO_2
MoO_2
OsO_2
HfO_2
$\Delta G_{CH_3O}/eV$
$\Delta G_{OH}/eV$

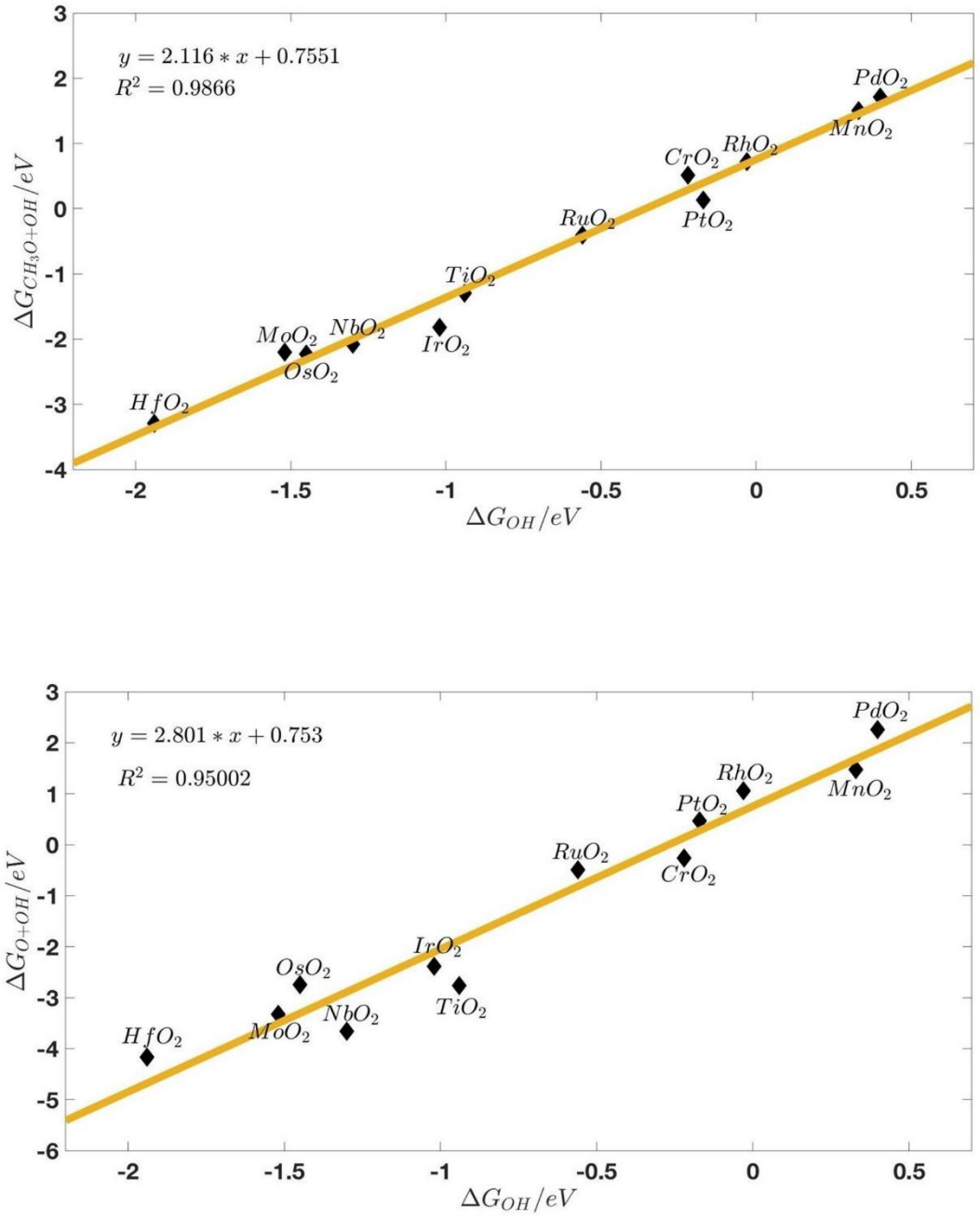

Figure S1: Scaling relations for CO2RR network studied in this work are illustrated in the above figures. This network includes OCHO, HCOOH, H_2COOH, O, CH_2O, CH_3O+OH, CH_3O, OH,

O+OH as intermediates. In these figures, it has been shown that the adsorption free energy of different intermediates correlate linearly with OH adsorption free energy.

3-Free Energy Diagrams:

RuO_2

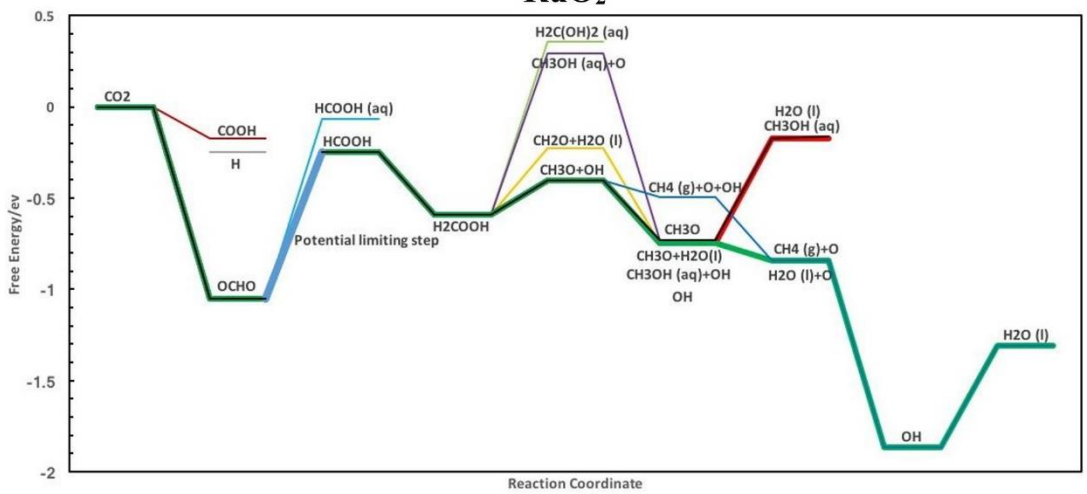

IrO_2 (Spectator on the bridge site)

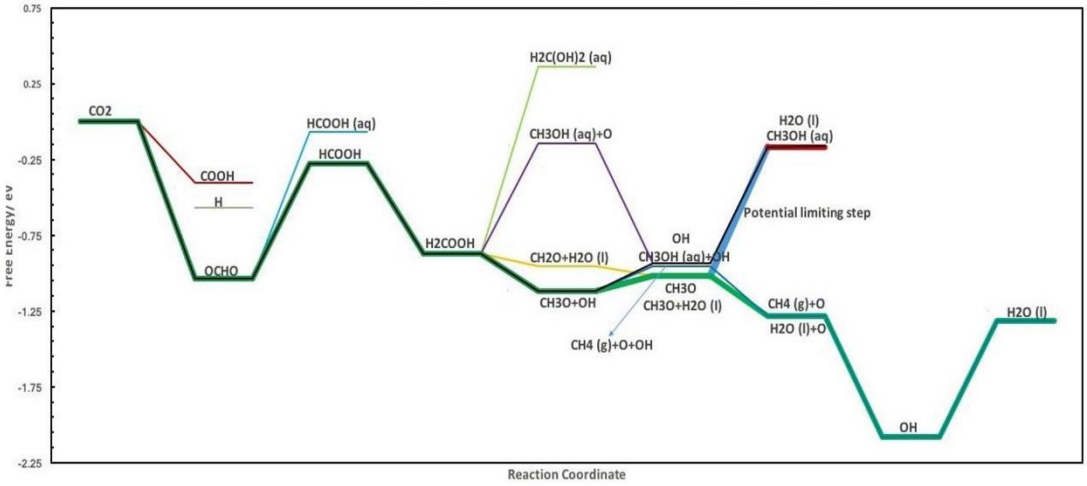

IrO_2 (Spectator on the cus site)

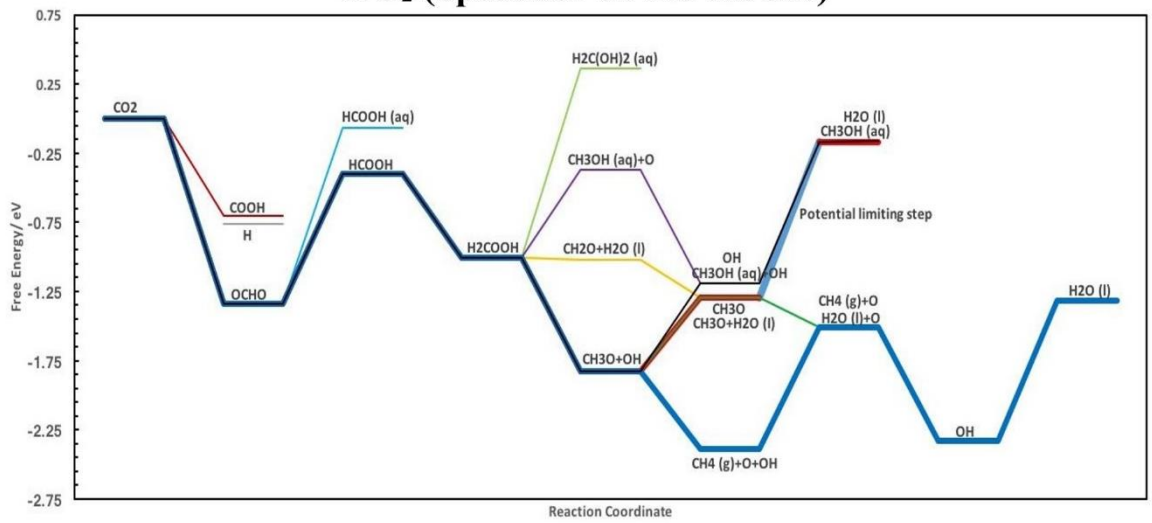

TiO_2

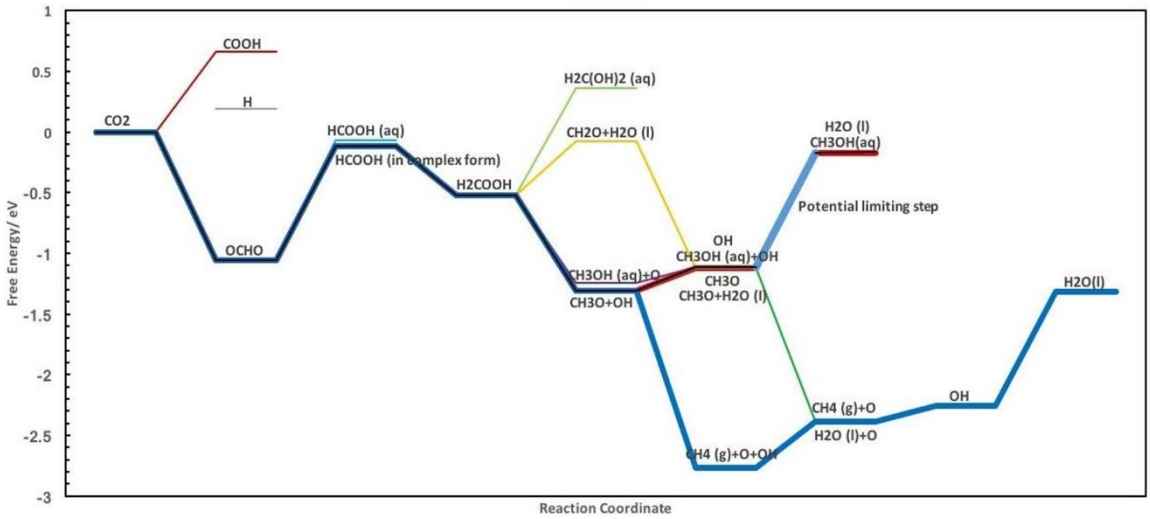

NbO_2

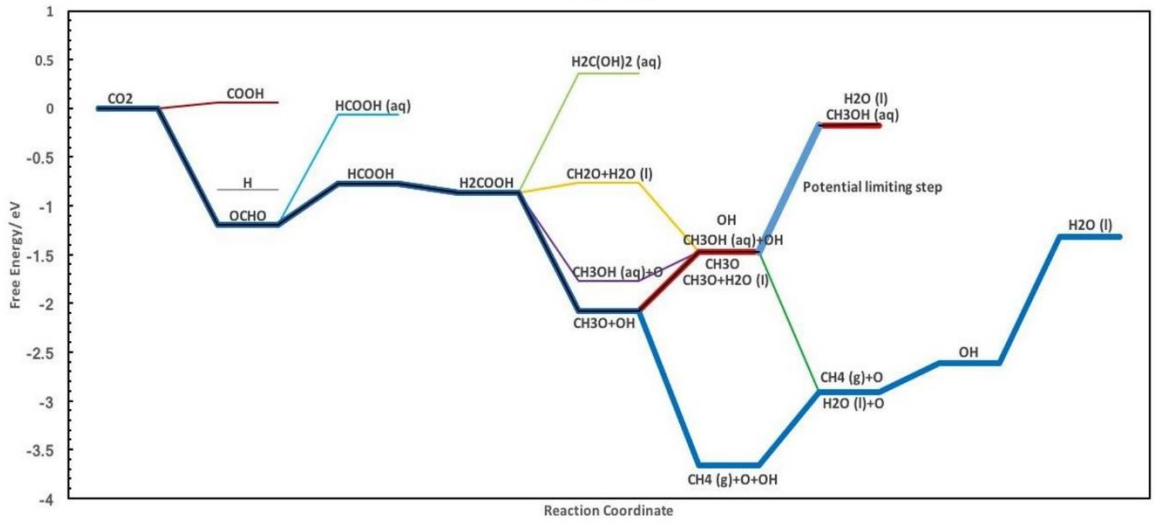
Free Energy/ eV
Reaction Coordinate
CO2
COOH
H
OCHO
HCOOH (aq)
HCOOH
H2COOH
H2C(OH)2 (aq)
CH2O+H2O (l)
CH3OH (aq)+O
CH3O+OH
OH
CH3OH (aq)+OH
CH3O
CH3O+H2O (l)
H2O (l)
CH3OH (aq)
Potential limiting step
CH4 (g)+O
H2O (l)+O
CH4 (g)+O+OH
OH
H2O (l)

OsO_2

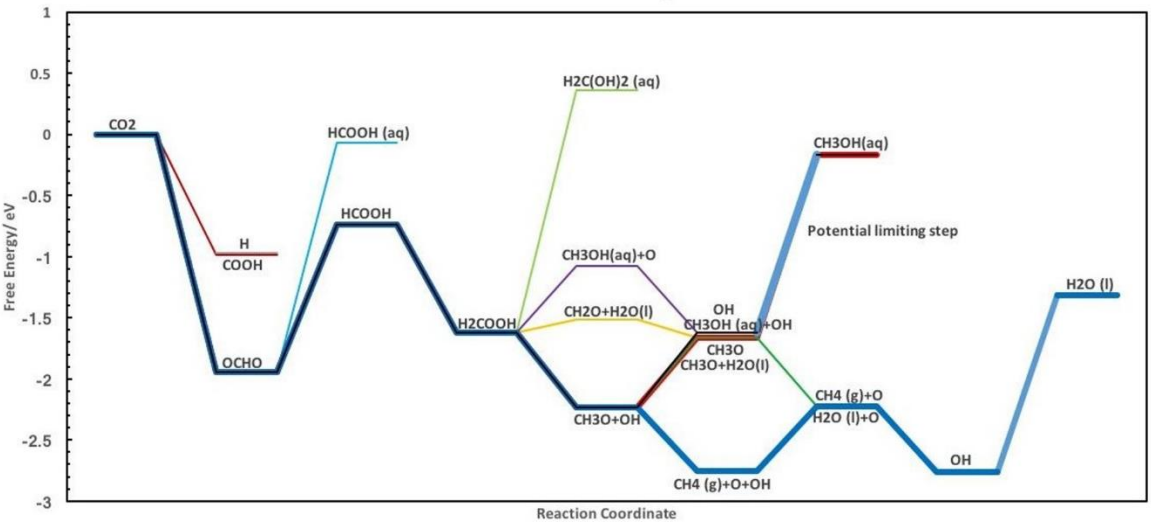
Free Energy/ eV
Reaction Coordinate
CO2
H
COOH
OCHO
HCOOH (aq)
HCOOH
H2COOH
H2C(OH)2 (aq)
CH3OH(aq)+O
CH2O+H2O(l)
CH3O+OH
OH
CH3OH (aq)+OH
CH3O
CH3O+H2O(l)
CH3OH(aq)
Potential limiting step
CH4 (g)+O
H2O (l)+O
CH4 (g)+O+OH
OH
H2O (l)

MoO_2

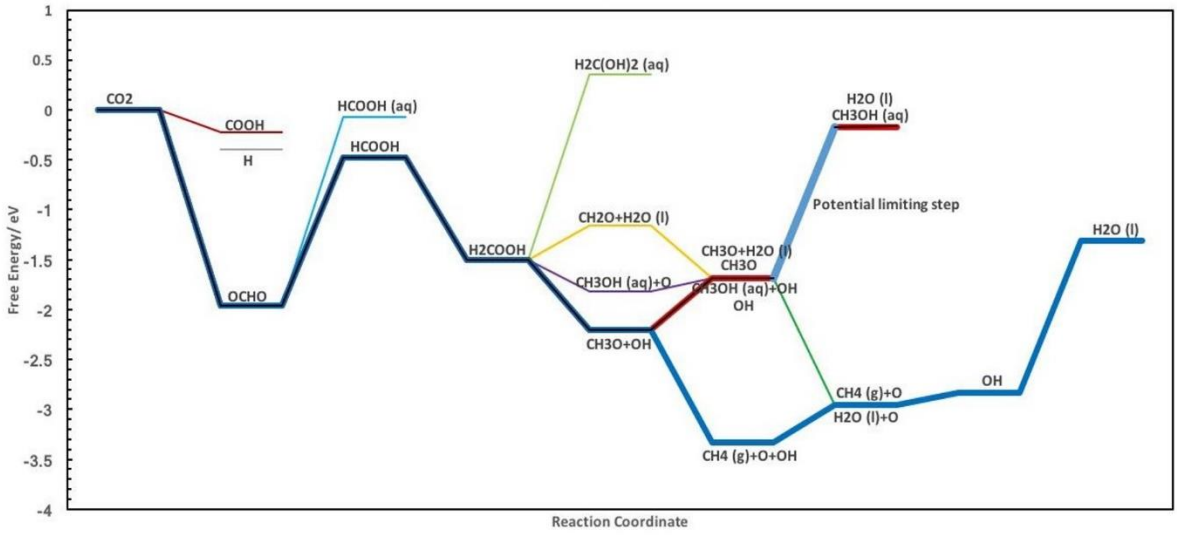
Free Energy/ eV
Reaction Coordinate
CO2
COOH
H
OCHO
HCOOH (aq)
HCOOH
H2COOH
H2C(OH)2 (aq)
CH2O+H2O (l)
CH3OH (aq)+O
CH3O+OH
CH3O+H2O (l)
CH3O
CH3OH (aq)+OH
OH
H2O (l)
CH3OH (aq)
Potential limiting step
CH4 (g)+O
H2O (l)+O
CH4 (g)+O+OH
OH
H2O (l)

HfO_2

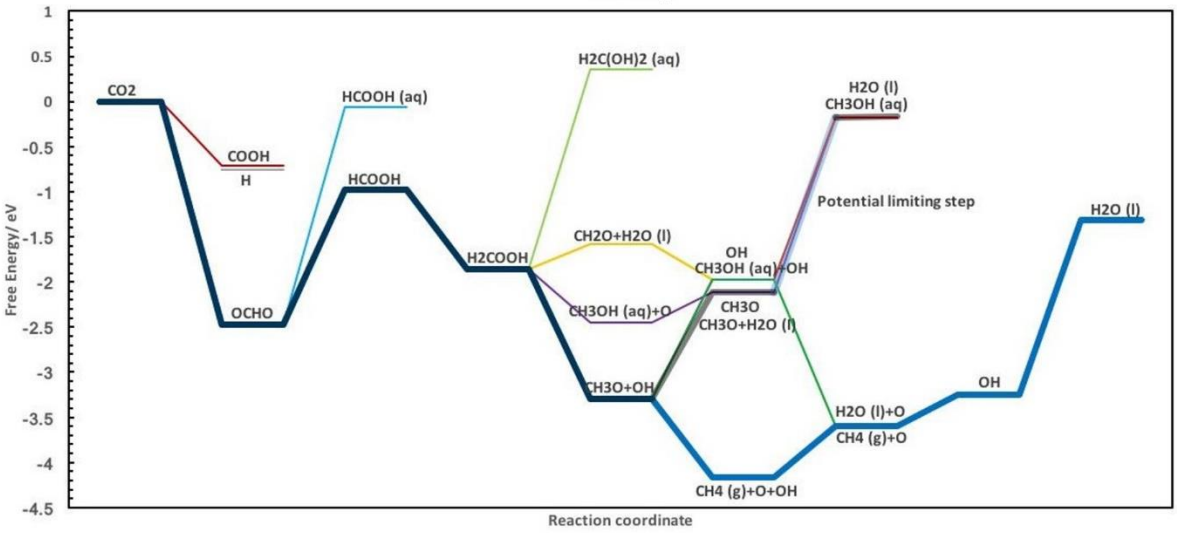
Free Energy/ eV
Reaction coordinate
CO2
COOH
H
OCHO
HCOOH (aq)
HCOOH
H2COOH
H2C(OH)2 (aq)
CH2O+H2O (l)
CH3OH (aq)+O
CH3O+OH
OH
CH3OH (aq)+OH
CH3O
CH3O+H2O (l)
H2O (l)
CH3OH (aq)
Potential limiting step
H2O (l)+O
CH4 (g)+O
CH4 (g)+O+OH
OH
H2O (l)

CrO_2

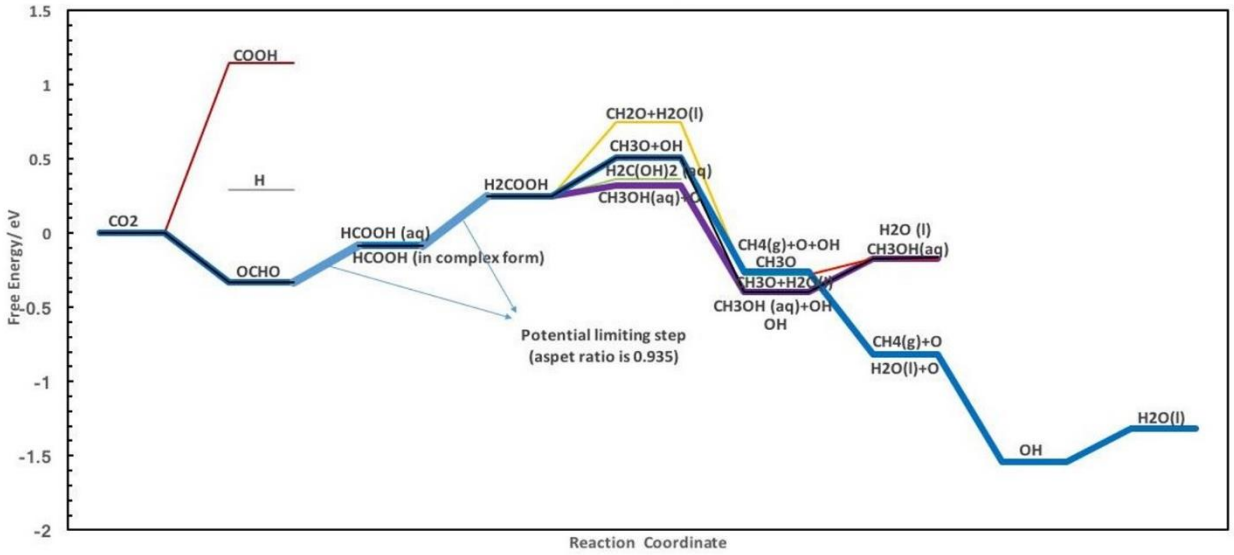
1.5
1
0.5
0
-0.5
-1
-1.5
-2
Free Energy/ eV
Reaction Coordinate
CO2
COOH
H
OCHO
HCOOH (aq)
HCOOH (in complex form)
H2COOH
CH2O+H2O(l)
CH3O+OH
H2C(OH)2 (aq)
CH3OH(aq)+O
CH4(g)+O+OH
CH3O
CH3O+H2O (l)
CH3OH (aq)+OH
OH
H2O (l)
CH3OH(aq)
CH4(g)+O
H2O(l)+O
OH
H2O(l)
Potential limiting step
(aspet ratio is 0.935)

PtO_2

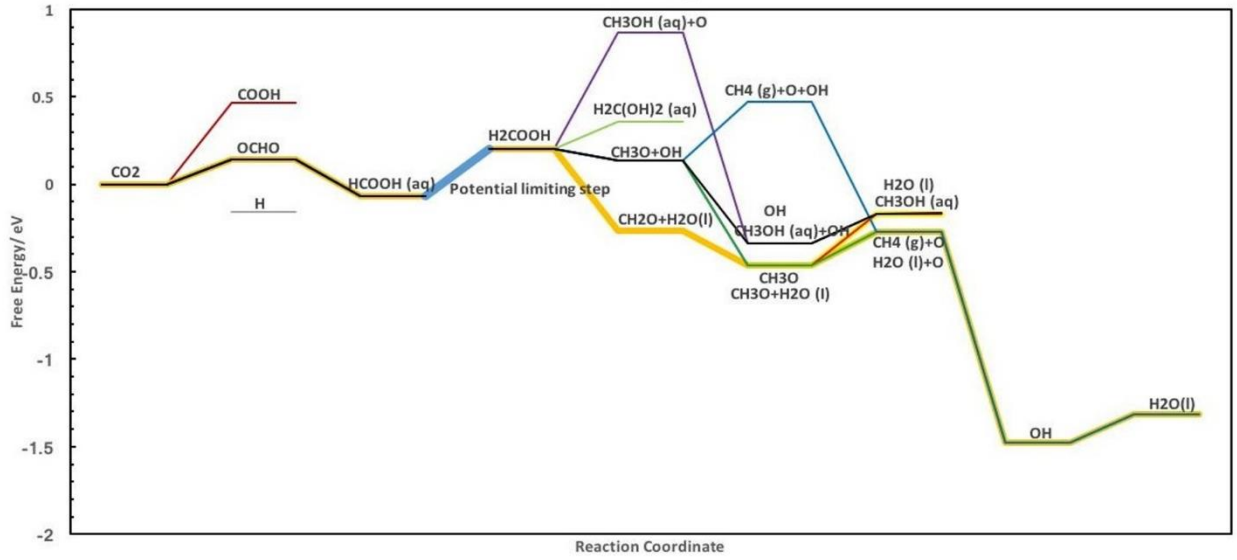
1
0.5
0
-0.5
-1
-1.5
-2
Free Energy/ eV
Reaction Coordinate
CO2
COOH
OCHO
H
HCOOH (aq)
Potential limiting step
H2COOH
CH3OH (aq)+O
H2C(OH)2 (aq)
CH3O+OH
CH2O+H2O(l)
CH4 (g)+O+OH
OH
CH3OH (aq)+OH
CH3O
CH3O+H2O (l)
H2O (l)
CH3OH (aq)
CH4 (g)+O
H2O (l)+O
OH
H2O(l)

RhO_2

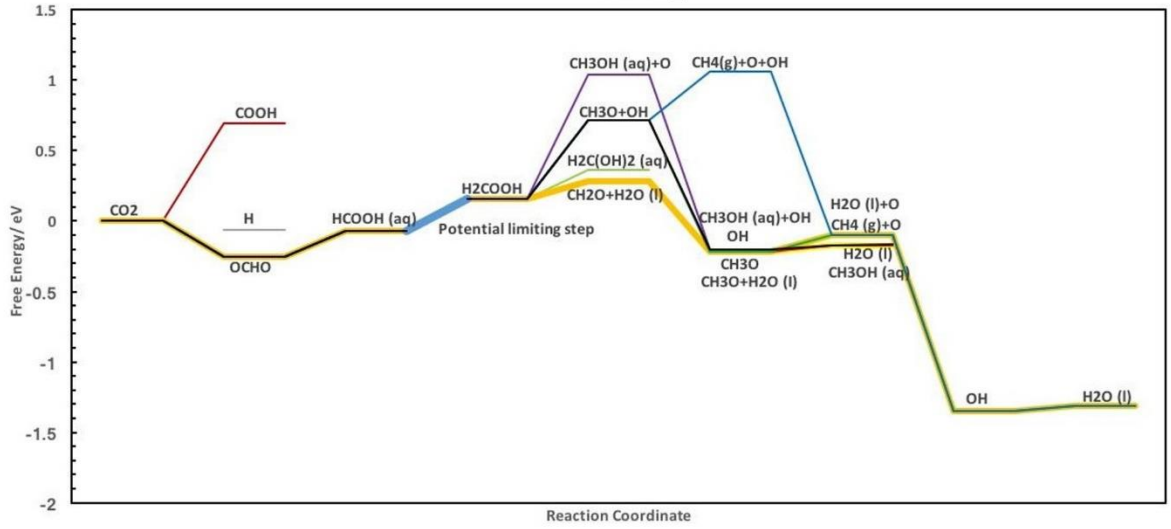
Free Energy/ eV
Reaction Coordinate
CO2
COOH
H
OCHO
HCOOH (aq)
H2COOH
Potential limiting step
CH3OH (aq)+O
CH4(g)+O+OH
CH3O+OH
H2C(OH)2 (aq)
CH2O+H2O (l)
CH3OH (aq)+OH
OH
CH3O
CH3O+H2O (l)
H2O (l)+O
CH4 (g)+O
H2O (l)
CH3OH (aq)
OH
H2O (l)

MnO_2

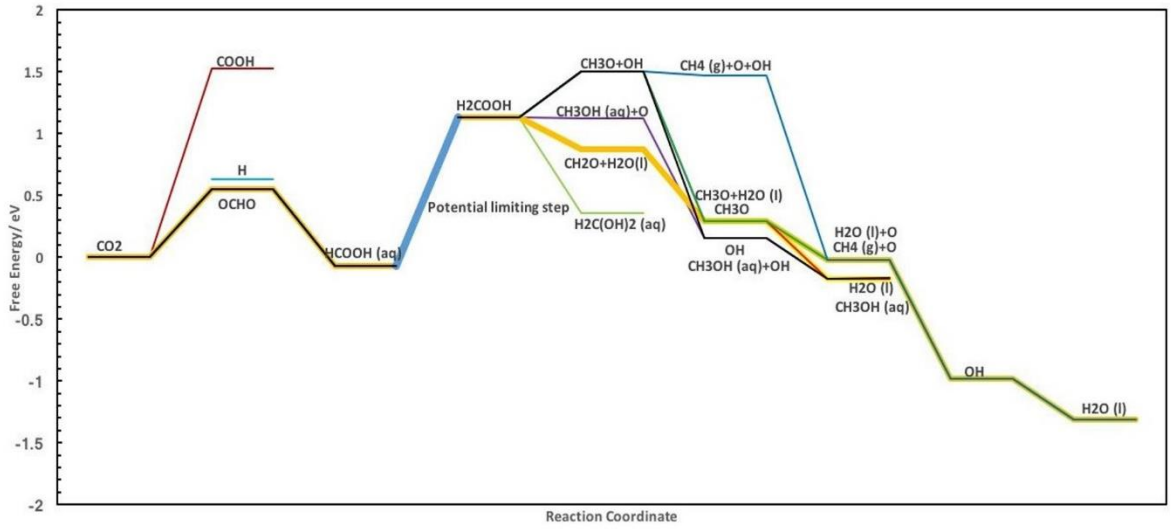
Free Energy/ eV
Reaction Coordinate
CO2
COOH
H
OCHO
HCOOH (aq)
H2COOH
Potential limiting step
CH3O+OH
CH4 (g)+O+OH
CH3OH (aq)+O
CH2O+H2O(l)
H2C(OH)2 (aq)
CH3O+H2O (l)
CH3O
OH
CH3OH (aq)+OH
H2O (l)+O
CH4 (g)+O
H2O (l)
CH3OH (aq)
OH
H2O (l)

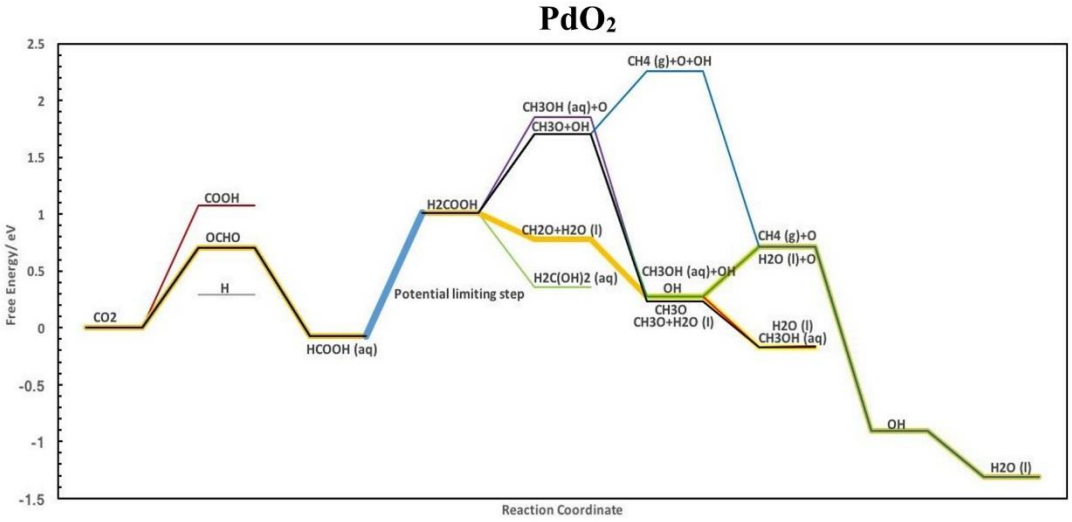

Figure S2: Free energy diagrams for all the metal oxide catalysts investigated in this work are provided in the above figures. Different reaction pathways for formic acid, methandiol, methanol, and methane products are also presented in these figures. Potential limiting step is only presented for methanol with highlighted blue line.

Paper II

Why do RuO_2 electrodes catalyze electrochemical CO_2 reduction to methanol rather than methane or perhaps neither of those?

Tayyebi, E.; Hussain, J.; Skúlason, E.

Chem. Sci., 2020, 11**, 9542-9553**


Volume 11
Number 32
28 August 2020
Pages 8327–8628
Chemical Science
rsc.li/chemical-science
ISSN 2041-6539
ROYAL SOCIETY OF CHEMISTRY
EDGE ARTICLE
Peyman Z. Moghadam, David Fairen-Jimenez et al.
Targeted classification of metal-organic frameworks in the Cambridge structural database (CSD)

Chemical Science

ROYAL SOCIETY OF CHEMISTRY

EDGE ARTICLE

View Article Online
View Journal

Cite this: DOI: 10.1039/d0sc01882a

All publication charges for this article have been paid for by the Royal Society of Chemistry

Why do RuO_2 electrodes catalyze electrochemical CO_2 reduction to methanol rather than methane or perhaps neither of those?†

Ebrahim Tayyebi, [a] Javed Hussain [a] and Egill Skúlason *[ab]

Received 1st April 2020
Accepted 28th July 2020

DOI: 10.1039/d0sc01882a

rsc.li/chemical-science

The electrochemical CO_2 reduction reaction (CO_2RR) on RuO_2 and RuO_2-based electrodes has been shown experimentally to produce high yields of methanol, formic acid and/or hydrogen while methane formation is not detected. This CO_2RR selectivity on RuO_2 is in stark contrast to copper metal electrodes that produce methane and hydrogen in the highest yields whereas methanol is only formed in trace amounts. Density functional theory calculations on RuO_2(110) where only adsorption free energies of intermediate species are considered, *i.e.* solvent effects and energy barriers are not included, predict however, that the overpotential and the potential limiting step for both methanol and methane are the same. In this work, we use both *ab initio* molecular dynamics simulations at room temperature and total energy calculations to improve the model system and methodology by including both explicit solvation effects and calculations of proton–electron transfer energy barriers to elucidate the reaction mechanism towards several CO_2RR products: methanol, methane, formic acid, CO and methanediol, as well as for the competing H_2 evolution. We observe a significant difference in energy barriers towards methane and methanol, where a substantially larger energy barrier is calculated towards methane formation than towards methanol formation, explaining why methanol has been detected experimentally but not methane. Furthermore, the calculations show why RuO_2 also catalyzes the CO_2RR towards formic acid and not CO(g) and methanediol, in agreement with experimental results. However, our calculations predict RuO_2 to be much more selective towards H_2 formation than for the CO_2RR at any applied potential. Only when a large overpotential of around −1 V is applied, can both formic acid and methanol be evolved, but low faradaic efficiency is predicted because of the more facile H_2 formation.

Introduction

The electrochemical CO_2 reduction reaction (CO_2RR) has received a lot of attention recently, as it can be a technology to convert carbon dioxide to particular alcohols and hydrocarbons.[1–14] The CO_2 gas can be captured from both industrial point sources as well as from the atmosphere which would mitigate the rising levels of anthropomorphic CO_2 emissions. Electrochemical processes are an appealing approach since the electricity can come from renewable sources (such as wind or solar energy) to make synthetic fuels for the existing infrastructure that uses fuels from fossil fuel sources. In this application, selective methanol formation would be highly desirable since it can be used directly as a liquid fuel.

The electrochemical CO_2RR catalyzed by metallic electrodes has been studied extensively in recent years. Insight into the mechanisms or the reaction pathways for reducing CO_2 to different products including HCOOH, CO, CH_3OH, CH_4, C_2H_4, C_2H_5OH *etc.*, has been obtained by both theoretical calculations[15–25] and experimental work.[7,9] Therein, it has been shown that previous theoretical studies using a thermochemical approach[26] where only the adsorption free energies of intermediate species are included, are quite successful in predicting experimental overpotentials (or onset potentials).[14,16] However, energy barriers of proton–electron transfer steps are required to elucidate the reaction mechanism and reaction pathways and capture the trends in product distribution as a function of applied potential seen in the experiments on pure metals.[21,23]

As a solvent, water usually plays an important role in various electrocatalytic reactions such as the CO_2RR. For electrocatalytic reactions carried out in water, including the effect of solvation of reactants, intermediates, and products at the surface may be essential as the mechanism may be different.[27–30] However, density functional theory (DFT) calculations reveal that modeling solid–liquid interfaces is complex and requires efficient functionals describing hydrogen bonding

[a]*Science Institute, University of Iceland, VR-III, 107 Reykjavík, Iceland. E-mail: egillsk@hi.is*

[b]*Faculty of Industrial Engineering, Mechanical Engineering and Computer Science, University of Iceland, VR-III, 107 Reykjavík, Iceland*

† Electronic supplementary information (ESI) available. See DOI: 10.1039/d0sc01882a

interactions.[31–34] Despite this complexity, several groups have developed reasonable solid–liquid interface models suitable to study electrochemical processes where some electrochemical phenomena can be explained, *e.g.* catalytic trends, rates, reaction pathways and mechanisms.[23–25,35–44]

A crucial step towards a rational design of new catalysts that are selective and efficient in reducing CO_2 to specific hydrocarbons and alcohols is to determine the detailed reaction mechanism for the process. To accomplish this, a detailed description of the electrochemical solid–liquid interface is required. Recently, it has been observed that a detailed description of the electrochemical solid–liquid interface model is successful in capturing the experimental trends of product distribution for the CO_2RR as a function of applied potential on pure metals[23] whereas the more approximated thermochemical model (TCM) and the implicit computational hydrogen electrode (CHE)[26] cannot capture these trends, but do capture the overpotentials for the CO_2RR and other electrochemical reactions quite well.[14–16,45,46] The reason for this achievement is that the molecular level structure of water on noble transition metals is qualitatively well known and therefore realistic model systems can be used. Unfortunately, for transition metal oxide (TMO) surfaces, the molecular scale structure of water is still controversial, and therefore, realistic model systems have not been fully developed yet. However, it has been shown that TMO surfaces strongly chemisorb molecular water *via* interaction between the lone pair of the oxygen atom in the water molecule and the 5-fold coordinately unsaturated site (CUS)[28,29,47] while on noble metal surfaces, a water bilayer is usually physisorbed on top of the metal surface.[23,33,34,37,40] The interaction of water with a RuO_2(110) surface has been studied experimentally by using high resolution electron energy loss spectroscopy (HREELS) and thermal desorption spectroscopy (TDS).[28] Using HREELS, it was shown that H_2O molecules chemisorb on Ru CUS sites through the oxygen atom of the water molecules. From HREELS and TDS results it was also found that water dissociation does not occur on the perfect RuO_2(110) surface while a small amount of water dissociation observed in HREELS is due to some vacant Ru bridge sites.

Copper has been shown to be the only pure metal electrode catalyzing the CO_2RR to hydrocarbons and alcohols where 15 carbon-containing products have been detected and where methane is the major product at high overpotentials (>40%).[9,48] Other pure metal electrodes form H_2(g), CO(g) or HCOOH(aq) as major products. For all these pure metal electrodes, methanol has been detected but in very low yields (<0.1%). Transition metal oxide surfaces, however, have been shown to catalyze the CO_2RR to methanol in high yields (2–76%) as well as to formic acid (1–78%), depending on the applied potential and other reaction conditions, where RuO_2-based electrodes have been studied the most.[49–53] Methane, CO and methanediol have not been detected, except in one study where trace amounts of methane and CO were reported.[52]

Recently, RuO_2 has been revisited experimentally for the CO_2RR by Mezzavilla *et al.*[54] where hydrogen gas (*via* the hydrogen evolution reaction, HER) was reported to be the main product at all applied potentials. This contradicts the previous experimental studies[49–53] where methanol and/or formic acid were observed to be the major products. At very high overpotentials (−0.75 and −0.9 V *vs.* RHE), some trace amounts of formate and CO were observed. By alloying RuO_2 with Ti, Cu or Sn, the faradaic efficiency of formate and CO increased to around 20% and 10%, respectively, at high overpotentials (−0.75 and −1 V *vs.* RHE). Furthermore, they show that even though RuO_2 is not an active catalyst for the CO_2RR to methanol, adsorbed CO is detected on the surface, when either CO or CO_2 are introduced into the electrolyte. To the best of our knowledge, all experimental results on RuO_2 and RuO_2-based electrodes are summarized in Table S1 in the ESI.†

Reaction pathways have been derived from DFT calculations using the TCM and CHE models for the CO_2RR on RuO_2 towards formic acid, methanediol, methanol and methane and are summarized in Table 1.[55–59] Methane and methanol are predicted to go through the same reaction pathway until the OCH_3 intermediate is formed. The next hydrogenation results in either methanol or methane formation, but in the latter process the adsorbed oxygen atom is reduced further to water to complete the catalytic cycle. The same reaction step is predicted to be the potential limiting step (PLS) for both products, or the OCHO to HCOOH step.[55–59] However, other elementary steps such as protonation of OCH_3 and OH removal to form water need similar applied potentials according to thermodynamics.

As described above, high yields of hydrogen,[54] formic acid or methanol[49–53] are detected experimentally whereas methane formation has not been reported in any studies. Clearly, the results from simple thermodynamic models (TCM and CHE) do not capture the experimental observations of these products. Therefore, a more detailed model is required, including explicit solvent effects and calculations of the proton–electron transfer energy barriers for all possible reaction steps. Within this study, the energy barriers for the HER and CO_2RR are calculated towards various products using the (110) facet of RuO_2 as the

Table 1 Reaction pathways from TCM calculations for the CO_2RR on RuO_2 towards formic acid, methanediol, methanol and methane formation[55–59]

Number of $H^+ + e^-$ steps								
Pathways	1	2	3	4	5	6	7	8
Formic acid	OCHO	HCOOH(aq)						
Methanediol	OCHO	HCOOH	H_2COOH	$H_2C(OH)_2$(aq)				
Methanol	OCHO	HCOOH	H_2COOH	CH_3O + OH	CH_3O + H_2O(l)	CH_3OH(aq)		
Methane	OCHO	HCOOH	H_2COOH	CH_3O + OH	CH_3O + H_2O(l)	CH_4(g) + O	OH	H_2O(l)

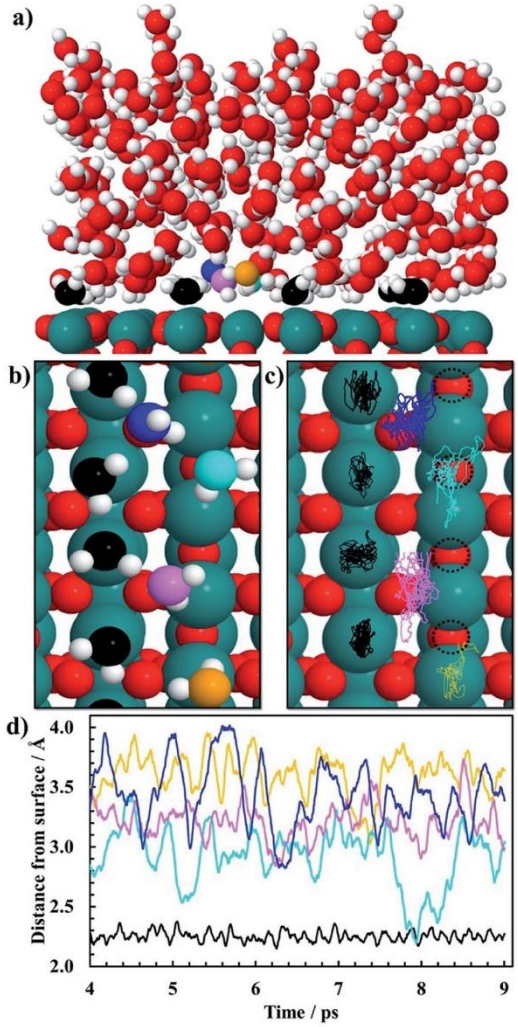

Fig. 1 Snapshots of the last configuration of a 9 ps AIMD sampling of 84 H_2O molecules above the RuO_2(110) surface at 300 K showing both the (a) side view and the (b) top view. RuO_2 is colored green for Ru and red for oxygen. H_2O is colored red for oxygen and white for hydrogen in panel (a) except for co-adsorbed water molecules on the CUS which are colored black for oxygen and white for hydrogen. In panel (b) the same color code is used for the co-adsorbed water molecules on the CUS while water molecules in the first water bilayer are colored orange, blue, cyan and pink for oxygen atoms and white for hydrogen atoms. In panel (c) the trajectories in the *xy*-plane for the last 5 ps of the 9 ps AIMD simulations (after equilibrium was reached) corresponding to the movement of the oxygen atoms in the water molecules are shown in panel (b) where the same color code is used. Dotted-circles in panel (c) represent vacant bridge sites. In panel (d) the trajectories in the *z* direction (or the distance of the oxygen atoms of the water molecules from the Ru(110) surface) are plotted as a function of the simulation time. Same color code as in (b) and (c). Black trajectory is calculated by taking the average *z* coordinates of CUS Ru atoms at a given time and subtracted from the average *z* coordinates of the oxygen atoms in the water molecules above the CUS Ru sites for the same time. The colored trajectories are calculated by taking the average *z* coordinates of the bridge Ru atoms on the surface which are subtracted from the *z* coordinates of the oxygen atom in each of the water molecules.

model system using one layer of co-adsorbed water to elucidate the reaction mechanisms to form hydrogen, methanol, methane, formic acid, methanediol and CO.

Model systems and computational details

Ab initio molecular dynamics (AIMD) simulations are carried out for the (110) facet of RuO_2 in reduced form with five layers of water above the surface (Fig. 1a). Born–Oppenheimer AIMD simulations are carried out using the freely available program package CP2K/Quickstep.[60,61] The density functional implementation in Quickstep is based on a hybrid Gaussian plane wave (GPW) scheme. Orbitals are described by an atom-centered Gaussian-type basis set, while an auxiliary plane wave basis is used to re-expand the electron density.[62] Analytic Goedecker–Teter–Hutter (GTH) pseudopotentials are employed to represent the core electrons.[63,64] The basis sets for the valence electrons consist of short-ranged (less diffuse) double-ζ basis functions with one set of polarization functions (DZVP).[65] The plane wave basis for the electron density is cut off at 400 Ry while the plane wave cut off of a reference grid covered by a Gaussian is 60 Ry. All our AIMD simulations only use the Γ point of the supercell for expansion of the orbitals. The GGA–PBE functional is utilized for all AIMD calculations.[66,67] The Grimme's D3 method is also used to include van der Waals interactions of water–water, water–Ru and water–surface oxygen.[68] The slab consists of three atomic layers with 16 metal atoms and 32 oxygen atoms in each layer, and the exposed liquid phase is presented by 84 H_2O molecules. The simulation box is 44 Å along the *z*-axis with a vacuum of 20 Å. The system is subject to periodic boundary conditions in all directions. Atoms in the slab along with the water molecules are allowed to reconstruct during the AIMD simulation. The simulations are performed using the Verlet algorithm with a time step of 1 fs at a temperature of 300 K within the canonical ensemble for a total simulation period of 9 ps. Generalized Langevin equation thermostats are used to enhance molecular dynamics simulations.[69,70] The convergence of the vertical energy gap can be monitored by the time accumulative averages, as shown in Fig. S1.† Since we perform the simulation at coverage significantly close to unity, which corresponds to bulk water in contact with the RuO_2 surface, a specific well-defined geometry is observed in the simulation during a 9 ps AIMD run of the system with 84 H_2O molecules at room temperature. A snapshot of the equilibrated system is shown in Fig. 1a where chemisorbed water molecules decorate the CUS Ru sites (oxygen atoms of those water molecules are black).

To estimate the free energy of an adsorbate in the CO_2RR and HER, static geometry optimization calculations are done using a plane-wave based pseudopotential formalism with a generalized gradient approximation (GGA) to describe the exchange–correlation effects within the BEEF–vdW functional[71] implemented in the periodic DFT package VASP.[72,73] All these calculations are done using a model system shown in Fig. 2 which will be further elaborated below. A plane wave basis set with

a cutoff energy of 350 eV is utilized to expand the valence electron orbitals and the PAW method is used to represent the core electrons.[74] In two separate studies, similar calculations for the CO_2RR on RuO_2(110) were conducted using two different cutoff values (one 350 eV (ref. 59) and the other 500 eV (ref. 56)) and they obtained similar results. Therefore, this indicates that a cutoff energy of 350 eV is accurate enough for the current study. The RuO_2(110) slab consists of four atomic layers with four metal atoms and eight oxygen atoms in each layer. The system is subject to periodic boundary conditions in all directions. Dipole correction is applied to decouple the electrostatic interaction between the periodically repeated slabs. Atoms in the bottom two layers are fixed while the atoms in the top two layers along with adsorbed intermediates are allowed to relax during optimization. The atomic structures are determined using a $4 \times 4 \times 1$ Monkhorst–Pack mesh for Brillouin-zone sampling until the energies are converged to within 10^{-5} eV and atomic forces drop below 0.03 eV $Å^{-1}$. The climbing image nudged elastic band (CI-NEB)[75,76] method is used to calculate activation energies for the HER and CO_2RR towards different intermediates and products on the RuO_2(110) surface.

In order to calculate the activation energy for proton–electron transfer of different intermediates for the CO_2RR and HER on RuO_2 with an explicit description of water, we consider only two water molecules (one monolayer, ML) on the 5-fold CUS metal site of RuO_2 (Fig. 2). Siahrostami and Vojvodic have shown this model to be sufficient to capture the electrostatic contributions from water in the case of the oxygen evolution reaction on RuO_2, IrO_2 and TiO_2.[44] Furthermore, we justify the choice of that model system with AIMD simulations at room temperature in Fig. 1 and we apply this model when calculating activation energies towards different intermediates and products in the CO_2RR and HER on the RuO_2(110) electrode. When a proton–electron transfer has been carried out from one of the co-adsorbed water molecules to reduce H or CO_2RR intermediates, an OH group is formed and adsorbed on the CUS site. This OH group should be easily protonated from the reservoir of protons in the bulk solution to regenerate co-adsorbed water molecules on the surface needed for the subsequent reduction steps.[77] We do not calculate the energy barriers to regenerate the co-adsorbed water molecules, but we assume that the co-adsorbed water is in equilibrium with adsorbed OH and solvated proton in the bulk of electrolyte solution. We therefore only calculate the thermodynamics of the reaction:

$$A + OH + \tfrac{1}{2}H_2(g) \rightarrow A + H_2O$$

where A is an intermediate in the CO_2RR network.

Previously, the concept of a CO spectator species in the CO_2RR on RuO_2(110) was introduced by Karamad *et al.*[55] and later used by Bhowmik *et al.*[56–58] and Tayyebi *et al.*[59] Therefore it is assumed that the CO_2RR takes place on a bridge site in the presence of a CO spectator which is located on every other bridge site as shown in Fig. 2. The source of adsorbed CO on the surface may therefore come from the reaction:

$$CO_2(g) \rightarrow OC^*O \xrightarrow{+(H^+ + e^-)} COOH \xrightarrow{+(H^+ + e^-)} CO + H_2O(l)$$

In the Results section below we indeed show that a low CO coverage will be formed on the RuO_2(110) electrode, justifying this model system and the role of CO as a spectator species during the CO_2RR.

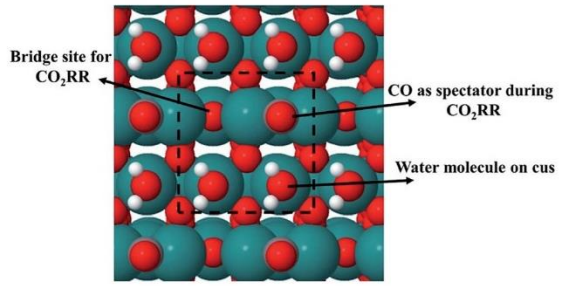

Fig. 2 A model system of a (110) surface of RuO_2 in its rutile crystal structure. Carbon and oxygen atoms are colored red for oxygen and grey for carbon, while hydrogen and Ru atoms are colored white for hydrogen and green for Ru. CO is a spectator species and, in all cases, located on the bridge site (oxygen vacant site) while two water molecules are located on the corresponding two CUS sites. The other oxygen vacant site (bridge site) is the only place where the CO_2RR occurs.

Results

AIMD simulations of equilibrated structures of 84 water molecules above the RuO_2(110) surface are shown in Fig. 1. Snapshots of the molecular structure are shown in Fig. 1a and b, where chemisorbed water molecules decorate the CUS Ru sites (black oxygen atoms). These results are in very good agreement with the HREELS and TDS studies for adsorption of water on RuO_2(110).[28] To obtain some further insight into the movement of the water molecules closest to the RuO_2(110) surface, trajectories of their oxygen atoms in the *xy*-plane and the *z*-direction are plotted in Fig. 1c and d, respectively. Fig. 1c shows that the water molecules on CUS Ru atoms stay relatively localized and remain close to their initial positions, although they exhibit some small fluctuations in the *xy*-plane. They are also found to be rather localized in the *z*-direction at around 2.25 ± 0.1 Å from the surface (black trajectory in Fig. 1d). The water molecules in the bilayer above the bridge sites of the RuO_2(110) surface become, however, much more disordered and delocalized in the *xy*-plane as shown with the colored trajectories in Fig. 1c. They are also highly mobile in the *z*-direction and located between 2.5 and 4 Å above the surface where each molecule fluctuates by around 1 Å (colored trajectories in Fig. 1d). This shows a very weak interaction of the water molecules above the bridge Ru sites, leaving them empty to catalyze the CO_2RR. These results support the choice of the reduced model system (Fig. 2) used to calculate the various elementary steps needed to obtain insight into the reaction mechanism.

Proton–electron transfer reaction barriers are calculated for the CO_2RR to CO(g), HCOOH(aq), $H_2C(OH)_2$(aq), CH_3OH(aq) and CH_4(g) on RuO_2(110) and compared with that of the

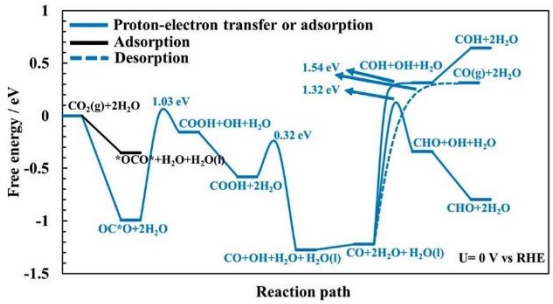

Fig. 3 Free energy of intermediates and energy barriers for the CO_2 reduction reaction at $U = 0$ V *vs.* RHE towards CO without any adsorbed CO as spectator species. OC*O indicates adsorbed CO_2 *via* the carbon atom while *OCO* is when CO_2 binds to the surface through both oxygen atoms (or bidentate).

competing H_2(g) formation. Free energy reaction pathways along with energy barriers, E_a, are presented in Fig. 3 and 4 for the CO_2RR and in Fig. 5 for the HER at $U = 0$ V *vs.* RHE, for a range of proton–electron transfer steps, reconfiguration steps and desorption steps. The minimum energy paths (MEPs) along with configurations of the initial states, saddle points and final states for a range of possible intermediates related to the CO_2RR and HER on RuO_2(110) can be found in the ESI.†

In the main part of this paper it is assumed that CO_2 is reduced on a bridge site of the surface in the presence of adsorbed CO as a spectator species which is located on every other bridge site, but water molecules are adsorbed on all CUS sites forming one ML of water coverage as explained above (Fig. 2). To start with in this paper, however, we do more detailed calculations than have been done so far in order to show that adsorbed CO is indeed a spectator species in the CO_2RR where it neither desorbs from the surface nor reduces further to adsorbed COH or CHO species (Fig. 3). Thereafter, a low CO coverage is used as a model system to investigate the reaction pathways of the CO_2RR towards formic acid, methanediol, methanol and methane on RuO_2(110) in more detail (Fig. 4).

CO formation on RuO_2(110): why CO is a spectator species

The CO_2RR is conducted on the RuO_2(110) surface with 1 ML of adsorbed H_2O molecules on the CUS Ru sites but without any adsorbed CO molecules. This represents the initial state of the surface we may expect at the time when CO_2 is introduced in the system of the experiments. The free energies of the intermediates from CO_2 to CO(g), CHO and COH are shown in Fig. 3 along with energy barriers of the elementary steps. We find that the way CO_2 binds to the surface can change the reaction mechanism towards different CO_2RR products but that is also discussed further below in relation with Fig. 4 (when we have the CO spectator species). Under these initial conditions, we obtain two different configurations for adsorption of CO_2 on the RuO_2(110) surface. CO_2 can either bind where the carbon atom (OC*O) binds to a bridge site (Fig. S2a†) or where the two oxygen atoms (*OCO*) bind bidentate to a bridge site and the adjacent CUS site where one of the water molecule desorbs from the surface (Fig. S2b†). OC*O is found to be a more stable intermediate compared to *OCO* (see Fig. 3). Therefore, the next step in the CO_2RR is to transfer a proton to the oxygen atom in OC*O to form COOH, and then further reduction of COOH leads to the formation of adsorbed CO on the bridge site. The highest energy barrier in the CO_2RR to form adsorbed CO is 1.03 eV at 0 V *vs.* RHE (Fig. 3). Since our results predict that methanol formation needs an overpotential of around −1 V *vs.* RHE (discussed below) this energy barrier will become around 0.5 eV at that potential assuming a transfer coefficient of 0.5. Such a negative applied potential increases the chance of building up some CO coverages on the surface. This is supported in the recent experiments by Mezzavilla *et al.*[54] where both adsorbed CO_2 and CO were detected on the RuO_2(110) surface at large negative potentials where it is concluded that adsorbed CO acts solely as a spectator species in the CO_2RR.[54] These detailed calculations, therefore, support earlier assumptions that adsorbed CO molecules may result from reduced CO_2 molecules during the CO_2RR experiment. There it was also shown that 25% CO coverage reproduces appropriate overpotentials for methanol formation on RuO_2(110).[55–59]

In all of the calculation done so far for the CO_2RR on RuO_2(110) using the TCM model, further desorption or reduction of adsorbed CO is assumed to be slow compared to the main pathway of the CO_2RR. Therefore, CO_2 will be reduced all the way to *e.g.* methanol while CO remains on the surface as a spectator.[55–59] Here we justify this assumption by calculating the energy barriers for desorption of CO to CO(g) (Fig. S6†) as well as for proton–electron transfer to CO to form either COH (Fig. S7†) or CHO (Fig. S8†) intermediates. Fig. 3 shows significant barriers for all these reaction steps (1.32–1.44 eV) predicting slow kinetics for further CO desorption/reduction which shows the validity of the assumption that has been made before in TCM simulations for the CO_2RR on RuO_2(110).

Reaction pathways of the CO_2RR on RuO_2(110) towards formic acid, methanediol, methanol and methane

Adsorption of CO_2 and proton–electron transfer barriers to either COOH or OCHO. In this section and subsequent sections, we include 25% CO coverage as a spectator species (shown in Fig. 2) and the whole reaction pathways towards different intermediates and products are shown in Fig. 4 as well as in several figures in the ESI† which will be referred to as the discussion progresses. The first step in the CO_2RR is to adsorb CO_2(g) on the RuO_2(110) surface which can either bind through the carbon atom (OC*O) or with both oxygen atoms (*OCO*), referred to as a bidentate adsorption. The presence of the CO spectator on the bridge site has strong repulsion forces with the OC*O intermediate which decreases the binding energy of OC*O considerably compared with when no CO spectator is included as was shown in Fig. 3. This effect is much smaller in the case of *OCO* where the binding free energy does not change much with or without the CO spectator present. The reason for that is because *OCO* binds to one bridge site and

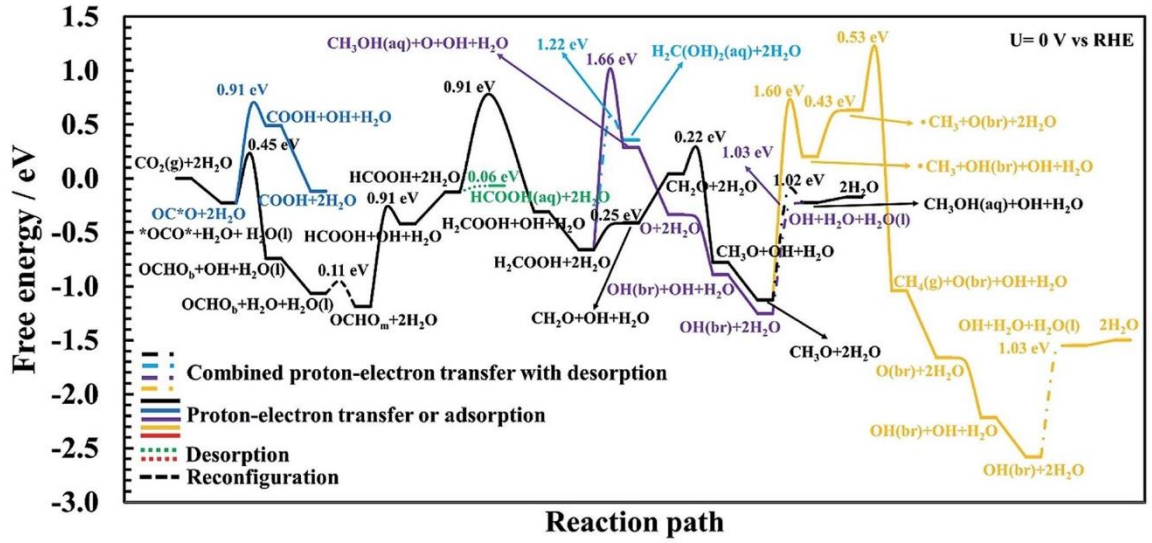

Fig. 4 Calculated free energy and activation energy for the CO_2RR on RuO_2(110) at $U = 0$ V *vs.* RHE in the presence of CO as a spectator. Blue curve: pathways toward COOH. Black curve: the optimal mechanism for methanol formation. Green curve: pathway toward formic acid. Cyan curve: pathway toward methanediol. Purple curve: alternative pathway toward methanol with a lower probability compared to the optimal pathway (black curve). Orange curve: pathways toward methane. Solid lines represent proton–electron transfer barriers or adsorption processes, dash-dotted lines represent combined proton–electron transfers with desorption barriers; the dotted line is for desorption and the dashed line is for reconfiguration.

the closest CUS site (where the H_2O molecules desorb) and the *OCO* intermediate does not get much repulsion from the CO spectator which is located on the other bridge site. This results in the OC*O and the *OCO* intermediates having the same binding free energy in the presence of the CO spectator (Fig. 4), in stark contrast with the results obtained without any CO spectator where OC*O binds much more strongly to the surface than the *OCO* intermediate (Fig. 3). Therefore, the next step plays an important role in the selectivity towards different CO_2RR products.

The first proton–electron transfer step can either lead to $OCHO_b$ or COOH, depending on which intermediate gets protonated, *OCO* or O*CO, respectively. Here we have distinguished the bidentate configuration ($OCHO_b$) where it is bonded through two oxygen atoms to a bridge site and the closest CUS site from the monodentate configuration ($OCHO_m$) where it is bonded through only one of the oxygen atoms, which is discussed further below. Our calculated energy barriers in Fig. 4 show that the required barrier for protonation of *OCO* to $OCHO_b$ is 0.45 eV (Fig. S9†) while for OC*O to COOH is estimated to be 0.91 eV (Fig. S4†). Therefore, $OCHO_b$ is predicted to form on RuO_2(110) instead of COOH in the presence of the CO spectator species. Here it is noted that *OCO* and $OCHO_b$ are the only intermediates that bind to the surface in a bidentate form. In both cases, one of the co-adsorbed water molecules needs to be moved approximately 1.3 Å above the CUS site to provide an empty site for those species to bind to the surface. In fact, we find that the only feasible way to transfer a proton to the carbon atom in CO_2 is that if it is adsorbed on the surface in a bidentate form (see Fig. S2b and S9†). When $OCHO_b$ is formed, the next step is to rearrange $OCHO_b$ to $OCHO_m$ (Fig. S10†) to continue the reduction further. This is a monodentate adsorbate that binds through only one oxygen atom to the bridge site of the surface and the two water molecules are chemisorbed to the CUS sites (see final state in Fig. S10† or initial state in Fig. S11†). The energy barrier for this reconfiguration is very low (0.11 eV) and this step is slightly downhill in free energy. This rearrangement will therefore be easily overcome at room temperature.

Proton–electron transfer barriers from $OCHO_m$ to HCOOH(aq) or H_2COOH. The protonation of $OCHO_m$ leads to adsorbed HCOOH on the surface with a barrier of 0.91 eV but a low additional barrier on top of the thermochemical barrier is observed (black curve in Fig. 4 and S11†). This barrier will be low at −1 V. The adsorbed HCOOH can easily desorb as formic acid from the surface with only a 0.06 eV barrier (green curve in Fig. 4 and S12†). Alternatively, the adsorbed HCOOH intermediate can be reduced further where the carbon atom gets protonated, resulting in adsorbed H_2COOH with a barrier of 0.91 eV (black curve in Fig. 4 and S13†). This step has a large additional barrier since this step is already downhill at $U = 0$ V. This transition state is also the highest point on the overall energy landscape in the optimum pathway towards methanol and is predicted here to be the rate limiting step (RLS) towards methanol.

Proton–electron transfer barriers of H_2COOH to CH_2O + H_2O(l), O + CH_3OH(aq) or $CH_2(OH)_2$(aq). The fourth proton–electron transfer in the CO_2RR which is of the H_2COOH admolecule may lead to different intermediates and products

(Fig. 4). The protonation of the –OH group can take place to form an adsorbed CH_2O intermediate and $H_2O(l)$ which is a part of the optimum mechanism towards methanol formation (black curve in Fig. 4), with an insignificant barrier on top of the thermodynamics (see also Fig. S14†). Another possible protonation step of H_2COOH is to the carbon atom and to directly desorb $CH_3OH(aq)$ at the same time as the O–C bond is broken, which results in an adsorbed oxygen atom on the surface (Fig. S15†). This step towards methanol formation has a large energy barrier, 1.66 eV, and is not a part of the optimum pathway towards methanol which will be discussed further below. In this pathway (purple curve in Fig. 4) the adsorbed oxygen atom is protonated further towards water with no additional barriers on top of the thermodynamics (Fig. S24 and S25†). The third possible protonation step of H_2COOH is to the oxygen atom resulting in methanediol ($CH_2(OH)_2(aq)$) formation (cyan curve, see also Fig. S16 and S17†). The energy barrier of 1.22 eV here at $U = 0$ V will be surmountable at -1 V applied potential, but the selectivity will be much more favored towards the CH_2O intermediate which can be reduced further to methanol. This is in agreement with several of the reported experiments where high efficiency towards methanol is reported whereas methanediol has not been detected in any of those.

Proton–electron transfer barriers of CH_2O to either methanol or methane. The protonation of CH_2O leads to adsorbed CH_3O on the surface (black curve in Fig. 4). The calculated activation energy for this reaction is estimated to be 0.22 eV (see also Fig. S18†). When the CH_3O intermediate is formed on the surface, it may be protonated to form methanol which desorbs directly from the surface with an energy barrier of 1.02 eV, but has a small additional barrier above the thermochemical barrier which will be low at -1 V applied potential (see also Fig. S19†). This is therefore the PLS for methanol formation.

In order to investigate methane formation, several possible pathways and mechanisms are considered. The mechanism with the lowest overall barrier is considered first but alternative mechanisms are explored below. The protonation of adsorbed CH_3O may also result in adsorbed CH_3OH and subsequent cleavage of the O–C bond in $HO–CH_3$, resulting in a planar $^{\bullet}CH_3$ radical desorbed slightly from the surface and leaving an OH species adsorbed at the bridge site on the surface, OH(br). This mechanism has a significantly higher barrier than when directly desorbing methanol as discussed above, with an energy barrier of 1.60 eV, and a considerably large additional barrier above the thermodynamics (yellow curve in Fig. 4 and S21†). The subsequent reduction of this $^{\bullet}CH_3$ radical to desorbed $CH_4(g)$ has also a significantly large overall barrier as described further here. After the planar $^{\bullet}CH_3$ radical is formed, the hydrogen atom in the adsorbed OH(br) intermediate is transferred back to adsorbed OH on the CUS site, forming co-adsorbed water on the surface (yellow curve in Fig. 4 and S22†). The additional barrier is insignificant, but the thermochemical barrier is uphill by 0.43 eV. This co-adsorbed water then transfers a proton–electron to the $^{\bullet}CH_3$ radical to form methane. The additional barrier is moderately high or 0.53 eV (Fig. S23†) but the overall barrier for this mechanism is large, or around 2.3 eV (yellow curve in Fig. 4). The difference in the overall barrier height between methanol formation (1.02 eV) and methane formation *via* this mechanism (2.3 eV) results in a large difference in selectivity towards these products. This difference in energy barriers between these two products corresponds to around a 10^{22} order of magnitude difference in rates at $U = 0$ V and under standard conditions.[23]

Since the mechanism of methane formation is a crucial step in the overall work and the mechanism presented above resulted in an overall high energy barrier it requires further investigation. The proton transfer can also be to the carbon atom of the $O–CH_3$ admolecule to form a desorbed $CH_4(g)$ molecule directly (not shown in Fig. 4, but shown Fig. S20†). The calculation of the minimum energy pathway for this mechanism results in the O–C bond in the adsorbed $O–CH_3$ being broken first, resulting in this same planar $^{\bullet}CH_3$ radical above the surface which is then protonated to form methane. The calculated activation energy for this combined mechanism is 2.77 eV, with a large additional barrier of more than 2 eV. Comparing the overall barrier of 2.77 eV for this mechanism with the one presented above (2.3 eV) shows that a lower barrier can be achieved by forming first methanol and then breaking the O–C bond before the $^{\bullet}CH_3$ radical is reduced. However, in both cases, an insignificant rate of methane formation is predicted at room temperature compared to the rate of methanol formation.

Because in both mechanisms presented above for methane formation a $^{\bullet}CH_3$ radical is first formed before it can be reduced to a $CH_4(g)$ molecule, yet another alternative mechanism is considered. Here we consider whether a water molecule in the first bilayer can assist in this reaction. The proton is shuttled from the co-adsorbed water to this additional water molecule *via* a Grotthuss mechanism and transferred to the methyl group of the $O–CH_3$ admolecule to form methane directly. A mechanism like this would bypass forming the $^{\bullet}CH_3$ radical first and could lower the overall barrier because this concerted mechanism should weaken the $O–CH_3$ bond. During simulation of this reaction path, however, a proton–electron transfer from the co-adsorbed water to the oxygen atom of the CH_3O admolecule results in an initial formation of a methanol molecule that desorbs from the surface instead of favoring the initially set reaction path. Therefore, it rather favors the mechanism presented initially having a barrier around 2.3 eV and the one included in Fig. 4. This shows that the proton–electron transfer is carried out with the co-adsorbed water rather than from a water molecule in the first bilayer.

The high barriers for methane formation presented above provide insight and reasoning as to why methane is not detected experimentally despite the fact that the simple TCM calculations predict the same overpotentials and PLS for both methane and methanol formation as introduced earlier in this work. It should be noted that we predict here the OCH_3 to $CH_3OH(aq)$ step to be the PLS whereas the HCOOH to H_2COOH is the RLS for methanol formation as explained above.

Hydrogen evolution. As described above, H_2 evolution has recently been concluded to be the dominant reaction on RuO_2 electrodes,[54] contradicting all previous reports where methanol

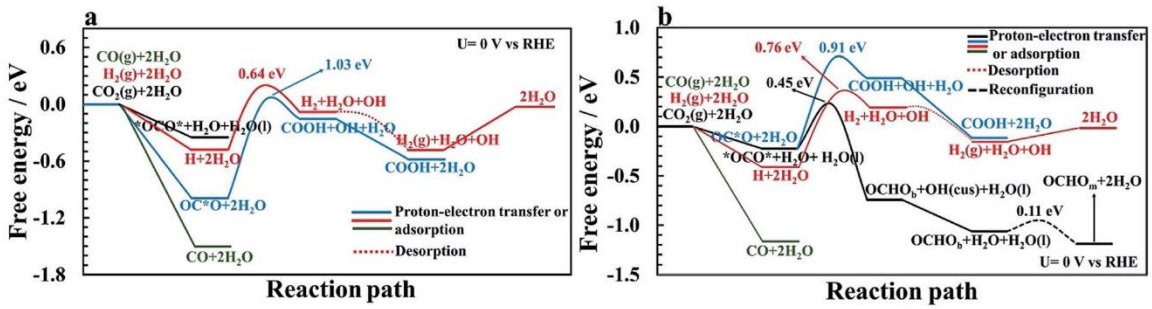

Fig. 5 Free energy diagrams and energy barriers for hydrogen evolution reaction pathways on RuO_2(110) at $U = 0$ V *vs.* RHE (a) without CO as a spectator and (b) with CO as a spectator (25% CO coverage). The first couple of reaction steps of the CO_2RR (from Fig. 3 and 4) are included for comparison of these competing reactions. Adsorption free energy of CO(g) is also included for comparison.

and/or formic acid were identified as the major products.[49–52] Therefore, the mechanism of the HER is calculated on the same model systems as presented above for the CO_2RR in order to determine the selectivity between the HER and CO_2RR. However, only using two co-adsorbed water molecules on the CUS results in a very high energy barrier (around 2 eV) for transferring the proton from the co-adsorbed water molecule to the vacant bridge site (Volmer reaction). This can be attributed to a relative long distance for the proton transfer in this case compared to when CO_2RR intermediates are adsorbed and reduced on the vacant bridge site presented above. Therefore, we include an additional water molecule from the first bilayer to assist in this reaction, similar as was done in one of the methane formation mechanisms presented above. The proton is then shuttled from the co-adsorbed water to this additional water molecule *via* a Grotthuss mechanism and transferred to the bridge vacant site and the calculated energy barrier for this reaction is 0.46 eV at $U = 0$ V *vs.* RHE (Fig. S26†). Adding protons to the active sites on the RuO_2(110) surface is therefore concluded to be facile at reducing potentials. For the H_2 formation step presented below we find that when the bridge site is already occupied by a hydrogen adatom the presence of this additional water molecule has a minor effect on the energy barrier, changing it by only +0.04 and −0.15 eV, without and with a CO spectator, respectively, as compared to when only using the two co-adsorbed water molecules. Therefore, in order to maintain constancy, proton–electron transfer barriers for the H_2 formation step are also carried out using the three water molecule model system.

Fig. 5a shows the comparison of the competing HER with the CO_2RR on a clean RuO_2(110) surface at $U = 0$ V *vs.* RHE. The adsorption free energy of OC*O is around −1 eV and binds stronger to the surface than a H adatom of around −0.5 eV where both intermediates adsorb to a bridge vacant site. Since in a CO_2-saturated solution the proton concentration is much higher than the CO_2 concentration it is reasonable to assume that these sites will have a higher coverage of H than adsorbed CO_2. However, when CO_2 comes into the double layer it will adsorb stronger than protons. Since the applied potential affects the proton adsorption much more strongly than the CO_2 adsorption, these results indicate that the adsorption free energies of H and CO_2 become equal at −0.5 V *vs.* RHE. After adsorption of hydrogen on the surface, the next step is to protonate hydrogen using co-adsorbed water and produce adsorbed H_2 on the surface. The calculated activation energy for this step is estimated to be 0.64 eV at $U = 0$ V. In the next step, H_2 leaves the surface without any energy barrier. This is compared with the CO_2RR pathway towards forming adsorbed CO on the surface, where the highest barrier is 1.03 eV. These results indicate that the HER is much more facile than the CO_2RR on the clean RuO_2(110) surface at reducing potentials, but when very negative potential is applied, some CO_2 will be reduced to adsorbed CO, in agreement with recent experimental results.[54] Another way to introduce adsorbed CO as a spectator species on the surface is to include some CO gas into the electrolyte before CO_2RR experiments. Fig. 5a shows that CO adsorbs much stronger to the surface than either protons or CO_2.

The same competing processes of the HER and CO_2RR are compared in Fig. 5b when a CO spectator is adsorbed on the surface. The presence of CO on the surface destabilizes the binding free energy of hydrogen slightly, or to a value of around −0.4 eV. While the adsorption free energy of *OCO* is only slightly affected by the presence of CO, the adsorption of OC*O is largely affected, and binds weaker than H. This results in even higher possibilities of the catalytic sites being occupied with H rather than CO_2, especially when reducing potentials are applied. The energy barrier for H_2 formation increases to around 0.76 eV at 0 V *vs.* RHE with the CO spectator (Fig. S28†), compared to a barrier of around 0.64 eV without CO (Fig. S27†). The H_2 formation steps are concluded to be the RLS for the HER as the energy barriers are higher than for the Volmer step presented above. Fig. 5b shows that the competing energy barrier for the formate pathway in the CO_2RR is only 0.45 eV at 0 V *vs.* RHE. As shown in Fig. 4, the PLS for formic acid formation is the reduction of the formate intermediate which requires −0.9 V. At these reducing potentials, most of the bridge sites will be covered with protons, resulting in much higher rates of the HER than the CO_2RR, in good agreement with recent experimental findings.[54]

Table 2 Calculated reaction energies (ΔE), energy barriers (E_a) and additional energy barriers on top of thermodynamics for several possible intermediates and products for the CO_2RR and HER on RuO_2(110). Here, S stands for the CO spectator. All energies are in eV

Reactions	Classification	ΔE	E_a	Additional barrier
$CO_2 + H_2O \rightarrow COOH + OH$	Transfer to O	0.78	0.88	0.10
$CO_2 + H_2O \rightarrow OCHO_b + OH$ (S)	Transfer to C	−0.87	0.45	0.45
$OCHO_b \rightarrow OCHOm$ (S)	Reconfiguration	−0.11	0.11	0.11
$OCHO + H_2O \rightarrow HCOOH + OH$ (S)	Transfer to O	0.72	0.86	0.14
$HCOOH \rightarrow HCOOH(aq)$ (S)	Desorption	0.20	0.20	0.00
$HCOOH + H_2O \rightarrow H_2COOH + OH$ (S)	Transfer to C	−0.33	0.91	0.91
$H_2COOH + H_2O \rightarrow H_2C(OH)_2 + OH$ (S)	Transfer to O	0.52	0.72	0.20
$H_2C(OH)_2 \rightarrow H_2C(OH)_2(aq)$ (S)	Desorption	0.60	0.60	0.00
$H_2COOH + H_2O \rightarrow CH_2O + H_2O(l) + OH$ (S)	Transfer to OH	0.78	0.78	0.00
$H_2COOH + H_2O \rightarrow CH_3OH(aq) + O + OH$ (S)	Transfer to C	1.13	1.66	0.53
$CH_2O + H_2O \rightarrow CH_3O + OH$ (S)	Transfer to C	−0.91	0.22	0.22
$CH_3O + H_2O \rightarrow CH_3OH(aq) + OH$ (S)	Transfer to O	0.94	1.06	0.12
$CH_3O + H_2O \rightarrow {}^*CH_3 + OH(br) + OH(CUS)$ (S)	Transfer to O	1.50	1.97	0.47
$OH(br) + OH(CUS) \rightarrow O(br) + H_2O(CUS)$ (S)	Reconfiguration	0.74	0.74	0.00
${}^*CH_3 + O(br) + H_2O \rightarrow CH_4(g) + O(br) + OH(CUS)$ (S)	Transfer to C	−1.42	0.53	0.53
$CH_3O + H_2O \rightarrow CH_4(g) + O + OH$ (S)	Transfer to C	0.64	2.77	2.13
$O + H_2O \rightarrow OH + OH$ (S)	Transfer to O	−0.62	0.00	0.00
$COOH + H_2O \rightarrow CO + H_2O(l) + OH$	Transfer to OH	−0.33	0.32	0.32
$CO + H_2O \rightarrow COH + OH$	Transfer to O	1.57	1.57	0.00
$CO + H_2O \rightarrow CHO + OH$	Transfer to C	0.97	1.41	0.44
$CO \rightarrow CO(g)$	Desorption	1.98	1.98	0.00
$H + H_2O \rightarrow H_2(g) + OH$	Transfer to H	0.30	0.64	0.34
$H + H_2O \rightarrow H_2(g) + OH$ (S)	Transfer to H	0.61	0.76	0.15

Table 3 Reaction pathways towards methanol and methane formation based on our current study

Pathways	1	2	3	4	5	6	7	8
Methanol	OCHO	HCOOH	H_2COOH	$CH_2O + H_2O(l)$	CH_3O	$CH_3OH(aq)$		
Methane	OCHO	HCOOH	H_2COOH	$CH_2O + H_2O(l)$	CH_3O	$CH_4(g) + O$	OH	$H_2O(l)$

Discussion

In this work, the proton–electron transfer barriers can be classified into four groups:

1. Proton–electron transfer to oxygen (*e.g.* O–CH–O to O–CH–OH)

2. Proton–electron transfer to the hydroxyl group (*e.g.* O–CH_2–OH to O–CH_2 + H_2O(l))

3. Proton–electron transfer to carbon (*e.g.* O–C–O to O–CH–O)

4. Proton–electron transfer to hydrogen

Overall, the proton–electron transfer steps presented in this paper show that attacking the –O or –OH groups of CO_2RR intermediates results in low additional barriers on the order of 0.0 to 0.3 eV while attacking the carbon atom results in higher additional barriers. For highly exergonic reactions they are around 0.2 to 0.5 eV. For the reaction having around thermoneutral or endergonic reaction free energies, the additional energy barrier is around 0.5 to 0.9 eV, except in the case of methane formation, which is over 2 eV. This is not surprising since oxygen is more electronegative than carbon which should favor a proton transfer. Finally, in the case of adsorbed H, our results show low additional barriers, or 0.34 and 0.15 eV, without and with a CO spectator, respectively. The energy barriers presented in this work are summarized in Table 2 where they are classified based on which atom of the CO_2RR or H intermediates protonation takes place.

In the case of pure metal electrodes, the reaction pathways are very different depending on whether a detailed solvation and kinetic model is used or a thermochemical one.[23] Despite a much more detailed modeling of the reaction paths presented in this work for RuO_2(110) than in previous studies using the TCM and CHE models,[55–59] both methods predict the same adsorbed intermediates between proton–electron transfer steps, except in one case. Table 3 summarizes the theoretical reaction pathways based on our current work for the CO_2RR towards methanol and methane and should be compared with the results in Table 1 which summarizes the pathways predicted by the TCM–CHE models. After the fourth proton–electron transfer step we predict with the detailed modeling that the H_2COOH admolecule is reduced to the CH_2O intermediate on the surface and an H_2O(l) molecule that desorbs from the surface (Table 3), whereas the simpler TCM model predicts the CH_3O + OH intermediates on the surface (Table 1). This is however not because of the negligible kinetic barrier we find for this step, but because of the presence of co-adsorbed water on the surface that imposes the formation of adsorbed CH_2O and H_2O(l) instead of forming the CH_3O and OH intermediates. The

CH_3O and OH intermediates will be formed when CH_2O is protonated further by co-adsorbed water (Fig. 4 and Table 3).

Finally, we address the question of why Cu is more selective towards methane than methanol while the opposite trend is observed and predicted here on RuO_2; *i.e.* more selective towards methanol than methane. There is a fundamental difference between these two types of catalysts which alters the binding configurations of the CO_2RR intermediates, which changes the selectivity. While all intermediates bind through the carbon atom on the Cu(111) surface,[23] they all bind through their oxygen atom(s) on the RuO_2(110) surface. As an example, on Cu(111) the first two intermediates are predicted to be COOH and CO where both bind to the surface through the carbon atom, while OCHO and HCOOH are predicted to be the first two intermediates on RuO_2(110), both binding through their oxygen atom(s). This is presumably because of the oxygen vacant bridge sites on RuO_2(110), which tend to bind intermediates through their oxygen atoms rather than through their carbon atom. Furthermore, we observe that when an intermediate binds to the surface through an oxygen atom, a very high activation energy is needed to break the O–C bond; as shown in the case of O–CH_3 reduction to O + CH_4 in Table 2. Therefore, O–CH_3 is much rather reduced to methanol than methane on RuO_2. In contrast, when intermediates bind through the carbon atom to the surface, breaking the C–O bond requires a very low activation energy, as shown in the case of COOH reduction to CO + H_2O in Table 2 for RuO_2 and has been shown previously for Cu(111).[23] This is why Cu is more selective towards methane than methanol where all intermediates bind through the carbon atom.

Conclusions

In this work, we calculate proton–electron transfer energy barriers for the CO_2RR and HER on RuO_2(110) using 1 ML of co-adsorbed water molecules on the CUS and low CO coverages on the surface to gain further insight into the reaction mechanisms towards hydrogen, methanol, methane, methanediol, formic acid and CO evolution. We obtained two substantial additional energy barriers on top of the thermodynamics. One is related to a proton–electron transfer to the O–CH–OH species to form O–CH_2–OH with an additional energy barrier of 0.91 eV which is the RLS towards methanol and methanediol. The highest energy barrier we find towards methanol is, however, 1.02 eV, for the reduction of the OCH_3 intermediate, but since the barrier mainly comes from the thermodynamics of that reaction step it is easily surmounted at room temperature at the required overpotential for methanol formation which is calculated to be around −1 V *vs.* RHE. The other substantial additional energy barrier we find in this work is related to the protonation of the O–CH_3 intermediate to form methane with an overall barrier of 2.3 eV or more. A few mechanisms are considered where they all resulted in having more than one elementary step. In all cases, high barriers for breaking the O–C bond are found to be limiting. These results show clearly from the energy barriers why methanol can be formed on RuO_2 electrodes at high overpotentials while methane formation seems impossible. The calculations predict, however, that hydrogen is the main product at all potentials which is consistent with the most recent experimental results.

Generally, we find that the additional energy barriers on top of the thermodynamics for proton–electron transfer to –O and –OH groups in CO_2RR intermediates are low. This indicates that these elementary steps are easily surmountable at the overpotential required for the reaction and they are not kinetically limited. In contrast, proton–electron transfer steps to the carbon atom in CO_2RR intermediates and for O–C scission steps are predicted to be kinetically limited in some cases even if the thermodynamics are favorable. Furthermore, we find that the required barriers to desorb CO from the RuO_2(110) surface or to further reduce it to COH or CHO are relatively high and this supports the hypothesis regarding CO as a spectator species on RuO_2 electrodes.

Conflicts of interest

There are no conflicts to declare.

Acknowledgements

This work was supported by the Icelandic Research Fund (grant no. 196437-051), the Research Fund of the University of Iceland and the 'Nordic Consortium for CO_2 Conversion' (NordForsk project no. 85378, http://site.uit.no/nordco2).

References

1 Y. Hori, A. Murata and R. Takahashi, *J. Chem. Soc., Faraday Trans. 1*, 1989, **85**, 2309–2326.
2 Y. Hori, H. Wakebe, T. Tsukamoto and O. Koga, *Electrochim. Acta*, 1994, **39**, 1833–1839.
3 M. R. Singh, Y. Kwon, Y. Lum, J. W. Ager and A. T. Bell, *J. Am. Chem. Soc.*, 2016, **138**, 13006–13012.
4 A. S. Varela, W. Ju, A. Bagger, P. Franco, J. Rossmeisl and P. Strasser, *ACS Catal.*, 2019, **9**, 7270–7284.
5 A. Vasileff, X. Zhi, C. Xu, L. Ge, Y. Jiao, Y. Zheng and S. Z. Qiao, *ACS Catal.*, 2019, **9**, 9411–9417.
6 H. Zhang, Y. Zhang, Y. Li, S. Ahn, G. T. R. Palmore, J. Fu, A. A. Peterson and S. Sun, *Nanoscale*, 2019, **11**, 12075–12079.
7 K. J. P. Schouten, Y. Kwon, C. J. M. Van Der Ham, Z. Qin and M. T. M. Koper, *Chem. Sci.*, 2011, **2**, 1902–1909.
8 K. J. P. Schouten, Z. Qin, E. P. Gallent and M. T. M. Koper, *J. Am. Chem. Soc.*, 2012, **134**, 9864–9867.
9 K. P. Kuhl, E. R. Cave, D. N. Abram and T. F. Jaramillo, *Energy Environ. Sci.*, 2012, **5**, 7050–7059.
10 W. Tang, A. A. Peterson, A. S. Varela, Z. P. Jovanov, L. Bech, W. J. Durand, S. Dahl, J. K. Nørskov and I. Chorkendorff, *Phys. Chem. Chem. Phys.*, 2012, **14**, 76–81.
11 R. Reske, M. Duca, M. Oezaslan, K. J. P. Schouten, M. T. M. Koper and P. Strasser, *J. Phys. Chem. Lett.*, 2013, **4**, 2410–2413.
12 A. S. Varela, C. Schlaup, Z. P. Jovanov, P. Malacrida, S. Horch, I. E. L. Stephens and I. Chorkendorff, *J. Phys. Chem. C*, 2013, **117**, 20500–20508.

13 K. J. P. Schouten, E. Pérez Gallent and M. T. M. Koper, *J. Electroanal. Chem.*, 2014, **716**, 53–57.
14 K. P. Kuhl, T. Hatsukade, E. R. Cave, D. N. Abram, J. Kibsgaard and T. F. Jaramillo, *J. Am. Chem. Soc.*, 2014, **136**, 14107–14113.
15 A. A. Peterson, F. Abild-Pedersen, F. Studt, J. Rossmeisl and J. K. Nørskov, *Energy Environ. Sci.*, 2010, **3**, 1311–1315.
16 A. A. Peterson and J. K. Nørskov, *J. Phys. Chem. Lett.*, 2012, **3**, 251–258.
17 X. Liu, P. Schlexer, J. Xiao, Y. Ji, L. Wang, R. B. Sandberg, M. Tang, K. S. Brown, H. Peng, S. Ringe, C. Hahn, T. F. Jaramillo, J. K. Nørskov and K. Chan, *Nat. Commun.*, 2019, 32.
18 X. Nie, M. R. Esopi, M. J. Janik and A. Asthagiri, *Angew. Chem., Int. Ed.*, 2013, **52**, 2459–2462.
19 F. Calle-Vallejo and M. T. M. Koper, *Angew. Chem., Int. Ed.*, 2013, **52**, 7282–7285.
20 H. Xiao, T. Cheng, W. A. Goddard and R. Sundararaman, *J. Am. Chem. Soc.*, 2016, **138**, 483–486.
21 J. Hussain, H. Jónsson and E. Skúlason, *Faraday Discuss.*, 2016, **195**, 619–636.
22 M. R. Singh, J. D. Goodpaster, A. Z. Weber, M. Head-Gordon and A. T. Bell, *Proc. Natl. Acad. Sci. U. S. A.*, 2017, **114**, E8812–E8821.
23 J. Hussain, H. Jónsson and E. Skúlason, *ACS Catal.*, 2018, **8**, 5240–5249.
24 A. Bagger, L. Arnarson, M. H. Hansen, E. Spohr and J. Rossmeisl, *J. Am. Chem. Soc.*, 2019, **141**, 1506–1514.
25 A. Bagger, R. M. Arán-Ais, J. Halldin Stenlid, E. Campos dos Santos, L. Arnarson, K. Degn Jensen, M. Escudero-Escribano, B. Roldan Cuenya and J. Rossmeisl, *ChemPhysChem*, 2019, **20**, 3096–3105.
26 J. K. Nørskov, J. Rossmeisl, A. Logadottir, L. Lindqvist, J. R. Kitchin, T. Bligaard and H. Jónsson, *J. Phys. Chem. B*, 2004, **108**, 17886–17892.
27 M. A. Henderson, *Surf. Sci. Rep.*, 2002, **46**, 1–308.
28 A. Lobo and H. Conrad, *Surf. Sci.*, 2003, **523**, 279–286.
29 R. Mu, Z. J. Zhao, Z. Dohnálek and J. Gong, *Chem. Soc. Rev.*, 2017, **46**, 1785–1806.
30 A. Rendón-Calle, S. Builes and F. Calle-Vallejo, *Appl. Catal., B*, 2020, **276**, 119147.
31 P. J. Feibelman, *Science*, 2002, **295**, 99–102.
32 H. Ogasawara, B. Brena, D. Nordlund, M. Nyberg, A. Pelmenschikov, L. G. M. Pettersson and A. Nilsson, *Phys. Rev. Lett.*, 2002, **89**, 276102.
33 S. Schnur and A. Groß, *New J. Phys.*, 2009, **11**, 125003.
34 X. Lin and A. Groß, *Surf. Sci.*, 2012, **606**, 886–891.
35 M. Van Den Bossche, E. Skúlason, C. Rose-Petruck and H. Jónsson, *J. Phys. Chem. C*, 2019, **123**, 4116–4124.
36 P. Lindgren, G. Kastlunger and A. A. Peterson, *ACS Catal.*, 2020, **10**, 121–128.
37 E. Skúlason, V. Tripkovic, M. E. Björketun, S. Gudmundsdóttir, G. Karlberg, J. Rossmeisl, T. Bligaard, H. Jónsson and J. K. Nørskov, *J. Phys. Chem. C*, 2010, **114**, 18182–18197.
38 M. H. Hansen and J. Rossmeisl, *J. Phys. Chem. C*, 2016, **120**, 29135–29143.
39 T. Cheng, H. Xiao and W. A. Goddard, *J. Phys. Chem. Lett.*, 2015, **6**, 4767–4773.
40 E. Tayyebi, Y. Abghoui and E. Skúlason, *ACS Catal.*, 2019, **9**, 11137–11145.
41 C. Zhang, J. Hutter and M. Sprik, *J. Phys. Chem. Lett.*, 2019, **10**, 3871–3876.
42 X. Liu, J. Xiao, H. Peng, X. Hong, K. Chan and J. K. Nørskov, *Nat. Commun.*, 2017, **8**, 15438.
43 J. D. Goodpaster, A. T. Bell and M. Head-Gordon, *J. Phys. Chem. Lett.*, 2016, **7**, 1471–1477.
44 S. Siahrostami and A. Vojvodic, *J. Phys. Chem. C*, 2015, **119**, 1032–1037.
45 J. Rossmeisl, Z. W. Qu, H. Zhu, G. J. Kroes and J. K. Nørskov, *J. Electroanal. Chem.*, 2007, **607**, 83–89.
46 P. M. Gíslason and E. Skúlason, *Nanoscale*, 2019, **11**, 18683–18690.
47 J. Lee, D. C. Sorescu, X. Deng and K. D. Jordan, *J. Phys. Chem. Lett.*, 2013, **4**, 53–57.
48 Y. Hori, in *Modern Aspects of Electrochemistry*, Springer New York, New York, NY, 2008, pp. 89–189.
49 A. Bandi, *J. Electrochem. Soc.*, 1990, **137**, 2157.
50 A. Bandi, *J. Electrochem. Soc.*, 1992, **139**, 1605.
51 J. P. Popić, M. L. Avramov-Ivić and N. B. Vuković, *J. Electroanal. Chem.*, 1997, **421**, 105–110.
52 N. Spataru, K. Tokuhiro, C. Terashima, T. N. Rao and A. Fujishima, *J. Appl. Electrochem.*, 2003, **33**, 1205–1210.
53 J. Qu, X. Zhang, Y. Wang and C. Xie, *Electrochim. Acta*, 2005, **50**, 3576–3580.
54 S. Mezzavilla, Y. Katayama, R. Rao, J. Hwang, A. Regoutz, Y. Shao-Horn, I. Chorkendorff and I. E. L. Stephens, *J. Phys. Chem. C*, 2019, **123**, 17765–17773.
55 M. Karamad, H. A. Hansen, J. Rossmeisl and J. K. Nørskov, *ACS Catal.*, 2015, **5**, 4075–4081.
56 A. Bhowmik, T. Vegge and H. A. Hansen, *ChemSusChem*, 2016, **9**, 3230–3243.
57 A. Bhowmik, H. A. Hansen and T. Vegge, *J. Phys. Chem. C*, 2017, **121**, 18333–18343.
58 A. Bhowmik, H. A. Hansen and T. Vegge, *ACS Catal.*, 2017, **7**, 8502–8513.
59 E. Tayyebi, J. Hussain, Y. Abghoui and E. Skúlason, *J. Phys. Chem. C*, 2018, **122**, 10078–10087.
60 J. Vandevondele, M. Krack, F. Mohamed, M. Parrinello, T. Chassaing and J. Hutter, *Comput. Phys. Commun.*, 2005, **167**, 103–128.
61 J. Hutter, M. Iannuzzi, F. Schiffmann and J. Vandevondele, *Wiley Interdiscip. Rev.: Comput. Mol. Sci.*, 2014, **4**, 15–25.
62 G. Lippert, J. Hutter and M. Parrinello, *Mol. Phys.*, 1997, **92**, 477–488.
63 S. Goedecker and M. Teter, *Phys. Rev. B: Condens. Matter Mater. Phys.*, 1996, **54**, 1703–1710.
64 C. Hartwigsen, S. Goedecker and J. Hutter, *Phys. Rev. B: Condens. Matter Mater. Phys.*, 1998, **58**, 3641–3662.
65 J. VandeVondele and J. Hutter, *J. Chem. Phys.*, 2007, **127**, 114105.
66 J. P. Perdew, J. A. Chevary, S. H. Vosko, K. A. Jackson, M. R. Pederson, D. J. Singh and C. Fiolhais, *Phys. Rev. B: Condens. Matter Mater. Phys.*, 1992, **46**, 6671–6687.

67 J. P. Perdew, J. A. Chevary, S. H. Vosko, K. A. Jackson, M. R. Pederson, D. J. Singh and C. Fiolhais, *Phys. Rev. B: Condens. Matter Mater. Phys.*, 1993, **48**, 4978.
68 S. Grimme, J. Antony, S. Ehrlich and H. Krieg, *J. Chem. Phys.*, 2010, **132**, 154104.
69 M. Ceriotti, G. Bussi and M. Parrinello, *Phys. Rev. Lett.*, 2009, **102**, 020601.
70 M. Ceriotti, G. Bussi and M. Parrinello, *J. Chem. Theory Comput.*, 2010, **6**, 1170–1180.
71 J. Wellendorff, K. T. Lundgaard, A. Møgelhøj, V. Petzold, D. D. Landis, J. K. Nørskov, T. Bligaard and K. W. Jacobsen, *Phys. Rev. B: Condens. Matter Mater. Phys.*, 2012, 235149.
72 G. Kresse and J. Furthmüller, *Phys. Rev. B: Condens. Matter Mater. Phys.*, 1996, **54**, 11169–11186.
73 D. Joubert, *Phys. Rev. B: Condens. Matter Mater. Phys.*, 1999, **59**, 1758–1775.
74 P. E. Blöchl, *Phys. Rev. B: Condens. Matter Mater. Phys.*, 1994, **50**, 17953–17979.
75 G. Henkelman, B. P. Uberuaga and H. Jónsson, *J. Chem. Phys.*, 2000, **113**, 9901–9904.
76 G. Henkelman and H. Jónsson, *J. Chem. Phys.*, 2000, **113**, 9978–9985.
77 V. Tripković, E. Skúlason, S. Siahrostami, J. K. Nørskov and J. Rossmeisl, *Electrochim. Acta*, 2010, **55**, 7975–7981.

Supporting Information

Why RuO_2 electrodes catalyze electrochemical CO_2 reduction to methanol rather than methane; or perhaps neither of those?

Ebrahim Tayyebi[1], Javed Hussain[1], Egill Skúlason[1,2,*]

[1]Science Institute, University of Iceland, VR-III, 107 Reykjavík, Iceland

[2]Faculty of Industrial Engineering, Mechanical Engineering and Computer Science, University of Iceland, VR-III, 107 Reykjavík, Iceland

*Corresponding Author: egillsk@hi.is

Table S1. Recent experimental results for electrochemical CO_2 reduction reaction on RuO_2 and RuO_2-based catalysts.

Electrode	**CO_2 saturated electrolyte**	**pH**	**Potential (V)**	**Time (min)**	**Faradic efficiency (%)**				
					CH_3OH	**HCOOH**	**H_2**	**CO**	**CH_4**
RuO_2 (35)/TiO_2 (65) [1]	0.05 M Hg_2SO_4	1.2	-0.15 vs RHE	>2400	24	2	---	---	---
Ag-doped RuO_2 (35) / TiO_2 (65) [1]	0.05 M Hg_2SO_4	1.2	-0.15 vs RHE	---	2	78	---	---	---
Rh_2O_3 (20)/ TiO_2 (80) [1]	0.05 M Hg_2SO_4	1.2	-0.15 vs RHE	---	5	---	---	---	---
RuO_2 (25) / MoO_2 (30) / TiO_2 (45) [1]	0.05 M Hg_2SO_4	1.2	-0.15 vs RHE	---	12	<1	---	---	---
RuO_2 (20) / Co_3O_4 (10) / SnO_2 (8) / TiO_2 (62) [1]	0.05 M Hg_2SO_4	1.2	-0.15 vs RHE	---	7	18	---	---	---
RuO_2/TiO_2 [1]	0.2 M Na_2SO_4	4.0	Water reduction potential	>2400	76	---	---	---	---

RuO_2/TiO_2 [1]	0.2 M phosphate buffer	5.2	Water reduction potential	>2400	35	---	---	---	---
RuO_2/TiO_2 [1]	0.5 M $KHCO_3$	7.6	Water reduction potential	>2400	5	---	---	---	---
RuO_2/TiO_2 [1]	0.2 M Na_2SO_4	4.0	Water reduction potential	>2400	53	---	---	---	---
Cu-doped RuO_2 (75) / TiO_2 (25) [2]	0.5 M $KHCO_3$	7.2 to 7.3	-0.15 vs RHE	---	29.8	4.2	---	---	---
RuO_2 [3]	0.5 M $NaHCO_3$	8.3	-0.15 vs RHE	480	17.2	---	---	---	---
Cu-doped RuO_2 [3]	0.5 M $NaHCO_3$	8.3	-0.15 vs RHE	480	41.3	---	---	---	---
Cd-doped RuO_2 [3]	0.5 M $NaHCO_3$	8.3	-0.15 vs RHE	480	38.2	---	---	---	---
RuO_2 – coated boron doped diamond [4]	0.05 M Hg_2SO_4	5.9	0.21 vs RHE	206	8.12	32.66	39.88	0.005	0.11
RuO_2 – coated boron doped diamond [4]	0.05 M Hg_2SO_4	7.3	0.09 vs RHE	356	4.77	37.45	44.85	0.003	0.12
RuO_2/TiO_2 nano particles composite [5]	0.5 M $NaHCO_3$	8.5	-0.15 vs RHE	120	40.2	---	---	---	---
RuO_2/TiO_2 nano tubes composite [5]	0.5 M $NaHCO_3$	8.5	-0.15 vs RHE	120	60.5	---	---	---	---
RuO_2 [6]	0.1 M $KHCO_3$	6.8	-0.50 vs RHE	>900	0.00	0.00	>95	0.00	0.00

RuO_2 [6]	0.1 M $KHCO_3$	6.8	-0.90 vs RHE	>900	0.00	<0.2	>90	0.1<	0.00
RuO_2 (50)/TiO_2 (50) [6]	0.1 M $KHCO_3$	6.8	-0.75 vs RHE	>900	0.00	0.5<	>95	0.5<	0.00
RuO_2 (25)/TiO_2 (75) [6]	0.1 M $KHCO_3$	6.8	-0.75 vs RHE	>900	0.00	0.00	>90	1.00<	0.00
Cu-doped RuO_2 (25)/TiO_2 (75) [6]	0.1 M $KHCO_3$	6.8	-0.75 vs RHE	>900	0.00	5.00<	83<	12.5<	0.00
RuO_2 (25)/SnO_2 (75) [6]	0.1 M $KHCO_3$	6.8	-1.00 vs RHE	>900	0.00	3.00<	95<	2.00<	0.00
RuO_2 (10)/SnO_2 (90) [6]	0.1 M $KHCO_3$	6.8	-1.00 vs RHE	>900	0.00	3.00<	94<	6.00<	0.00

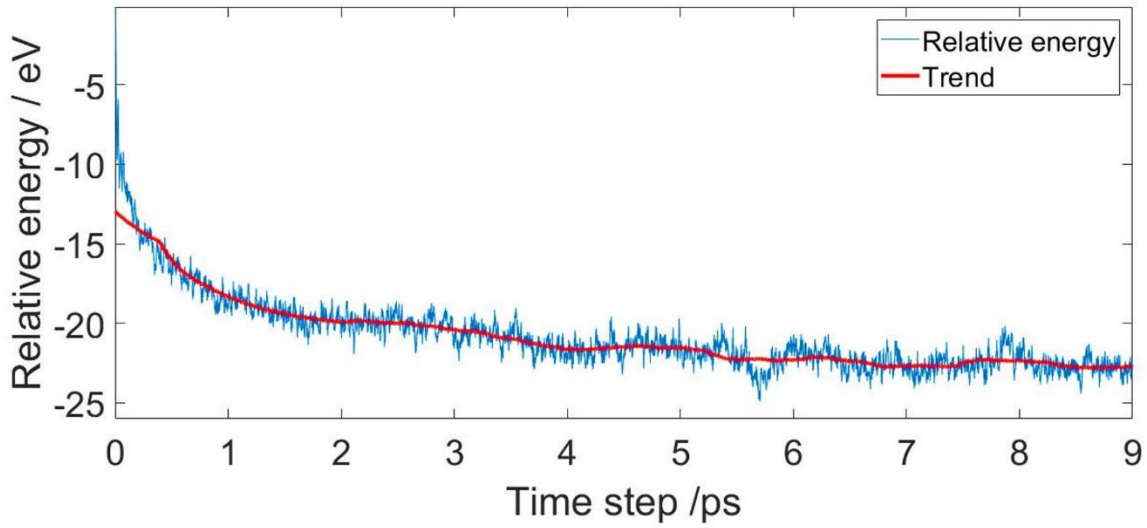

Figure S1:Relative energy as a function of elapsed time from *ab initio* molecular dynamic simulation at 300 K of 84 H_2O molecules on top of a RuO_2(110) surface.

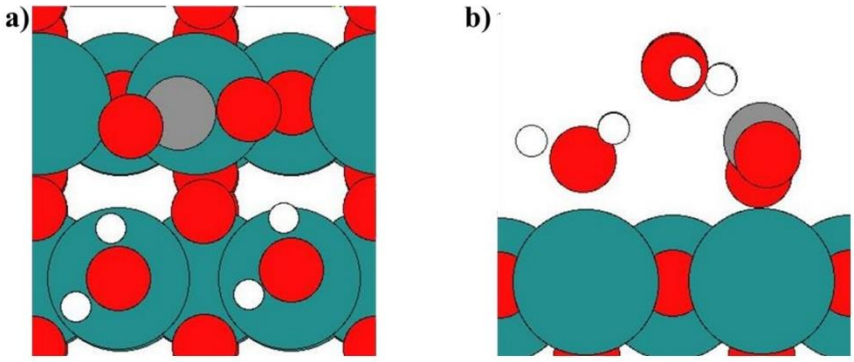

Figure S2. a) top view of O*CO where the carbon atom binds to a bridge site and b) side view of *OCO* where two oxygen atoms bind to a bridge site and the adjacent CUS.

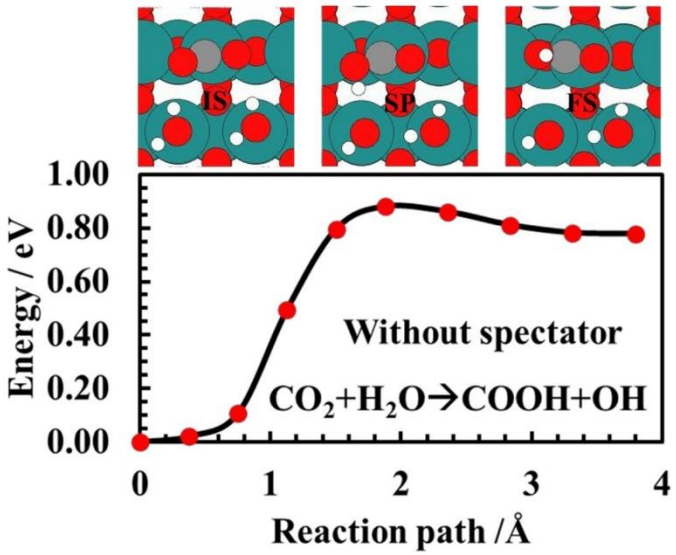

Figure S3. DFT calculated barrier for CO_2 protonation to COOH on RuO_2(110) surface. Similar value for activation energy of CO_2 to COOH has been obtained on RuO_2(110) when there is one CO as spectator on the surface (figure S2). (IS) initial state, (SP) saddle point and (FS) final state are shown on the top of the figure.

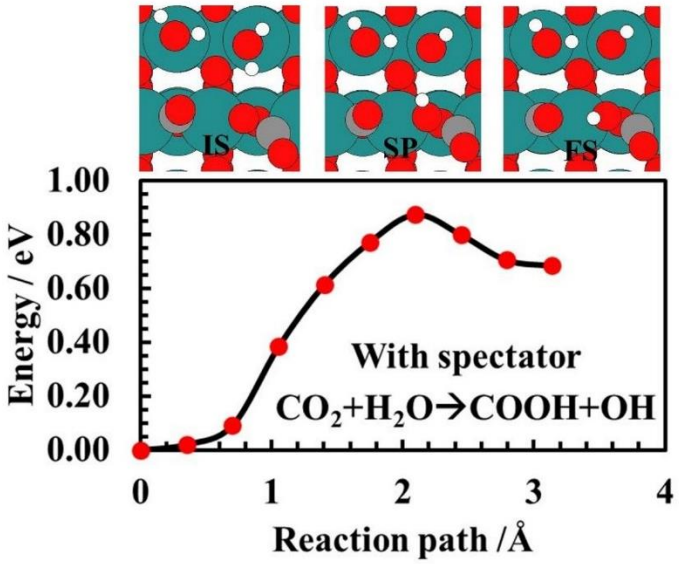

Figure S4. DFT calculated barrier for CO_2 protonation to COOH on RuO_2(110) surface where CO spectator is included. (IS) initial state, (SP) saddle point and (FS) final state are shown on the top of the figure.

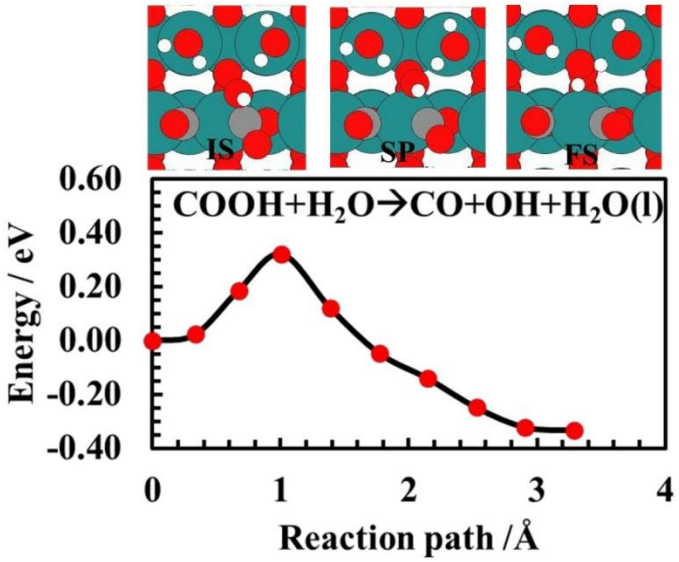

Figure S5. DFT calculated barrier for COOH protonation to CO and H_2O on RuO_2(110) surface. Similar value for activation energy is expected to be obtained on RuO_2(110) surface even without the presence of spectator. (IS) initial state, (SP) saddle point and (FS) final state are shown on the top of the figure.

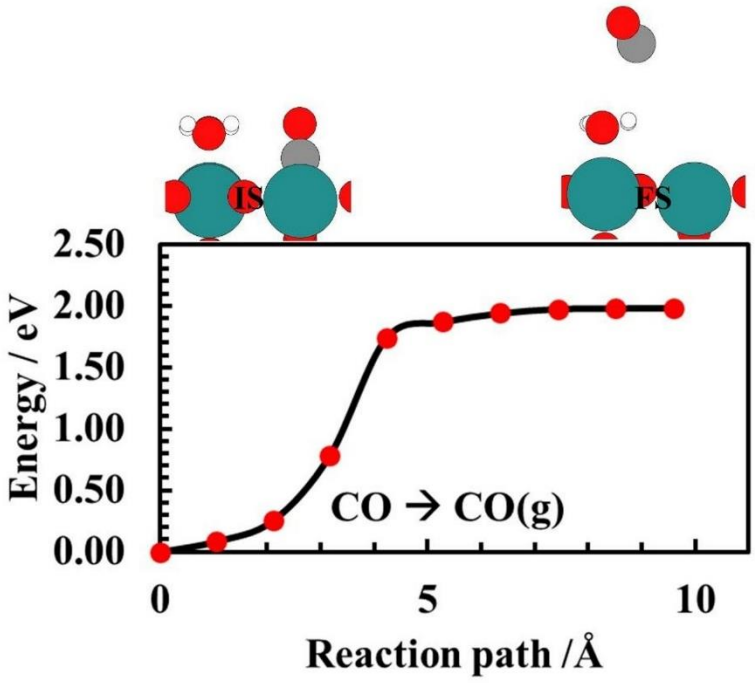

Figure S6. DFT calculated barrier for CO desorption on RuO_2(110) surface. (IS) initial state and (FS) final state are shown on the top of the figure.

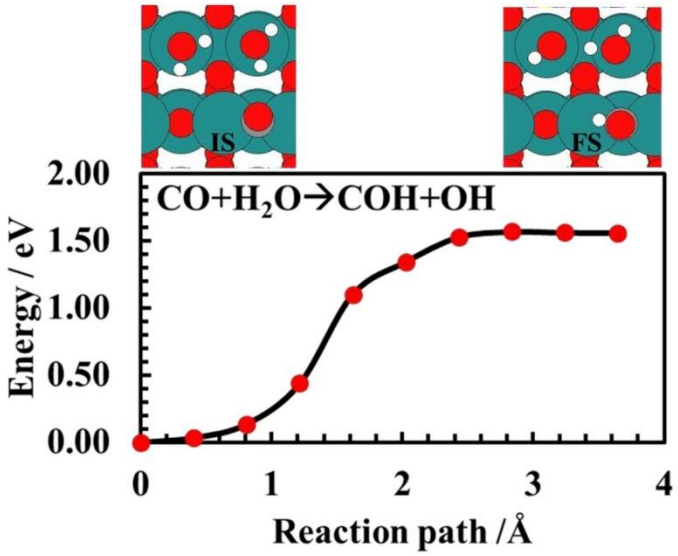

Figure S7. DFT calculated barrier for CO protonation to COH on RuO_2(110) surface. (IS) initial state and (FS) final state are shown on the top of the figure. The proton is transferred to CO from the adjacent H_2O molecule using a concerted Grotthuss mechanism of proton transfer from the next H_2O molecule on the CUS.

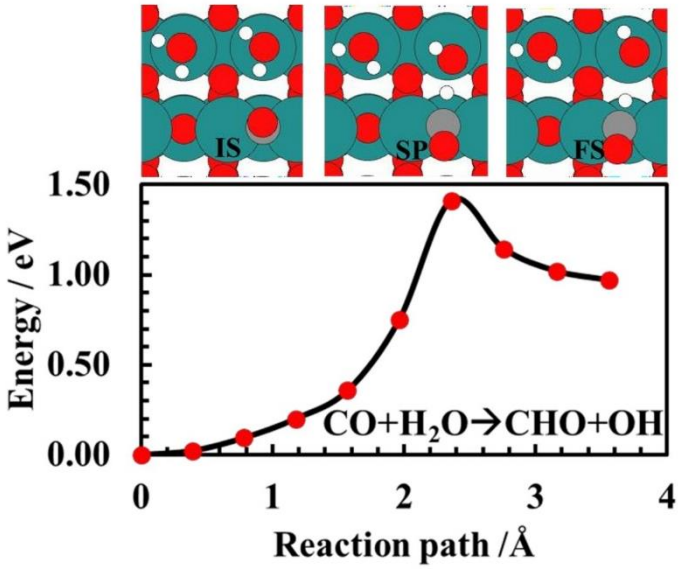

Figure S8. DFT calculated barrier for CO protonation to CHO on RuO_2(110) surface. (IS) initial state, (SP) saddle point and (FS) final state are shown on the top of the figure.

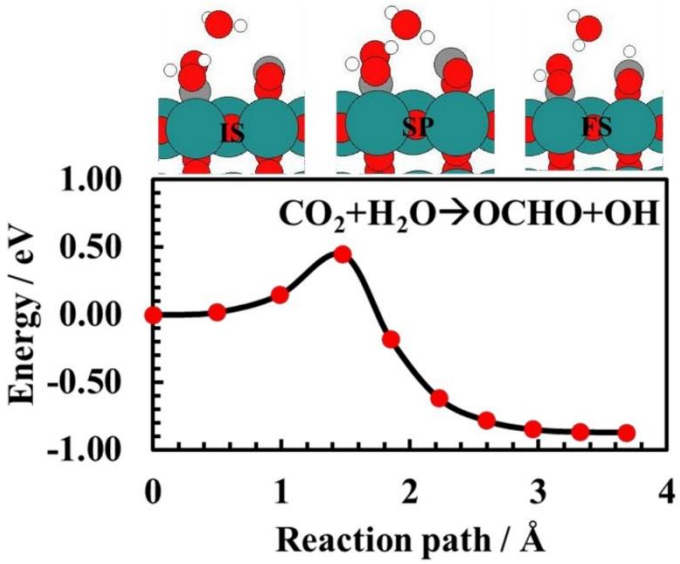

Figure S9. DFT calculated barrier for CO_2 protonation to $OCHO_b$ in a bidentate adsorption configuration on RuO_2(110) surface. (IS) initial state, (SP) saddle point and (FS) final state are shown on the top of the figure.

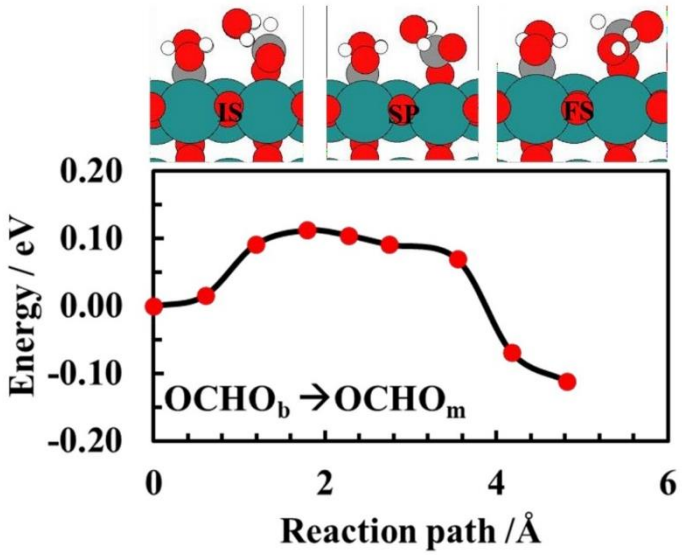

Figure S10. DFT calculated barrier for OCHO reconfiguration from bidentate configuration $OCHO_b$ to monodentate configuration $OCHO_m$ on RuO_2(110) surface. (IS) initial state, (SP) saddle point and (FS) final state are shown on the top of the figure.

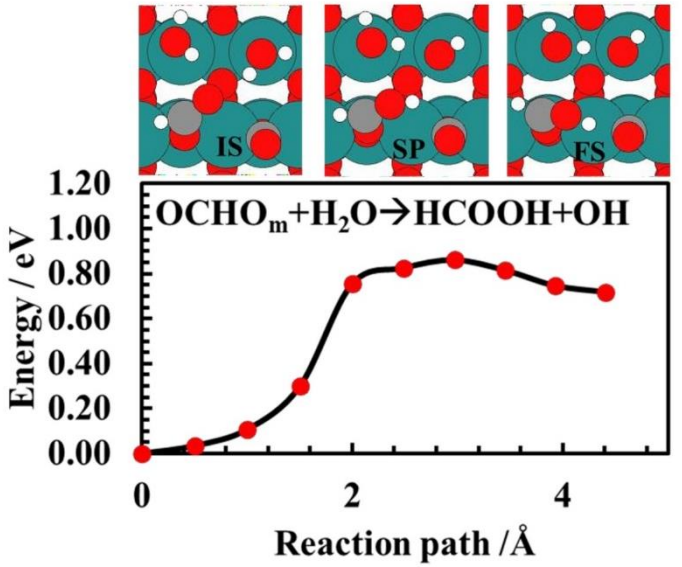

Figure S11. DFT calculated barrier for $OCHO_m$ protonation to HCOOH on RuO_2(110) surface. (IS) initial state, (SP) saddle point and (FS) final state are shown on the top of the figure.

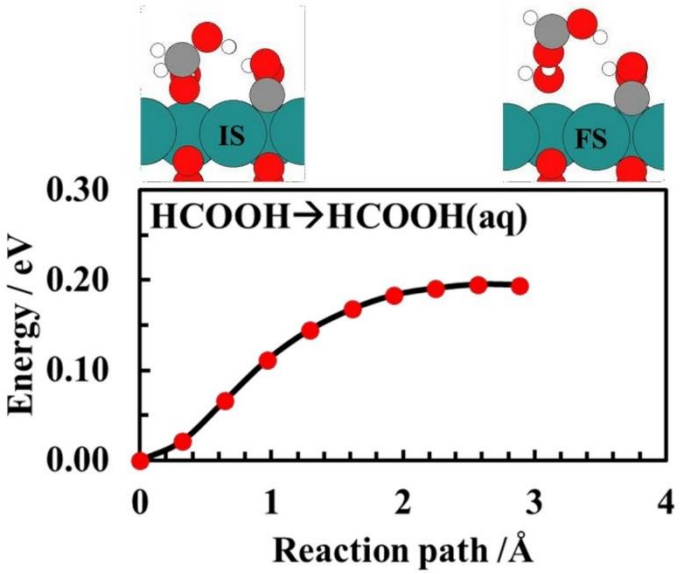

Figure S12. DFT calculated barrier for formic acid desorption on RuO_2(110) surface. (IS) initial state and (FS) final state are shown on the top of the figure.

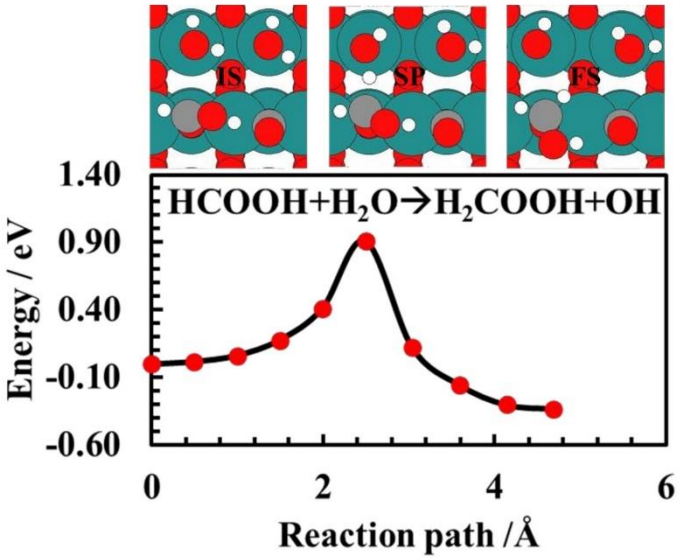

Figure S13. DFT calculated barrier for HCOOH protonation to H_2COOH on RuO_2(110) surface. (IS) initial state, (SP) saddle point and (FS) final state are shown on the top of the figure.

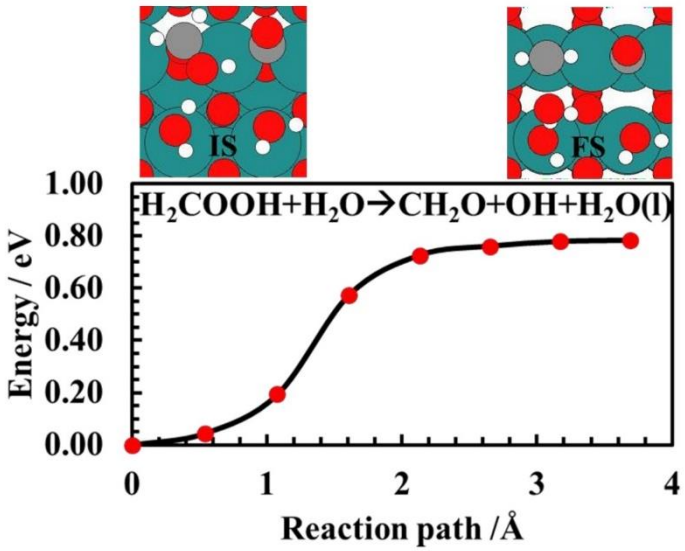

Figure S14. DFT calculated barrier for H_2COOH protonation to CH_2O and H_2O on $RuO_2(110)$ surface. (IS) initial state and (FS) final state are shown on the top of the figure.

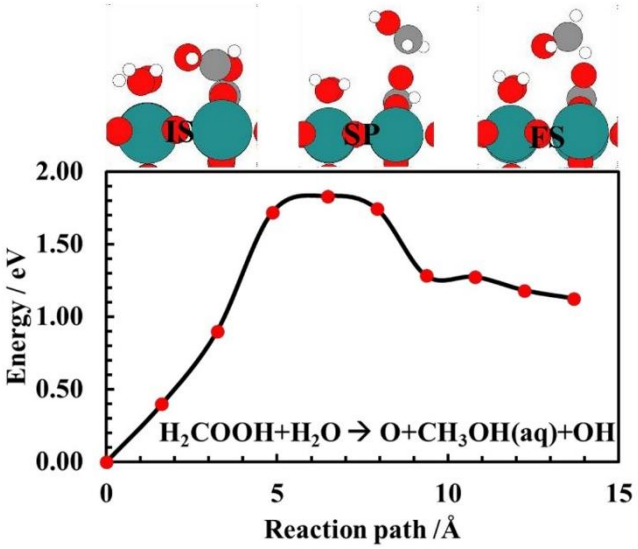

Figure S15. DFT calculated barrier for H_2COOH protonation to $H_2C(OH)_2$ on $RuO_2(110)$ surface. (IS) initial state, (SP) saddle point and (FS) final state are shown on the top of the figure.

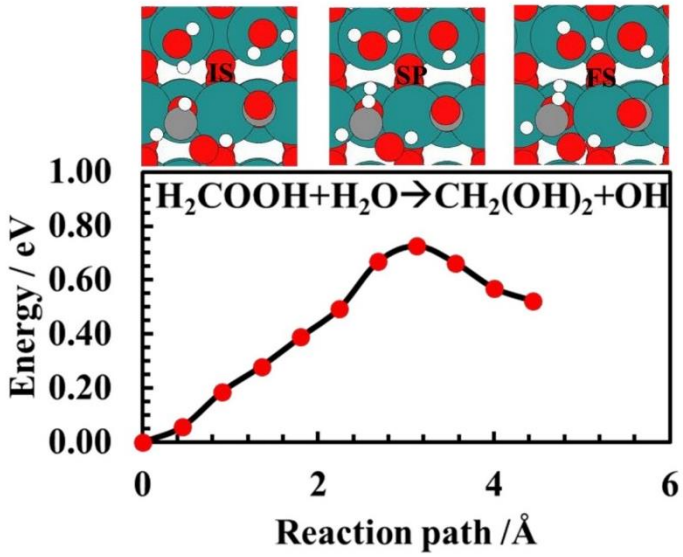

Figure S16. DFT calculated barrier for H_2COOH protonation to $H_2C(OH)_2$ on $RuO_2(110)$ surface. (IS) initial state, (SP) saddle point and (FS) final state are shown on the top of the figure.

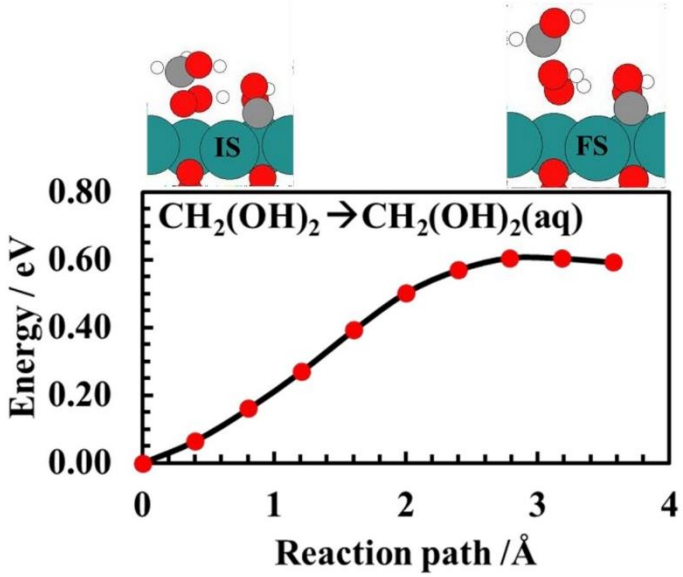

Figure S17. DFT calculated barrier for methanediol desorption on $RuO_2(110)$ surface. (IS) initial state and (FS) final state are shown on the top of the figure.

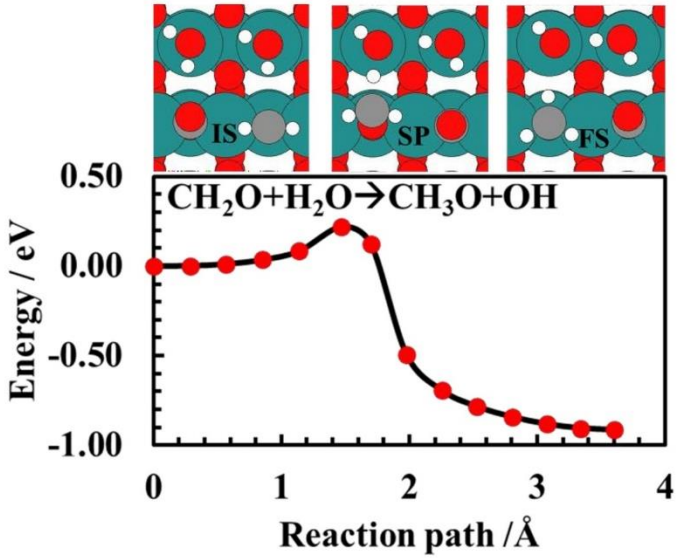

Figure S18. DFT calculated barrier for CH_2O protonation to CH_3O on $RuO_2(110)$ surface. (IS) initial state, (SP) saddle point and (FS) final state are shown on the top of the figure.

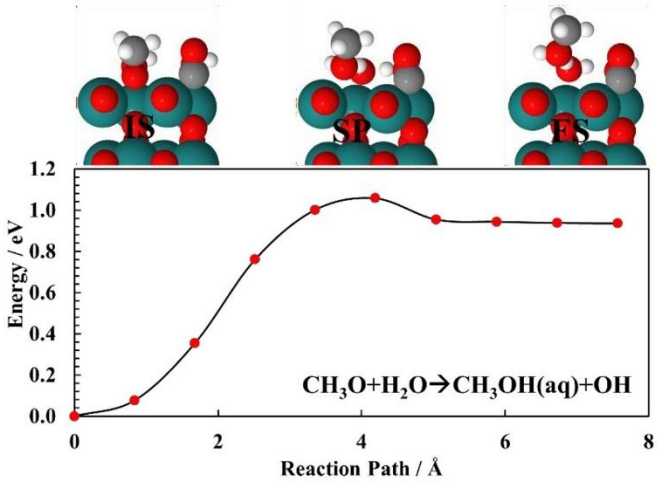

Figure S19. DFT calculated barrier for CH_3O protonation to $CH_3OH(aq)$ on $RuO_2(110)$ surface. (IS) initial state, (SP) saddle point and (FS) final state are shown on the top of the figure.

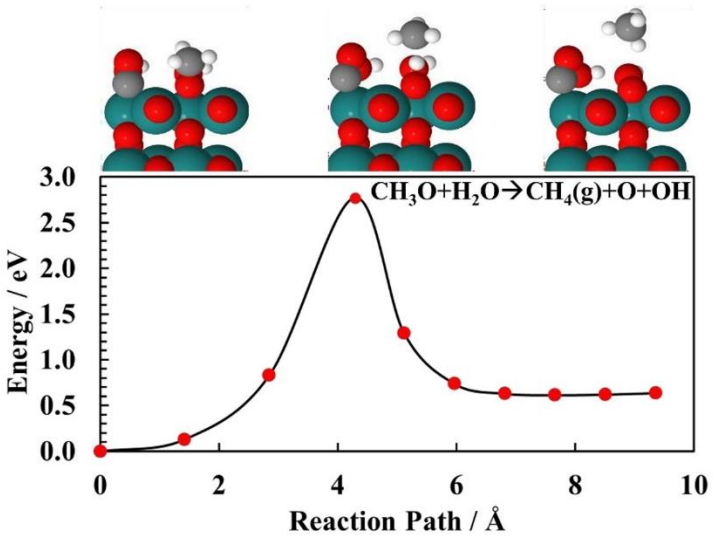

Figure S20. DFT calculated barrier for CH_3O protonation to CH_4(g) on RuO_2(110) surface. (IS) initial state, (SP) saddle point and (FS) final state are shown on the top of the figure.

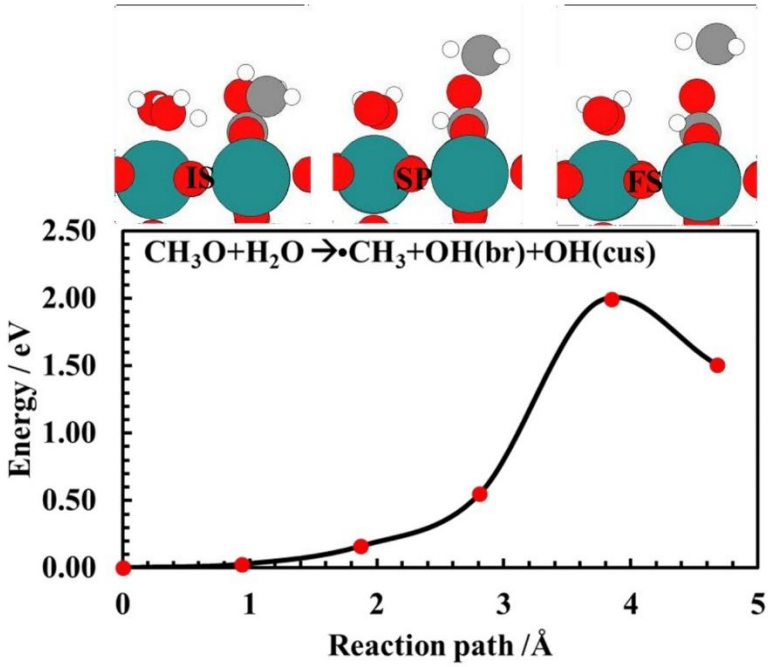

Figure S21. DFT calculated barrier for CH_3O protonation to •CH_3+OH(br)+OH(cus) on RuO_2(110) surface. (IS) initial state, (SP) saddle point and (FS) final state are shown on the top of the figure.

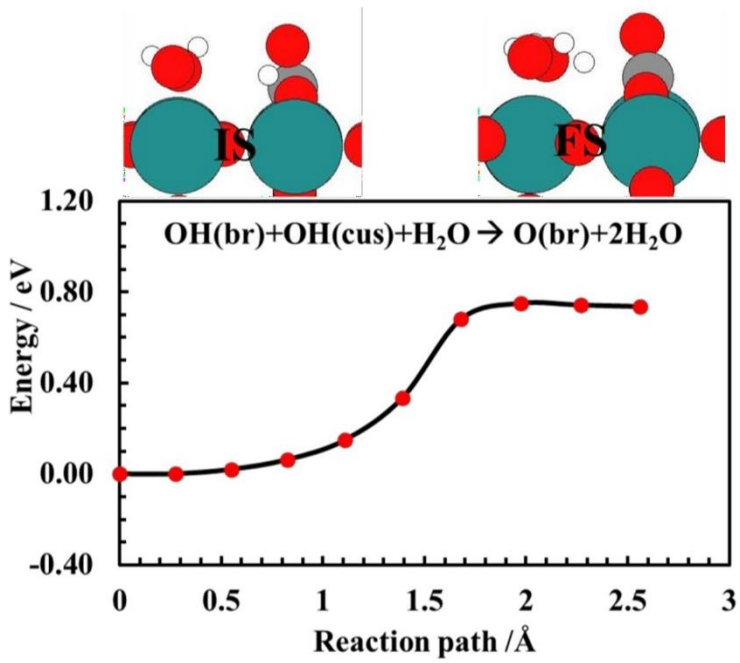

Figure S22. DFT calculated barrier for OH (br) reconfiguration to O(br) on RuO_2(110) surface. (IS) initial state, and (FS) final state are shown on the top of the figure.

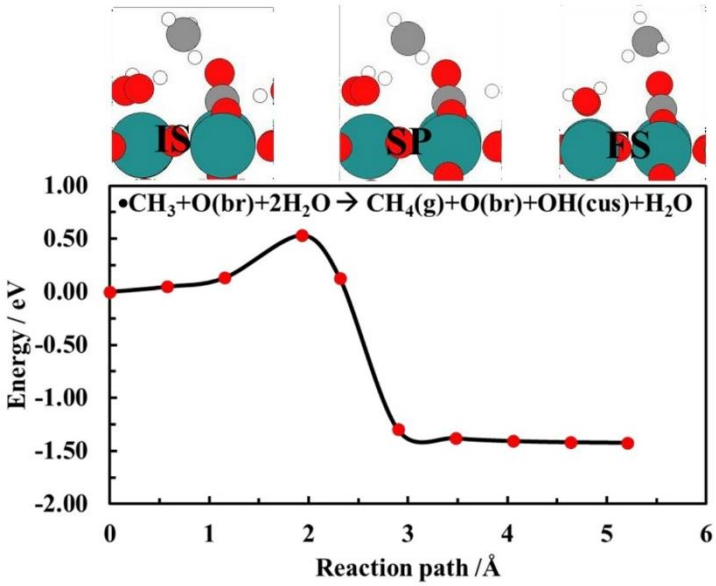

Figure S23. DFT calculated barrier for •CH_3 protonation to CH_4(g) on RuO_2(110) surface. (IS) initial state, (SP) saddle point and (FS) final state are shown on the top of the figure.

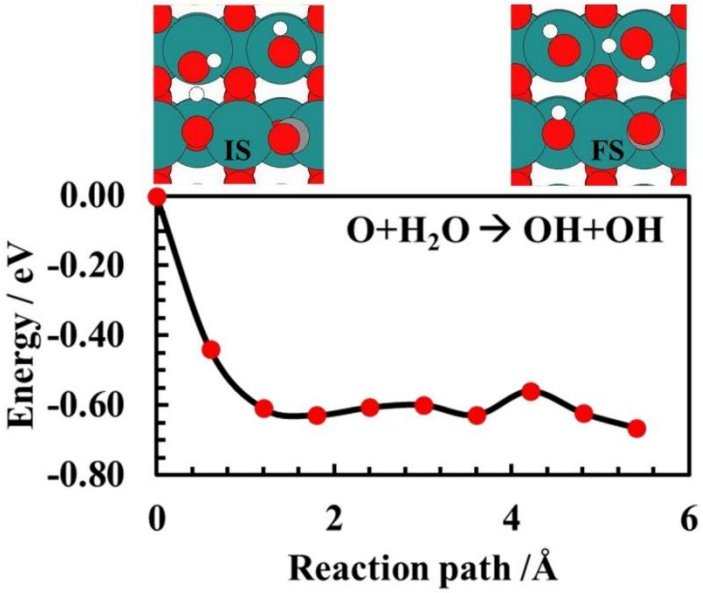

Figure S24. DFT calculations for O protonation to OH on RuO_2(110) surface. (IS) initial state and (FS) final state are shown on the top of the figure.

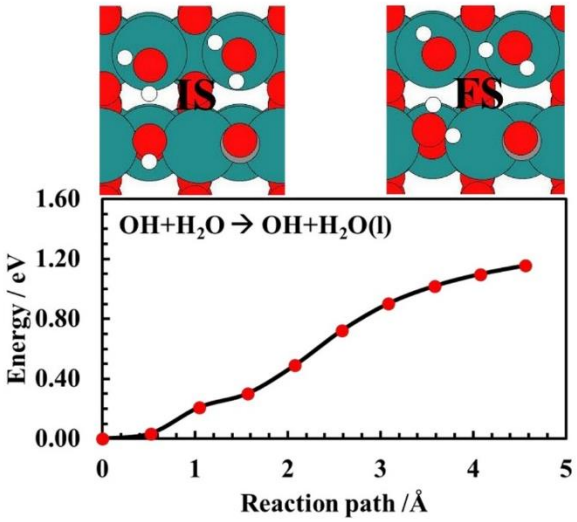

Figure S25. DFT calculations for OH protonation to H_2O(l) on RuO_2(110) surface. (IS) initial state and (FS) final state are shown on the top of the figure.

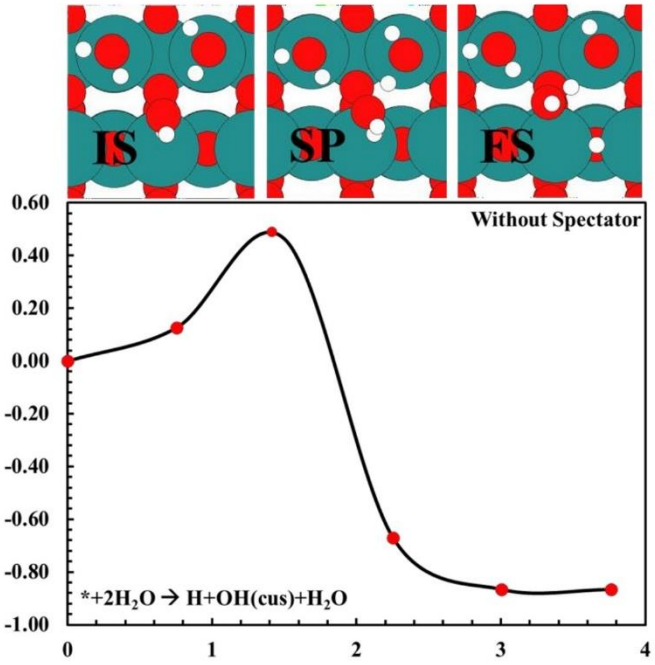

Figure S26. DFT calculations for transferring H to vacant bridge site on RuO_2(110) surface. (IS) initial state, (SP) saddle point and (FS) final state are shown on the top of the figure.

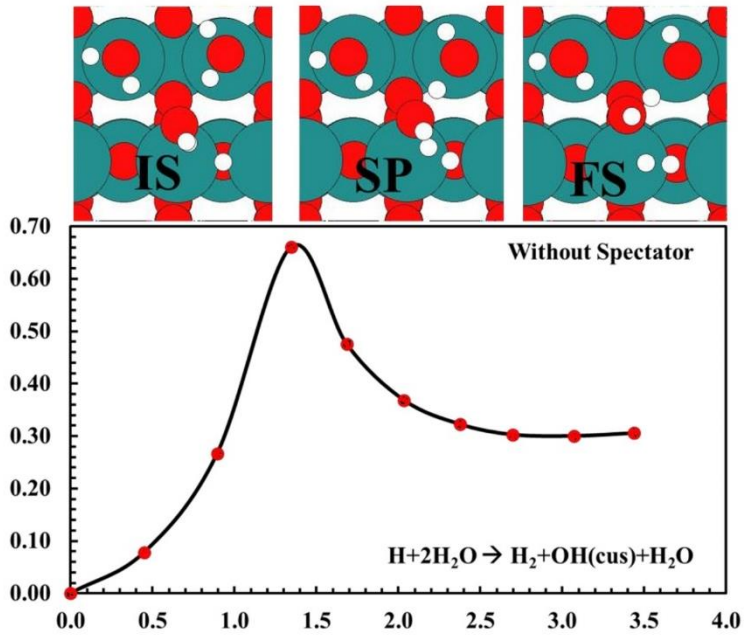

Figure S27. DFT calculations for H protonation to H_2 on RuO_2(110) surface. (IS) initial state, (SP) saddle point and (FS) final state are shown on the top of the figure.

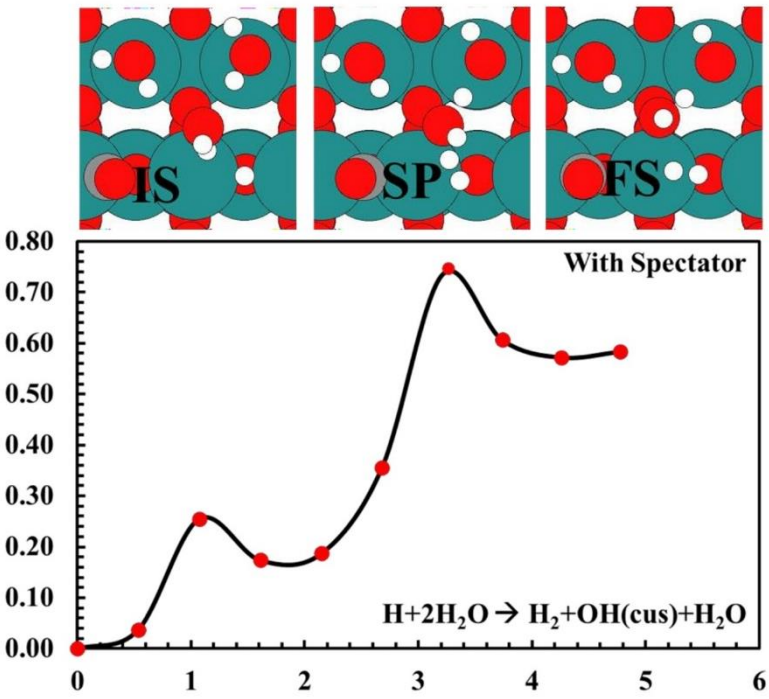

Figure S28. DFT calculations for H protonation to H_2 on RuO_2(110) surface where CO is spectator. (IS) initial state, (SP) saddle point and (FS) final state are shown on the top of the figure.

References

1 A. Bandi, *J. Electrochem. Soc., 1990, **137**, 2157.*

2 A. Bandi*, J. Electrochem. Soc., 1992, **139**, 1605.*

3 J. P. Popić, M. L. Avramov-Ivić and N. B. Vuković, *J. Electroanal. Chem*., 1997, **421**, 105–110.

4 N. Spataru, K. Tokuhiro, C. Terashima, T. N. Rao and A. Fujishima, *J. Appl. Electrochem*., 2003, **33**, 1205–1210.

5 Qu, J., Zhang, X., Wang, Y. & Xie, C. *Electrochim. Acta* **50**, 3576–3580 (2005).

6 S. Mezzavilla, Y. Katayama, R. Rao, J. Hwang, A. Regoutz, Y. Shao-Horn, I. Chorkendorff and I. E. L. Stephens, *J. Phys. Chem. C*, 2019, **123**, 17765–17773.

Paper III

Elucidating the Mechanism of Electrochemical N_2 Reduction at the Ru (0001) Electrode.

Tayyebi, E.; Abghoui, Y.; Skúlason, E.

ACS Catalysis 2019, 9, 11137-11145.

ACS Catalysis
DECEMBER 2019 VOLUME 9 NUMBER 12 PUBS.ACS.ORG/ACSCATALYSIS

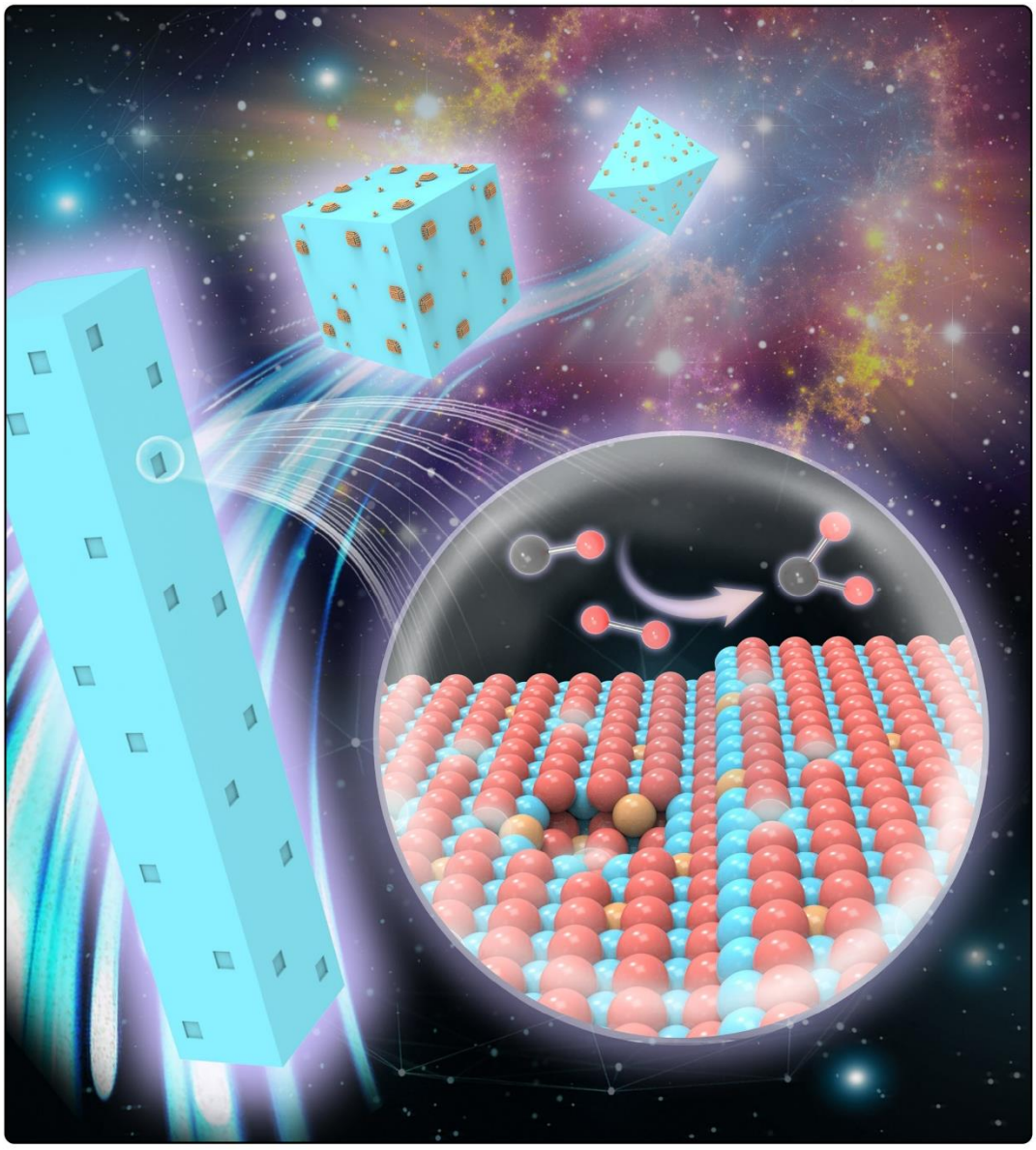

ACS Publications
Most Trusted. Most Cited. Most Read.
www.acs.org

ACS Catalysis

Research Article

Cite This: ACS Catal. 2019, 9, 11137−11145

pubs.acs.org/acscatalysis

Elucidating the Mechanism of Electrochemical N_2 Reduction at the Ru(0001) Electrode

Ebrahim Tayyebi,[†] Younes Abghoui,[†] and Egill Skúlason*[,†,‡]

[†]Science Institute and [‡]Faculty of Industrial Engineering, Mechanical Engineering and Computer Science, University of Iceland, VR-III, 107 Reykjavík, Iceland

Supporting Information

ABSTRACT: Density functional theory calculations are used to elucidate the mechanism of the nitrogen reduction reaction (NRR) in an electrochemical double layer on the Ru(0001) electrode, where all possible proton−electron transfer steps and N−N scission steps during NRR are considered. The model includes a negatively charged electrode and an explicit solvation bilayer of water including hydronium ion(s). We find that all elementary steps in which a proton is transferred to an adsorbate have small additional barriers on the order of 0.0−0.25 eV at an applied potential of −0.6 V versus the reversible hydrogen electrode. The first proton−electron transfer step where an end-on N_2 admolecule is reduced to NNH has a negligible additional barrier, whereas the thermochemical barrier is 0.8 eV at −0.6 V. This elementary reaction step is found to be rate-limiting and potential-limiting for NRR on Ru(0001). We predict that NRR will follow an associative distal pathway where after the third proton−electron transfer, the N−N bond is broken in N−NH_3, and the first ammonia molecule is released and a nitrogen atom occupies the surface. The nitrogen atom is reduced further to form the second ammonia molecule. The predicted reaction pathway here on Ru(0001), including all possible electrochemical and nonelectrochemical energy barriers, is the same as predicted from the thermochemistry of adsorbed intermediates. This indicates that the less-expensive thermochemical calculations and the computational hydrogen electrode can be used quite reliably to predict catalytic trends such as reaction pathways and overpotentials of NRR on at least the Ru electrode and presumably also on other types of catalysts.

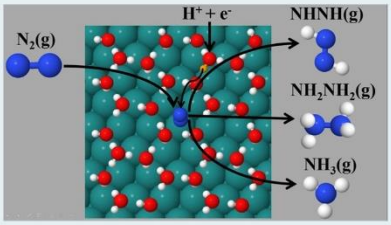

KEYWORDS: *nitrogen reduction reaction, electrocatalysis, density functional theory calculations, electrochemical solid−liquid interface, proton−electron transfer barriers*

INTRODUCTION

Ammonia (NH_3) is the key ingredient and the building block in production of nitrogen fertilizer on which the agriculture heavily relies for food supply. Because of the ever-expanding human population, it is an important challenge to develop a sustainable method to produce ammonia. The Nobel-prize winning Haber−Bosch process has been the dominant route for NH_3 synthesis since the early 20th century. In this process, nitrogen and hydrogen gas molecules are heated to 430 °C, pressurized to 150 bar, and passed over either Fe or Ru surface to catalyze the following overall reaction.[1]

$$N_2(g) + 3H_2(g) \rightarrow 2NH_3(g)$$

The $H_2(g)$ for this process is often produced from coal or natural gas, both of which lead to increased production of various greenhouse gases. A cleaner, but more expensive approach for the $H_2(g)$ supply for the process, is via water splitting. Today, the global ammonia production industry is responsible for at least 1% of global $CO_2(g)$ emissions, adding its share to global warming.

Electrochemical nitrogen reduction reaction (NRR) is an attractive approach that can provide a sustainable and zero-carbon footprint alternative for ammonia synthesis.[2−12] Recently, several density functional theory (DFT) calculations have predicted possibility of electrolytic ammonia production at ambient conditions. In this process, which is mimicking a biological version of ammonia production in nature,[13] NH_3 is produced from solvated protons, electrons, and atmospheric nitrogen at ambient conditions. Here, early transition metals (TMs),[14,15] TM nitrides,[16−23] TM oxides,[24] and TM sulphides[25] were predicted to be promising as electrocatalysts, selectively catalyzing the reduction of N_2 to NH_3. In several cases, these predictions have been confirmed experimentally, for example, for Ru,[26−31] NbO_2,[32] VN,[33−35] and MoN.[36]

All this theoretical work has been done in the realm of a simple thermochemical model (TCM), using the computational hydrogen electrode (CHE)[37] to implicitly account for the effect of the applied potential. Although TCM−CHE has been quite successful in the prediction of the overpotential needed for hydrogen evolution reaction (HER),[38] oxygen reduction reaction,[39] and CO_2 reduction reaction (CO_2RR),[40−44] the mechanism and product distribution as a functional of applied potential is not reproduced through this simple model when dealing with more complex reactions such as CO_2RR. Therefore, a more detailed model is needed; the

Received: September 11, 2019
Published: October 25, 2019

DOI: 10.1021/acscatal.9b03903
ACS Catal. 2019, 9, 11137−11145

electrochemical solid−liquid interface (ESLI) model,[45,46] but that model was developed first and applied to the HER and the hydrogen oxidation reaction.[47−49] The model is comprised of a solid surface, additional electrons in the metal, and solvated protons (or other cations) in the water above the surface. In this model, a water layer on the surface includes the effect of solvation, and the electric potential is applied and varied explicitly by varying the proton−electron concentration at the interface. In this setup, proton−electron transfer barriers can be calculated for elementary reaction steps to distinguish between possible branching paths and toward different products. This atomic scale model resembles schematic models developed for over 150 years, originated by Helmholtz[50] and improved later by Gouy, Chapman, Stern, and Grahame.[51−53] Using this simulation approach, it has been possible to identify the atomic scale mechanism for the electrochemical CO_2RR toward, for example, methane, methanol, ethylene, ethanol, CO, and H_2, on pure TM electrodes.[45,46] The results of the calculations are in excellent agreement with the trends in the experimental measured rates as a function of applied potentials for these products.

Recently, the first calculations of energy barriers for NRR have been reported on several metal electrodes.[15,54] There, only two elementary steps were included; NH to NH_2 and N_2 to N_2H, which are the two steps predicted to be potential limiting steps (PLSs) from the TCM−CHE approach.[14] The model of the "electrochemical interface" is very simplified in this work where only one H_2O molecule is included, and the so-called H-shuttle mechanism model is used, where the proton starts as an H adatom on the surface before it is transferred to the water molecule and then reacts with the adsorbate. The mechanism for a reduction process in the H-shuttle model therefore always starts with a Volmer oxidation step of a hydrogen adatom. Along this pathway, a hydronium ion is formed above the surface, but it is unsolvated because no other water molecules are used in the model. Kinetics of NRR on Fe surfaces have also been studied using the same model.[55] Elementary reaction barriers of NRR were calculated on two low index Fe surfaces. All the reported barriers are greater than 1 eV at 0 V versus the reversible hydrogen electrode (RHE), and it is concluded that high overpotentials are required for NRR on Fe surfaces.

The energy barriers for N−N scission for several intermediates during NRR have been calculated by Back and Jung on a B_5 step of Ru(0001).[15] The reported barrier for N_2(g) dissociative adsorption is around 1.7 eV while others have calculated that the barrier on the same type of step to be around 0.15−0.5 eV,[56−58] which is in good agreement with experimentally determined barrier of around 0.4 eV.[56] Furthermore, the energy barriers for the same reaction step on the flat Ru(0001) surface have been determined to be 1.3 eV experimentally and 1.9 eV using DFT calculations.[56]

Recently, Ru has been tested experimentally by two different research groups[30,31] where low reaction rates and current efficiency for NRR are reported in aqueous solutions, in agreement with previous DFT calculations.[14] Andersen et al. conducted NRR in 0.1 M KOH solution, and the ammonia concentration was reported to be around 10 ppb (around the detection limit) with a current efficiency slightly above 0.001% at −1.5 V versus RHE where almost all the current goes into H_2 formation.[30] Yao et al. did NRR in 0.1 M $HClO_4$ solution where the aim of that study was to gain insight into the NRR mechanism on a Ru catalyst by using powerful surface-enhanced infrared absorption spectroscopy (SEIRAS).[31] The applied potential was scanned between +0.4 and −0.4 V in order to adsorb N_2 on a clean surface at positive potentials, and then the protonation of N_2 can be measured as the potential is decreased to negative values. From the SEIRAS measurements, N_2, NNH, NHNH, and NH_2 were identified to be intermediates on the surface. These are, however, only a few intermediates out of all the possible intermediates that could be formed on the surface from one nitrogen molecule to two ammonia molecules. A few possible pathways are proposed by Yao and co-workers for the reduction of the NHNH intermediate to ammonia which will be discussed in the end of this article and compared with our results.

In this article, we use a novel theoretical model (the ESLI model) to gain further insight into the mechanism of the electrochemical NRR on Ru(0001). Since NRR is a complex reaction and there are experimental limitations to identify reaction intermediates, we use these calculations to determine the reaction mechanism, limiting steps, and optimal reaction pathway on the Ru(0001) electrode. DFT calculations are used to explicitly calculate the elementary reaction barriers of NRR on Ru(0001) at −0.6 V applied potential. Ru is chosen here because it is one of the metals having the lowest thermochemical barrier for NRR, despite the fact that HER will dominate on this surface.[14] In this work, we will therefore answer the question whether any substantial additional barriers exist for NRR on Ru, and if the thermodynamics of intermediates is sufficient in describing the reaction mechanism. Proton−electron transfer steps are calculated for all possible mechanisms and branching paths for NRR toward ammonia, hydrazine (N_2H_4), and diazene (N_2H_2) along with all possible nitrogen dissociation barriers along the reaction pathways.

Computational Details and Model System. We use periodic DFT calculations with a plane-wave expansion of the wave function and a projector-augmented wave representation of the ionic cores[59] to determine the atomic and electronic structure of the theoretical models. All the calculations have been done within the framework of the detailed ESLI model using the Vienna Ab initio Simulation Package (VASP).[60,61] In order to calculate activation energies for NRR toward different products on the Ru(0001) surface, the climbing image nudge elastic band (CI-NEB) method is used.[62,63] A plane wave basis set with a cutoff energy of 400 eV is used to expand the valence electron orbitals. The Monkhorst Pack grid is utilized in order to reduce the number of *k*-points, which are 4 × 4 × 1 in all cases. The atomic structure of the various reactants and products is found by minimizing the energy until atomic forces have dropped below 0.03 eV/Å.

A slab of three atomic layers represents the electrode with 12 metal atoms in each layer (3 × 4 unit cell), and the slabs are separated with at least 16 Å of vacuum. Atoms in the bottom two layers are fixed while those in the top layer along with the adsorbed intermediates are allowed to fully relax. It is noteworthy that we have seen modeling the slab with three atomic layers is a good compromise between accuracy and computational cost.[46,47,49] The dipole correction is used in all cases to decouple the electrostatic interaction between the periodically repeated slabs.

To estimate the free energy of an adsorbate for NRR, we use BEEF−vdW[64] functional because this functional includes nonlocal interactions that are the key to the behavior of molecular systems on the catalyst surface (especially when the

DOI: 10.1021/acscatal.9b03903
ACS Catal. 2019, 9, 11137−11145

admolecules become large), and they can be captured by special exchange correlation functional like vdW-DF2.[44,65]

In order to carry out activation energy calculation of different intermediates for NRR on Ru(0001) with an explicit description of water, we changed the functional to RPBE.[66] This allows to avoid the complexity arises from BEEF−vdW in NEB calculation because of the water bilayer in our system. Because of the presence of van der Waals forces, the BEEF−vdW functional will, in some cases, adsorb water strongly on the surface during proton−electron transfer reactions and subsequently results in some difficulties for NEB to converge on the minimum energy path (MEP).

The model system is the Ru(0001) surface with eight water molecules in the first bilayer. According to refs,[67,70] water adsorbs intact on the Ru(0001) surface in a metastable state at low temperature, and partially dissociated layers are formed at temperature above ∼150 K. The dissociation barrier on Ru(0001) has been reported to be around 0.5 eV,[71] which can be overcome by heating (above 140 K) or by electron exposure.[67−70] In this study, after relaxation of the water bilayer on Ru(0001) by BEEF−vdW, it is observed that two of the water molecules adsorb on the surface. This is in close agreement with the metastable state at low temperatures (Figure S1a,b). In order to mimic NRR condition and produce appropriate negative potential for NRR, we insert one proton/electron couple in the system. The calculated potential is estimated to be −0.58 V (or −0.6 V) in the presence of one extra proton in the water bilayer (Figure S2). By inserting this extra proton, the two adsorbed water molecules start to desorb, and after a complete relaxation, a water bilayer is formed on Ru(0001) (Figure S1c,d). Therefore, under reducing conditions (negatively applied potentials), a full bilayer of water on Ru(0001) is a represented model system rather than the partially dissociative water layer observed at UHV conditions or when no potential is applied. It has also been shown that one bilayer of water is enough to capture the most important feature of the ESLI (potential profile) and to capture the energetics correctly, where great comparison with experimental data was observed.[46,48,49,72]

In order to avoid complexities because of the presence of water in NEB calculation, energy barrier calculations for breaking $N_{2(g)}$ to 2N, NNH to NH + N, NHNH to NH + NH, NH_2NH to NH_2 + NH and NH_2NH_2 to NH_2 + NH_2 are done on bare Ru(0001) with the RPBE functional. A test calculation is done in the presence of the protonated water layer, and the difference between that and the bare Ru surface is around 0.1 eV, Figure S21. Because the presence of water does not play an important role in calculating barrier for nonelectrochemical steps, making such approximation will help to reduce computational cost and also remove difficulties arise from hydrogen bond networks in the water layer during optimization of the NEB calculations. Moreover, desorption and adsorption activation energies are also performed on bare Ru(0001) without the presence of water. In fact, we believe that a full bilayer of water is a very good model to generate required potentials for NRR on Ru(0001) and perform proton−electron transfer barriers but probably is not good enough to capture the whole hydrogen bond networks to explain adsorption and desorption barriers correctly. Therefore, the effect of stabilization of water on calculated barriers for desorption and adsorption might change the reported value here slightly.

Throughout this paper, subscripts H and V for intermediates specify its horizontal (H) or vertical (V) position on the surface, respectively. Here, an asterisk (*) is not used to show the state of intermediates on the surface, but (g), (aq), and (l) are used to show the state of reactants and products.

RESULTS

Reaction Pathways of NRR toward Ammonia, Hydrazine, and Diazene on Ru(0001). The simulated system and the atomic scale mechanism of the proton−electron transfer to $N_{2,V}$ to form NNH_V at −0.6 V versus the standard hydrogen electrode are shown in Figure 1, but that is

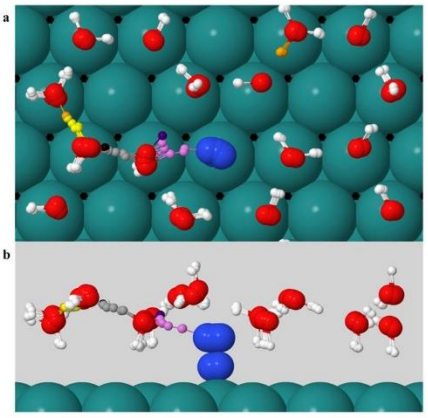

Figure 1. Proton−electron transfer to $N_{2,V}$ to form NNH_V in the optimal NRR mechanism on the Ru(0001) surface at −0.6 V. (a) Top view and (b) side view of six selected images along the MEP of a transferred proton to adsorbed N_2 starting with the initial state and ending at the final state. Protons are colored orange in their initial states and Ru atoms are green, while H_2O is colored red for oxygen and white for hydrogen. The transferred protons along the MEP have brighter colors (yellow, gray, and purple) while darker colors (orange, black, and dark purple) represent their initial states.

the slowest step in NRR on the Ru(0001), as discussed further below. The solvated proton is transferred via a Grotthuss-type mechanism toward the admolecule at the same time as an electron is transferred from the electrode. Similar calculations are done for all proton−electron transfer steps possible for NRR on Ru(0001) and are explained further below. For each intermediate, we check several possibilities of adsorption configuration, such as if the molecule is adsorbed vertically to the surface or horizontally, and we report the lowest energy configuration. After NNH, NH_xH_y is always located horizontally on the surface because it is the lowest energy configuration.

The calculated free energy diagram for NRR to form NH_3 on Ru(0001) at −0.6 V applied potential is shown in Figure 2. The free energy of the intermediates is calculated on a clean Ru(0001) surface, and the energy barriers for the proton−electron transfer steps are superimposed on the free energy landscape. The figure shows that the rate-limiting step (RLS) and the potential-limiting step (PLS) are the activation of $N_{2,V}$ to form NNH_V or around 0.8 eV at the −0.6 V applied potential. Therefore, our estimation of the overpotential needed to start the NRR on Ru(0001) is around −1.4 V in good comparison with the experimental value of −1.5 V.[30] Below, each step will be described in more details from the

DOI: 10.1021/acscatal.9b03903
ACS Catal. 2019, 9, 11137−11145

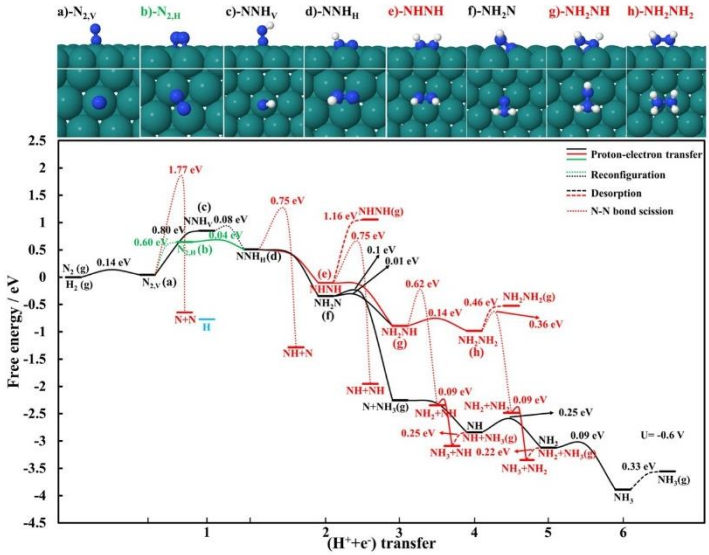

Figure 2. Calculated free energy and activation energy for NRR at a Ru(0001) electrode. Black curve: the optimal mechanism for ammonia formation when a potential of −0.6 V is applied. Red curve: pathways toward diazene and hydrazine and alternative pathways toward ammonia with a lower probability compared to the optimal pathway (black curve). The blue line denotes hydrogen-binding free energy, and the green curve shows a very low probability of the $N_{2,H}$ intermediate in NRR because it is a nonelectrochemical step. Solid lines represent proton−electron transfer barriers, dashed lines represent desorption or adsorption barriers of different products, and dotted lines are reconfiguration or N−N bond cleavage barriers. The insets in the top panel show selected intermediates that are labeled on the free energy diagram. The protonated water layer has been removed for clarity.

N_2(g) reactant toward ammonia, hydrazine, and diazene, with all possible branching paths. At the end, the possibilities to break the N−N bond during these pathways will be explored. The MEPs along with configurations of initial, transition, and final states for all possible intermediates related to NRR on Ru(0001) are presented in the Supporting Information (Figures S3−S24).

Adsorption of N_2(g) and Proton−Electron Transfer Barriers to NNH_H. The first step is to adsorb N_2(g) on the surface of Ru(0001) in the vertical position ($N_{2,V}$), and the calculated activation energy is 0.14 eV (Figures 2 and S3). The applied potential will only have a minor effect here, but because of polarization of the N_2 molecule, the adsorption energy will become slightly greater in a strong electric field.[73] Then, the next step is to either protonate $N_{2,V}$ directly to NNH_V (Figures 1 and S4) and then to rearrange it to NNH_H (Figure S5) or to first transform $N_{2,V}$ to $N_{2,H}$ position (Figure S6) and then transfer a proton and an electron to form NNH_H (Figure S7). Transforming $N_{2,V}$ to the $N_{2,H}$ position has a free energy change of 0.60 eV, which will be very slow at room temperature, and the applied potential will have negligible effects because this is a nonelectrochemical step. A direct proton−electron transfer to $N_{2,V}$ to form NNH_V has no additional energy barrier, but the free energy change of this step is 0.80 eV at −0.6 V and therefore this is the PLS for the overall NRR mechanism. Rearranging NNH_V to NNH_H has only a 0.08 eV barrier and will be easily overcome at room temperature. Therefore, our proposed pathway includes NNH_V because we expect that the barrier for proton−electron transfer to adsorbed $N_{2,V}$ will be easily surmountable at very negative potentials needed for NRR on Ru(0001) or −1.4 V (−0.6 V applied potential plus −0.80 V for the $N_{2,V}$ to NNH_V step). It should be noted that a potential of −0.6 V is found to be necessary to keep NNH vertically on the surface while a potential of 0 V results in that this intermediate is highly unstable and dissociates back to $N_{2,V}$, and the proton is transferred back to the water bilayer.

Proton−Electron Transfer Barriers of NNH_H to Either NHNH or NH_2N. The second proton−electron transfer step is protonation of NNH_H to either NHNH (Figure S8) or NH_2N (Figure S9). Figure 2 shows that the energy barriers for both steps are negligible, but the free energy of the NH_2N intermediate is slightly lower than of the NHNH intermediate (around 0.24 eV). Therefore, both species are predicted to be formed on the Ru(0001) surface, but a higher coverage of the NH_2N species is predicted than of the NHNH species. In the following, the pathways from NH_2N to ammonia will be described first, but thereafter, the pathways from NHNH to hydrazine and diazene will be described. However, it should be noted that a few possible branching paths between this reaction network are also considered.

Proton−Electron Transfer Barriers of NH_2N to Either NH_2NH or N + NH_3(g). Protonation of NH_2N may lead to adsorbed NH_2NH on the surface or N + NH_3(g). From the free energy diagram in Figure 2, it is shown that the N binding free energy and the free energy of released ammonia is considerably more negative than the NH_2NH binding free energy. Therefore, N + NH_3(g) is predicted to be a part of the lowest free energy pathway toward ammonia. The calculated activation energy shows a barrier of 0.01 eV for the NH_2N protonation toward NH_2NH, while a protonation of NH_2N to N + NH_3(g) has a barrier of 0.1 eV. Although this step is considerably more complicated (described further below and in Figure S10) than to form NH_2NH (Figure S11), the low activation energy will result in fast kinetics at room temperature (assuming a normal prefactor). The NH_2N

DOI: 10.1021/acscatal.9b03903
ACS Catal. 2019, 9, 11137−11145

intermediate is adsorbed in a horizontal position (NH_2N_H) on the surface but changes its adsorption configuration on the surface to a vertical position such that NH_2N_V is formed. Then, the $-NH_2$ group becomes highly exposed to the water bilayer, facilitating proton−electron transfer to the $-NH_2$ group which leads to a very low barrier for N−N bond cleavage of the NH_3N_V species, with an overall barrier of only 0.1 eV (see Figure S10). This is known as the associative distal pathway for NRR toward ammonia, where the same nitrogen atom in the N_2 molecule is reduced to ammonia before protonation of the other nitrogen takes place.

Proton−Electron Transfer Barriers of N to NH_3(g). The forth proton−electron transfer step in the NRR pathway on Ru(0001) is the protonation of N to NH (Figure S12). Figure 2 shows a negligible energy barrier for this reaction. Proton−electron transfer to form NH_2 (Figure S13) and NH_3 (Figure S14) adsorbed on the surface and finally to release NH_3(g) (Figure S15) from the surface have energy barriers of 0.25, 0.09, and 0.33 eV, respectively (black curve in Figure 2). It should be noted that the energy barrier for NH_3 to NH_3(g) has been calculated on a bare Ru(0001) surface without the presence of water. Therefore, the interaction from the surrounding water molecules with the adsorbed NH_3 intermediate, which desorbs from the surface, may slightly change the reported value here.

Proton−Electron Transfer Barriers of NHNH to NH_2NH_2. As discussed above, the second proton−electron transfer step may either lead to NH_2N or NHNH intermediates on the surface. The pathway from NH_2N to N + NH_3(g) and subsequent reduction of adsorbed N to the second NH_3(g) formation has been described above. Here below, we illustrate the pathway when NHNH is reduced further. The third proton−electron transfer in the NRR pathway from NHNH will lead to NH_2NH with a negligible energy barrier. Compared with the high barriers to break the N−N bond in NHNH of 0.75 eV (Figure S22) or to desorb NHNH as a diazene molecule of 1.16 eV (Figures 2 and S16), these calculations show that further proton−electron transfer is much more favorable. The next steps are either the protonation of NH_2NH to adsorbed NH_2NH_2 (Figure S17) or to break NH_2NH to NH + NH_2 on the surface (Figure S23), with energy barriers of 0.14 and 0.62 eV, respectively. Therefore, we predict that a further protonation of NHNH will lead to adsorbed NH_2NH_2 on the surface. This is known as the associative alternating pathway of NRR toward ammonia, and we have shown here that that pathway is less favorable than the associative distal pathway described above.

Energy Barriers of Reducing NH_2NH_2 to NH_2 + NH_3(g) or Desorption to NH_2NH_2(g). When the NH_2NH_2 intermediate is formed on the surface, it may either directly desorb from the surface as a hydrazine molecule or be protonated further in order to form ammonia. The calculated activation energy for desorbing NH_2NH_2 from the surface to NH_2NH_2(g) is 0.46 eV, which has been done on bare Ru(0001) without the presence of water (Figure S18). NH_2NH_2 may also split into NH_2 + NH_2 (Figure S24), followed by a proton−electron transfer to either of the NH_2 admolecules to yield ammonia. Activation energy for N−N bond scission in NH_2NH_2 is found to be 0.36 eV (Figure 2 and Table 1), and then, proton−electron transfer to form NH_2 + NH_3 is around 0.09 eV, and finally required barrier to release NH_3 from the surface is estimated to be 0.22 eV (Figure 2). Therefore, we find that the energy barrier toward ammonia via this pathway is 0.1 eV less than the barrier of desorbing hydrazine from the surface. As discussed above, the main NRR pathway to ammonia formation goes through the $NH_2N \rightarrow NH_3$(g) + N → $2NH_3$(g) route or the so-called associative distal pathway.

Table 1. DFT-Calculated Energy Barriers (E_a), Reaction Energies (ΔE), and Reaction Free Energies (ΔG) for N−N Bond Cleavage of N_2(g) and of Adsorbed $N_{2,H}$, NNH_H, NHNH, NH_2NH, and NH_2NH_2 in NRR at a Ru(0001) Electrode[a]

dissociation reaction	E_a/eV	ΔE/eV	ΔG/eV	N−N bond distance/Å
N_2(g) → 2N	1.81	−1.16	−0.60	1.12
$N_{2,H}$ → 2N	1.17	−1.35	−1.25	1.22
NNH_H → NH + N	0.75	−1.80	−1.80	1.35
NHNH → NH + NH	0.75	−1.82	−1.85	1.39
NH_2NH → NH_2 + NH	0.62	−1.37	−1.45	1.46
NH_2NH_2 → NH_2 + NH_2	0.36	−1.42	−1.50	1.47

[a]The N−N bond distance at the initial state is given.

N−N Bond Cleavage of Intermediates in NRR. Above, we have described all the possible proton−electron transfer steps for NRR toward ammonia, hydrazine, and diazene. However, along this pathway, several possible N−N bond scissions are possible. DFT-calculated barriers for N−N bond cleavage of several species derived during the NRR on Ru(0001) are shown in Table 1. This illustrates relatively high barriers for breaking N_2, NNH, NHNH, and NH_2NH on the surface, or 1.81−0.62 eV, compared to the low additional barriers found for the proton−electron transfer steps, or 0.0−0.25 eV (see further Figures 2 and S18−S24). The reaction energies and reaction free energies of the N−N dissociation are exergonic in all cases. The N−N bond distance increases with further hydrogenation as the bond goes from being a triple bond to a double bond and to a single bond.

Table 1 shows that the energy barrier for N−N bond cleavage in NH_2NH_2 is considerably lower than for the other NH_xNH_y species (where $x + y$ can be 0, 1, 2 or 3). In the case of NH_2NH_2, the N−N bond cleavage barrier is only 0.36 eV, or 0.26 eV lower than breaking the N−N bond of NH_2NH, which is 0.62 eV. This shows higher possibility for breaking the N−N bond in NH_2NH_2 than for any other NH_xNH_y intermediate where adsorbed NH_x and NH_y species are formed. As shown above, however, breaking the N−N bond of the $N-NH_3$ intermediate and forming adsorbed N + NH_3(g) are negligible. The barrier to break the N−N bond in NH_2NH_2 (0.36 eV) compared to desorbing NH_2NH_2(g) from the surface (0.46 eV) shows that the formation of hydrazine on Ru(0001) is slightly less likely than forming ammonia via this route, but the primary route to form ammonia is shown in the black curve in Figure 2.

Overall, in the present study, we predict that NRR on Ru(0001) will follow an associative distal pathway where the second proton−electron transfer step leads to NH_2N in a horizontal position on the surface. Then, the NH_2N species transfers from a horizontal position to a vertical position where the third proton−electron transfer occurs to form NNH_3 species, resulting in considerably weakening of the N−N bond, and subsequently ammonia is released. The mechanism continues by transferring protons and electrons to the

DOI: 10.1021/acscatal.9b03903
ACS Catal. 2019, 9, 11137−11145

adsorbed N on the surface until the second ammonia is released.

DISCUSSIONS

An atomistic model of the ESLI is chosen here to obtain the kinetics of NRR on Ru(0001) because this model has been successful in capturing the experimental trends of CO_2RR[46] and HER[49] on TM surfaces. In the case of CO_2RR, the TCM−CHE approach does not predict the correct reaction pathway toward the major product methane on a copper surface. However, here we find that the detailed kinetic study using the ESLI model predicts quiet similar reaction pathway as previously reported using the TCM−CHE model.[14] The reason for this is presumably because the overall NRR is simpler than CO_2RR, with fewer possible branching paths and fewer possibilities of product formation. Therefore, this work indicates that the simple TCM−CHE model can be used quite reliable to predict catalytic trends such as reaction pathways and overpotentials of NRR.

In this study, the effect of hydrogen coverage on activation energies is not taken into account because the main focus of this work is to find the reaction pathway for NRR on Ru(0001). In fact, the hydrogen-binding free energy is used as an estimation of hydrogen evolution activity. Comparing hydrogen evolution activity with NRR activity shows that Ru(0001) is more selective toward HER than NRR (see Figure 2).

Recently, Rostamikia et al[54] used DFT calculations and the H-shuttle model (an interface model with only one water molecule) to evaluate nonelectrochemical barriers for NRR on late TM surfaces. A symmetry factor of 0.5 was then used to get the effect of applied potential. In their work, they only considered a few elementary steps (N_2 dissociation, N_2 hydrogenation to NNH and NH hydrogenation to NH_2), the ones that have been predicted to be limiting by thermodynamics.[14] In the case of Ru(0001), Rostamikia et al. only calculated the activation energy for hydrogenation of adsorbed $N_{2,H}$ to NNH_H although simple thermochemical studies[14] and also our detailed work here show that $N_{2,V}$ is about 0.60 eV more stable than $N_{2,H}$ (see Figures 2 and S6). Therefore, the elementary step considered on Ru(0001) by Rostamikia et al. is not a part of the optimal mechanism presented here. We find that the first proton−electron transfer step starts from $N_{2,V}$ to form NNH_V and this is our predicted RLS and PLS, with an overpotential of −1.4 V.

Yao et al.[31] have recently conducted experiments for NRR on a Ru surface in order to identify possible reaction intermediates using SEIRAS measurements. They apply potentials up to +0.4 V in order to adsorb the N_2 molecule because there the hydrogen coverage is neglectable. A bipolar band assigned to N═N stretch appeared at around +0.2 V and did not increase much down to 0 V. Then they decrease the potential further down and are able to reduce the N_2 admolecule to N_2H and NHNH at potentials of only −0.2 and −0.4 V, where the intensity of the band increased significantly as the potential became more negative, suggesting that higher and higher coverage of N_2H_x species are being formed. According to our results on Ru(0001), a minimum potential of −1.4 V is needed to reduce N_2 to N_2H. That is also seen in the experiments by Andersen et al. where −1.5 V potential was needed to get any measurable amount of ammonia.[30] However, the B_5 steps on Ru(0001) which are predicted to have the same reaction pathway as the Ru(0001) surface have an overpotential of around −0.4 V[14] which explains the low overpotentials reported in the SEIRAS measurements.[31]

An N═N double bond is detected in the SEIRAS measurements and they conclude it is related to the N_2, N_2H, and NHNH species on the surface. Besides these intermediates, the NH_2 species is detected via an N−H stretch. A few possible pathways are suggested that could lead to ammonia formation: (i) NHNH desorption (leading to decomposition to NH_3 and N_2 in the solution), (ii) NHNH dissociation resulting in adsorbed NH and then further protonation to NH_2 species, or (iii) protonation of NHNH further to form adsorbed N_2H_4 species. They concluded that (i) would be the preferred pathway for ammonia formation because they claim that the NHNH desorption barrier is lower than the barriers involved in (ii) and (iii). This conclusion seems to arise from the fact that they did not measure any N_2H_3 or N_2H_4 intermediates on the Ru surface. In our study, however, we show that (i) is the least possible pathway because the free energy barrier is around 1.16 eV to desorb diazene from the surface (see Figure S16), (ii) is very slow because the energy barrier to dissociate NHNH is around 0.75 eV, but (iii) has a neglectable energy barrier for protonation of NHNH to NH_2NH and a barrier of 0.14 eV to protonate it further to NH_2NH_2 adsorbed on the surface. These intermediates (red curves in Figure 2) are, however, not predicted to belong to the optimal reaction pathway in our calculations (black curve in Figure 2). Reduction of NNH to either NHNH and NH_2N has neglectable barriers in both cases, but the NH_2N intermediate is more stable than the NHNH intermediate. Therefore, we predict that both the NHNH and NH_2N intermediate can be formed on the surface, but the NH_2N intermediate belongs to the optimal reaction mechanism, leading to N, NH, NH_2, and NH_3 intermediates.

A possible reason why NH_2N was not detected in the SEIRAS experiments is presumably because that intermediate live shortly on the surface, but the barrier to reduce it further is very small, and the step toward N + NH_3(g) is very exergonic. It should be noted that the N−H stretch and bending in NH, NH_2, and NH_3 are very similar, according to our calculations, and therefore, the wavenumber reported in the SEIRAS measurements can arise because of all these intermediates on the surface. Finally, the reason for not detecting the N adatom (as in our proposed mechanism) is because the highest wavenumber for N on Ru is around 530 cm^{-1}, according to our calculations and this is outside the window of the SEIRAS experiments (1250−4000 cm^{-1}). Our results are, therefore, in perfect agreement with the intermediates measured in the SEIRAS experiments (N_2, NNH, NHNH, and NH_2), which further supports the predicting power of the calculations presented here. Our results furthermore predict intermediates not detected in the SEIRAS measurements and propose a mechanism entirely different from the ones suggested by Yao et al.[31]

A number of experimental studies have been carried out recently to investigate the NNR to ammonia on surfaces which are composed of either Ru nanoparticles or single Ru atoms on nitrogen-doped carbon or zirconium oxide.[26−29] In all cases, they performed both experiments and DFT calculations and reached to the conclusion that Ru is active for NRR at low applied potentials. To further validate the experimental results, a series of DFT calculation were done to better elucidate the reaction mechanisms for NRR, and in all cases, they got very

DOI: 10.1021/acscatal.9b03903
ACS Catal. 2019, 9, 11137−11145

consistent results with the experiments without doing more sophisticated calculations like what we have done here. In fact, these works highly support the importance of our conclusions here in a way that after doing these very high-level calculations, we showed the CHE and the less expensive thermochemical model can be used quite reliably to predict catalytic trends such as reaction pathways and overpotentials of NRR on Ru. In the case of CO_2RR,[46] the situation is different, and it has been found that in order to predict catalytic trends, it is really necessary to perform more advanced calculations like what we did here. Moreover, in all of these experimental works, the studied systems were something beyond the flat Ru(0001) surface. However, a recently published paper by Andersen et al.,[30] which we believe is the most reliable one, shows the required overpotential for NRR on the polycrystalline Ru electrode is −1.5 V, which is in a very good agreement with our calculated overpotential here (−1.4 V). Finally, in all of the aforementioned papers, the proposed pathways for NRR on Ru are highly different from the concluded results from Yao et al.[31]

■ CONCLUSIONS

In this article, we use the ESLI model to gain further insight into reaction mechanism for electrochemical NRR on the Ru(0001) electrode. In this regard, different pathways toward ammonia are investigated. We find that the initial activation of N_2(g) to be the limiting factor on Ru(0001). The first step is to adsorb N_2(g) on the surface of Ru(0001) in a vertical position ($N_{2,V}$) whereas the next steps are to either protonate $N_{2,V}$ to NNH_V and then transform NNH_V to NNH_H or to first transform $N_{2,V}$ to $N_{2,H}$ position (a nonelectrochemical step) and then protonate $N_{2,H}$ to NNH_H. The calculated energy barrier for the nonelectrochemical step of transforming $N_{2,V}$ to $N_{2,H}$ is 0.6 eV, which will be difficult to be overcome at room temperature, and therefore the $N_{2,H}$ species is not predicted to be an intermediate of the NRR mechanism on Ru(0001). Protonation of $N_{2,V}$ to NNH_V has no additional energy barrier and it is totally limited by the thermodynamics. This is the RLS of NRR on Ru(0001).The calculated free energy change for this electrochemical step is 0.8 eV at −0.6 V, which will only be surmounted at very negative potentials, or around −1.4 V. Therefore, we predict that the protonation of $N_{2,V}$ to NNH_V, which then transforms to NNH_H, to be a part of the main pathway of NRR toward ammonia on Ru(0001).

The optimal mechanism of NRR toward ammonia on Ru(0001) follows an associative distal pathway where the third proton−electron transfer step results in an $N-NH_3$ intermediate. The dissociation of the N−N bond will then happen spontaneously, releasing the first NH_3 molecule and leaving N adsorbed on the surface. The activation barrier for this reaction is calculated to be 0.1 eV, which will be easily overcome at room temperature. The proton−electron transfer steps to reduce the adsorbed N atom to ammonia are calculated to be low (0.0−0.33 eV).

In addition to forming ammonia during NRR on Ru(0001), the side product formation of hydrazine and diazene is also calculated. The desorption free energy barrier of diazene is calculated to be 1.16 eV, but protonation of NHNH further has negligible barriers. We find that protonation of N_2 to hydrazine proceeds via NNH_V, NHNH, NH_2NH, and NH_2NH_2. The activation energy for dissociating NH_2NH_2 to NH_2 + NH_2 is calculated to be 0.36 eV, whereas the activation energy of desorbing NH_2NH_2 to NH_2NH_2(g) is calculated to be 0.46 eV, which indicates a lower chance of forming hydrazine than ammonia in NRR on Ru(0001), in agreement with experimental literature.

■ ASSOCIATED CONTENT

Supporting Information

The Supporting Information is available free of charge on the ACS Publications website at DOI: 10.1021/acscatal.9b03903.

Additional figures showing the water bilayer (with and without a solvated proton) on the Ru(0001) surface, the integral free energy of the protons in the double layer to determine the applied potential in the system, and the MEPs for each elementary reaction step in the entire NRR network including proton−electron transfer steps, reconfiguration steps, adsorption/desorption steps, and N−N bond scission steps (PDF)

■ AUTHOR INFORMATION

Corresponding Author

*E-mail: egillsk@hi.is.

ORCID

Egill Skúlason: 0000-0002-0724-680X

Notes

The authors declare no competing financial interest.

■ ACKNOWLEDGMENTS

This work was supported by the Icelandic Research Fund (grant nos. 196437-051, 185051-051, 152619-051) and the Research Fund of the University of Iceland.

■ REFERENCES

(1) Jennings, J. R. *Catalytic Ammonia Synthesis: Fundamentals and Practice*; Plenum Press: New York, 1991.

(2) Amar, I. A.; Lan, R.; Petit, C. T. G.; Tao, S. Solid-State Electrochemical Synthesis of Ammonia: A Review. *J. Solid State Electrochem.* **2011**, *15*, 1845−1860.

(3) Giddey, S.; Badwal, S. P. S.; Kulkarni, A. Review of Electrochemical Ammonia Production Technologies and Materials. *Int. J. Hydrogen Energy* **2013**, *38*, 14576−14594.

(4) Shipman, M. A.; Symes, M. D. Recent Progress towards the Electrosynthesis of Ammonia from Sustainable Resources. *Catal. Today* **2017**, *286*, 57−68.

(5) Kyriakou, V.; Garagounis, I.; Vasileiou, E.; Vourros, A.; Stoukides, M. Progress in the Electrochemical Synthesis of Ammonia. *Catal. Today* **2017**, *286*, 2−13.

(6) Van Der Ham, C. J. M.; Koper, M. T. M.; Hetterscheid, D. G. H. Challenges in Reduction of Dinitrogen by Proton and Electron Transfer. *Chem. Soc. Rev.* **2014**, *43*, 5183−5191.

(7) Medford, A. J.; Hatzell, M. C. Photon-Driven Nitrogen Fixation: Current Progress, Thermodynamic Considerations, and Future Outlook. *ACS Catal.* **2017**, *7*, 2624−2643.

(8) Cui, X.; Tang, C.; Zhang, Q. A Review of Electrocatalytic Reduction of Dinitrogen to Ammonia under Ambient Conditions. *Adv. Energy Mater.* **2018**, *8*, 1800369.

(9) Yan, Z.; Ji, M.; Xia, J.; Zhu, H. Recent Advanced Materials for Electrochemical and Photoelectrochemical Synthesis of Ammonia from Dinitrogen: One Step Closer to a Sustainable Energy Future. *Adv. Energy Mater.* **2019**, 1902020.

(10) Zhao, R.; Xie, H.; Chang, L.; Zhang, X.; Zhu, X.; Tong, X.; Wang, T.; Luo, Y.; Wei, P.; et al. Recent Progress in the Electrochemical Ammonia Synthesis under Ambient Conditions. *EnergyChem.* **2019**, *1*, 100011.

(11) Comer, B. M.; Fuentes, P.; Dimkpa, C. O.; Liu, Y. H.; Fernandez, C. A.; Arora, P.; Realff, M.; Singh, U.; Hatzell, M. C.;

DOI: 10.1021/acscatal.9b03903
ACS Catal. 2019, 9, 11137−11145

Medford, A. J. Prospects and Challenges for Solar Fertilizers. *Joule* **2019**, *3*, 1578−1605.
(12) Tang, C.; Qiao, S. Z. How to Explore Ambient Electrocatalytic Nitrogen Reduction Reliably and Insightfully. *Chem. Soc. Rev.* **2019**, *48*, 3166−3180.
(13) Stryer, L. *Biochemistry*; WH Freeman, 2010.
(14) Skúlason, E.; Bligaard, T.; Gudmundsdóttir, S.; Studt, F.; Rossmeisl, J.; Abild-Pedersen, F.; Vegge, T.; Jónsson, H.; Nørskov, J. K. A Theoretical Evaluation of Possible Transition Metal Electro-Catalysts for N_2 reduction. *Phys. Chem. Chem. Phys.* **2012**, *14*, 1235−1245.
(15) Back, S.; Jung, Y. On the Mechanism of Electrochemical Ammonia Synthesis on the Ru Catalyst. *Phys. Chem. Chem. Phys.* **2016**, *18*, 9161−9166.
(16) Abghoui, Y.; Garden, A. L.; Hlynsson, V. F.; Björgvinsdóttir, S.; Ólafsdóttir, H.; Skúlason, E. Enabling Electrochemical Reduction of Nitrogen to Ammonia at Ambient Conditions through Rational Catalyst Design. *Phys. Chem. Chem. Phys.* **2015**, *17*, 4909−4918.
(17) Abghoui, Y.; Garden, A. L.; Howalt, J. G.; Vegge, T.; Skúlason, E. Electroreduction of N_2 to Ammonia at Ambient Conditions on Mononitrides of Zr, Nb, Cr, and V: A DFT Guide for Experiments. *ACS Catal.* **2016**, *6*, 635−646.
(18) Howalt, J. G.; Vegge, T. Electrochemical Ammonia Production on Molybdenum Nitride Nanoclusters. *Phys. Chem. Chem. Phys.* **2013**, *15*, 20957.
(19) Michalsky, R.; Pfromm, P. H.; Steinfeld, A. Rational Design of Metal Nitride Redox Materials for Solar-Driven Ammonia Synthesis. *Interface Focus* **2015**, *5*, 20140084.
(20) Zeinalipour-Yazdi, C. D.; Hargreaves, J. S. J.; Catlow, C. R. A. Nitrogen Activation in a Mars−van Krevelen Mechanism for Ammonia Synthesis on Co_3Mo_3N. *J. Phys. Chem. C* **2015**, *119*, 28368−28376.
(21) Sangiovanni, D. G.; Mei, A. B.; Hultman, L.; Chirita, V.; Petrov, I.; Greene, J. E. Ab Initio Molecular Dynamics Simulations of Nitrogen/VN(001) Surface Reactions: Vacancy-Catalyzed N_2 Dissociative Chemisorption, N Adatom Migration, and N_2 Desorption. *J. Phys. Chem. C* **2016**, *120*, 12503−12516.
(22) Li, Q.; He, L.; Sun, C.; Zhang, X. Computational Study of MoN_2 Monolayer as Electrochemical Catalysts for Nitrogen Reduction. *J. Phys. Chem. C* **2017**, *121*, 27563−27568.
(23) Zeinalipour-Yazdi, C. D.; Hargreaves, J. S. J.; Catlow, C. R. A. Low-T Mechanisms of Ammonia Synthesis on Co_3Mo_3N. *J. Phys. Chem. C* **2018**, *122*, 6078−6082.
(24) Höskuldsson, Á. B.; Abghoui, Y.; Gunnarsdóttir, A. B.; Skúlason, E. Computational Screening of Rutile Oxides for Electrochemical Ammonia Formation. *ACS Sustain. Chem. Eng.* **2017**, *5*, 10327−10333.
(25) Abghoui, Y.; Sigtryggsson, S. B.; Skúlason, E. Biomimetic Nitrogen Fixation Catalyzed by Transition Metal Sulfide Surfaces in an Electrolytic Cell. *ChemSusChem* **2019**, *12*, 4265−4273.
(26) Geng, Z.; Liu, Y.; Kong, X.; Li, P.; Li, K.; Liu, Z.; Du, J.; Shu, M.; Si, R.; Zeng, J. Achieving a Record-High Yield Rate of 120.9 μg_{NH3} $mg_{cat.}^{-1}$ h^{-1} for N_2 Electrochemical Reduction over Ru Single-Atom Catalysts. *Adv. Mater.* **2018**, *30*, 1803498.
(27) Wang, D.; Azofra, L. M.; Harb, M.; Cavallo, L.; Zhang, X.; Suryanto, B. H. R.; MacFarlane, D. R. Energy-Efficient Nitrogen Reduction to Ammonia at Low Overpotential in Aqueous Electrolyte under Ambient Conditions. *ChemSusChem* **2018**, *11*, 3416−3422.
(28) Tao, H.; Choi, C.; Ding, L.-X.; Jiang, Z.; Han, Z.; Jia, M.; Fan, Q.; Gao, Y.; Wang, H.; Robertson, A. W.; et al. Nitrogen Fixation by Ru Single-Atom Electrocatalytic Reduction. *Chem* **2019**, *5*, 204−214.
(29) Suryanto, B. H. R.; Wang, D.; Azofra, L. M.; Harb, M.; Cavallo, L.; Jalili, R.; Mitchell, D. R. G.; Chatti, M.; MacFarlane, D. R. MoS_2 Polymorphic Engineering Enhances Selectivity in the Electrochemical Reduction of Nitrogen to Ammonia. *ACS Energy Lett* **2019**, *4*, 430−435.
(30) Andersen, S. Z.; Čolić, V.; Yang, S.; Schwalbe, J. A.; Nielander, A. C.; McEnaney, J. M.; Enemark-Rasmussen, K.; Baker, J. G.; Singh, A. R.; Rohr, B. A.; et al. A Rigorous Electrochemical Ammonia Synthesis Protocol with Quantitative Isotope Measurements. *Nature* **2019**, *570*, 504−508.
(31) Yao, Y.; Wang, H.; Yuan, X.-z.; Li, H.; Shao, M. Electrochemical Nitrogen Reduction Reaction on Ruthenium. *ACS Energy Lett* **2019**, *4*, 1336−1341.
(32) Huang, L.; Wu, J.; Han, P.; Al-Enizi, A. M.; Almutairi, T. M.; Zhang, L.; Zheng, G. NbO_2 Electrocatalyst Toward 32% Faradaic Efficiency for N_2 Fixation. *Small Methods* **2019**, *3*, 1800386.
(33) Zhang, X.; Kong, R.-M.; Du, H.; Xia, L.; Qu, F. Highly Efficient Electrochemical Ammonia Synthesis *via* Nitrogen Reduction Reactions on a VN Nanowire Array under Ambient Conditions. *Chem. Commun.* **2018**, *54*, 5323−5325.
(34) Yang, X.; Nash, J.; Anibal, J.; Dunwell, M.; Kattel, S.; Stavitski, E.; Attenkofer, K.; Chen, J. G.; Yan, Y.; Xu, B. Mechanistic Insights into Electrochemical Nitrogen Reduction Reaction on Vanadium Nitride Nanoparticles. *J. Am. Chem. Soc.* **2018**, *140*, 13387−13391.
(35) Zhang, R.; Zhang, Y.; Ren, X.; Cui, G.; Asiri, A. M.; Zheng, B.; Sun, X. High-Efficiency Electrosynthesis of Ammonia with High Selectivity under Ambient Conditions Enabled by VN Nanosheet Array. *ACS Sustain. Chem. Eng.* **2018**, *6*, 9545−9549.
(36) Zhang, L.; Ji, X.; Ren, X.; Luo, Y.; Shi, X.; Asiri, A. M.; Zheng, B.; Sun, X. Efficient Electrochemical N_2 Reduction to NH_3 on MoN Nanosheets Array under Ambient Conditions. *ACS Sustain. Chem. Eng.* **2018**, *6*, 9550−9554.
(37) Nørskov, J. K.; Rossmeisl, J.; Logadottir, A.; Lindqvist, L.; Kitchin, J. R.; Bligaard, T.; Jónsson, H. Origin of the Overpotential for Oxygen Reduction at a Fuel-Cell Cathode. *J. Phys. Chem. B* **2004**, *108*, 17886−17892.
(38) Greeley, J.; Jaramillo, T. F.; Bonde, J.; Chorkendorff, I.; Nørskov, J. K. Computational High-Throughput Screening of Electrocatalytic Materials for Hydrogen Evolution. *Nat. Mater.* **2006**, *5*, 909−913.
(39) Greeley, J.; Stephens, I. E. L.; Bondarenko, A. S.; Johansson, T. P.; Hansen, H. A.; Jaramillo, T. F.; Rossmeisl, J.; Chorkendorff, I.; Nørskov, J. K. Alloys of Platinum and Early Transition Metals as Oxygen Reduction Electrocatalysts. *Nat. Chem.* **2009**, *1*, 552−556.
(40) Peterson, A. A.; Abild-Pedersen, F.; Studt, F.; Rossmeisl, J.; Nørskov, J. K. How Copper Catalyzes the Electroreduction of Carbon Dioxide into Hydrocarbon Fuels. *Energy Environ. Sci.* **2010**, *3*, 1311−1315.
(41) Peterson, A. A.; Nørskov, J. K. Activity Descriptors for CO_2 electroreduction to Methane on Transition-Metal Catalysts. *J. Phys. Chem. Lett.* **2012**, *3*, 251−258.
(42) Karamad, M.; Hansen, H. A.; Rossmeisl, J.; Nørskov, J. K. Mechanistic Pathway in the Electrochemical Reduction of CO_2 on RuO_2. *ACS Catal.* **2015**, *5*, 4075−4081.
(43) Bhowmik, A.; Hansen, H. A.; Vegge, T. Role of CO* as a Spectator in CO_2 Electroreduction on RuO_2. *J. Phys. Chem. C* **2017**, *121*, 18333−18343.
(44) Tayyebi, E.; Hussain, J.; Abghoui, Y.; Skúlason, E. Trends of Electrochemical CO_2 Reduction Reaction on Transition Metal Oxide Catalysts. *J. Phys. Chem. C* **2018**, *122*, 10078−10087.
(45) Hussain, J.; Jónsson, H.; Skúlason, E. Faraday Efficiency and Mechanism of Electrochemical Surface Reactions: CO_2 reduction and H_2 formation on Pt(111). *Faraday Discuss.* **2016**, *195*, 619−636.
(46) Hussain, J.; Jónsson, H.; Skúlason, E. Calculations of Product Selectirvity in Electrochemical CO_2 Reduction. *ACS Catal.* **2018**, *8*, 5240−5249.
(47) Skúlason, E.; Karlberg, G. S.; Rossmeisl, J.; Bligaard, T.; Greeley, J.; Jónsson, H.; Nørskov, J. K. Density Functional Theory Calculations for the Hydrogen Evolution Reaction in an Electrochemical Double Layer on the Pt(111) Electrode. *Phys. Chem. Chem. Phys.* **2007**, *9*, 3241−3250.
(48) Rossmeisl, J.; Skúlason, E.; Björketun, M. E.; Tripkovic, V.; Nørskov, J. K. Modeling the Electrified Solid−Liquid Interface. *Chem. Phys. Lett.* **2008**, *466*, 68−71.
(49) Skúlason, E.; Tripkovic, V.; Björketun, M. E.; Gudmundsdóttir, S.; Karlberg, G.; Rossmeisl, J.; Bligaard, T.; Jónsson, H.; Nørskov, J. K. Modeling the Electrochemical Hydrogen Oxidation and Evolution

DOI: 10.1021/acscatal.9b03903
ACS Catal. 2019, 9, 11137−11145

Reactions on the Basis of Density Functional Theory Calculations. *J. Phys. Chem. C* **2010**, *114*, 18182−18197.
(50) Helmholtz, H. Ueber Einige Gesetze Der Vertheilung Elektrischer Ströme in Körperlichen Leitern Mit Anwendung Auf Die Thierisch-elektrischen Versuche. *Ann. Phys.* **1853**, *165*, 211−233.
(51) Gouy, M. Sur La Constitution de La Charge Électrique à La Surface d'un Électrolyte. *J. Phys. Théorique Appliquée* **1910**, *9*, 457−468.
(52) Stern, O. Zur Theorie Der Elektrolytischen Doppelschicht. *Zeitschrift für Elektrochemie Angew. Phys. Chemie* **1924**, *30*, 508−516.
(53) Grahame, D. C. The Electrical Double Layer and the Theory of Electrocapillarity. *Chem. Rev.* **1947**, *41*, 441−501.
(54) Rostamikia, G.; Maheshwari, S.; Janik, M. J. Elementary Kinetics of Nitrogen Electroreduction to Ammonia on Late Transition Metals. *Catal. Sci. Technol.* **2019**, *9*, 174−181.
(55) Maheshwari, S.; Rostamikia, G.; Janik, M. J. Elementary Kinetics of Nitrogen Electroreduction on Fe Surfaces. *J. Chem. Phys.* **2019**, *150*, 041708.
(56) Dahl, S.; Logadottir, A.; Egeberg, R. C.; Larsen, J. H.; Chorkendorff, I.; Törnqvist, E.; Nørskov, J. K. Role of Steps in N_2 Activation on Ru(0001). *Phys. Rev. Lett.* **1999**, *83*, 1814−1817.
(57) Honkala, K.; Hellman, A.; Remediakis, I. N.; Logadottir, A.; Carlsson, A.; Dahl, S.; Christensen, C. H.; Nørskov, J. K. Ammonia Synthesis from First-Principles Calculations. *Science* **2005**, *307*, 555−558.
(58) Garden, A. L.; Skúlason, E. The Mechanism of Industrial Ammonia Synthesis Revisited: Calculations of the Role of the Associative Mechanism. *J. Phys. Chem. C* **2015**, *119*, 26554−26559.
(59) Blöchl, P. E. Projector Augmented-Wave Method. *Phys. Rev. B* **1994**, *50*, 17953−17979.
(60) Kresse, G.; Furthmüller, J. Efficient Iterative Schemes for Ab Initio Total-Energy Calculations Using a Plane-Wave Basis Set. *Phys. Rev. B Condens. Matter Mater. Phys.* **1996**, *54*, 11169−11186.
(61) Joubert, D.; Joubert, D. From Ultrasoft Pseudopotentials to the Projector Augmented-Wave Method. *Phys. Rev. B Condens. Matter Mater. Phys.* **1999**, *59*, 1758−1775.
(62) Henkelman, G.; Uberuaga, B. P.; Jónsson, H. Climbing Image Nudged Elastic Band Method for Finding Saddle Points and Minimum Energy Paths. *J. Chem. Phys.* **2000**, *113*, 9901−9904.
(63) Henkelman, G.; Jónsson, H. Improved Tangent Estimate in the Nudged Elastic Band Method for Finding Minimum Energy Paths and Saddle Points. *J. Chem. Phys.* **2000**, *113*, 9978−9985.
(64) Wellendorff, J.; Lundgaard, K. T.; Møgelhøj, A.; Petzold, V.; Landis, D. D.; Nørskov, J. K.; Bligaard, T.; Jacobsen, K. W. Density Functionals for Surface Science: Exchange-Correlation Model Development with Bayesian Error Estimation. *Phys. Rev. B Condens. Matter Mater. Phys.* **2012**, *85*, 235149.
(65) Bhowmik, A.; Vegge, T.; Hansen, H. A. Descriptors and Thermodynamic Limitations of Electrocatalytic Carbon Dioxide Reduction on Rutile Oxide Surfaces. *ChemSusChem* **2016**, *9*, 3230−3243.
(66) Hammer, B.; Hansen, L. B.; Nørskov, J. K. Improved Adsorption Energetics within Density-Functional Theory Using Revised Perdew-Burke-Ernzerhof Functionals. *Phys. Rev. B Condens. Matter Mater. Phys.* **1999**, *59*, 7413−7421.
(67) Clay, C.; Haq, S.; Hodgson, A. Intact and Dissociative Adsorption of Water on Ru(0001). *Chem. Phys. Lett.* **2004**, *388*, 89−93.
(68) Andersson, K.; Nikitin, A.; Pettersson, L. G. M.; Nilsson, A.; Ogasawara, H. Water Dissociation on Ru(001): An Activated Process. *Phys. Rev. Lett.* **2004**, *93*, 196101.
(69) Faradzhev, N. S.; Kostov, K. L.; Feulner, P.; Madey, T. E.; Menzel, D. Stability of Water Monolayers on Ru(0001): Thermal and Electronically Induced Dissociation. *Chem. Phys. Lett.* **2005**, *415*, 165−171.
(70) Maier, S.; Salmeron, M. How Does Water Wet a Surface? *Acc. Chem. Res.* **2015**, *48*, 2783−2790.
(71) Michaelides, A.; Alavi, A.; King, D. A. Different Surface Chemistries of Water on Ru{0001}: From Monomer Adsorption to Partially Dissociated Bilayers. *J. Am. Chem. Soc.* **2003**, *125*, 2746−2755.
(72) Tripkovic, V.; Björketun, M. E.; Skúlason, E.; Rossmeisl, J. Standard Hydrogen Electrode and Potential of Zero Charge in Density Functional Calculations. *Phys. Rev. B* **2011**, *84*, 115452.
(73) Gudmundsdóttir, S.; Tang, W.; Henkelman, G.; Jónsson, H.; Skúlason, E. Local Density of States Analysis Using Bader Decomposition for N_2 and CO_2 Adsorbed on Pt(110)-(1 × 2) Electrodes. *J. Chem. Phys.* **2012**, *137*, 164705.

DOI: 10.1021/acscatal.9b03903
ACS Catal. 2019, 9, 11137−11145

Supporting Information

Elucidating the mechanism of electrochemical N_2 reduction at the Ru(0001) electrode

Ebrahim Tayyebi[1], Younes Abghoui[1], Egill Skúlason[1,2,*]

[1]Science Institute, University of Iceland, VR-III, 107 Reykjavík, Iceland

[2]Faculty of Industrial Engineering, Mechanical Engineering and Computer Science, University of Iceland, VR-III, 107 Reykjavík, Iceland

*Corresponding Author: egillsk@hi.is

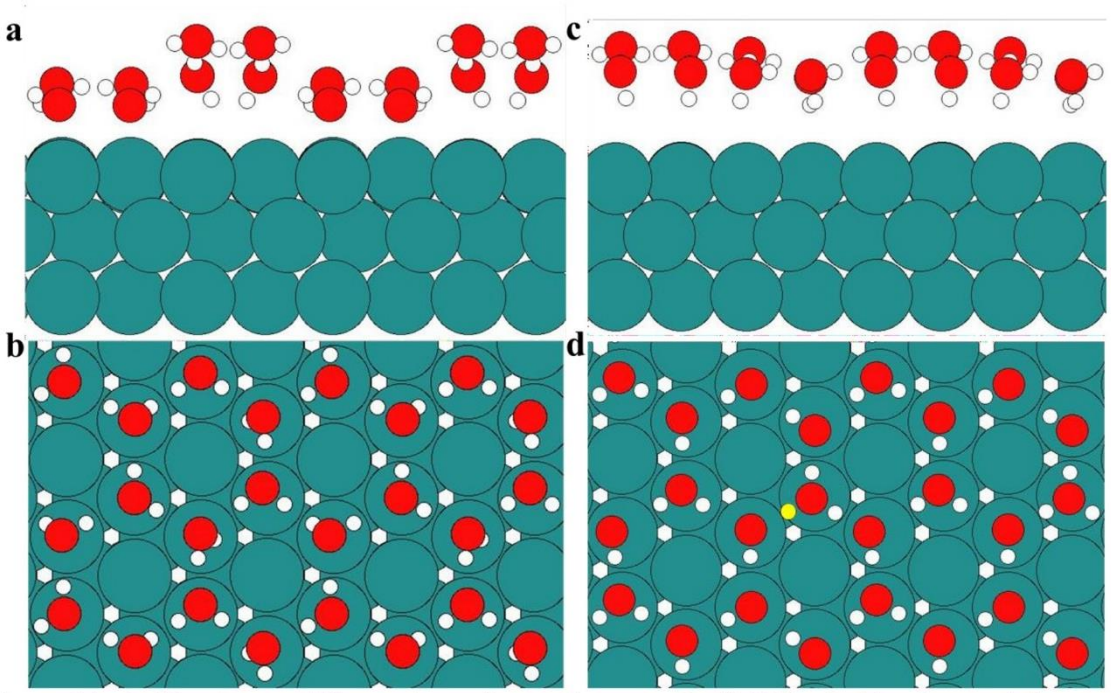

Figure S1. a) side view and b) top view of water layer on Ru (0001). c) side view and d) top view of water bilayer on Ru(0001) in the presence of one extra proton (-0.6 V applied potential). The extra proton is colored yellow.

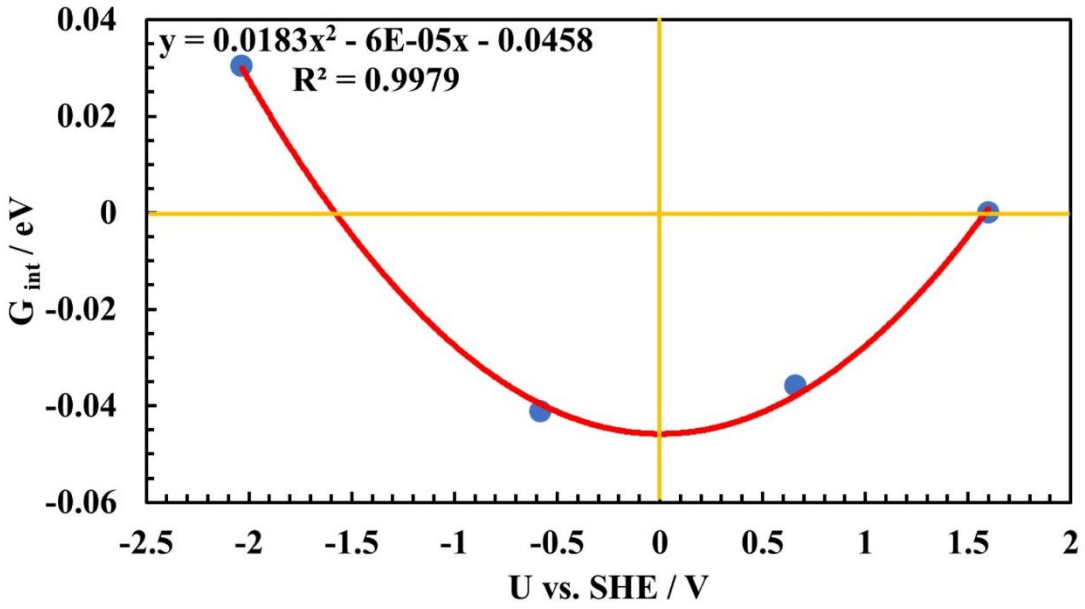

Figure S2. Integral free energy of the protons in the double layer as a function of the applied potential obtained from the work function. Systems with four different proton-electron concentrations are used to obtain the parabola. The chemical potential of hydrogen is at standard conditions and therefore the minimum free energy defines zero potential vs. SHE[1,2]. The system with -0.6 V applied potential is used to evaluate the energy barriers in this work.

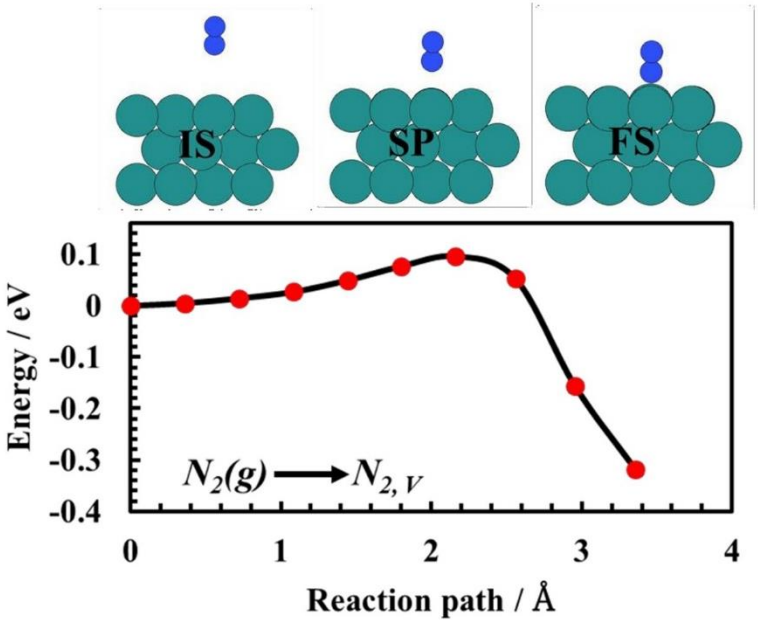

Figure S3. DFT calculated barrier for N_2(g) adsorption on Ru(0001) surface. (IS) initial state (SP) saddle point and (FS) final state are shown on the top of the figure.

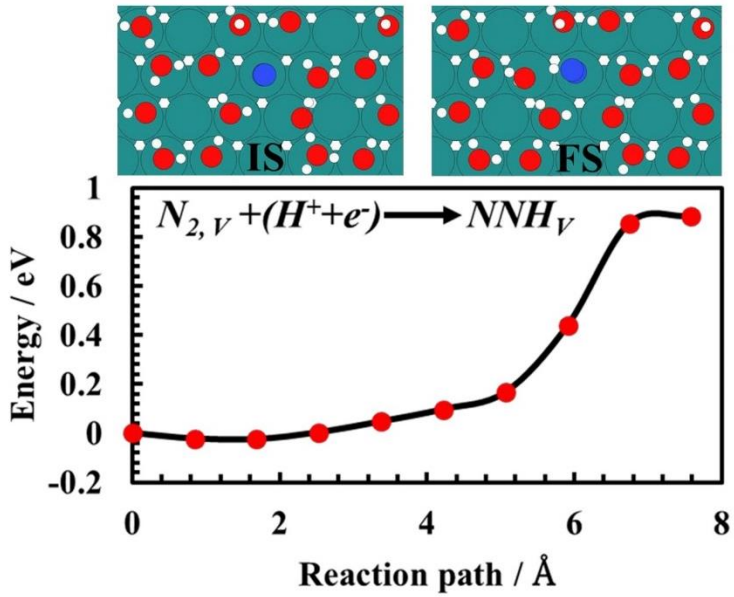

Figure S4. DFT calculated barrier for $N_{2,V}$ protonation to NNH_V on Ru(0001) surface. (IS) initial state and (FS) final state are shown on the top of the figure.

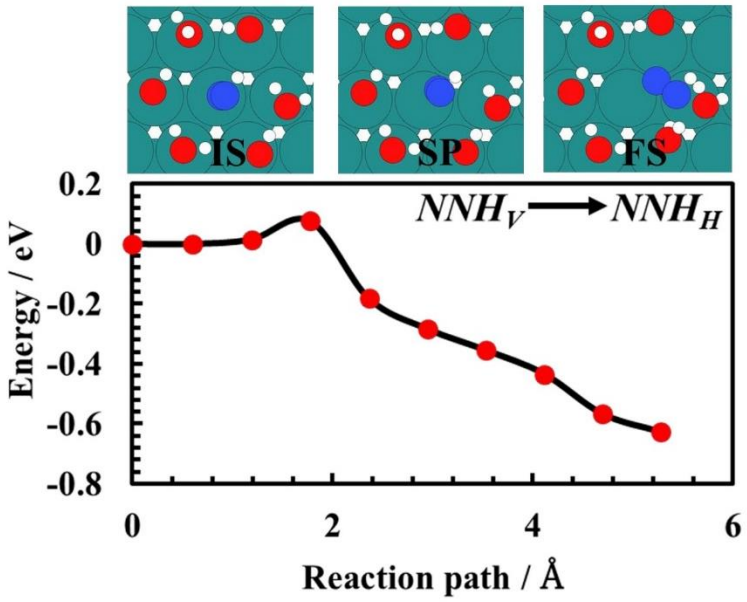

Figure S5. DFT calculated barrier for NNH_V to NNH_H on Ru(0001) surface. (IS) initial state, (SP) saddle point and (FS) final state are shown on the top of the figure.

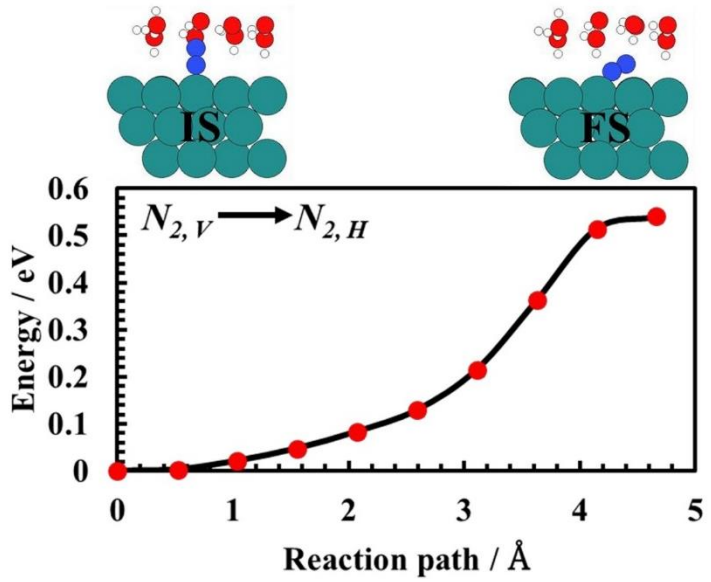

Figure S6. DFT calculated barrier for $N_{2,V}$ to $N_{2,H}$ on Ru(0001) surface. (IS) initial state and (FS) final state are shown on the top of the figure.

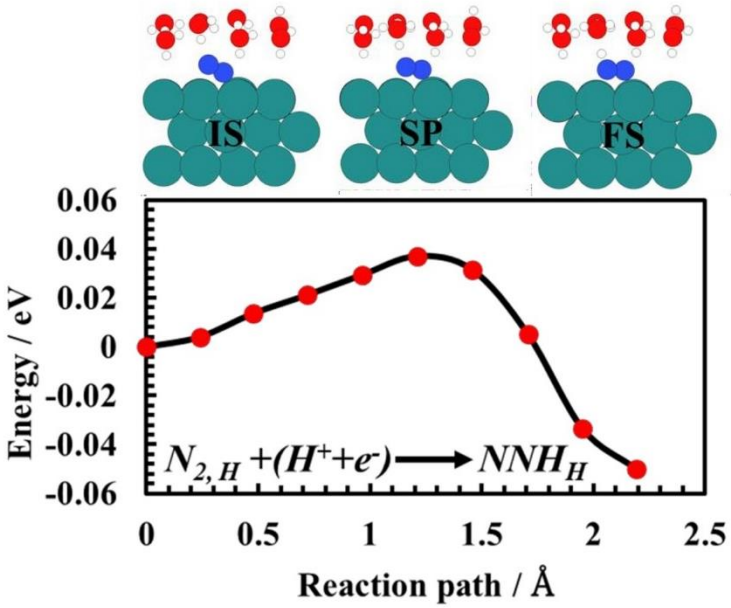

Figure S7. DFT calculated barrier for $N_{2,H}$ protonation to NNH_H on Ru(0001) surface. (IS) initial state, (SP) saddle point and (FS) final state are shown on the top of the figure.

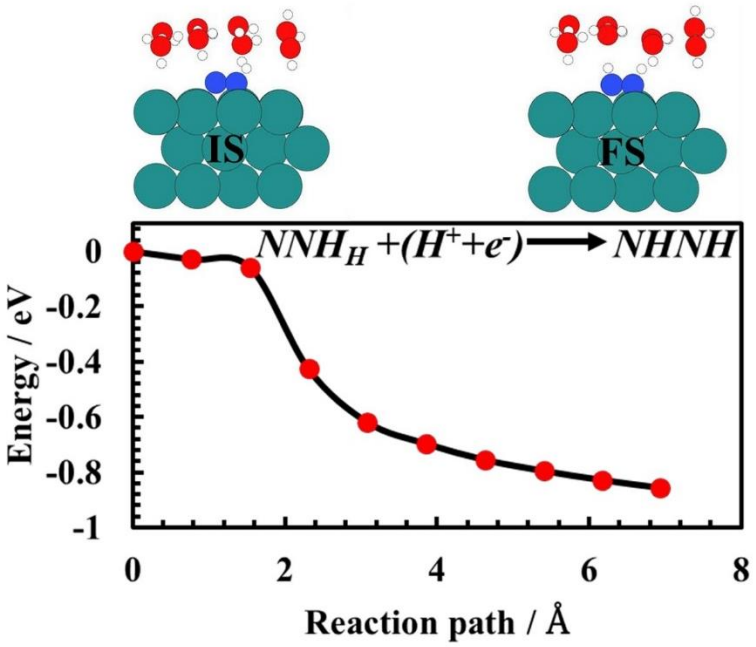

Figure S8. DFT calculated barrier for NNH_H protonation to NHNH on Ru(0001) surface. (IS) initial state and (FS) final state are shown on the top of the figure.

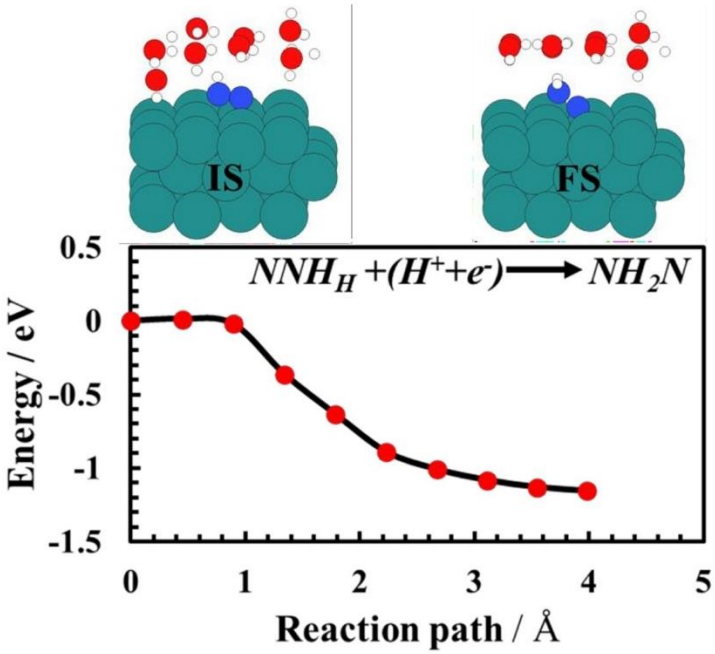

Figure S9. DFT calculated barrier for NNH_H protonation to NH_2N on Ru(0001) surface. (IS) initial state and (FS) final state are shown on the top of the figure.

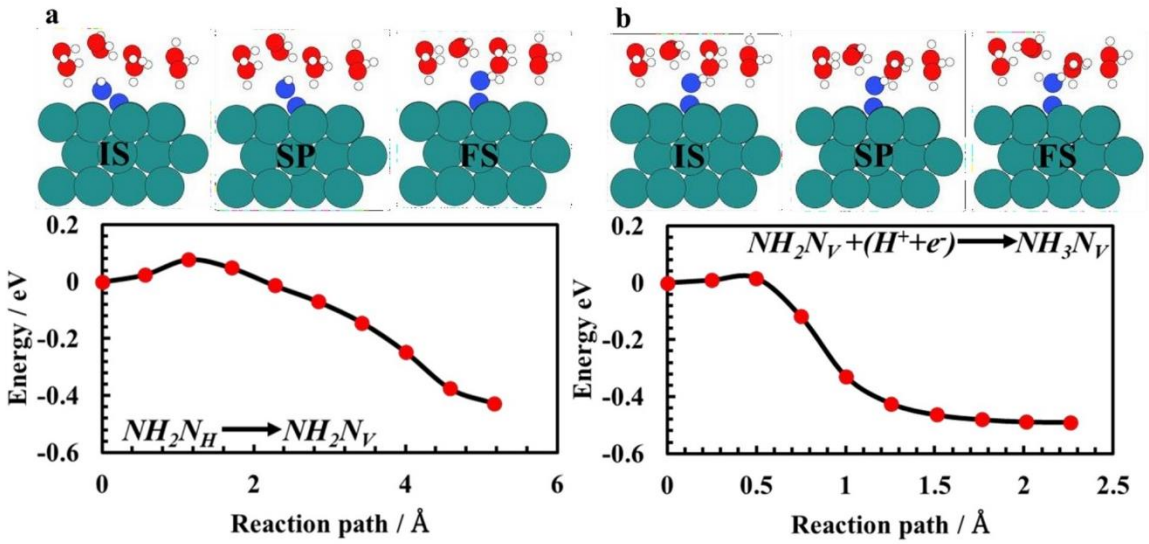

Figure S10. DFT calculated barrier for a) NH_2N_H to NH_2N_V and b) NH_2N_V protonation to NH_3N_V on Ru (0001) surface. (IS) initial state, (SP) saddle point and (FS) final state are shown on the top of the figure.

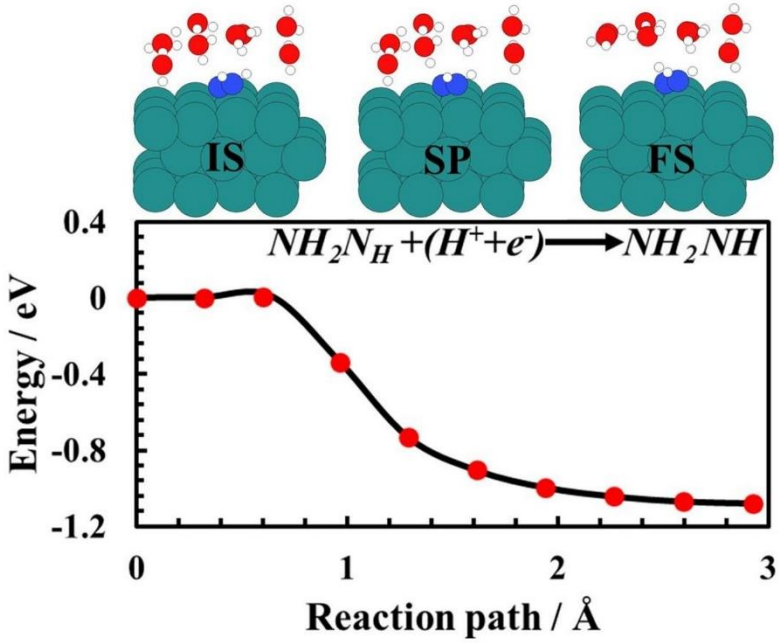

Figure S11. DFT calculated barrier for NH_2N protonation to NH_2NH on Ru(0001) surface. (IS) initial state, (SP) saddle point and (FS) final state are shown on the top of the figure.

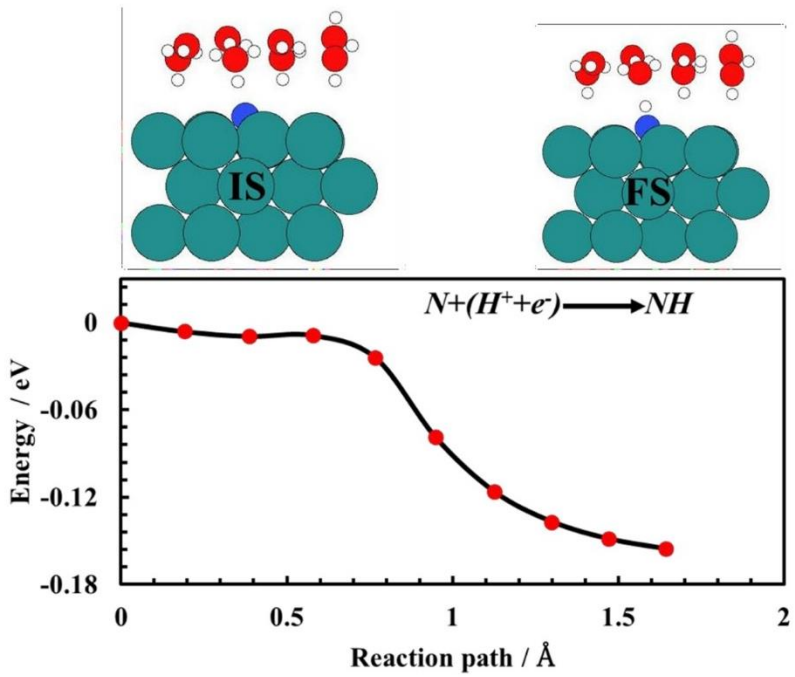

Figure S12. DFT calculated barrier for N protonation to NH on Ru(0001) surface. (IS) initial state and (FS) final state are shown on the top of the figure.

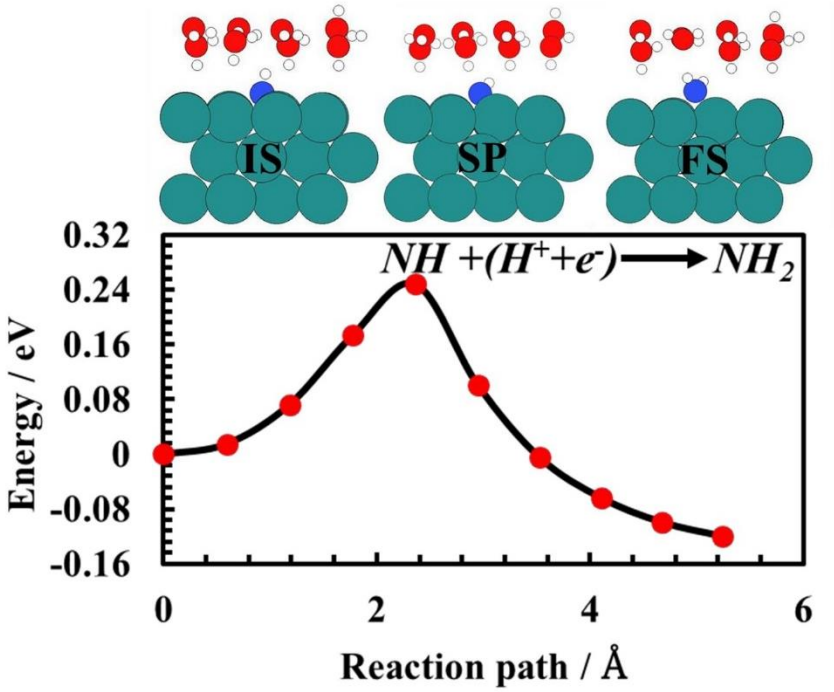

Figure S13. DFT calculated barrier for NH protonation to NH_2 on Ru(0001) surface. (IS) initi state, (SP) saddle point and (FS) final state are shown on the top of the figure.

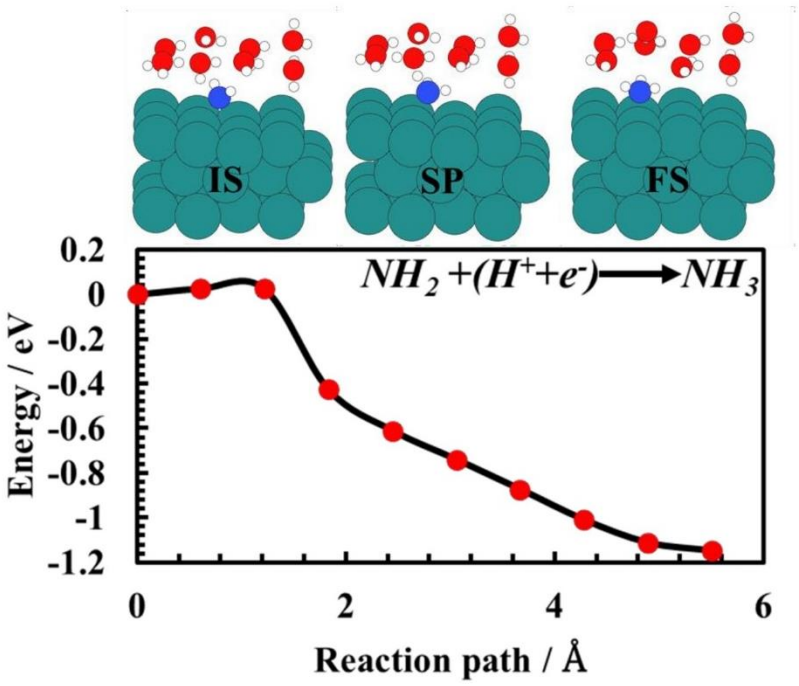

Figure S14. DFT calculated barrier for NH_2 protonation to NH_3 on Ru(0001) surface. (IS) initial state, (SP) saddle point and (FS) final state are shown on the top of the figure.

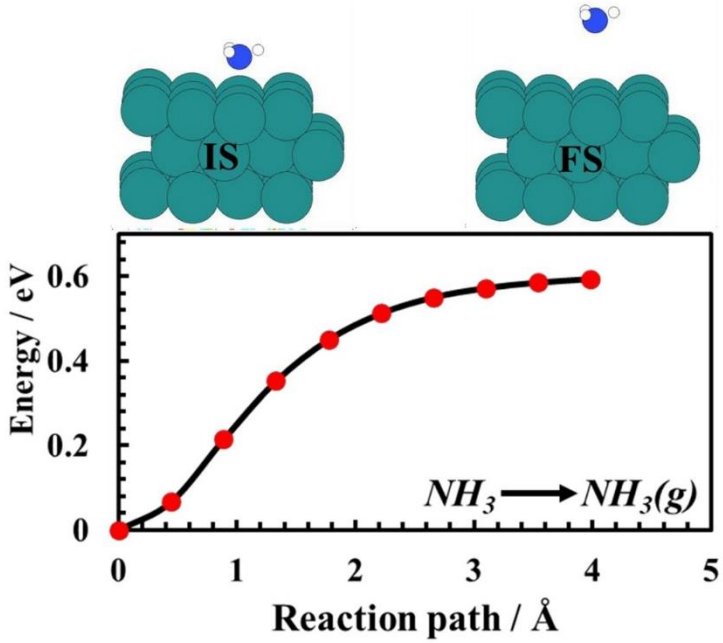

Figure S15. DFT calculated barrier for NH_3 desorption on Ru(0001) surface. (IS) initial state and (FS) final state are shown on the top of the figure.

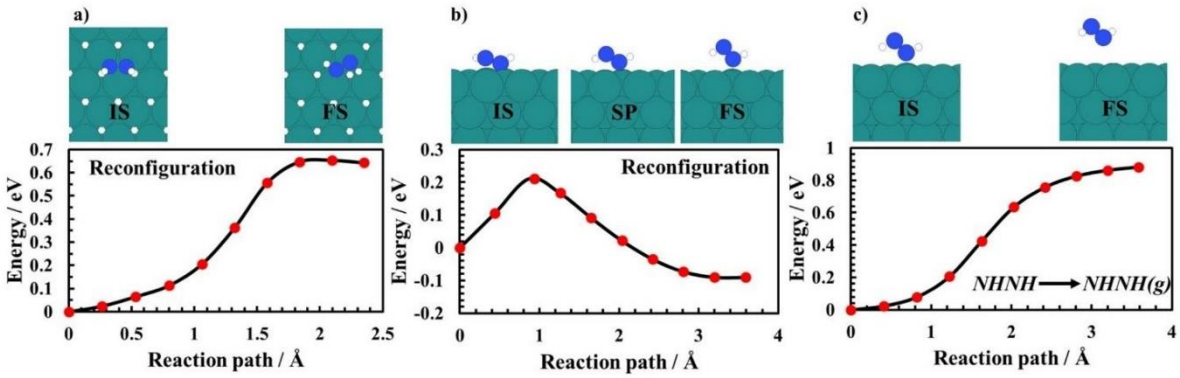

Figure S16. DFT calculated barrier for **a)** and **b**) NHNH reconfiguration and **c**) NHNH desorption on Ru (0001) surface. (IS) initial state, (SP) saddle point and (FS) final state are also shown on the top of the figure.

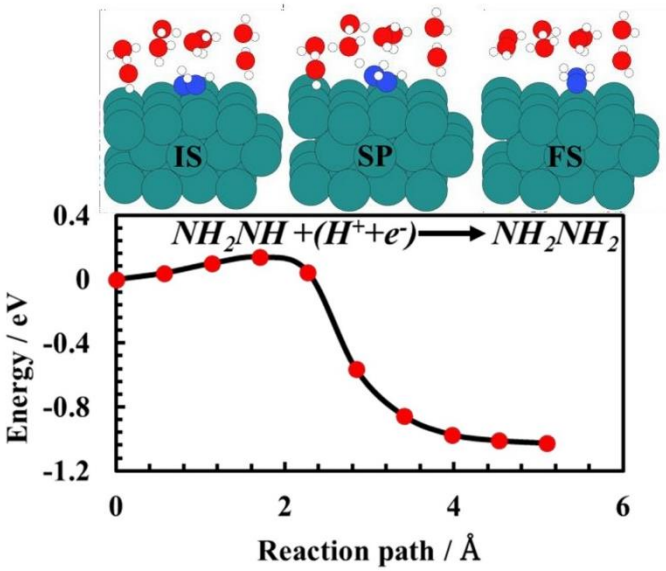

Figure S17. DFT calculated barrier for NH_2NH protonation to NH_2NH_2 on Ru(0001) surface. (IS) initial state, (SP) saddle point and (FS) final state are shown on the top of the figure.

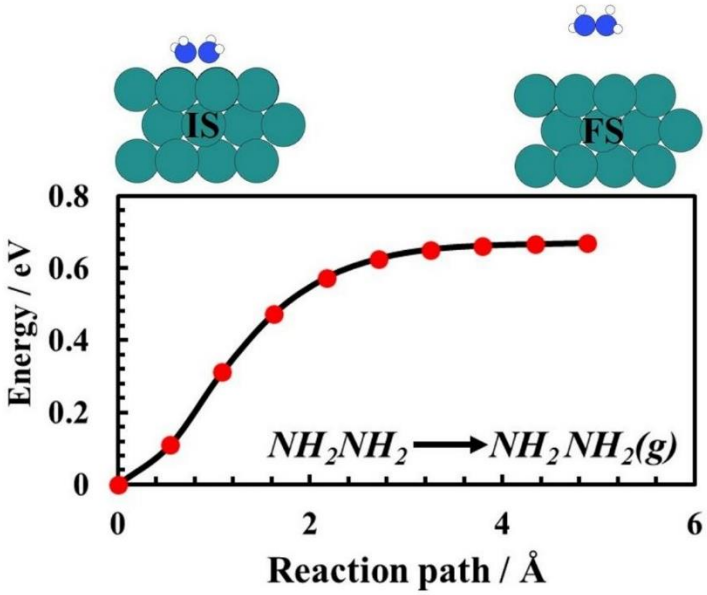

Figure S18. DFT calculated barrier for NH_2NH_2 desorption on Ru(0001) surface. (IS) initial state and (FS) final state are shown on the top of the figure.

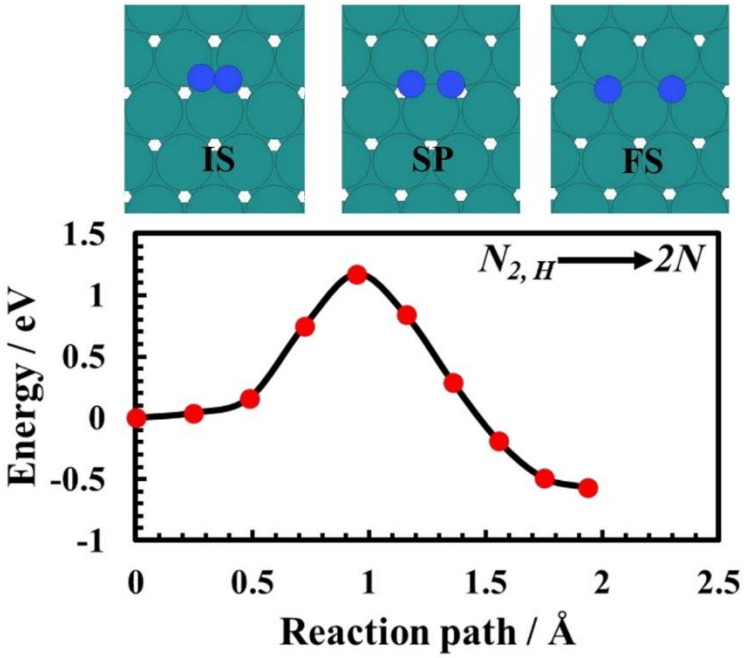

Figure S19. DFT calculated $N_{2,H}$ dissociation barrier on Ru (0001) surface. (IS) initial state, (SP) saddle point and (FS) final state are shown on the top of the figure.

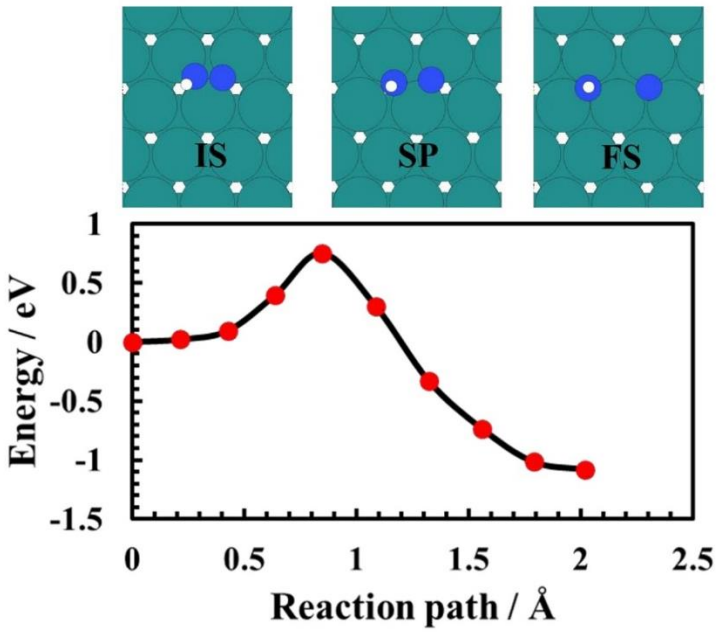

Figure S20. DFT calculated NNH_H dissociation barrier on Ru(0001) surface. (IS) initial state, (SP) saddle point and (FS) final state are also shown on the top of the figure.

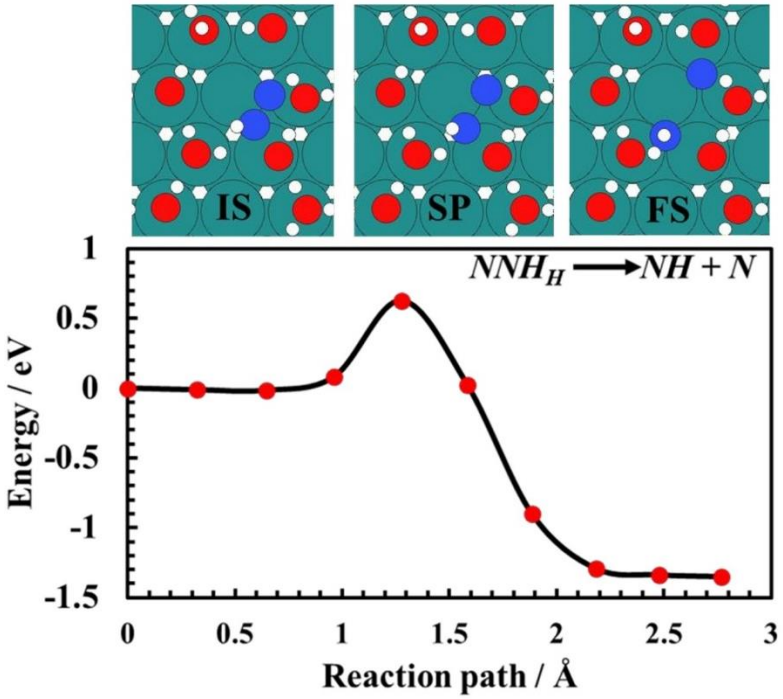

Figure S21. DFT calculated NNH_H dissociation barrier on Ru(0001) surface in the presence of protonated water layer. (IS) initial state, (SP) saddle point and (FS) final state are also shown on the top of the figure.

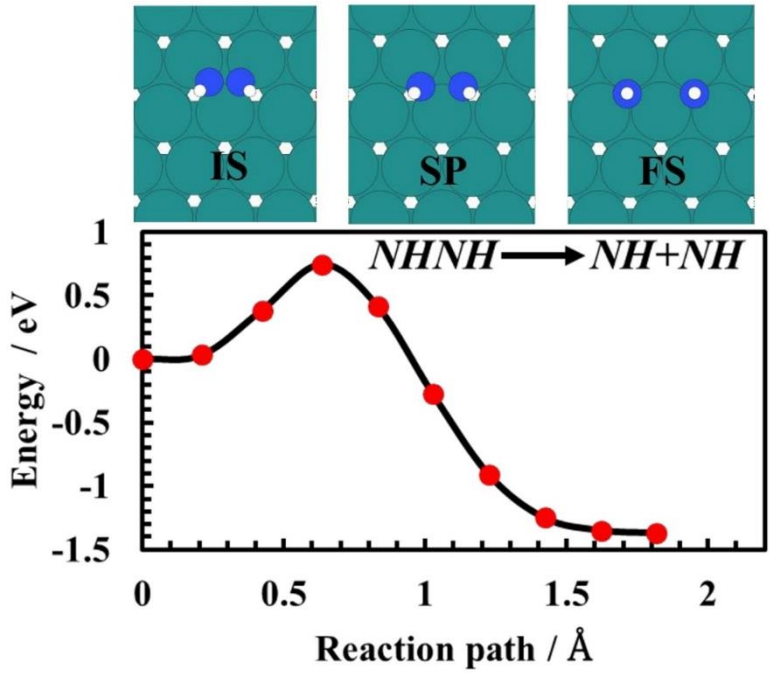

Figure S22. DFT calculated NHNH dissociation barrier on Ru(0001) surface. (IS) initial state, (SP) saddle point and (FS) final state are shown on the top of the figure.

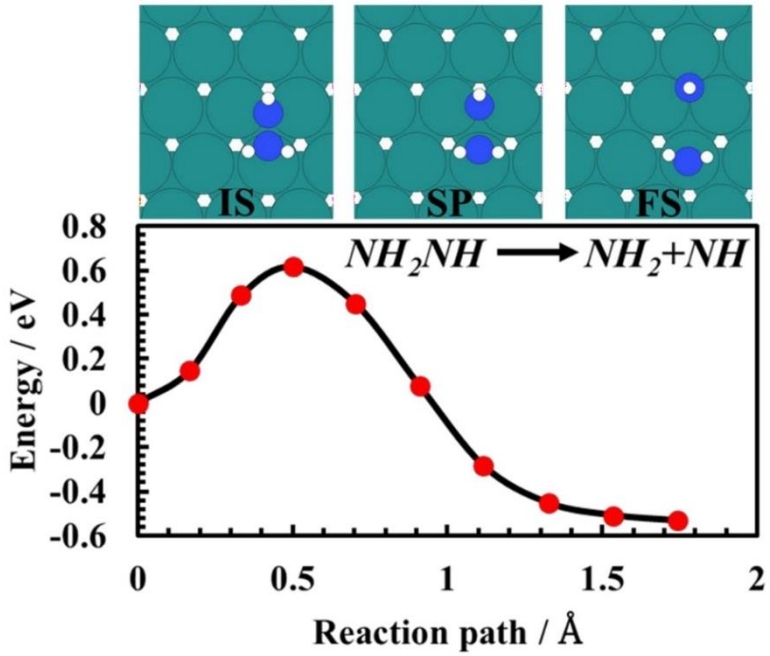

Figure S23. DFT calculated NH_2NH dissociation barrier on Ru(0001) surface. (IS) initial state, (SP) saddle point and (FS) final state are shown on the top of the figure.

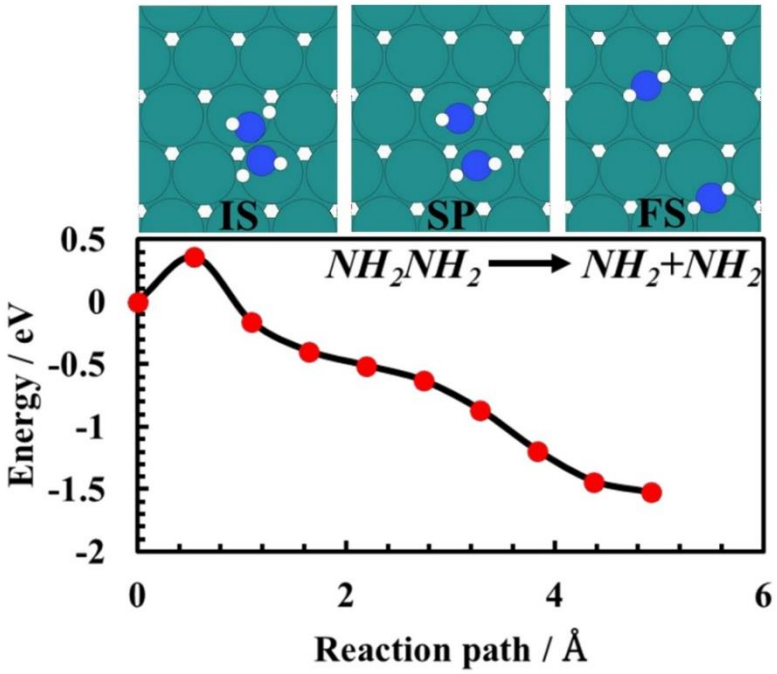

Figure S24. DFT calculated NH_2NH_2 dissociation barrier on Ru(0001) surface. (IS) initial state, (SP) saddle point and (FS) final state are shown on the top of the figure.

References

(1) Rossmeisl, J.; Skúlason, E.; Björketun, M. E.; Tripkovic, V.; Nørskov, J. K. Modeling the Electrified Solid–liquid Interface. *Chem. Phys. Lett.* **2008**, *466*, 68–71.

(2) Skúlason, E.; Tripkovic, V.; Björketun, M. E.; Gudmundsdóttir, S.; Karlberg, G.; Rossmeisl, J.; Bligaard, T.; Jónsson, H.; Nørskov, J. K. Modeling the Electrochemical Hydrogen Oxidation and Evolution Reactions on the Basis of Density Functional Theory Calculations. *J. Phys. Chem. C* **2010**, *114*, 18182–18197.